

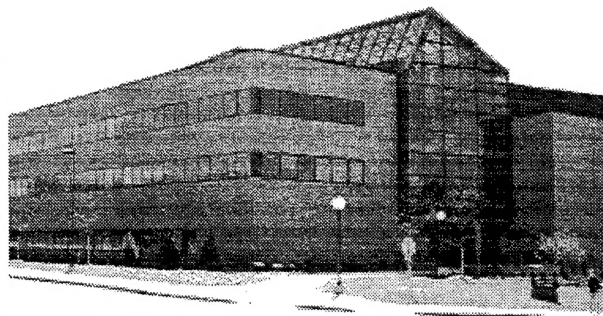
AFOSR CONTRACTORS MEETING IN AIRBREATHING COMBUSTION



Department of Aerospace Engineering
The University of Michigan
Ann Arbor, Michigan

June 13-15, 1995

19950824 194



REPORT DOCUMENTATION PAGE

Form Approved
OMB No. 0704-0188

Public reporting burden for this collection of information is estimated to average 1 hour per response, including the time for reviewing instructions, searching existing data sources, gathering and maintaining the data needed, and completing and reviewing the collection of information. Send comments regarding this burden estimate or any other aspect of this collection of information, including suggestions for reducing this burden, to Washington Headquarters Services, Directorate for Information Operations and Reports, 1215 Jefferson Davis Highway, Suite 1204, Arlington, VA 22202-4302, and to the Office of Management and Budget, Paperwork Reduction Project (0704-0188), Washington, DC 20503.

1. AGENCY USE ONLY (Leave blank)		2. REPORT DATE 19 June 1995		3. REPORT TYPE AND DATES COVERED Technical	
4. TITLE AND SUBTITLE (U) AFOSR Contractors Meeting in Airbreathing Combustion				5. FUNDING NUMBERS PE - 61102F PR - 2308	
6. AUTHOR(S) J. M. Tishkoff					
7. PERFORMING ORGANIZATION NAME(S) AND ADDRESS(ES)				8. PERFORMING ORGANIZATION REPORT NUMBER	
9. SPONSORING/MONITORING AGENCY NAME(S) AND ADDRESS(ES) AFOSR/NA 110 Duncan Avenue, Suite B115 Bolling AFB DC 20332-0001 NA				10. SPONSORING/MONITORING AGENCY REPORT NUMBER	
11. SUPPLEMENTARY NOTES					
12a. DISTRIBUTION/AVAILABILITY STATEMENT Approved for public release; distribution is unlimited				12b. DISTRIBUTION CODE	
13. ABSTRACT (Maximum 200 words) Abstracts are given for research in airbreathing combustion and propulsion diagnostics supported by the Air Force Office of Scientific Research. Approved for public release, distribution unlimited AIR FORCE OF SCIENTIFIC RESEARCH (AFSC) NOTICE OF TRANSMITTAL TO DTIC This technical report has been reviewed and approved for public release by AFR 190-12 distribution unlimited. Joan Bogge STINFO Procs DTIC QUALITY INSPECTED 5					
14. SUBJECT TERMS Flames, Propulsion, Gas Turbines, Combustion, Shear Layer, Supersonic, Soot, Sprays, Lasers, Fluorescence, Spectroscopy, Scramjets				15. NUMBER OF PAGES 154	
17. SECURITY CLASSIFICATION OF REPORT Unclassified				18. SECURITY CLASSIFICATION OF THIS PAGE Unclassified	
19. SECURITY CLASSIFICATION OF ABSTRACT Unclassified				20. LIMITATION OF ABSTRACT UL	
16. PRICE CODE					

AFOSR CONTRACTORS MEETING

IN

AIRBREATHING COMBUSTION

**Campus Inn
Ann Arbor MI 48104
13-15 June 1995**

TUESDAY, 13 JUNE 1995

- 1:00 - 1:10 Welcome and Opening Remarks
- 1:10 - 1:30 Status of Air Force Basic Research in Airbreathing
Combustion
Julian Tishkoff, AFOSR/NA

TURBULENCE

Chair: David Mann, Army Research Office

- 1:30 - 2:00 Turbulent Combustion
W M Roquemore, WL/POSC
- 2:00 - 2:30 Two- And Three-Dimensional Measurements in Flames
M B Long, Yale University
- 2:30 - 3:00 BREAK
- 3:00 - 3:30 Turbulence-Chemistry Models for Highly Turbulent Flames
S M Correa, GE Corporate Research and Development
- 3:30 - 4:00 Modeling Mixing and Reaction in Turbulent Combustion
S B Pope, Cornell University
- 4:00 - 4:30 Reaction Zone Models for Vortex Simulation of Turbulent
Combustion
A F Ghoniem, Massachusetts Institute of Technology
- 4:30 - 7:15 BREAK
- 7:15 - 9:15 WORKSHOP
- Defining Future Thrusts for Airbreathing Combustion
Research

For	
1	<input checked="" type="checkbox"/>
2	<input type="checkbox"/>
3	<input type="checkbox"/>
4	
5	
6	
7	
8	
9	
10	
11	
12	
13	
14	
15	
16	
17	
18	
19	
20	
21	
22	
23	
24	
25	
26	
27	
28	
29	
30	
31	
32	
33	
34	
35	
36	
37	
38	
39	
40	
41	
42	
43	
44	
45	
46	
47	
48	
49	
50	
51	
52	
53	
54	
55	
56	
57	
58	
59	
60	
61	
62	
63	
64	
65	
66	
67	
68	
69	
70	
71	
72	
73	
74	
75	
76	
77	
78	
79	
80	
81	
82	
83	
84	
85	
86	
87	
88	
89	
90	
91	
92	
93	
94	
95	
96	
97	
98	
99	
100	

A-1

WEDNESDAY, 14 JUNE 1995

SUPERSONIC COMBUSTION

Chair: Edward J Mularz, Army Aviation Activity

- 9:00 - 9:30 Ramjet Research
A S Nejad, WL//POPT
- 9:30 - 10:00 Research on Supersonic reacting Flows
C T Bowman, R K Hanson, M G Mungal, and W C
Reynolds, Stanford University
- 10:00 - 10:30 High Resolution Measurements of Supersonic Mixing and
Combustion in Coflowing Turbulent Jets
W J A Dahm and J F Driscoll, University of Michigan
- 10:30 - 11:00 BREAK
- 11:00 - 11:45 Chemical Reactions in Turbulent Mixing Flows
P E Dimotakis and A Leonard, California Institute of
Technology
- 11:45 - 1:00 LUNCH

UNSTEADY AND DETONATION PHENOMENA

Chair: A S Nejad, WL/POPT

- 1:00 - 1:30 Studies on High-Pressure and Unsteady Flame Phenomena
C K Law, Princeton University
- 1:30 - 2:00 Numerical Studies of the Ram Accelerator
E S Oran, J P Boris, K Kailasanath, and C Li, Naval
Research Laboratory
- 2:00 - 2:30 BREAK
- 2:30 - 4:00 BUSINESS SESSION
- Contractors, Grantees, and Air Force Laboratory Task
Managers in Dr. Tishkoff's Program Only
- 4:00 ADJOURN

THURSDAY, 15 JUNE 1995

Optional Workshop on Supercritical Fuel Behavior - Contact Dr. Tishkoff at (202)767-0465 or Dr. Tim Edwards, (513)255-3524 for additional information

TURBULENT COMBUSTION

AFOSR: 2308S705

Principal Investigator: Dr. W. M. Roquemore

WL/POSC
Building 490
1790 Loop Road North
Wright-Patterson Air Force Base OH 45433-7103

SUMMARY/OVERVIEW:

The local Lewis number near the flame surface of a H_2/N_2 jet diffusion flame is known to be lower than unity. Previous computational studies by Katta et al. [1,2,3] suggest that when a laminar flamelet is compressed, the flame temperature changes due to the preferential diffusion, resulting from the non-unity Lewis number, and not because of incomplete chemical reactions. These studies also indicate that production of NO is significantly affected due to the flame stretching or compression. In order to verify these predictions, fluctuations in temperature and NO concentration are investigated by performing a combined numerical and experimental study on a low-speed dynamic H_2/N_2 flame that has vortical structures outside the flame surface. Two experimental studies have been undertaken. One experiment is being conducted by Carter et al. [4] and the second by Grisch, Attal-Tretout and Bouchardy [5]. Another experiment, being performed by Hancock [6], is investigating similar predictions when the vortex is formed inside the flame. This presentation gives comparisons of predictions with each of the three experiments. However, this written description is confined to a discussion of Carter's results. The results show there is very good agreement between the predictions and experiments. The implication of this work is that local Lewis Number effects can be very important in individual turbulent events involving vortex-flame interactions and this can have a large impact on the production of NO.

TECHNICAL DISCUSSION

The temperature and species distributions in the flame zone of a turbulent flame strongly influence combustion efficiency and pollutant production. A flame is considered to be fully turbulent, according to Hottel and Hawthorne [7], when its entire surface area becomes a flame brush, i.e., highly wrinkled, bumpy, and rough. The wrinkles and bumps in the flame are the localized protrusions of the flame surface that result from the interaction of the three-dimensional fluid elements with the reaction zone. Photographs taken with high-speed cameras indicate that these interacting fluid elements in a turbulent flame are often associated with vortices of different sizes, shapes, and strengths. A turbulent flame can be thought of as an ensemble of these individual vortex-flame interaction events. In order to develop mathematical models for a turbulent flame based on this statistical description, an

understanding of laminar flames, in which vortex-flame interactions take place deterministically, is essential.

A vertically mounted jet diffusion flame formed between coannular fuel and air jets provides a controlled system for studies of vortex-flame interactions. When the annulus air flow is low, buoyancy-influenced toroidal vortices form outside the flame surface. As these vortices are convected downstream, they interact with the flame and create locally stretched and compressed flamelets and, thereby, form wrinkles on the flame surface [8].

Recent numerical studies of a vortex-flame interaction, in a buoyant hydrogen/nitrogen jet diffusion flame, have predicted that significant changes occur in local temperature and OH and NO concentrations as an outside vortex interacts with the flame (Katta et al. [1] and Katta and Roquemore [2]). The changes are shown to be due to local variations in Lewis number that are manifested as changes in preferential diffusion as the flame is stretched. The local temperature and concentration of NO are predicted to increase in the compressed region of the flame and decrease in the stretched regions of the flame surface. A very different effect is expected from a laminar flame theory that uses a unity Lewis number. Laminar flamelet theory [9] suggests that when a diffusion flame is stretched, as in a vortex-flame interaction, the flame temperature decreases due to the increased reactant fluxes and the reduced Damkohler number (ratio of residence time to reaction time). This effect should have resulted in a decrease in flame temperature in a region of the flame where Katta et al. [1,2] predict preferential diffusion will cause the temperature to increase. The predictions are qualitatively consistent with studies by Law [10] on premixed flames that indicate preferential diffusion, resulting from the non-unity Lewis number, strongly influences the flame temperature when the flame is being stretched. To our knowledge, no one has experimentally observed changes in local temperature and species concentrations in a stretched diffusion flame that was attributable to preferential diffusion instead of changes in local Damkohler number. It is very rare in the field of combustion that a new, interesting, and potentially important effect is predicted before being experimentally observed. The rarity of the situation and its potential importance to understanding turbulent combustion processes demand that an experimental confirmation or rejection of the prediction be performed.

For the predictions, the time-dependent, axisymmetric Navier-Stokes equations written in the cylindrical-coordinate system are solved along with species- and energy-conservation equations[3]. The body-force term due to the gravitational field is included in the axial-momentum equation. A detailed chemical-kinetics model is used to describe the hydrogen-air combustion. This model consists of twelve species (H_2 , O_2 , H, O, OH, H_2O , HO_2 , H_2O_2 , N, NO, NO₂ and N₂) and 52 elementary reactions[11]. Temperature- and species-dependent properties are incorporated. The governing equations are integrated on a non-uniform staggered-grid system. An orthogonal grid having rapidly expanding cell sizes in both the axial and the radial direction is employed. The finite-difference forms of the momentum equations are obtained by an implicit QUICKEST scheme[12] and those of the species and energy equations by a hybrid scheme of upwind and central differencing. At every time-step, the pressure field is calculated by solving all the pressure Poisson equations simultaneously and utilizing the LU (Lower and Upper diagonal) matrix-decomposition technique.

A vertically mounted jet diffusion flame was established by burning a mixture of hydrogen and nitrogen emerging from a 10-mm-diameter contoured nozzle. The volumetric ratio between the hydrogen and nitrogen was 2.22. The fuel jet had a mass averaged velocity of 4.62 m/s at the exit of the nozzle. The flame was surrounded by a 150-mm-diameter co-annular air jet having a velocity

of 40 cm/s which helped to shield the central jet flame from room-air disturbances. Large vortical structures were periodically formed outside the flame as a result of buoyancy. The convective frequency of these structures was 15.2 Hz. All measurements were phase locked to this frequency, which was sufficiently stable that simultaneous temperature and concentration measurements did not have to be made. Temperature measurements were made radially using the Thin Filament Pyrometer (TFP) technique with a 15 micron diameter SiC filament. Phase locked measurements were made of NO and OH concentrations using laser induced fluorescence.

A comparison of the experimental and computational results are given in Fig. 1. The y-axis gives the time evolution of the measured and calculated quantities as the flow is convected past the axial measurement station of 85 mm. The experimental and computational result are given on the left and right sides of each flame image, respectively. The peak flame temperature is used to define the flame location in the calculations. The peak temperatures are identified by the dots. Comparisons are given for temperature, NO, and OH concentrations. These data show a very good agreement with the experimental results. The calculations show that more than 50% of all of the NO formed in this flame is formed in the local hot spot resulting from the vortex-flame interaction. Also, the influence of local non-unity Lewis numbers on the temperature and NO-concentration fields in the investigated flame are not observed when only the time-averaged and steady-state flames are examined.

REFERENCES

- 1) Katta, V. R., Goss, L. P., and Roquemore, W. M., *Comb. and Flame* 96:60 (1994).
- 2) Katta, V. R., and Roquemore, W. M., *Comb. and Flame* 100:61 (1995).
- 3) Katta, V. R., Goss, L. P., and Roquemore, W. M., *AIAA J.* 32:84 (1994).
- 4) Carter, L. P., et al., Proceedings, Central and Western States Sections and Mexican Section of the International Combustion Institute, pp. 429-434, April (1995).
- 5) Katta, V. R. et al., Proceedings, Central and Western States Sections and Mexican Section of the International Combustion Institute, pp. 173-178, April (1995).
- 6) Hancock, R. D., et al., Proceedings, Central and Western States Sections and Mexican Section of the International Combustion Institute, pp. 179-184, April (1995).
- 7) Hottel, H. C., and Hawthorne, W. R. in *Third Symposium (International) on Combustion, Flame and Explosive Phenomena*, The Combustion Institute, Pittsburgh, 1949, p. 254.
- 8) Chen, L.-D., Seaba, J. P., Roquemore, W. M., and Goss, L. P., in *Twenty-Second Symposium (International) on Combustion*, The Combustion Institute, Pittsburgh, 1988, p. 677.
- 9) Peters N., and Williams, F. A., *AIAA J.* 21:423 (1983).
- 10) Law, C. K., in *Progress in Energy and Combustion Science*, Great Britain, 1984, Vol. 10, p. 295.
- 11) Kee, R. J., Rupley, F. M., and Miller, J. A., Sandia Report No. SAND89-8009B, Sandia National Laboratories, Albuquerque, New Mexico, 1989.
- 12) Leonard, B. P., *Comp. Meth. Appl. Mech. Eng.* 19:59 (1979).

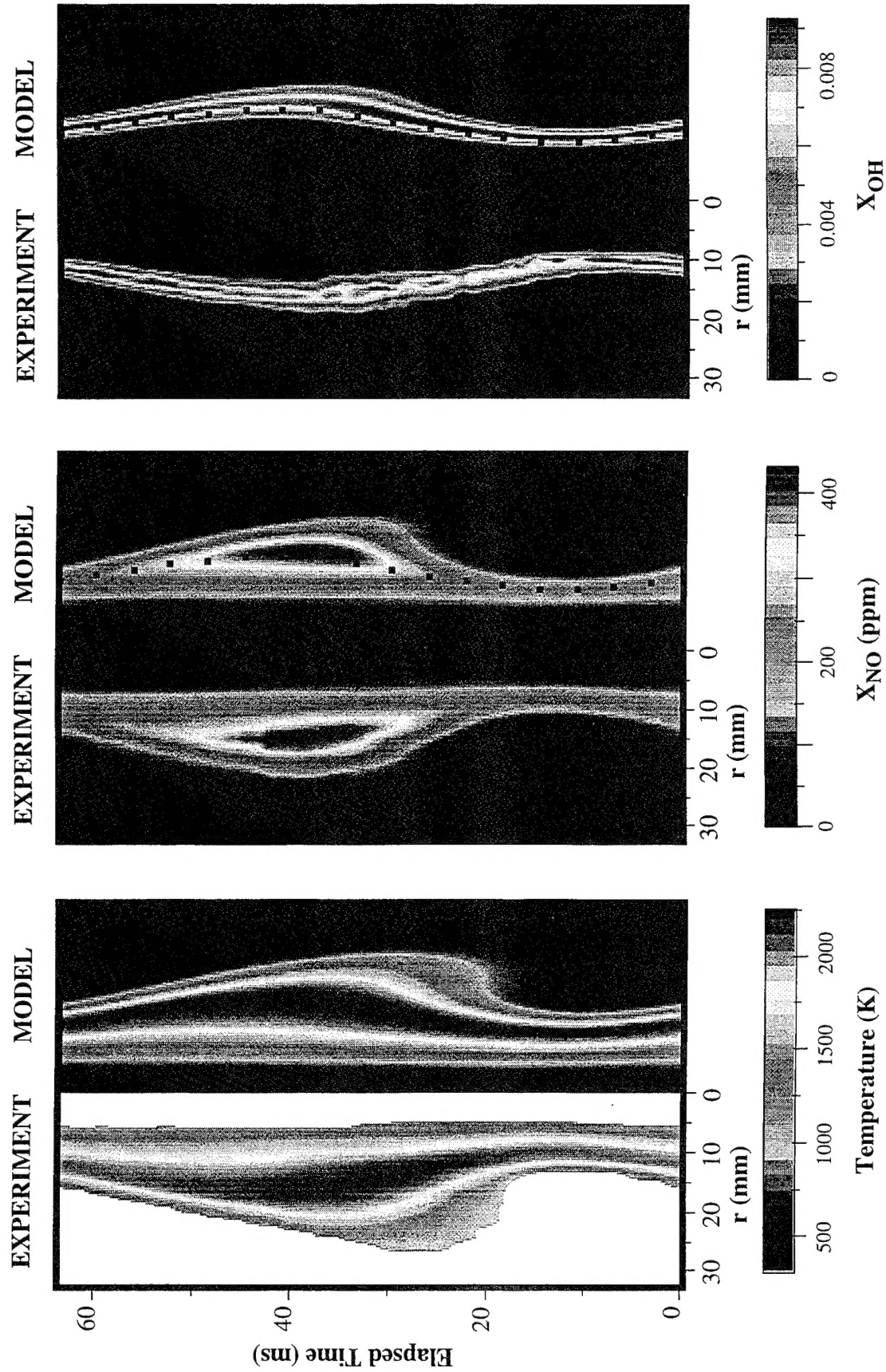


Figure 1. Vortex-Flame Interactions of a H_2/N_2 Jet Diffusion Flame ($z = 85$ mm)

TWO- AND THREE-DIMENSIONAL MEASUREMENTS IN FLAMES

AFOSR Grant No. 94-1-0135
Co-Principal Investigator: Marshall B. Long

Yale University
Department of Mechanical Engineering and Center for Laser Diagnostics
New Haven, Connecticut 06520-8284

SUMMARY/OVERVIEW

Laser-based imaging techniques are being developed and applied to the study of turbulent reacting flows. These techniques incorporate a variety of light scattering mechanisms to allow the measurement of the spatial distributions of temperature, species concentrations, velocity, and most recently, the mixture fraction. The data provided by these measurements can afford a better understanding of the interaction of turbulence and chemistry in turbulent flames. During the past year, progress has been made on two fronts: we have developed and applied a new intracavity technique for mixture fraction imaging, and new capabilities for simultaneous scalar and velocity imaging have been established.

TECHNICAL DISCUSSION

Within the past few years, significant effort has been put into the development of mixture fraction imaging techniques in turbulent nonpremixed flames. The mixture fraction is defined as the mass fraction of atoms originating in the fuel stream and is independent of the chemical reaction occurring in the flame. The gradient of the mixture fraction is needed to find the scalar dissipation, χ , which determines the rate of molecular mixing in the flow ($\chi = 2D|\nabla\xi|^2$, where D is the diffusivity and ξ the mixture fraction). The mixture fraction and its gradient are important parameters in the modeling of turbulent flames, and the experimental determination of mixture fraction over a wide field is essential for testing these models.

A two-scalar approach for mixture fraction determination was developed using single-point Raman and Rayleigh data in a turbulent methane flame by Dr. Sten Ståmer and Prof. Robert Bilger at the University of Sydney. Since 1992, we have been collaborating with them to extend the two-scalar approach to imaging experiments. The method assumes unity Lewis number and a simplified one-step reaction between fuel and oxidizer. It has been shown that the measurement of fuel concentration and Rayleigh scattering is sufficient to determine the mixture fraction.

In the context of our mixture fraction imaging experiments, the fuel concentration has been obtained using one of two techniques: (1) laser-induced fluorescence of the fuel or a fuel marker, or (2) Raman scattering from the fuel.¹ The fuel fluorescence work showed early promise due to its high signal strength, but failed due to pyrolysis of the fluorescing species just rich of stoichiometric. The use of Raman scattering to determine the fuel concentration allows the use of simpler hydrocarbons as fuel, resulting in less severe pyrolysis problems. In one set of Raman/Rayleigh experiments, a two-pass arrangement was used to image along a 1.2 mm wide sheet. The resulting data yielded mixture fraction with acceptable signal/noise to obtain valuable statistics on the scalar dissipation,² but the limited dimensions of the images made viewing of the larger structures impossible.

To extend the field over which mixture fraction can be imaged using the Rayleigh/Raman technique, we have developed a novel intracavity laser imaging configuration³ (see Fig. 1). The output coupler from a flashlamp-pumped dye laser is replaced with a cylindrical mirror and the

cavity is extended to approximately 2.75 meters. An antireflection-coated cylindrical lens is placed within the cavity such that light reflected by the cylindrical mirror is recollimated and fed back into the active medium. (The use of a cylindrical lens without AR coating was found to make minimal difference in the sheet intensity, which suggests the possibility of using this approach even in the presence of windows.) Since the end mirrors are perpendicular to the beam, sheet intensity modulations occur only parallel to the beam, making corrections quite simple. The thickness of the intracavity laser sheet was measured to be 0.56 mm FWHM. In addition, the intracavity approach provided a signal 4.2 times larger than that obtained with a conventional extracavity setup.

The scattered Raman and Rayleigh light were detected with two intensified CCD cameras located on opposite sides of the laser sheet. The Raman-scattered light from methane (C-H stretch at 2915 cm^{-1}) was isolated with an interference filter and focused onto a single-stage intensifier. The output of this intensifier was optically coupled to a cooled CCD detector. The Rayleigh light was collected with a camera lens, isolated with an interference filter, and imaged onto a single-stage intensifier, which was optically coupled to the second CCD. Flame luminosity was suppressed by gating the intensifiers around the 3 μs laser pulse. The images obtained were then transferred to a computer for storage and processing.

Once in the computer, the two images were scaled, rotated and cropped to allow comparison on a pixel-by-pixel basis. After this matching, each pixel corresponded to a volume of $0.06 \times 0.06 \times 0.56 \text{ mm}^3$, with the largest value being the sheet thickness. Images were recorded 25 diameters downstream from a 6.1 mm axisymmetric piloted nonpremixed methane-air flame. The burner was placed in a 7 m/s filtered coflow to prevent particles from interfering with the Rayleigh data, as well as to reduce soot interference. Flames with nozzle Reynolds numbers ranging from laminar to 34,800, were investigated using air-diluted methane as fuel (30% methane by volume). In order to account for the shot-to-shot fluctuations in the laser profile and energy, the edge of each Rayleigh image contained a region of ambient air. The Rayleigh intensity measured in this region was used to correct the laser profile fluctuations in both the Rayleigh and Raman images. This approach works quite well. In a 50 image turbulent flame data set, the rms sheet intensity modulation in the central 8 mm of the ambient-air portion of each image was calculated. On average, the modulation was reduced from 12% to less than 0.7% (signal/noise ≈ 80). For a Raman image from pure methane, the signal/noise across the beam was 39. A sample of the corrected Rayleigh/Raman data, along with temperature and mixture fraction are shown in Fig. 2.

In order to further increase the signal/noise ratio in the Raman data, some degree of smoothing is desirable. One possibility is to average over a fixed-size sub domain using a Gaussian weight function. This type of smoothing leads to an improvement in signal/noise of 3-5 times, but leads to a loss of some of the gradient information required to produce accurate scalar dissipation measurements. Because the Raman and Rayleigh images are highly correlated in the regions where the Raman signal is non-zero, the Rayleigh image can be used to optimize the smoothing of the Raman image. By performing smoothing of the Raman image along constant intensity contours derived from the Rayleigh image, we have shown that it is possible to increase the signal/noise by a factor of 10, while retaining the gradient information.⁴

A second focus area during the current funding period has been to improve upon our initial attempts at velocity/scalar imaging and to move beyond the technique-demonstration phase. We have performed a series of measurements in a turbulent premixed propane/biacetyl/air flame. In these experiments two separate lasers were used for the PIV and biacetyl fluorescence. The second harmonic of a double-pulsed Nd:YAG laser was used for the PIV measurements. With this laser, the interpulse time could be adjusted continuously from 25-200 μs to enable PIV measurements over a range of flow velocities and spatial resolutions. Biacetyl fluorescence was excited with a flashlamp-pumped dye laser using Coumarin-440 dye. Both laser beams were overlapped with a dichroic beam splitter and then formed into a single sheet to illuminate a planar region of the flow. The timing of the lasers was arranged so that the dye laser pulse occurred during the period between the two pulses from the Nd:YAG laser.

The flame selected for study was an unsteady premixed propane/biacetyl/air flame, stabilized on a 1.1 cm diameter piloted axisymmetric burner. The average velocity at the burner exit was

4.1 m/s, giving $Re = 2700$. To enhance the turbulence, a perforated plate with 1 mm diameter holes was placed inside the burner. The air was seeded with both biacetyl vapor and submicron alumina particles and then mixed with propane. Alumina was chosen for particle seeding so that the particles would survive the flame and allow velocity measurements to be performed on both sides of the flame front. The 1.7 cm diameter annular pilot consisted of a premixed propane/air flame that aided in anchoring the main flame to the burner.

For the PIV measurements, Lorenz-Mie scattering from the aerosols was imaged onto a cooled 2048 x 2048 pixel CCD detector oriented normal to the laser sheet. The imaging optics consisted of two camera lenses and an interference filter to block flame luminosity, biacetyl fluorescence, and Lorenz-Mie scattering of the dye laser by seed particles. In two separate sets of experiments, imaging optics having different magnifications were used to collect the PIV data. The magnifications were 1.1 and 3.8, and the velocity measurements were performed over regions measuring $14.9 \times 13.9 \text{ mm}^2$ and $5.2 \times 5.2 \text{ mm}^2$, respectively. On the opposite side of the flow, a second cooled CCD detector with an optically-coupled single-stage image intensifier was used to image the biacetyl fluorescence.

One of the challenges of performing PIV in a flame is related to the difference in seeding density between the unburned reactants and the hot combustion products. The large linear dynamic range and low readout noise of the cooled CCD detector proves advantageous in obtaining valid PIV data in both these regimes. Since the fluorescence image provides a map of the reactants (where the particle seeding density is high), it is possible to increase the spatial resolution of the velocity measurement in the unburned regions of the flow. In our low magnification PIV measurements, the sampling area used in the computerized PIV processing routine was varied by using the PLIF measurements to indicate the presence of reactant. In the unburned regions, each vector was calculated from the average particle displacement within a $0.6 \times 0.6 \text{ mm}^2$ area, while in the burned regions, a $1.2 \times 1.2 \text{ mm}^2$ area was used for the velocity calculation. The task of automating this procedure was simplified by the electronic acquisition and processing of the PIV and PLIF data.

This ability to vary the PIV processing based on scalar measurements was further developed using the high magnification (and hence resolution) PIV configuration. In this data set, each vector represented the average velocity over a $0.33 \times 0.33 \text{ mm}^2$ area. The separation between vectors was 0.165 mm. With the increase in resolution, the acceleration of the product gases associated with the heat release near the flame front was evident. By using both the scalar and velocity fields, the locations of velocity vectors were identified with either the reactant or the product regions of the flow. The mean reactant and mean product velocity fields were thus obtained from a data set containing 54 independent PIV/PLIF measurements. Instantaneous velocity fluctuations were obtained by subtracting the appropriate mean (reactant or product) velocity from the velocity measured at each point in the flow field.

The PIV/PLIF measurements obtained to date demonstrate the feasibility of obtaining detailed information on interactions of flames with turbulent flows. Several possibilities for incorporating information extracted from scalar images into the PIV processing routine have also been demonstrated. These include varying the processing resolution in the unburned and burned regions of the flame, masking techniques to improve velocity measurements near the flame front, and measuring velocities along a contour obtained from the scalar image. Results of these experiments have been submitted to Combustion and Flame.⁵

REFERENCES

1. J.H. Frank, K.M. Lyons, D.F. Marran, M.B. Long, S.H. Stårner, and R.W. Bilger, "Mixture Fraction Imaging in Turbulent Nonpremixed Hydrocarbon Flames," *Twenty Fifth Symposium (International) on Combustion*, The Combustion Institute, p. 1159 (1994).
2. S.H. Stårner, R.W. Bilger, K.M. Lyons, J.H. Frank, and M.B. Long, "Conserved Scalar Measurements in Turbulent Diffusion Flames by a Raman and Rayleigh Ribbon Imaging Method," *Combust. Flame*, **99**, 347 (1994).

3. D.F. Marran, J.H. Frank, M.B. Long, S.H. Stårner, and R.W. Bilger, "An Intracavity Technique for Improved Raman/Rayleigh Imaging in Flames," *Opt. Lett.* **20**, 791, 1995.
4. S.H. Stårner, R.W. Bilger, and M.B. Long, "A Method for Contour-Aligned Smoothing of Joint 2D Scalar Images in Turbulent Flames," *Combust. Sci. Tech.* (in press).
5. J.H. Frank, K.M. Lyons, and M.B. Long, "Simultaneous Scalar/Velocity Field Measurements in Turbulent Gas-Phase Flows," submitted to *Combust. Flame*.

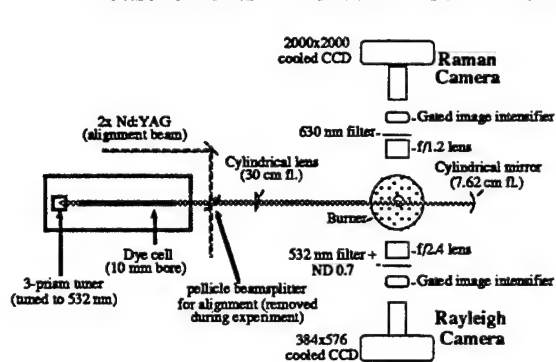


Figure 1. Experimental configuration for intracavity Raman/Rayleigh imaging.

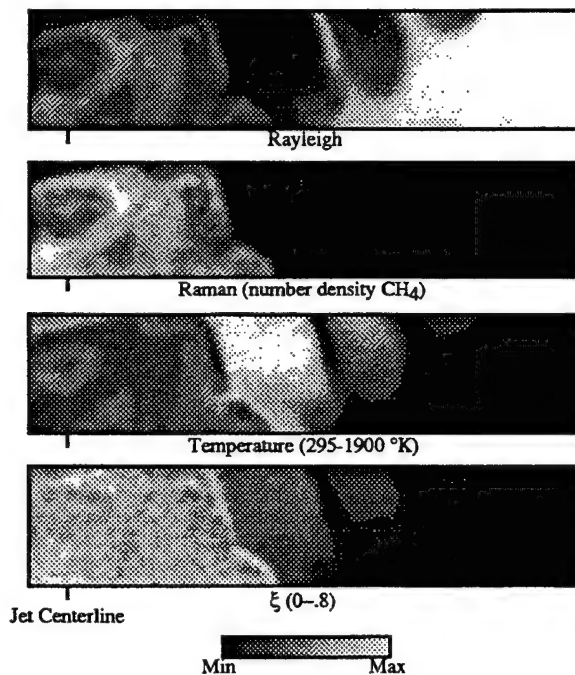


Figure 2. Raman/Rayleigh images from a piloted methane-air flame ($Re = 21,300$). The measurements were taken 25 diameters downstream ($d = 6.1$ mm) and cover 6.5 mm in the axial by 30 mm in the radial direction. Also shown are the calculated temperature, and mixture fraction (ξ) for this image pair.

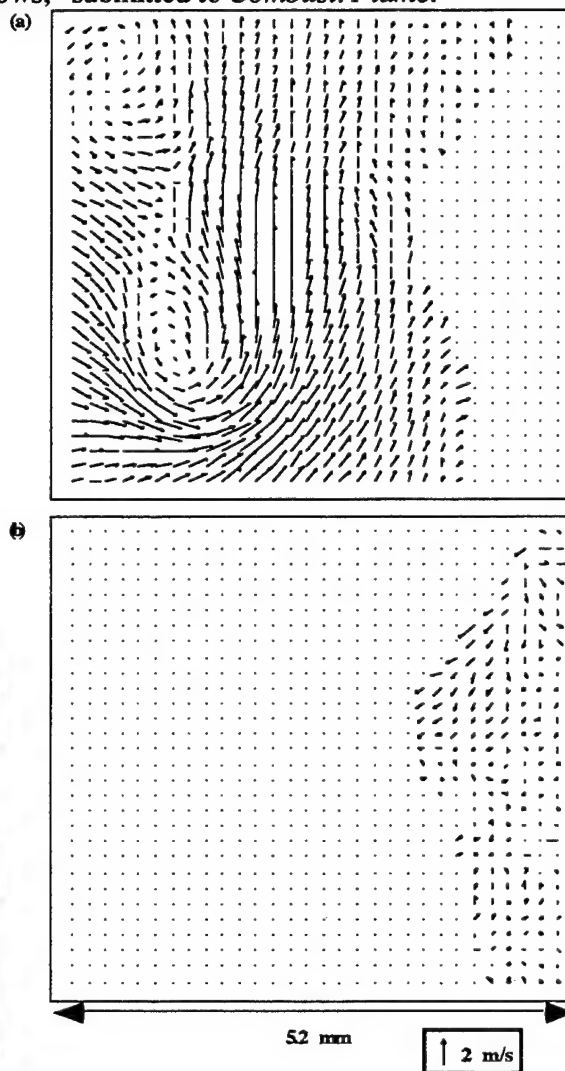


Figure 3. Instantaneous reactant (a) and product (b) velocity fluctuation fields computed by subtracting the appropriate mean reactant or product velocities from an instantaneous velocity measurement. The scalar image was used in conjunction with the velocity image to identify regions as being either in the reactants or products.

TURBULENCE-CHEMISTRY MODELS IN HIGHLY STRAINED NON-PREMIXED FLAMES

AFOSR Contract F49620-94-C-0020

Sanjay M. Correa and Iris Z. Hu
General Electric Corporate Research and Development Center
Schenectady, New York, 12301

SUMMARY: OBJECTIVES AND PRIOR RESULTS

The practical objective of turbulent combustion modeling is to increase engineering productivity and hence the rate of technological innovation, by contributing to design codes for the prediction of flame stability, flow/temperature fields and emissions from air-breathing combustors. The specific objective of this research program is to develop and assess models for turbulence-chemistry interactions in highly strained flames.

Work has proceeded along two tracks. Prior results include:

- (i) PDF/CFD An "elliptic" 2D axisymmetric CFD code was combined with the joint velocity-composition pdf model. A 2-variable partial equilibrium scheme was used for CO/H₂-air chemistry [1]. A 4-step 5-variable scheme was used for CH₄-air chemistry [2]. In each case, the calculations compared favorably with Raman data (mixture fraction, major species, and temperature). Hence this approach is being used in design codes. However, the work also indicated inadequacies in the physical and chemical sub-models.
- (ii) PaSR To address some of the latter inadequacies in greater detail, the Partially Stirred Reactor (PaSR) model was developed. We have used the PaSR to study premixed CO/H₂ flames with full or partial equilibrium chemistry [3]; CH₄ flames with full and 25-step or 4-step reduced chemistry schemes [4]; alternate methods for computational "parallelization" of particle tracking algorithms [4]; comparison of the Curl, modified Curl and IEM mixing models in the context of full chemistry [5]; the effect of the level of initial unmixedness on autoignition delay time (including comparison with premixed data in the baseline case of zero initial unmixedness) [6]; and to test a global three-variable chemistry scheme for kerosene [7].

PROGRESS MADE OVER THE PAST YEAR

I. PDF Model

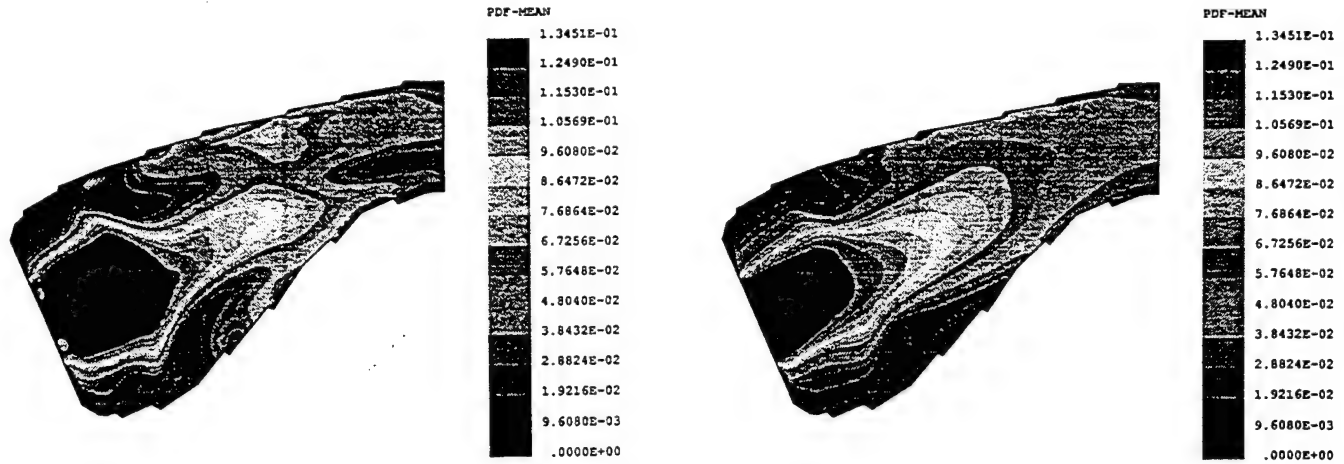
(i) We previously identified significant discrepancies between calculations and data of CO in non-premixed CH₄-air flames [2]. The issue is relevant because high CO emissions (followed by blowout at decreasing load) can be the limiting factor on high-performance low-emissions combustor designs. Work is in progress to address this issue. Standard reduced chemistry schemes appear to be unable to handle the incipient blowout problem.

(ii) Particle-tracking and other techniques from the PDF model activity have been transitioned to a practical 3D design code. The design code uses particle tracking for the scalar(s) pdf. Figure 1 compares the mean passive scalar field in an isothermal turbulent flow, computed using the Monte Carlo technique with that computed using the gradient diffusion technique. The two should agree in this case, since the random walk parameters were obtained from the local turbulence quantities.

II. A Model for Non-premixed Flames Based on a PSR Microstructure and Full Kinetic Schemes

This model is intended to address two issues:

- (i) Given the complexity of the phenomena and of the fuels of interest, full rather than reduced chemistry schemes will probably be required. In principle, the laminar flamelet model (LFM) is available.
- (ii) In the context of the intensely turbulent combustors within gas-turbines, the LFM breaks down because



(a) Particle tracking Monte Carlo model.

(b) Gradient diffusion model.

Figure 1. Comparison of mean passive scalar field in an isothermal 3D turbulent flow.

the reaction zone is not thin and the fluctuation of mixture fraction in the reaction zone is not small [8]. Here, an alternative to the LFM is developed. The turbulent fine-scale structure of the flame is assumed to be in the "distributed reaction zone" regime.

The assumed shape PDF approach is adopted as a first step. Assuming that fluctuations in the mixture fraction ξ and the scalar dissipation rate χ are statistically independent, their joint pdf $P(\chi, \xi)$ is separable

$$P(\chi, \xi) = P_1(\chi) P_2(\xi) \quad (1)$$

Following Liew et al. [9], the pdf of the scalar dissipation χ is taken to be log normal

$$P_1(\chi) = \frac{1}{\chi \sigma \sqrt{2\pi}} \exp \left[-\frac{(\ln \chi - \mu)^2}{2\sigma^2} \right] \quad (2a)$$

where μ is the mean and σ is the standard deviation of $\ln \chi$, so that

$$\bar{\chi} = \exp \left[\mu + \frac{\sigma^2}{2} \right] \quad (2b)$$

The mean scalar dissipation $\bar{\chi}$ is related to the local turbulence kinetic energy k , the local dissipation rate ϵ , and the local variance of mixture fraction g , as follows

$$\bar{\chi} = C_{g2} \frac{\epsilon}{k} g \quad (3)$$

where C_{g2} is a constant in the $k-\epsilon-g$ model.

The residence time " τ " in the fine scales is related to the dissipation by

$$\tau = (\nu/\varepsilon)^{1/2} \quad (4)$$

While Magnussen et al. [10] ascribed a single residence time to the fine scales, we consider the pdf of the residence times and relate it to the pdf of the scalar dissipation.

Following the standard $k-\varepsilon-g$ model, $P_2(\xi)$ is assumed to be a beta function

$$P_2(\xi) = [\xi^{a-1} (1-\xi)^{b-1}] / \int_0^1 \xi^{a-1} (1-\xi)^{b-1} d\xi \quad (5)$$

where "a" and "b" are related to the local mean and variance of the fluctuations in the mixture fraction,

$$a \equiv \bar{\xi} \left(\frac{\bar{\xi}(1-\bar{\xi})}{g} - 1 \right) \quad \text{and} \quad b \equiv (1-\bar{\xi}) \left(\frac{\bar{\xi}(1-\bar{\xi})}{g} - 1 \right) \quad (6)$$

Finally, the mean of a thermochemical quantity $\bar{\phi}_k$ ("k" represents the species mass fractions, density, and temperature) at a point in the turbulent reacting gas is obtained by convolution with the pdf at that point

$$\bar{\phi}_k = \int_0^1 \int_0^1 \phi_k(\xi, \tau) P(\xi, \tau) d\xi d\tau \quad (7)$$

where $\phi_k(\xi, \tau)$ describes the dependence of ϕ_k on mixture fraction and PSR residence time.

Calculations are being compared with prior calculations and with Raman scattering measurements of major species and temperature from the non-premixed bluff-body-stabilized $\text{CO}/\text{H}_2/\text{N}_2$ -air and CH_4 -air flames of Refs. 1 and 2. Preliminary results for the $\text{CO}/\text{H}_2/\text{N}_2$ flame are shown in Fig. 2.

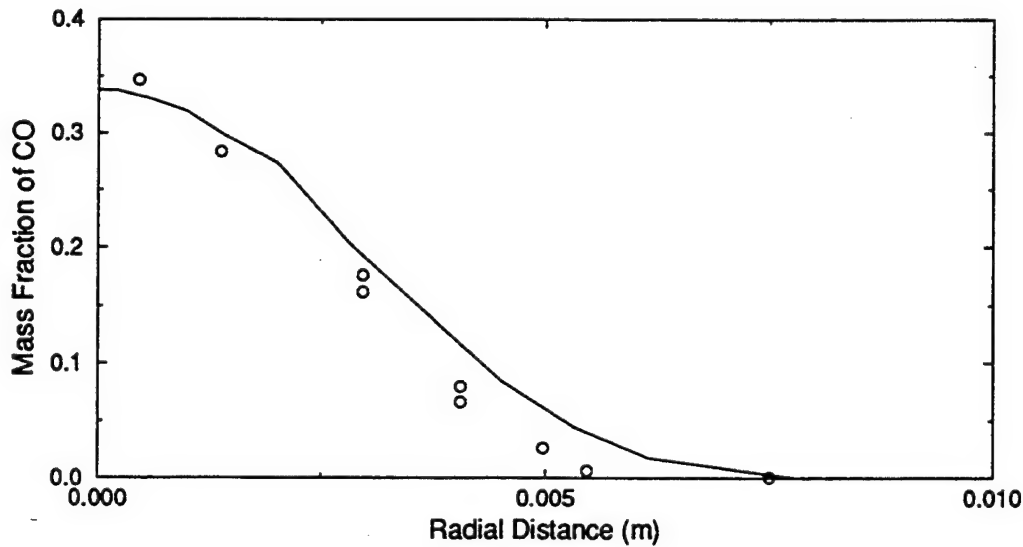


Figure 2. Radial profile of mean CO at $x/d=10$: preliminary computations using the model of Section II.

III. Kinetic Schemes for Complex Fuels

Since aeropropulsion gas-turbine engines burn fuels such as kerosene, (i) appropriate (full or reduced) kinetic schemes are needed and (ii) combustion models must be able to accommodate the schemes. The literature offers some schemes. We were following an approach in which kerosene is pyrolyzed to n-butane in a global step, and then the n-butane is oxidized per a detailed reaction scheme [11]; however, this scheme does not work at higher pressures. Supported by experiments on kerosene oxidation at high pressure, a detailed chemical kinetic scheme for n-decane has been used to represent kerosene reactions [12].

We plan to evaluate these types of chemical schemes, first in PaSR and then in PDF/CFD calculations. In the former case, our interest is to study the PaSR in a range of numerical parameters representative of a prototypical cell in a CFD mesh. Further, interest is confined to the high mixing frequency regime which approximates intense turbulent combustion ("distributed" reaction zones). At low mixing frequencies, the PaSR is not relevant to turbulent combustion because a flame would tend to behave like a laminar flame and not like a plug flow reactor.

REFERENCES

1. Correa, S.M. and Pope, S.B., Twenty-Fourth Symposium (International) on Combustion, The Combustion Institute, Pittsburgh, PA, pp. 279-285, 1992.
2. Correa, S.M., Gulati, A., and Pope, S.B., Twenty-Fifth Symposium (International) on Combustion, The Combustion Institute, Pittsburgh, PA, pp. 1167-1173, 1994.
3. Correa, S.M., *Comb. and Flame*, 93, pp. 41-60, 1993.
4. Correa, S.M. and Braaten, M.E., *Comb. and Flame*, 94, pp. 469-486, 1993.
5. Correa, S.M., "A Direct Comparison of Pair-Exchange and IEM Models in Premixed Combustion," in press, *Comb. and Flame*.
6. Correa, S.M. and Dean, A.J., Twenty-Fifth Symposium (International) on Combustion, The Combustion Institute, Pittsburgh, PA, pp. 1293-1299, 1994.
7. Correa, S.M., "Assessment of a 3-Variable Reduced Kinetic Scheme in Prescribed Turbulence," in press, *J. Prop. Power*.
8. Correa, S.M., *Computing Systems in Engineering*, Vol. 5, No. 2, pp. 135-145, 1994.
9. Liew, S.K., Bray, K.N.C., and Moss, J.B., *Comb. and Flame* 56, pp. 199-213, 1984.
10. Magnussen, B.F., Hjertager, B.H., Olsen, J.G., and Bhaduri, D., Seventeenth Symposium (International) on Combustion, The Combustion Institute, Pittsburgh, PA, pp. 1383-1393, 1979.
11. Gueret, C., Cathonnet, M., Boettner, J.-C., and Gaillard, F., Twenty-Third Symposium (International) on Combustion, The Combustion Institute, Pittsburgh, PA, pp. 211-216, 1990.
12. Dagaut, P., Reuillon, M., Boettner, J.-C., and Cathonnet, M., Twenty-Fifth Symposium (International) on Combustion, The Combustion Institute, Pittsburgh, PA, pp. 919-926, 1994.

MODELLING MIXING AND REACTION IN TURBULENT COMBUSTION

AFOSR Grant F49620-94-1-0098
Principal Investigator: S. B. Pope

Mechanical & Aerospace Engineering
Cornell University
Ithaca, NY 14853

SUMMARY

The aim of the research project is to further develop PDF methods for modelling turbulent combustion, and to apply the methods to turbulent jet diffusion flames. Areas of recent progress include: manifold methods for simplified combustion chemistry; the EMST mixing model; two substantial advances in turbulence modelling; and applications to piloted jet diffusion flames.

MANIFOLD METHODS

Our quantitative knowledge of combustion chemistry is embodied in detailed reaction mechanisms, which continue to advance in their scope and accuracy. In computations of combustion in complex flows (e.g. multidimensional laminar flows, turbulence simulations or turbulent combustion modelling) the computational cost of using a detailed reaction mechanism is excessive, and usually prohibitive. Consequently, there is motivation to develop computationally-simpler approximate methods based on detailed reaction mechanisms.

A fundamental assumption in all simplification strategies—made explicit in manifold methods—is that the thermochemical compositions everywhere in a reactive flow lie close to a low-dimensional manifold in the high-dimensional composition space. Figure 1 shows recent laminar-flame calculations based on the ILDM (Intrinsic Low-Dimensional Manifold) method, in which the full kinetics is reduced to just two variables. As may be seen from the figure, there is excellent agreement between the manifold method and full kinetics.

Although these calculations clearly demonstrate the accuracy and practicality of the method, it is not as simple to implement as desirable. Work is in progress on a modified manifold method that will be straightforward to implement in PDF methods for different fuels and conditions.

EMST MIXING MODEL

The term “mixing model” refers to a turbulence sub-model that describes the evolution of the pdf of composition. In the Lagrangian-pdf framework, the mixing model specifies how the composition $\phi(t)$ evolves following a fluid particle. In one popular model (IEM) $\phi(t)$ relaxes to the local mean value $\langle\phi\rangle$ at a specified rate. In another class of models (particle-interaction models), the composition of the n -th particle in an ensemble $\phi^{(n)}(t)$ changes by an exchange with another randomly selected particle (m , say, with composition $\phi^{(m)}(t)$).

Such mixing models have been extensively examined for inert flows (e.g. Pope 1982) and several shortcomings have been identified and are now well-appreciated. More recently a different shortcoming—peculiar to reacting flows—has been identified. Specifically, the physics of the problem shows that mixing is *local in composition space* whereas the models cited above are non-local.

We have developed a model which is asymptotically local, and which reduces to the mapping closure in the one-composition case. It is based on Euclidean minimum spanning trees (EMST). In the last year, this model has been implemented in a 2D PDF code and applied to a number of test problems. This has confirmed that in several circumstances the EMST model is (at least) qualitatively correct, whereas the IEM model is qualitatively incorrect.

TURBULENCE FREQUENCY

In modelling approaches to turbulent flows, a crucial ingredient is the equation that determines the scale of the turbulence. In the k - ϵ model this is the ϵ equation, and similarly in the k - ω model championed by Wilcox (1993) it is the ω equation. In our current PDF approach we include ω within the PDF description. Wilcox

(1993) observes that the $k-\omega$ model has several advantages over the $k-\varepsilon$ model, but that it has difficulties at free boundaries. In our previous work on PDF methods we encountered similar difficulties, which were remedied only by an *ad hoc* adjustment to ω at the edge of the flows.

We have now developed a new, general treatment that appears to be very successful. It is based on a conditional mean of ω defined by

$$\Omega \equiv C_{\Omega} \langle \omega | \langle \omega \rangle \geq 0 \rangle,$$

where C_{Ω} is a constant specified so that the conditional mean Ω and the unconditional mean $\langle \omega \rangle$ are equal in homogeneous turbulence. Figure 2 shows calculations using this model for a constant-density temporal shear layer. It may be seen that the profile of Ω is quite different from that of $\langle \omega \rangle$, and provides the required higher value of turbulence frequency at the edge of the flow.

RAPID DISTORTIONS

In practical combustors, complex mean velocity fields are the norm. Examples are swirling jets and jets into a cross flow. It is well-known that models such as $k-\varepsilon$ provide a poor representation of such flows. In Reynolds-stress and PDF methods, the modelling of the "rapid pressure" is crucial for such flows; and a limiting test of rapid-pressure models is rapid distortions.

Recently work of Reynolds & Kassinos (1994) has shown that Reynolds-stress closures are incapable of correctly accounting for rapid distortions with rotation. However, based on their suggestions, we have developed a PDF closure that is **exact for homogeneous rapid distortions**. It is based on the joint PDF of velocity \mathbf{u} and a unit wavenumber \mathbf{e} , $f(\mathbf{v}, \boldsymbol{\eta}; t)$, where \mathbf{v} and $\boldsymbol{\eta}$ are sample-space variables corresponding to \mathbf{u} and \mathbf{e} . The evolution equation for f is:

$$\begin{aligned} \frac{\partial f}{\partial t} = & \frac{\partial \langle U_k \rangle}{\partial x_j} (\delta_{ik} - 2\eta_i \eta_k) \frac{\partial}{\partial v_i} (f v_j) \\ & + \frac{\partial \langle U_k \rangle}{\partial x_j} \frac{\partial}{\partial \eta_i} (f [\eta_k \delta_{ij} - \eta_i \eta_j \eta_k]), \end{aligned}$$

where $\partial \langle U_k \rangle / \partial x_j$ is the imposed mean velocity gradient tensor.

As an example, Fig. 3 shows the Reynolds-stress anisotropies obtained from the solution of this equation for the case of successive plane strains. This evolution corresponds to an exact solution of the Navier-Stokes equations in the rapid-distortion limit.

The method is being developed to treat both slow and rapid distortions, and will be tested on a variety of flows, including swirling jets.

REFERENCES

- Maas, U. and Pope, S. B., (1994) Twenty-fifth Symp. (Int'l.) on Combust., p. 1349
- Norris, A. T. & Pope, S. B. (1995) Combust. Flame **100**, 211.
- Pope, S. B. (1982) Combust. Sci. Technol. **28**, 131.
- Reynolds, W. C. and Kassinos, S.C. (1994) Bull. Am. Phys. Soc. **39**, 1953.
- Wilcox, D. C. (1993) Turbulence Modelling for CFD, DCW Industries.

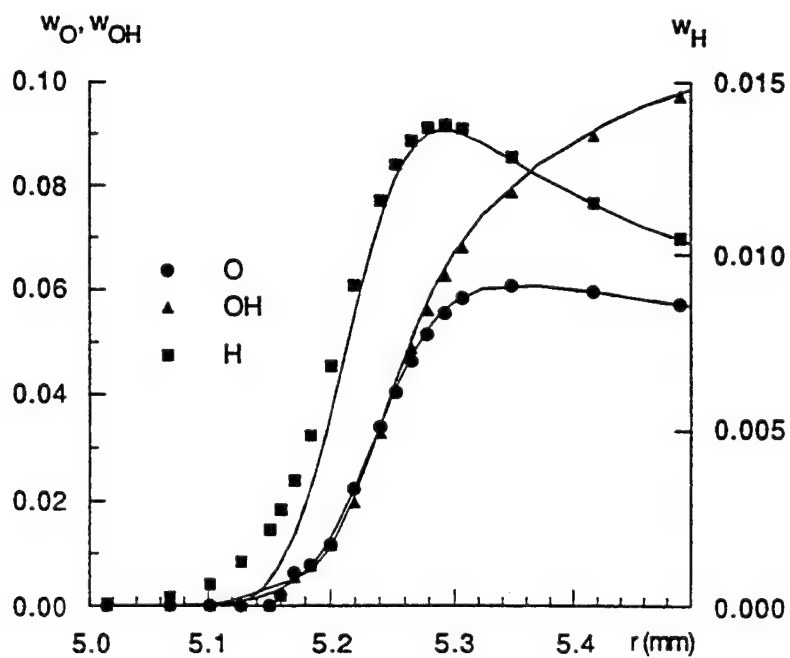
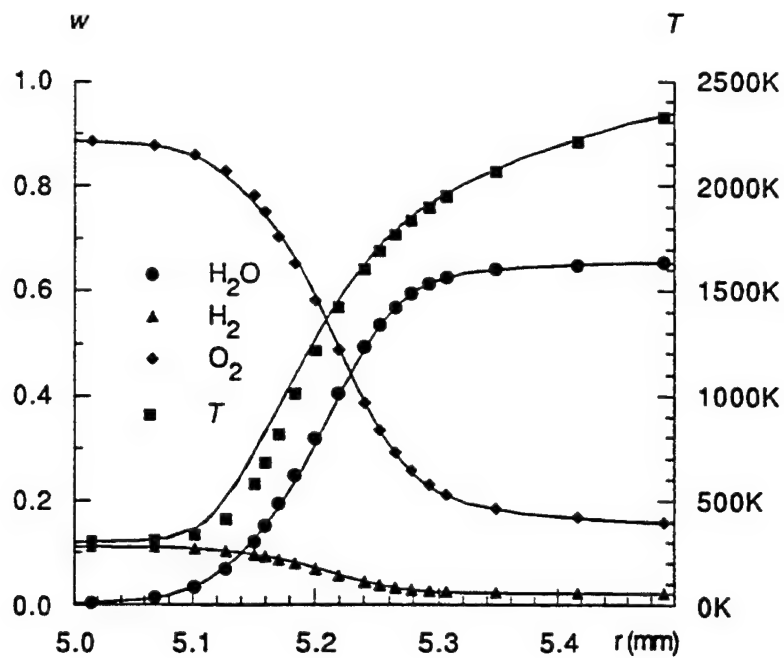


Fig. 1: Profiles in a laminar premixed stoichiometric H_2-O_2 flame at atmospheric conditions: lines, detailed kinetics; symbols ILDM with two degrees of freedom. (From Maas & Pope 1994.)

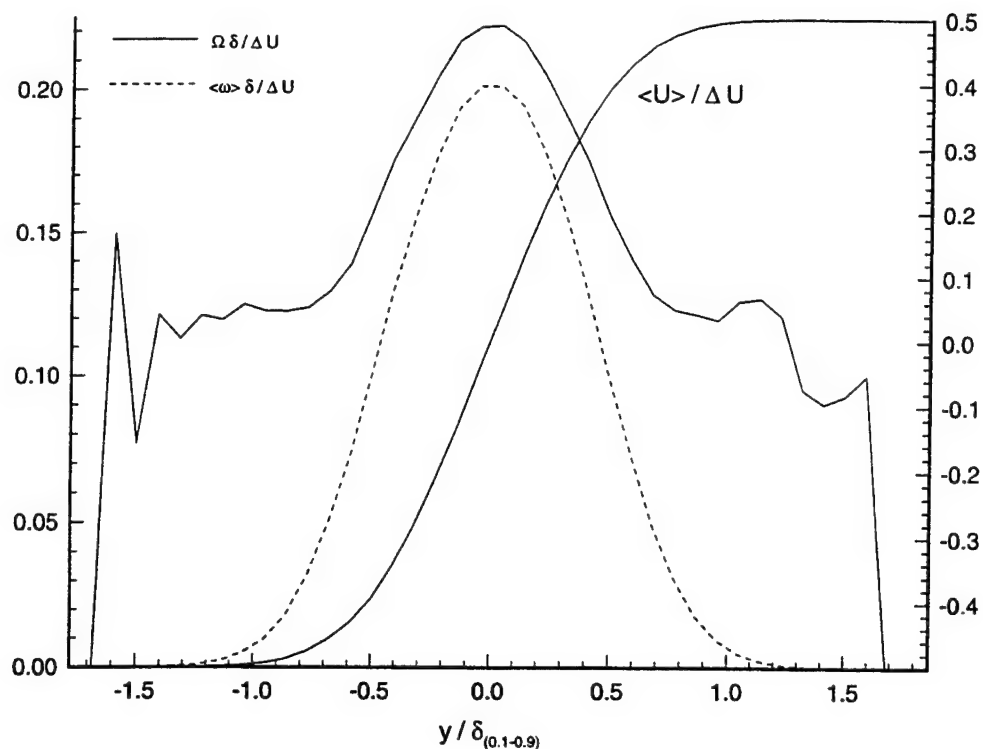


Fig. 2: Profiles in the self-similar temporal mixing layer obtained from the $U - \omega$ joint PDF method, showing that in the intermittent region the conditional mean Ω remains appreciable, while the unconditional mean $\langle \omega \rangle$ asymptotes to zero. (As the intermittency factor tends to zero, there are large statistical errors in Ω : but there is negligible impact on the calculation in the turbulent region.)

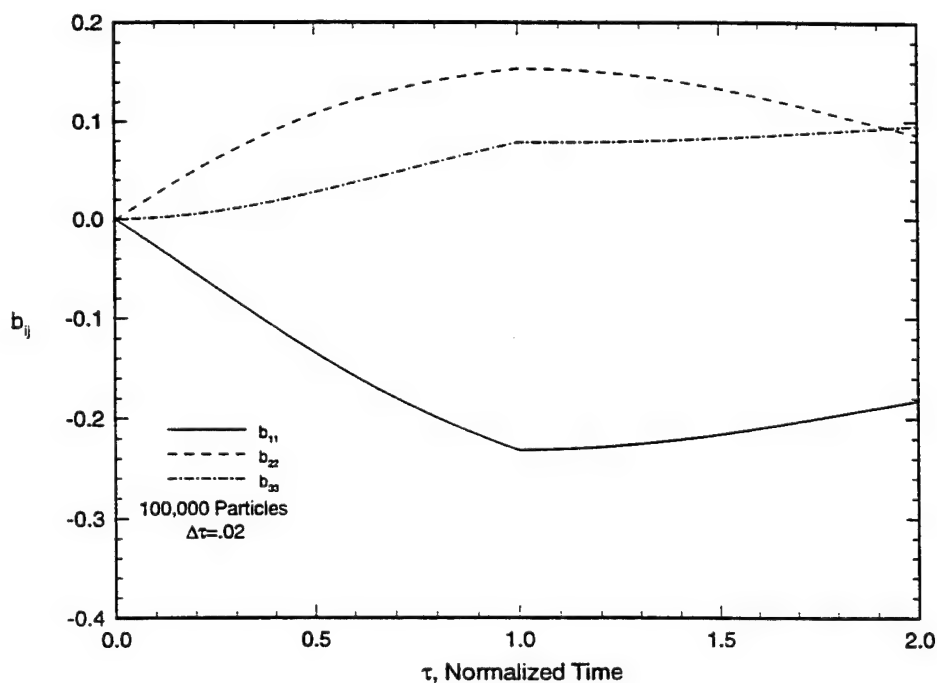


Fig. 3: Reynolds-stress anisotropies ($b_{ij} \equiv \langle u_i u_j \rangle / \langle u_k u_k \rangle - \frac{1}{3} \delta_{ij}$) for successive rapid plane strains. Imposed mean velocity gradients: $\tau < 1$, $\partial \langle U_1 \rangle / \partial x_1 = -\partial \langle U_2 \rangle / \partial x_2 = 1$; $\tau > 1$, $\partial \langle U_1 \rangle / \partial x_2 = \partial \langle U_2 \rangle / \partial x_1 = \frac{1}{2}$. Exact solution to the Navier-Stokes equations in the rapid distortion limit obtained from Monte Carlo solution of the equation for the joint PDF of velocity \mathbf{u} and unit wavenumber \mathbf{e} .

REACTION ZONE MODELS FOR VORTEX SIMULATION OF TURBULENT COMBUSTION

(AFOSR Grant No. 92-J-0445)

Principal Investigator: Ahmed F. Ghoniem

Department of Mechanical Engineering
Massachusetts Institute of Technology
Cambridge, MA 02139

SUMMARY/OVERVIEW

The objectives of this work are to develop reaction zone models which are: (1) compatible with vortex simulations of turbulent flows in which a Lagrangian view of the small scale dynamics is used to construct solutions of the governing equation in physical space; (2) consistent with the view that at large Damkohler numbers, combustion occurs across thin convoluted surfaces which are generated by the flow, strained by the local velocity gradients and eliminated by merging and local consumption; (3) capable of properly incorporating, at some reasonable level of detail, the chemical kinetics and molecular transport of fuel-air mixtures; and, (4) designed to take advantage of modern computer architecture in which massively parallel processing is performed on a small number of supernodes with maximum memory and minimum communications. During the past year we attained progress in three connected projects: (1) massively parallel implementation of three dimensional vortex method as applied to the prediction of flows in complex geometry and to mixing and combustion in a reacting swirling jet; (2) development of a flow-combustion interaction approach in which a reaction zone model is used for the implementation of unsteady strained thin flame representation of non premixed combustion in turbulent reaction flow simulations; and, (3) development of an unsteady strained thin flame model of non premixed combustion with detailed chemical kinetic and transport processes at the molecular level.

TECHNICAL DISCUSSION

We have been pursuing the development of a novel approach for the numerical simulation of turbulent combustion in which the vortex method is used to solve the Navier-Stokes equations and a compatible algorithm, the transport element method, is applied to integrate the species and energy transport equations. We have shown this to be a very powerful approach due to some intrinsic properties which endow the underlying methodology with efficiency, accuracy and flexibility. In brief, these methods view the flow field as a collection of small scale vortices: (i) generated due to wall shear and/or pressure gradient-density gradient interactions; (ii) convected with the local velocity field which results from the action of all the vorticity in the field augmented by the volumetric expansion occurring within the reaction zones and both forced to satisfy the normal velocity conditions at the domain boundary; (iii) diffused by the action of molecular viscosity at the level of the smallest scales allowed in the flow; and, (iv) stretched by the local velocity gradients. The smallest scale of an elementary vortex, which it reaches after several decades of stretch-and-divide processes, determines the smallest scale captured by the simulations. The Lagrangian, self-adaptive nature of the simulations allows one to start with a relatively coarse discretization of the large scales. Following that, the computations automatically refine the resolution wherever and whenever necessary in order to capture the small scales as they are generated. Thus vortex simulations are, by construction, adaptive in time and space, and the number of elements used increases in time to accommodate the formation and rapid multiplication of small scale, albeit within a small volume of the flow.

As an example of the complex structures encountered in reacting turbulent flows, which must be captured and properly resolved using a numerical simulation, we show in figure 1 a sample of a

simulation of a swirling reacting jet. The initial state of this shear flow is a fuel stream on the inside and an oxidizer stream on the outside, separated by a sleeve of azimuthal vorticity uniformly distributed in the direction tangential to the sleeve. To enhance the mixing rate, a swirl, modeled by streamwise vorticity whose direction is the same as the fuel jet velocity, is added. As seen in the figure, the formation of streamwise vortices around the azimuthal vortex ring, the combination of which forms spiral vortex "worms," is supported by the presence of an initial streamwise vorticity component. The figure shows the convolution of the "flame," the plane initially separating the fuel and oxidizer, and the formation of flow scales, in the form of vortical structures, whose size cover a wide spectrum. The total number of elements used in these simulations increased, nonuniformly in space as the figure shows, by an order of magnitude during the run, indicating that the flow was exposed to strain rates an order of magnitude higher than the initial shear in the flow.

To simulate the combustion within this ever stretched, convoluted and strained flame, we have to be able to resolve both the diffusive and reactive zone structure of this flow, i.e., we have to ensure high enough resolution across the elements to be able to capture the species and temperature gradients within a strained flame. This can be done by applying the transport element method in which several layers of element are used to resolve the initial vorticity and scalar gradients across the initial shear zone. Employing several layers between the two uniform states guarantees that as the flow evolves and the strain rate increases thus by reducing the distance between neighboring layers there will be enough resolution to capture the diffusive structure of the flame. Properly implemented, this algorithm allows for a direct numerical simulation of the flow, i.e., the resolution of all the scales as they form and evolve, as well as all the gradients within the reaction zone. This, however, comes at the cost of employing a large number of layers in the direction normal to the flow at $t = 0$ or at the inlet boundary conditions. In most cases, 10-20 layers should be used, increasing the amount of computations by two orders of magnitude. Clearly the higher the Zeldovich number, i.e., the thinner the reaction zone with respect to the diffusion zone within the flame, the larger the number of layers required.

An approach to overcome the difficulty described above, obtained naturally by taking the limit of the transport element solution when the number of elements utilized to discretize the gradients is reduced to one, is to adopt the notion that the flame structure should be regarded as a subgrid model in a large eddy simulation performed using the vortex method. Employing one single layer of transport elements at the interface between the fuel and oxidizer streams is sufficient in order to capture the ensuing flow scales, while the detail of the combustion process occurring across these elements are computed in a different domain. This transition from a direct Lagrangian simulation to a large eddy Lagrangian simulation by passing through the limit of high Damkohler number, without changing the rudiments of the underlying algorithms, leads to our "flamelet transport algorithm." To implement this approach, the physical domain and the original reacting flow equations are decomposed into an "outer" non reacting flow model, in a domain in which the flame is infinitely thin, whose solution is obtained using the vortex method, and an "inner" reacting flow model describing the combustion zone as an unsteady strained flame in a stagnation point flow in the domain in which the flame structure reaches the free stream at "infinity." The interaction between the two solution domains is captured in the form of: (i) volumetric expansion across the flame; (ii) vorticity generation across the flame in the form of vorticity dipoles; (iii) a time dependent strain acting locally on the flamelet; and, (iv) a convoluted flame area generated by the flow structures which affects the boundary conditions across each flamelet zone.

Figure 2 shows the results of applying this approach for the simulation of a two-dimensional shear layer. The results shown are obtained by evaluating the combustion field across each flamelet, assuming a single step Arrhenius kinetics and $Da = 19,213$, as it moves along the shear layer in a transformed domain. The concentration field is the obtained by sampling over the entire shear layer to find the local flamelet contributions. As can be seen, very high resolution can be achieved using this approach. The resolution is not limited by the resolution of the flow field simulation except for its contribution to the convolution of the flame front and the

strain field. The solution compares very well with our previous direct Lagrangian simulations of the same flow.

The third project is concerned with evaluating the flame structure within the strained flamelets using detailed chemical kinetics and molecular transport. Since we are interested in unsteady simulations of turbulent combustion processes, the model must accommodate the impact of unsteady strain and boundary conditions on the flame structure. For this purpose we have developed two approaches: a direct approach in which the boundary layer equations describing the flame in a stagnation point flow are integrated on an adaptive domain, and a uniform strain model which relies on a series of transformations of the governing equations, assuming that the strain rate is constant across the flame, to recast the original convection-diffusion-reaction equations into a simpler set of diffusion-reaction equations. The simplicity and efficiency of the latter are the reasons for developing it as a model. Careful assessment of its accuracy, however, is needed before it can be used in the turbulent combustion simulations.

Figure 3 shows a sample of the solution obtained using the two approaches for a diffusion flame and a premixed flame, both strained, in methane-air mixtures. Results show that the uniform strain model performs quite well, although the effective strain appears to be different than the actual applied strain. This is because the actual strain changes by a factor of $\sqrt{\rho_b/\rho_n}$ across the flame zone, a fact ignored in the model. To correct for this deficiency, one must use the geometric mean strain across the flame when using this model, as was done to obtain the results in the figures. On the other hand, the model runs faster and appears to be more robust than the direct solution, especially when reduced chemistry models are used. This is because, while in the case of detailed chemical kinetics simulations, the evaluation of the source term dominates the computations, as the number of reaction steps is reduced, the time spent in evaluating the convective derivatives becomes significant.

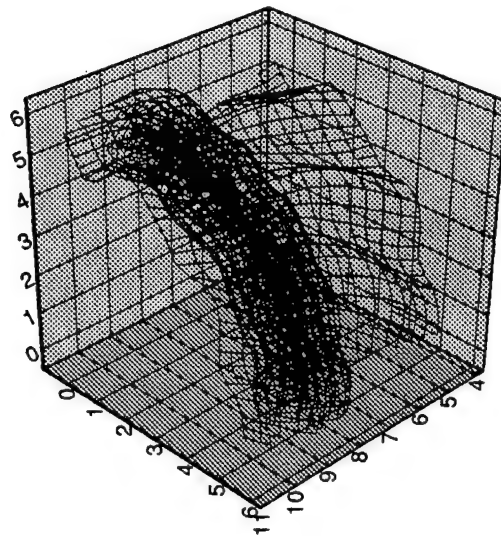


Figure 1. The convoluted fuel-air interface in a swirling jet, showing the formation of azimuthal and streamwise vortical structures.

REFERENCES

1. Soteriou, M.C. and Ghoniem, A.F., "Numerical Study of Exothermic Combustion on Mixing Layer using Finite and Infinite Reacting Rate Models," *Combust. Sci. Tech.*, in press.
2. Soteriou, M. and Ghoniem, A.F., "Effects of the Free-Stream Density Ratio on Free and Forced Spatially-Developing Shear Layers," accepted for publication in *Phys. Fluids*.
3. Soteriou, M.C. and Ghoniem, A.F., "Wake Effects on an Exothermic Spatially Developing Shear Layer," *33rd Aerospace Sciences Meeting*, Reno, NV, 1995, AIAA-95-0807.
4. Petrov, C.A. and Ghoniem, A.F., "An Unsteady Strained Flame Model for Turbulent Combustion Simulation," presented at the *32nd Aerospace Sciences Meeting*, to appear in *Combust and Flame*.
5. Petrov, C. and Ghoniem, A.F., "An Unsteady Strained Flame Model with Reduced Reaction Mechanism for Turbulent Combustion Simulation," *33rd Aerospace Sciences Meeting*, Reno, NV 1995, AIAA-95-0380.



Figure 2. The product distribution evaluated from the contribution of all the flamelets along the mixing layer. In the flow simulation, the dynamic effect of heat release was neglected to obtain maximum flame convolution. Based on the vorticity-thickness of the inlet profile, the effective Peclet number is 1500, the Damkohler number is 19,213 and the Karlovitz number is 0.02. Note that at these parameters, there is very limited interaction between neighboring flamelets, especially at the early stages of the flow evolution.

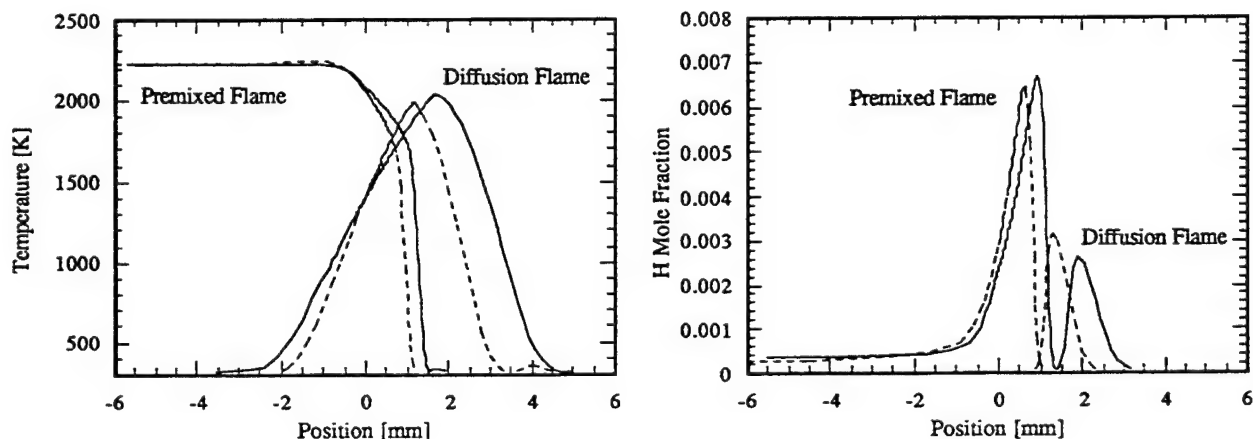


Figure 3. A comparison between the steady-state profiles obtained using uniform strain model (solid lines) and direct method (dashed lines) for diffusion flame (strain rate = 100/s) and stoichiometric premixed flame (strain rate = 100 1/s). Left figure shows the temperature profiles, right figure shows the mole fraction profiles of the hydrogen radical.

INJECTION AND MIXING IN SUPERSONIC FLOWS

AFOSR TASK 2308BW

Principal Investigators: Gruber, M., Glawe, D., Chen, T., Nejad, A.

Aero Propulsion and Power Directorate
Wright-Patterson AFB, OH 45433-7251

SUMMARY:

An experimental investigation of supersonic mixing is being conducted at the Aero Propulsion and Power Directorate to gain a better understanding of fuel-air mixing in supersonic flows. The primary objective of this effort is to develop and apply optical diagnostic techniques for qualitative and quantitative observation of the three-dimensional unsteady flowfields associated with the transverse and parallel injection of under-expanded jets into supersonic freestreams. The secondary objective of this effort is to incorporate passive means to promote rapid fuel-air mixing for use in scramjet engines.

Technical Discussion:

One of the primary areas of technological challenge in the development of scramjet powered vehicles is the design of a flowpath capable of sustaining net positive thrust over a wide flight Mach number range. The challenge is to make accurate predictions/measurements of the engine/airframe aerothermal loads which in turn can be used for the design and development of other key technologies such as high temperature materials/structures, fuel systems, avionics, sensors, etc. Mixing in compressible turbulent shear layer flows combined with the turbulence-chemistry interaction, i.e., ignition, flame stability, and flameholding, are the least understood mechanisms in supersonic combustors [Ferri, 1973, Waltrup, 1986]. The role of large-scale structures which engulf large amounts of one fluid into another and initiate the turbulent energy cascade down to molecular mixing is considered to be important. Beyond the macro-scale transport of one fluid into another, the role of large-scale turbulence in promotion of mixing is rather uncertain. Unfortunately, the inherent stability of supersonic shear layers prevent rapid growth and mixing of fuel-air streams [Papamoschou and Roshko, 1986, Schadow, 1986, Chinzei, et al., 1986] to the point that mixing is the limiting phenomenon in supersonic combustion. Therefore, much effort has been expended to enhance fuel-air mixing in supersonic flows.

Scramjet injector design can be divided into two basic categories. The simplest geometry is associated with flush wall normal injection of fuel into a supersonic freestream. Although this configuration results in adequate fuel-air mixing, it suffers from excessive stagnation pressure loss due to the generation of a relatively strong three-dimensional bow shock. Furthermore, the interaction of the bow shock with the boundary layer results in the formation of a separation bubble upstream of the jet which in most instances acts as a flameholder requiring extensive local cooling. Many investigators have suggested alternative approaches such as injection at an oblique angle to reduce shock-induced losses while maintaining good mixing characteristics. Parallel or co-flow injection of fuel is the second most extensively used configuration. Although mixing associated with this class of injectors is not satisfactory, they can provide a significant portion of the engine thrust at high flight Mach numbers, ($M > 12$). Realizing the merits and limitations of each scheme, many investigators have suggested incorporation of aerodynamic vortex generators as passive means to promote mixing in supersonic flows. Ramped injectors, which have been studied in the past, are examples of such devices. The objective of the present work is to gain a better understanding of the temporal characteristics of the large-scale eddies which exist along the jet/freestream interface of under-expanded jets in supersonic freestreams. It is hoped that the investigation of the interfacial structures will lead to a better interpretation of the mixing characteristics of each injector by revealing the large- and small-scale motions associated with each. Finally, this work will be used as a baseline for future, more exhaustive studies of complex injector designs.

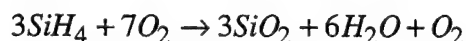
Experiments have been carried in the supersonic combustion facility located at the Aero Propulsion and Power Directorate, Wright-Patterson AFB. This facility has a 5" by 6" test section operating at a nominal Mach number of 2. The test section allows optical access through either side walls and top wall using fused silica windows. Injectors mount into interchangeable test inserts housed within the bottom wall. Mixing characteristics of circular and elliptical jets issuing transversely into the crossflow are examined in detail. The circular transverse jet serves as a baseline for comparison to the elliptical jet, which is chosen based on the axis-switching results presented earlier. This nozzle may represent a passive method for increasing near-field mixing. The planar imaging technique used in this study relies on the collection of light scattered by particles suspended in the flowfield of interest. A thin laser sheet illuminates the particle laden flowfield. The pulse duration of the laser sheet is typically 10-ns, which is sufficiently short to freeze the flow. The pixel array of a CCD camera obtains an image of the flowfield by collecting the light scattered from the particles. The resulting image contains relative intensity information where high intensities correspond to high particle concentration, assuming that the particles are passive participants in the mixing process. It is important to note that the mixing information obtained from passive scalars is only spatially resolvable down to the scale of the imaging pixels. Since the sheet light has a finite thickness, a small amount of signal integration occurs as in conventional techniques such as schlieren photography. Thus, the pixel array yields an average intensity over a small pixel volume defined by the pixel area and the sheet thickness, thereby limiting mixing interpretations to those involving large-scale "stirring" of fluids rather than molecular mixing. For the present study, a pair of frequency doubled Spectra Physics Nd:YAG lasers operating at 532-nm were used. The beams passed through appropriate sheet forming optics resulting in two 200- μ m thick coincident planar laser sheets. Mirrors directed these sheets into the test section through the top wall window. Two Princeton Instruments ICCD cameras (384 x 578 pixel array) were used to obtain the flowfield images through the opposing side wall windows. The cameras were water cooled and purged with nitrogen for better signal-to-noise ratio. Two Nikon UV-Nikkor 105-mm f/4.5 telephoto lenses were used to obtain high pixel resolution. A novel synchronization and laser sheet delay system was used to gate each camera around its own laser sheet such that independent however temporally correlated images were obtained. Two 486 based computers were also synchronized and collected the images to allow for post-processing. Particle response characteristics in high speed flows are important. The seed particles must follow the turbulent fluctuations so that the collected images can represent the flowfield with high fidelity. Accurate particle response requires a Stokes number defined by

$$\text{Stokes Number} = \frac{t_p}{t_\delta} = \frac{\text{particle response time}}{\text{large eddy rollover time}},$$

of less than about 0.5. The two time scales involved in determining the Stokes number are

$$t_p = (1 + 2.76 \cdot Kn) \frac{\rho_p d_p}{18\mu} \quad \text{and} \quad t_\delta = \frac{\delta}{\Delta U}$$

where Kn is the Knudsen number (ratio of mean free path length to particle diameter), ρ_p and d_p are the particle density and diameter, μ is the dynamic viscosity, δ is the shear layer vorticity thickness, and ΔU is the velocity difference across the shear layer. In this investigation, air was seeded with silicone dioxide resulting from the following reaction:



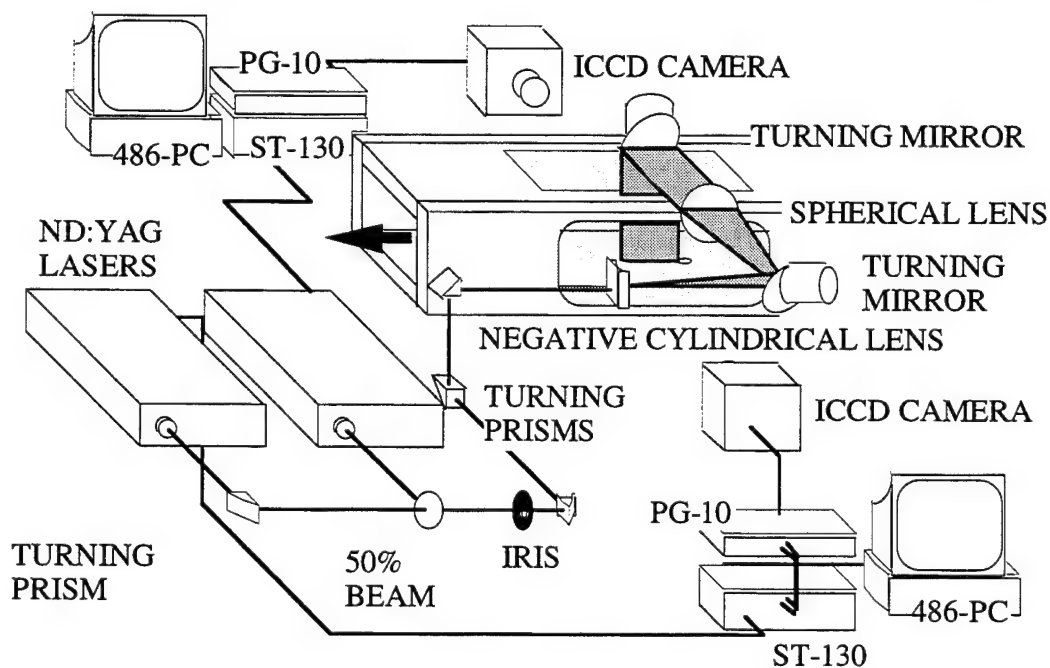
This reaction produces SiO_2 particles with nominal diameters of approximately 0.2- μ m. Polarization of the incident laser light significantly affected the signal-to-noise ratio of the images. This indicates that the resulting particles remain small enough to be considered in the Rayleigh scattering regime. Estimating the Stokes number using the fluid dynamic results from the images

and particle characteristics results in a value of approximately 0.1. Thus, the images are considered to accurately represent the highly turbulent flowfield of this study.

Some initial results of the scattering experiments are shown. The digital photos show pairs of images obtained from each case examined. Freestream flow is from left to right. Since two different cameras were used in these experiments, the signal-to-noise ratios of the images are somewhat different. However, structural activity can clearly be seen in each image so that convection velocities can be determined. Each image covers approximately 1.4" in the streamwise direction and 1" in the transverse direction, and the time delays between the images appear in each figure caption. Finally, freestream fluid appears as light regions while injectant fluid (fuel) appears as dark regions. Close visual examination of the image pairs reveals very obvious structural movement. The small time delays used here allow the individual structures to maintain their shapes from shot to shot, thus eliminating subjectivity when analyzing the image pairs. Preliminary results of a visual analysis are tabulated in Table 1. Also presented are freestream and jet exit velocities for reference. These data should be considered preliminary at this point; a more detailed analysis using correlation techniques is currently in progress.

Table 1 Preliminary Results of Image Pair Analysis

Case	J	U_{∞} (m/s)	U_j (m/s)	γ_j	Displacement (μm)	U_c (m/s)
1C	2.9	516	318	1.40	616.2	308.1
2E	2.9	516	318	1.40	509.4	254.7
3C	2.9	516	883	1.67	267.0	267.0
4E	2.9	516	883	1.67	283.6	236.3



Schematic of Double Pulsed Mie Scattering Optical Arrangement

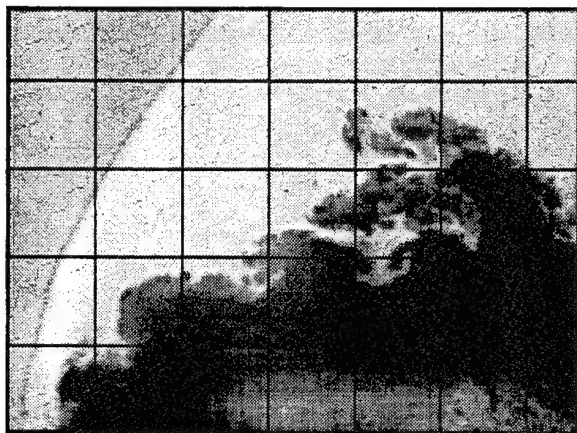


Image Pair Obtained for Circular Injection of Air ($\Delta t = 2 \mu s$)

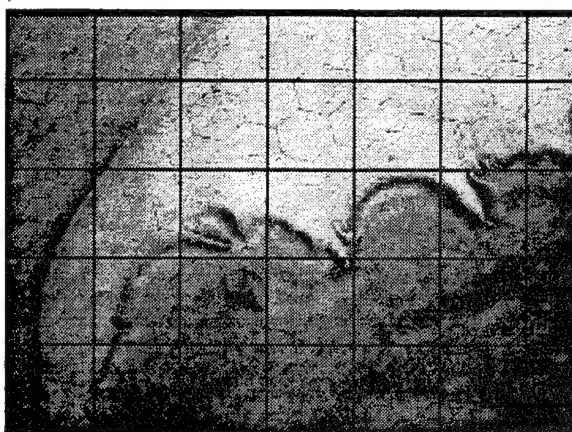
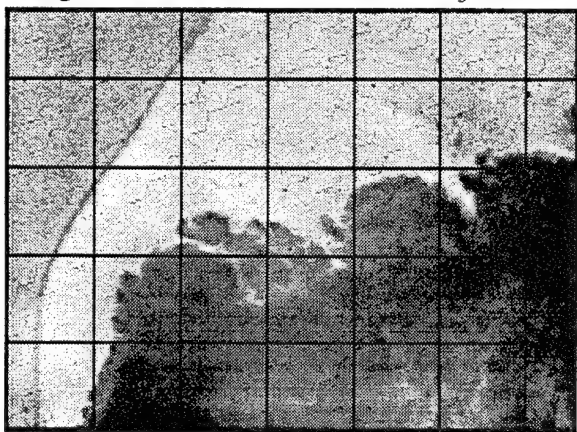


Image Pair Obtained for Circular Injection of Helium ($\Delta t = 1 \mu s$)

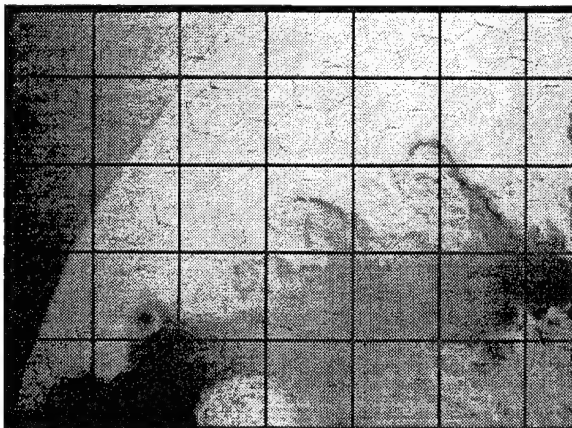
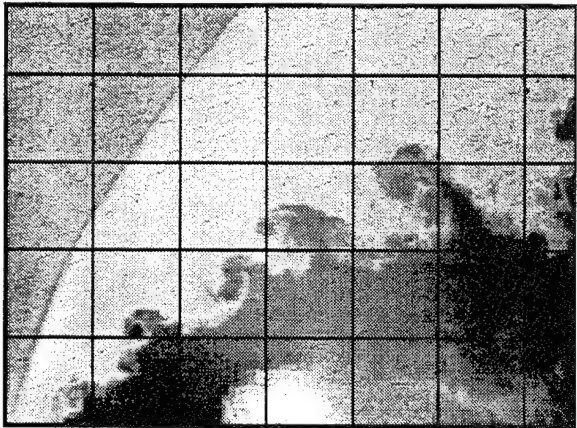


Image Pair Obtained for Elliptical Injection of Air ($\Delta t = 2 \mu s$)

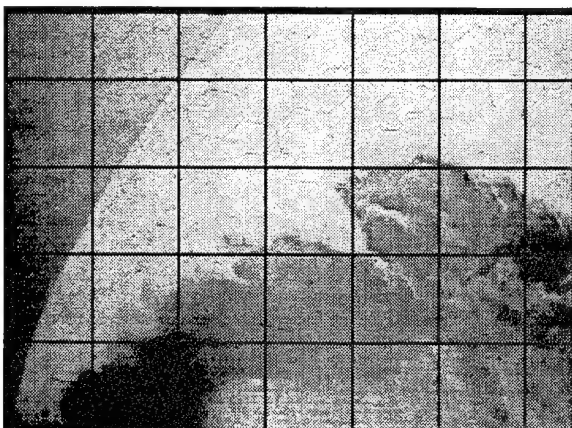
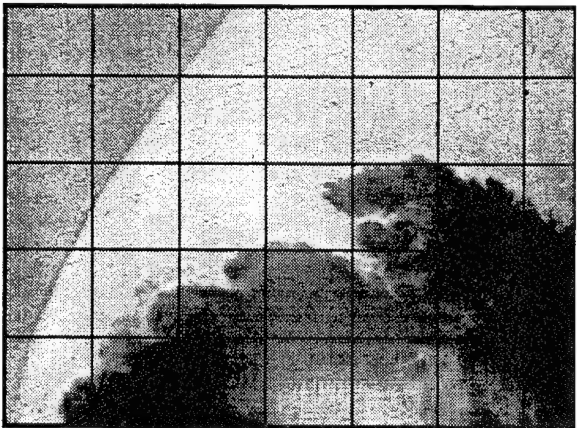


Image Pair Obtained for Elliptical Injection of Helium ($\Delta t = 1.2 \mu s$)

RESEARCH ON SUPERSONIC REACTING FLOWS

AFOSR Grant No. F49620-94-1-0152

Principal Investigators: C. T. Bowman, R. K. Hanson, M. G. Mungal and W. C. Reynolds

**Department of Mechanical Engineering
Stanford University
Stanford, CA 94305-3032**

SUMMARY/OVERVIEW:

A major technological challenge in achieving sustained hypersonic flight is the development of advanced air-breathing propulsion systems in which combustion takes place in supersonic flow. Combustion in supersonic flow is fundamentally different from combustion in the subsonic flow regime employed in existing air-breathing propulsion systems. The current understanding of fundamental aspects of supersonic combustion is inadequate to support the development of these advanced propulsion systems.

Recent advances in diagnostics capabilities and significant improvements in our abilities to compute complex flows offer new opportunities to obtain needed fundamental understanding of flow physics and chemistry interactions in compressible reacting flows. To achieve this understanding, a combined experimental and computational investigation of supersonic flows is in progress.

The primary elements of the investigation are mixing and combustion studies, refinement of previously-developed laser-based diagnostics for application in the experiments, and analysis and simulation. Specific accomplishments during the past year are summarized below.

TECHNICAL DISCUSSION:

Experiments on Supersonic Mixing and Combustion

Previous experiments performed in our supersonic combustion tunnel were aimed at understanding the effects of compressibility upon combustion in a two-dimensional supersonic mixing layer. A full discussion of these findings can be found in the Ph. D. thesis of M. F. Miller (1994). A main conclusion of this work was that compressibility leads to a change in entrainment ratio, which in turn affects the overall stoichiometry and combustion process. In addition, the efficiency of mixing under compressible conditions, has not been definitively compared to that under incompressible conditions. Hence, some of our work during the past year has been aimed at resolving some of these issues. Knowledge of mixing efficiency will also allow us to study the advantages of various mixing enhancements which can be applied to the compressible layer.

To this end, our experimental efforts have centered on verifying and applying a recently-reported PLIF technique (Clemens & Paul 1993) to quantitatively evaluate molecular mixing. This "cold chemistry" technique mimics a chemical reaction by quenching nitric oxide fluorescence with oxygen to provide a measurement of fluid unmixedness. From the unmixedness, the fraction of the mixing layer consisting of mixed fluid can be determined. Unlike a passive scalar measurement, the cold chemistry result is independent of the imaging system spatial resolution, allowing an accurate assessment of mixing at the molecular level. With the diagnostic, the effect of compressibility on mixing efficiency and the performance of various mixing enhancement strategies can be evaluated.

The accuracy of the diagnostic was verified through extensive static cell experiments. A small static cell capable of operation over variable temperature and pressure ranges was constructed. The fluorescence signal was collected from controlled gas mixtures for temperature and pressure ranges spanning the conditions found in the supersonic mixing layer facility. Good agreement between theoretical fluorescence models and the measured signal was found, thus providing confidence in the cold-chemistry technique.

Passive scalar and cold chemistry PLIF measurements have been made for low and high compressibility mixing layers. Example images are shown in Figure 1. In the passive scalar case, the nitric oxide tracer was diluted with pure nitrogen streams to provide a largely unquenched fluorescence environment, yielding significantly higher signal-to-noise images than previously available for the compressible mixing layer. For the cold chemistry technique, the tracer stream mixes with an oxygen-bearing stream which effectively quenches the fluorescence and results in a sharp interface between pure fluid and mixed fluid. From such images and similar images for which the nitric oxide bearing stream and the oxygen bearing stream are exchanged ("flipped"), the mixed fluid probability density functions and mixing efficiency of the mixing layer have been determined for low and high compressibility mixing layers, thus allowing a clearer interpretation of the work of Miller (1994). Our future work will allow us to directly compare the undisturbed layer, and one for which various mixing enhancements, such as streamwise vortices, have been applied.

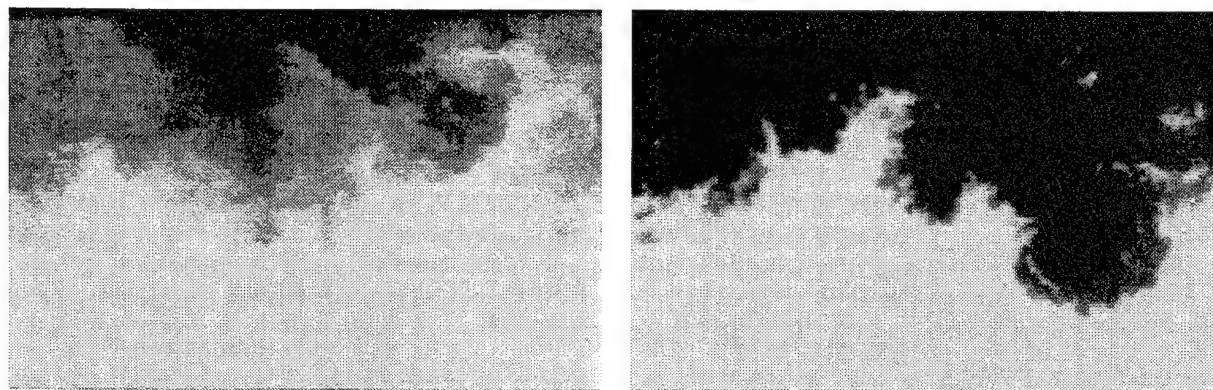


Figure 1: Passive scalar (left) and cold chemistry (right) PLIF side-view images of a low compressibility mixing layer. The passive scalar image indicates degree of mixing by variation in signal level whereas the cold chemistry image is nearly binary and shows regions of pure fluid.

PLIF Thermometry in Supersonic Flows

Good progress was made during the past year in optimizing our diagnostics strategy for temperature imaging in high-speed flows. The approach taken is based on ratioing two single-shot PLIF images obtained through excitation of separate rotational states of a single species, presently OH (Palmer and Hanson, 1995). The technique development and validation are done in an underexpanded axisymmetric free jet of combustion gases (5% H_2 , 5% O_2 , balance Ar) produced at the end wall of a conventional pressure-driven shock tube, using the experimental arrangement shown schematically in Fig. 2. These experiments are also used for velocity imaging, and as a result the laser sheets are directed at an angle to the flow. Each excimer-pumped dye laser pulse is split and introduced from either side of the flow, with one beam delayed slightly. The signals are recorded on two gated, intensified CCD detectors mounted above and below the test section.

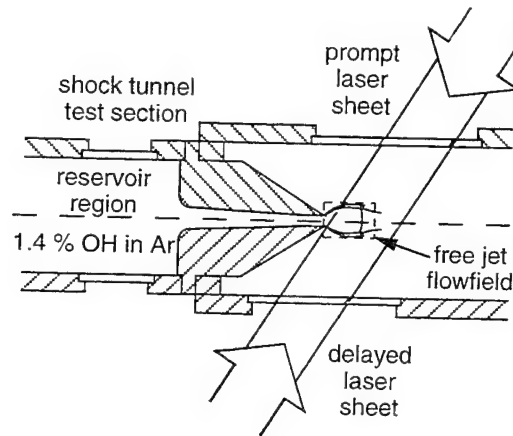


Figure 2: Mid-plane view of shock tunnel test section with counter-propagating laser sheets and imaged region of free jet flowfield shown.

Opposite Doppler shifts of the absorption frequency at each point in the flow result in a velocity dependence in the resultant image pair. A difference-to-sum combination of the signals, with an analysis of the single-shot laser spectrum and the assumption of flowfield symmetry may be used to infer the instantaneous two-component velocity field of the free jet. The rotational temperature field is obtained by taking the ratio of images acquired by exciting two different rovibrational transitions with laser pulses having similar lineshapes and relative detuning from their unshifted absorption linecenters. Results of the imaging experiments are shown in Fig. 3, along with the temperature field from a method of characteristics (MOC) simulation. Although the thermometry technique was demonstrated here using a single excitation system, making the acquisition of images during sequential facility firings necessary, it is extendible to instantaneous measurements in a straight-forward manner.

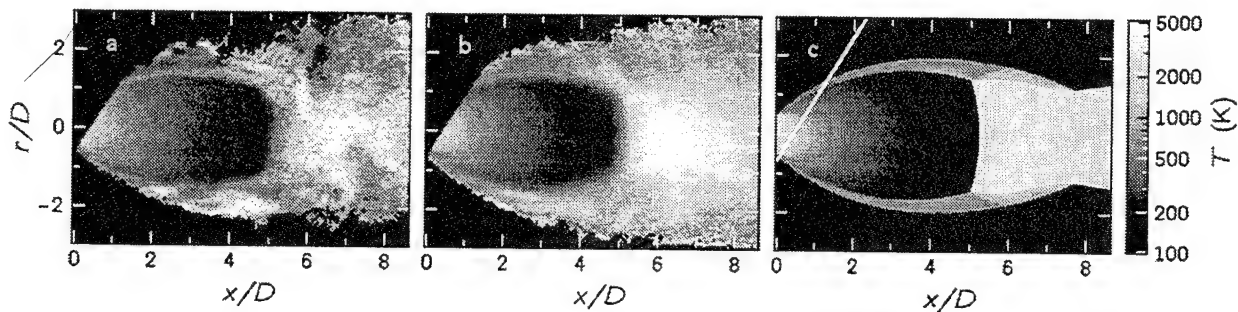


Figure 3: Single-shot and frame-averaged temperature fields, inferred from ratios of $Q_1(5):P_1(1)$ images (a and b), and a prediction by the MOC (c). The images are $8.61 \times 5.89 D$ (139×95 pixels) in size. The conditions of the free jet were: $T_s = 3350$ K, $P_s = 3.2$ atm, $P_s/P_a = 61$, with 1.4% OH in Ar and $D = 5$ mm.

Stability analysis and numerical simulation

The objective of this portion of the program is to provide guidance for the experimental research and contribute a diagnostic tool to aid in the interpretation of experimental results through access to the detailed flow physics. Linear stability analysis has been applied to a regime extending

beyond the current experimental limitations to provide insight into the effect of compressibility and heat release on the structure of the supersonic reacting mixing layer. This investigation is specifically focused on the regions of the parameter space that predict the emergence of a "colayer" structure (Planche and Reynolds, 1992). Our previous numerical investigations have shown this condition to cause significant reductions in mixing and combustion efficiency. Preliminary results from the linear stability analysis suggest colayer formation will be biased towards situations in which high heat release appears with low compressibility. Direct numerical simulations of the time-developing compressible reacting mixing layer with single-step chemistry will be used to detail this effect and evaluate the use of streamwise vortices to improve mixing and combustion in colayer conditions.

References

1. N. T. Clemens and P. H. Paul (1993) Scalar Measurements in Compressible Axisymmetric Mixing Layers, AIAA 93-0220, 31st AIAA Aerospace Sciences Meeting, Reno, NV.
2. Miller, M. F. (1994) An Experimental Investigation of the Effect of Compressibility on a Turbulent Reacting Mixing Layer, Ph. D. Thesis, Mechanical Engineering Department, Stanford University.
3. Palmer, J. L. and Hanson, R. K. (1995) Single-Shot OH PLIF Thermometry in a Reacting, Supersonic Free Jet. AIAA-95-0517, 33rd Aerospace Sciences Meeting, Reno, NV.
4. Planche, O. H. and Reynolds, W. C. (1992) A Numerical Investigation of the Compressible Reacting Mixing Layer, Report No. TF-56, Thermosciences Division, Mechanical Engineering Department, Stanford University.

HIGH RESOLUTION MEASUREMENTS OF SUPERSONIC MIXING AND COMBUSTION IN COFLOWING TURBULENT JETS

AFOSR Grant No. 89-0541

Werner J.A. Dahm
James F. Driscoll

*Gas Dynamics Laboratories
Department of Aerospace Engineering
The University of Michigan
Ann Arbor, MI 48109-2118*

Summary/Overview

Supersonic mixing and combustion in coflowing turbulent jets are being investigated and compared with results from compressible mixing layers to identify generic features of supersonic turbulent reacting shear flows. Experiments are used to investigate mixing and combustion in a turbulent fuel jet issuing into a supersonic ($M_\infty = 2.2$) coflowing air stream with stagnation temperatures as high as 600 K. Results are compared with supersonic turbulent mixing layers under investigation elsewhere to discern changes in large-scale and small-scale structure due to compressibility, and identify consequent effects on mixing and combustion properties. The coflowing turbulent jet is ideally suited for such comparisons. The incompressible flow follows non-algebraic similarity scalings that are well understood and documented. The large scale structure in the jet-like limit are also well documented and combustion properties have been previously investigated, allowing effects of compressibility to be readily identified. Comparisons with results from compressible mixing layer studies at Stanford and Caltech allow identification of compressibility effects that are common to supersonic combustion in turbulent shear flows from those that are specific to the mixing layer only.

Technical Discussion

To develop the necessary technical base for future supersonic airbreathing combustion systems, research has thus far focused on effects of compressibility on mixing and combustion in two-dimensional turbulent mixing layers. Several effects of compressibility in mixing layers have been documented, including changes in the similarity scaling properties of the flow (e.g. effects of compressibility on layer growth rate) as well as changes in the structure and dynamics of the large scales (e.g. two-layer structure). Implicit in these studies is the assumption that many of these phenomena are generic compressibility effects that will be seen in similar fashion in other turbulent reacting shear flows.

However, certain effects of compressibility seen in mixing layer studies are likely to result from the large scale structure and dynamics specific to that particular shear flow. Conclusions as to the generic effects of compressibility on mixing and combustion from studies in mixing layers alone may therefore be misleading. It is likely that flows with other scaling properties, and thus other large scale structure characteristics, will demonstrate some of the effects of compressibility seen in mixing layers, and will show other effects not seen in mixing layers. Aside from these changes in the large scale structure due to compressibility, it is likely that there are changes in the small scale structure as well. Classical scalings between the inner (small) scales of turbulent shear flows to the outer (large) scales rely on a balance in the energy

transfer process between them. When shock waves and expansion waves are present, nonequilibria in the energy transfer can potentially lead to changes in the inner-outer scale ratio, or even changes in the physical structure of the small scales themselves. Moreover, in the presence of heat release values typical of hydrogen or hydrocarbon fuels, the associated volumetric expansion near the reaction zones can potentially lead to further changes in the small scale hydrodynamics with attendant changes in the scalar mixing structure at the small scales. Identifying these effects of compressibility requires high resolution measurements to compare with results for the small scale structure in incompressible turbulent shear flows.

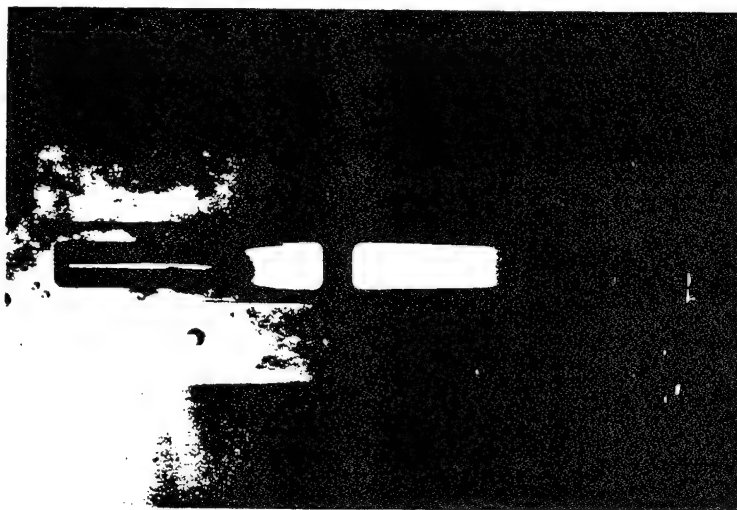
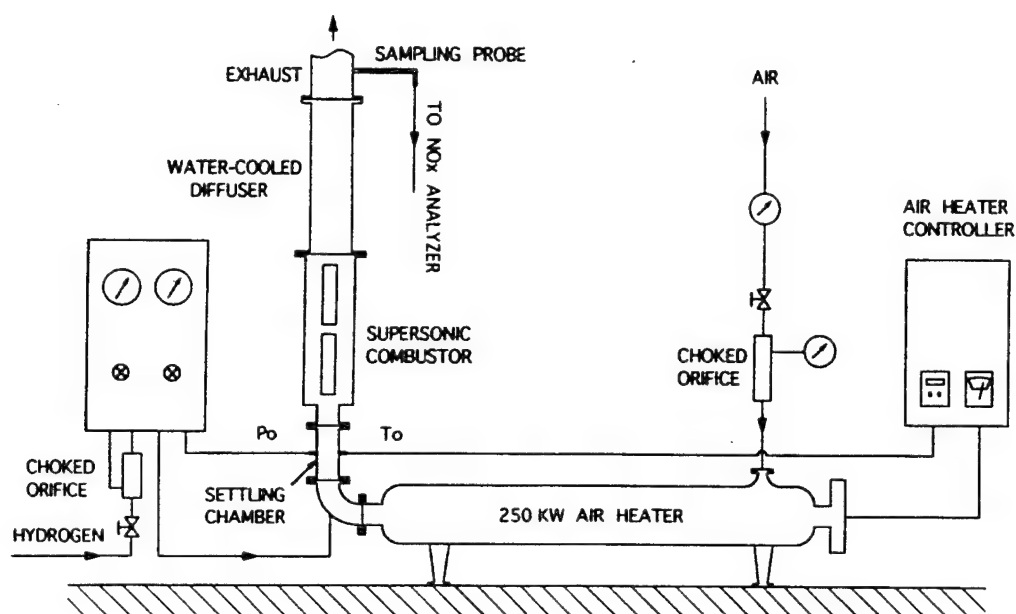
The present study is the first to obtain measurements in a compressible turbulent shear flow (other than the mixing layer studies mentioned above) that has been intentionally designed to permit examination of the large-scale and small-scale flow properties under reacting and nonreacting flow conditions. The work is being done in a novel supersonic combustion tunnel, designed and built at Michigan over the past three years. Diagnostics involve currently-available planar Rayleigh imaging measurements and acetone PLIF measurements of scalar mixing in nonreacting supersonic jets, together with density measurements based on planar Rayleigh imaging as well as planar OH imaging in supersonic jets with combustion. Results allow comparisons with comparable work in turbulent shear layers to identify generic effects of compressibility on the structure and dynamics of supersonic turbulent shear flows.

The Michigan Supersonic Combustion Facility

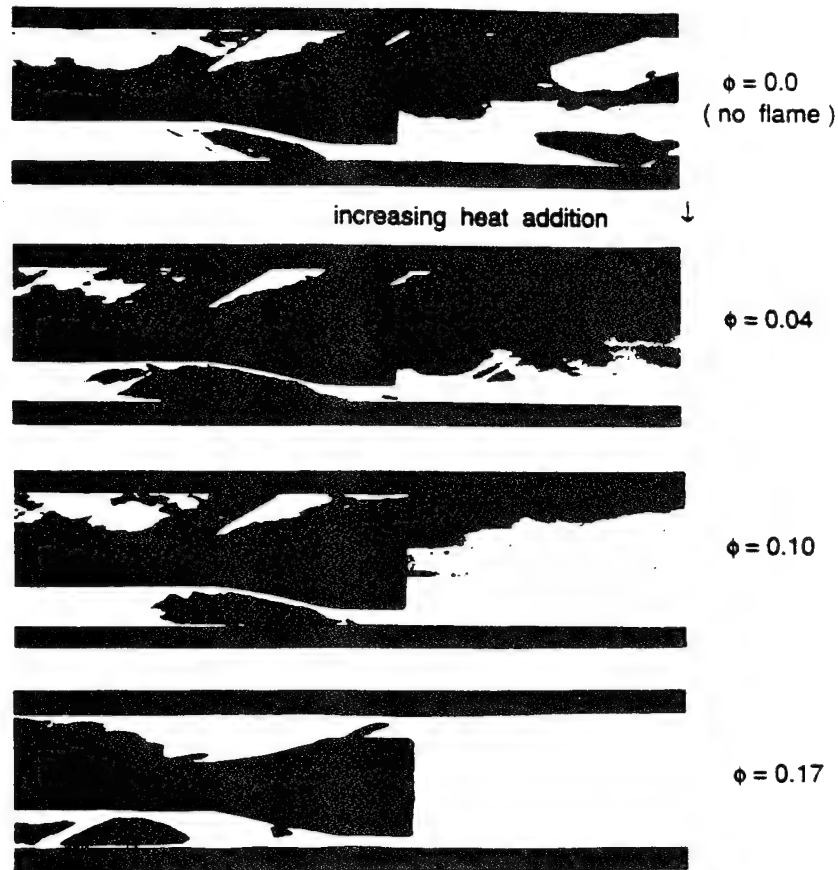
A novel, high-quality, flow facility has been designed and assembled for supersonic turbulent combustion studies in coflowing jets. This facility, shown in Figs. 1 and 2, is currently operational and has been used in exploratory studies over the past year. Primary components and capabilities include:

- a supersonic combustion section designed for Mach 2.2 air flow with stagnation temperatures up to 600K and nominal test section stagnation pressure of 6.44 atm. The combustion section is 55 cm long and nominally 5.77 cm \times 4.06 cm in cross section, and has plane parallel sidewalls for optical access, with wall divergence angles adjustable from 0–6° to eliminate thermal choking. A total of 30 static pressure taps and pitot probe ports are located on the test section walls to monitor the wall static pressure distribution and test section Mach number distribution. Access for advanced optical diagnostics is provided by 8 Vycor and quartz glass windows. A settling chamber immediately upstream of the two-dimensional supersonic nozzle contains a 42% blockage perforated plate and quieting section for inflow turbulence control. Typical flow conditions at the test section entrance are listed in Tables 2.1 and 2.2.
- a 250 kW electric air heater, with a length of 5.3 m, capable of heating up to 1.0 kg/sec air flow to temperatures as high as 1100K. A digital control circuit maintains constant stagnation temperature to within ± 0.5 K in the settling section. Electric heating was chosen over a vitiated air design to avoid radical concentrations present in vitiated air streams.
- a diffuser and exhaust duct section located at the exit of the supersonic test section. The water-cooled diffuser section has a constant area of 5.1 cm \times 11.9 cm and is 78.7 cm long, and is outfitted with 5 static pressure taps and two 1.3 cm \times 29 cm Vycor glass windows. The exhaust duct section has a circular cross-section, 10.8 cm in diameter, with two sampling probe ports located 125 cm and 240 cm from the supersonic test section entrance.
- a fuel injection tube located 16.5 cm downstream of the test section inlet. Gaseous fuel is injected to form a supersonic coflowing turbulent jet in the test section. Six ignition ports are located near the test section entrance. The current fuel tube has an inner diameter of 0.70 cm, and can be fitted with four different bluff body tips, having outer diameters ranging from 0.84 cm to 2.54 cm, to create recirculation zones of varying size. The resulting primary reaction zone length is typically 40 cm long when using hydrogen fuel.

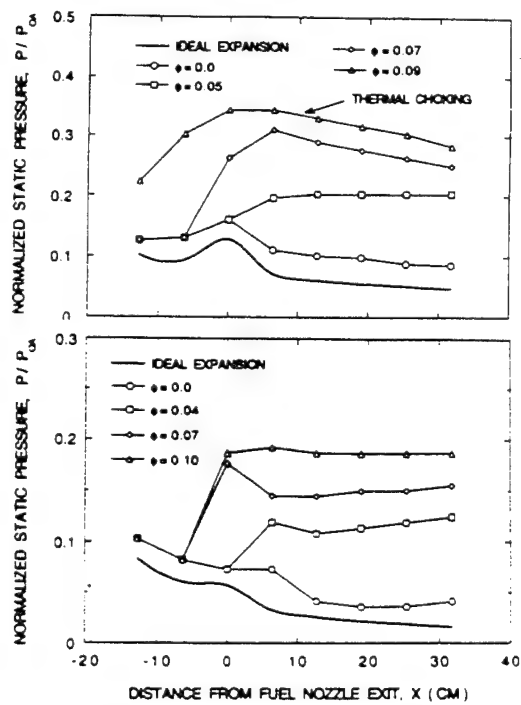
Schlieren photographs of the test section are shown in Figs. 3 and 4. These demonstrate the wave patterns and the thermal choking phenomenon with varying wall divergence angles. In practice, wall divergence angle is set to avoid choking and maintain constant Mach number within the test section. Measurements have also been made to verify the flow quality in the supersonic test section, both for cold flow testing as well as for flows under supersonic combustion conditions. Figures 5 and 6 respectively show typical results for the wall static pressure distribution along the test section, as well as the resulting Mach number distribution. Photographs of the supersonic coflowing turbulent jet flame are shown in Figs. 7 and 8. Work is currently underway to document effects of compressibility on the nonreacting flow. Subsequent work will examine effects of compressibility on combustion.



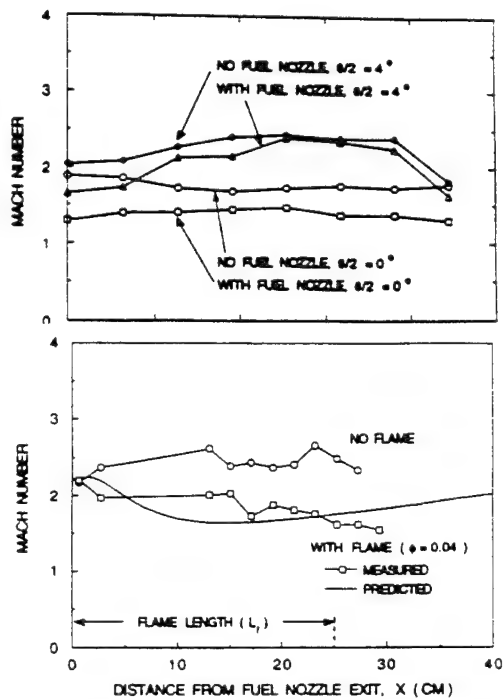
Figs. 1 & 2. The Michigan supersonic turbulent combustion facility, showing a schematic of the major facility components at top (Fig. 1) and a photograph of the facility at bottom (Fig. 2), for studies of compressibility effects on mixing and combustion properties in coflowing turbulent jets.



Figs. 3 & 4. Schlieren photographs of the supersonic coflowing turbulent jet.



Figs. 5 & 6. Wall static pressure distributions in the coflowing turbulent jet facility.



Figs. 7 & 8. Mach number distributions in the coflowing turbulent jet facility.

CHEMICAL REACTIONS in TURBULENT MIXING FLOWS

AFOSR Grant F49620-94-1-0353

P. E. Dimotakis and A. Leonard

Graduate Aeronautical Laboratories

California Institute of Technology, Pasadena, CA 91125

Summary/Overview

The purpose of this research is fundamental investigations of mixing, chemical reaction, and combustion processes; in turbulent, subsonic, and supersonic free-shear flows. The program is comprised of an experimental effort; an analytical, modeling, and computational effort; and a diagnostics and data-acquisition development effort, as dictated by the specific needs of the experimental effort. The computational studies are focused on fundamental issues pertaining to the numerical simulation of compressible flows with strong fronts, in both chemically-reacting and nonreacting flows. Parts of this effort are cosponsored by AFOSR URI Grant No. F49620-93-1-0338.

Technical discussion

A substantial upgrade and a GALCIT-internal safety review of the Supersonic Shear Layer (S³L) Facility have been completed. Specifically, the pressure-relief system of the high-pressure supply tank for the top stream has been redesigned, the test section in the new configuration has been rebuilt to withstand the higher pressures anticipated in the higher Mach-number runs and modified for improved optical access, a new catch-bag has been installed with a volume increased to 5,000 ft³, and an enclosure has been constructed for acoustic insulation, as well as to protect the catch bag and vent the surrounding air in the event of a bag failure. Many other redundancy/safety features have also been incorporated. Chemically-reacting runs in this facility are scheduled to resume in early June 1995.

As part of a continuing investigation of the behavior of all-hyperbolic, turbulent, mixing-layer flows, we have studied a moderate-compressibility, bi-supersonic flow. A schlieren photograph visualization of this mixing layer, $M_1 = 1.5$ [He], $M_2 = 1.2$ [N₂] (nominal freestream-inlet conditions), is shown in Fig.1. Two different pressure-wave systems are evident in this photograph: a lab-frame-stationary system generated by the increase in displacement thickness when the two freestream

flows first interact (extreme left-hand side of Fig. 1) and a traveling system in the bottom freestream. Stationary-wave refractions across the mixing layer and into the other freestream would be disallowed if one of the freestreams was elliptic. These finite-strength, wave-turbulence interactions do not appear to have a significant effect on the growth rate of the layer (*cf.*, also, Shau *et al.* 1993).¹ The little, or no, response of the growth rate to the wave interactions, in this high-density-ratio ($\rho_2/\rho_1 \approx 5$) flow, is noteworthy, considering the (net) baroclinic vorticity that these waves, which are refracted across to the other freestream, can generate.

The traveling-wave system is of the same character as those observed earlier,²⁻⁴ in supersonic, turbulent-jet flows and, more recently, in supersonic, mixing-layer flows.⁵ These waves appear to be associated with large-scale turbulent features, convecting supersonically with respect to the bottom freestream (in this case).

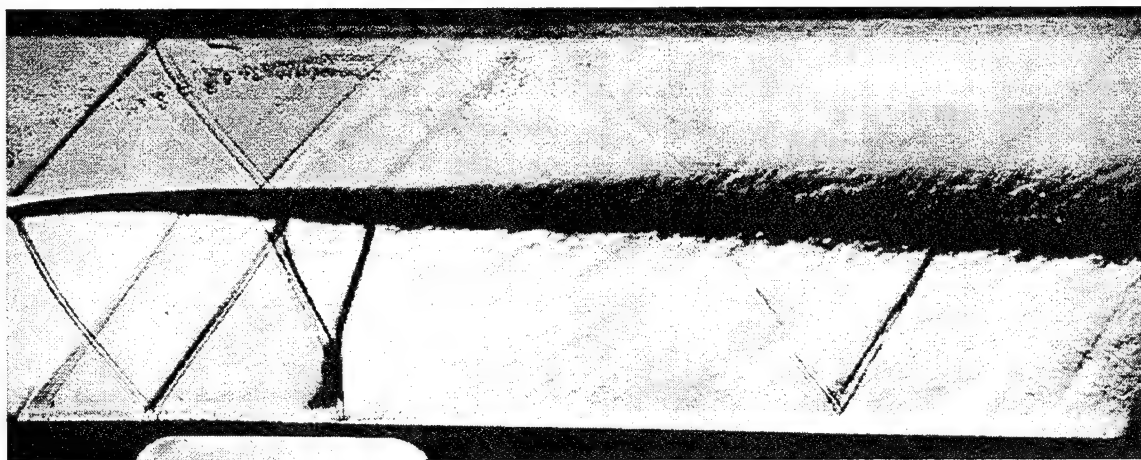


FIG. 1 Schlieren (vertical knife edge) photograph of hyperbolic, $M_1 = 1.5$ [He], $M_2 = 1.2$ [N₂], mixing-layer flow.

In our continuing investigations of turbulent mixing in liquid-phase jets, we have analyzed 2-D, high-resolution, high-signal-to-noise-ratio images of the jet-fluid concentration, using laser-induced-fluorescence techniques. These images are slices perpendicular to the jet axis, through the 3-D, far-field ($x/d \approx 300$) of the jet, and span the local transverse extent of the jet. Jet Reynolds numbers for these data were in the range, $4.5 \times 10^3 \leq Re \leq 18 \times 10^3$. Analysis of these data shows that this range spans a mixing transition in the jet far-field, as has also been documented, at comparable Reynolds numbers, in other flows.⁶ This is manifested in the pdf of the scalar field, as well as in the geometry of the scalar isosurfaces. Classical as well as fractal measures of the scalar-field level sets were computed and

found to be functions of both scalar threshold and Reynolds number, reflecting a transition between different turbulent-mixing states in the Reynolds-number range investigated. We have also recorded 3-D, (x, y, t) -image data, at $Re = 9.0 \times 10^3$, using custom-developed, multiple-frame, image-acquisition hardware developed under AFOSR support. These indicate a highly-complex, 3-D, isoscalar-surface geometry.

An effort to provide high signal-to-noise, 2-D images for gas-phase, fully-developed, turbulent jets, using Rayleigh laser-scattering of dissimilar gases at elevated pressures, is presently in progress.

We have continued our development of Image Correlation Velocimetry (ICV) techniques as a means of estimating the velocity field of a flow from images that are closely-spaced in time.⁷ The method relies on an iterative, global minimization of the difference between the second image and a mapping of the first. The resulting (smooth) mapping then yields the desired velocity-field information. In the current implementation, the mapping (and velocity field) is represented using multivariate B-splines. These allow the proper continuity and smoothness criteria to be satisfied, as well as the appropriate velocity-field boundary conditions to be specified. An improved initialization scheme has been developed that is designed also to avoid convergence to local minima and is based on iterative, multigrid evaluation of the correlation function of relatively large regions of the flow, akin to DPIV methods.

The first silicon wafers containing a new, dual-image, CCD, especially designed in collaboration with Jim Janesick and Andy Collins of the Imaging Group of the Caltech Jet Propulsion Laboratory, were just fabricated (RETICON). The new CCD, dubbed the "Mach-CCD", allows a pair of high-quality, high-resolution images to be recorded as close as $1 - 2 \mu s$ apart. The electronic camera head and data-acquisition interfaces for the new CCD, which should be available in late June of 1995, are also nearing completion. The new, high-speed, dual-image system is targeted for use in high-speed, subsonic and supersonic, gas- and liquid-phase flows.

In our computational effort, we have developed an unsplit algorithm for the simulation of chemically-reacting flows. The algorithm finds surfaces in space-time where appropriate Riemann invariants hold,⁸ permitting us to integrate the complete flow/chemistry evolution equations accurately and robustly. The resulting code has been tested for various cases of steady and unsteady 1-D detonation waves. Our results are in excellent agreement with existing results in the literature.^{9,10} Furthermore, we obtained results for ZND detonations with very low overdrive factors (documented numerical results for these cases are not available). Linear-stability

analysis suggests that for 1-D detonations near the Chapman-Jouguet point we should expect multi-mode instabilities. Our numerical simulations reveal an unstable, almost chaotic behavior, characterized by the creation of pockets of reaction behind the leading-shock front, accompanied by the formation of secondary-shock wave systems with very large heat release. We are presently working on a multi-dimensional implementation of this algorithm for simulations of chemically-reacting flows.

References

- ¹ Shau, Y. R., Dolling, D. S., and Choi, K. Y., "Organized structure in a compressible turbulent shear layer," *AIAA J.* **31**(8), 1398-1405 (1993).
- ² Lowson, M. V., and Ollerhead, J. B., "Visualization of noise from cold supersonic jets," *J. Acoust. Soc. Am.* **44**, 624 (1968).
- ³ Tam, C. K. W., "Directional acoustic radiation from a supersonic jet," *J. Fluid Mech.* **46**, 757-768 (1971).
- ⁴ Oertel, H., "Mach wave radiation of hot supersonic jets investigated by means of the shock tube and new optical techniques," *12th Int. Symp. on Shock Tubes and Waves*, 266-275 (1979).
- ⁵ Hall, J. L., Dimotakis, P. E., and Rosemann, H., "Experiments in non-reacting compressible shear layers," *AIAA J.* **31**(12), 2247-2254 (1993).
- ⁶ Dimotakis, P. E., "Some issues on turbulent mixing and turbulence," GALCIT Report FM93-1a (1993).
- ⁷ Tokumaru, P. T., and Dimotakis, P. E., "Image Correlation Velocimetry," *Exp. in Fluids* (1995).
- ⁸ Lappas, T., Leonard, A., and Dimotakis, P. E., "Riemann Invariant Manifolds for the Multidimensional Euler Equations. Part I: Theoretical Development. Part II: A Multidimensional Godunov Scheme," GALCIT FM94-6 report (1994).
- ⁹ Fickett, W., and Wood, W., "Flow calculation for pulsating one-dimensional detonation," *Phys. Fluids* **9**, 903-916 (1966).
- ¹⁰ Bourlioux, A., Majda, A., and Roytburd, V., "Nonlinear Development of Low Frequency One-Dimensional Instabilities for Reacting Shock Waves," *SIAM J. Appl. Math.* **51**, 303-343 (1991).

STUDIES ON HIGH PRESSURE AND UNSTEADY FLAME PHENOMENA

(AFOSR Grant No. F49620-95-1-0092)

Principal Investigator: Chung K. Law

Princeton University
Princeton, NJ 08544

SUMMARY/OVERVIEW

The objective of the present program is to study the structure and response of steady and unsteady laminar premixed and nonpremixed flames in reduced and elevated pressure environments through (a) non-intrusive experimentation, (b) computational simulation using detailed flame and kinetic codes, and (c) asymptotic analysis with reduced kinetic mechanisms. During the reporting period progress has been made in the following projects: (1) An analytical and experimental study of unsteady diffusion flames. (2) A computational and experimental study of the effects of thermophoresis on seeding particles in LDV measurements of flames. (3) A re-examination of the accuracy of the counterflow flame technique for the determination of laminar flame speeds. (4) Review articles written covering research performed under AFOSR support in recent years.

TECHNICAL DISCUSSIONS

1. Studies on Unsteady Diffusion Flames

An important influence on the flame behavior which so far has not been adequately addressed is the effect of unsteadiness of the environment on the flame behavior. This issue is of particular relevance to the modeling of turbulent flames through the concept of laminar flamelets. These flamelets are subject to fluctuating flows with various intensities of straining, and it is reasonable to expect that the flame would respond differently in an oscillating strained flow field than in a steady strained flow field.

During the reporting period we have first extended a previous asymptotic analysis on counterflow diffusion flames subject to *small-amplitude, sinusoidal* strain rate perturbations (Publication No. 1) to *arbitrary* strain rate as a function of time, with the assumptions of constant density and unity Lewis number. When specialized to the case of an impulsively-applied strain rate, the characteristic relaxation time as well as the extinction delay time are derived. For the sinusoidal strain rate, the reaction sheet oscillation is found to be asymmetrical with respect to its initial location, protruding more toward the freestream side. Furthermore, the amplitude of the oscillation decreases with frequency, and its phase delay approaches $\pi/2$ in the high frequency limit, as observed in previous experimental and numerical studies. For a given amplitude of oscillation, the flame is more easily extinguished when the characteristic time of oscillation is sufficiently long. When this result is applied to the current understanding of turbulent flames, it suggests that the laminar flame sheet can be sustained at higher Reynolds numbers. This is because there exists a range of eddies which, while possessing a sufficiently large strain rate to extinguish the flame in the steady limit, do not have sufficiently long characteristic time to effect extinction. Thus it seems reasonable to suggest that the applicable range of the laminar flamelet regime may be wider than can be expected from quasi-steady considerations.

The above concept is schematically shown in Fig. 1, in which we have plotted a normalized Damkohler number of an eddy versus the characteristic eddy size. The solid line represents the variation based on steady state considerations such that extinction of the eddy is expected when it crosses the maximum extinction Damkohler number line. However, allowing for unsteadiness, the

dotted lines show that crossing of this limit either is delayed or may not occur at all. Results from the above theoretical study are reported in Publication No. 2.

Experimentally, we have constructed a counterflow burner with strain rate oscillations being applied by loud speakers. An important consideration here is the ability to independently vary the frequency and amplitude of the oscillation. Preliminary results seem to indicate that, for a given frequency, extinction occurs at a constant maximum strain rate regardless of the steady-state strain rate. This would imply that extinction is a quasi-steady process, with the reaction zone only affected by the instantaneous strain rate it experiences. Unsteadiness, however, does seem to have a second order effect in that the instantaneous extinction strain rate is found to increase with frequency, as shown in Fig. 2.

2. Thermophoretic Effects on Seeding Particles in LDV Measurements of Flames

In a recent experimental and computational study on the detailed dynamic, thermal, and chemical structure of adiabatic, laminar counterflow premixed flames, we noticed that while close quantitative agreement between the measured and computed results exists for the scalar structure of the flame, the LDV-measured axial velocity profile consistently lags the calculated values by substantial amounts in the preheat zone of the flame, as shown in Fig. 3. Order of magnitude estimates showed that such a lag could be due to the influence of thermophoresis on the LDV seeding particles in the high-temperature-gradient environment of the preheat zone. Indeed, when detailed calculations were performed for the motion of the seeding particles, under the influence of drag and thermophoresis and by using the computationally-determined flame structure to evaluate the various transport coefficients, the computed particle trajectory agreed well with the measured LDV velocity profile, as shown in Fig. 3.

Since temperature increases monotonically in the direction of the flow in an adiabatic *premixed* flame, the effect of thermophoresis can be readily visualized as in Fig. 3. However, for a counterflow *diffusion* flame, the temperature peaks in the flow field such that the thermophoretic force acts in opposite direction in the fuel and oxidizer sides of the flame. Furthermore, since the flow is uni-directional in crossing the flame, and the direction also switches when the flame moves across the stagnation surface, the net dynamic response of the LDV particles can be very rich. Figure 4 shows the evolution of the measured particle velocity profiles and computed gas velocity profiles for flames with the same calculated adiabatic flame temperature but different stoichiometric mixture fractions and hence locations relative to the stagnation surface. The richness and complexity with which the particle velocity can be modified by thermophoresis is quite evident.

There are several implications of this finding. First, thermophoresis appears to be a factor that needs to be estimated and possibly accounted for when measuring flame properties and responses using LDV and PIV, especially for thin flames in local flow field of low convective velocities. Its potential influence on measuring the velocity statistics in turbulent flames also needs to be examined. Furthermore, caution is also needed in the study of flame chemistry by directly extracting the local temperature profile from the local LDV-velocity profile, without considering thermophoresis.

The above work is reported in Publication Nos. 3 and 4.

3. Re-Examination of the Counterflow Technique in Laminar Flame Speed Determination

The accuracy of the laminar flame speed determination by using the counterflow twin flame technique has been computationally and experimentally examined in light of the recent understanding that linear extrapolation of the reference upstream velocity to zero strain rate would yield a value higher than that of the laminar flame speed, and that such an over-estimate can be reduced by using either lower strain rates and/or larger nozzle separation distances. A systematic evaluation of the above concept has been conducted and verified for the ultra lean hydrogen/air flames which have relatively large Karlovitz numbers, even for small strain rates, because of their very small laminar flame speeds. Consequently, the significantly higher values of the previous experimentally measured flame speeds, as compared to the independently calculated laminar flame speeds, can now be attributed to the use of nozzle separation distances which were not sufficiently large and/or strain rates which were not sufficiently small. Thus by using lower strain rates and larger nozzle separation distances the experimentally and computationally re-determined values of these ultra lean hydrogen/air flames agree well with the calculated laminar flame speeds (Fig. 5).

The laminar flame speeds of methane/air and propane/air mixtures have also been experimentally re-determined over extensive ranges of the equivalence ratio and are found to be slightly lower than previously reported experimental values. Figure 6 shows the data and comparison for the propane/air flames.

This work is reported in Publication No. 5.

4. Review Articles

Two major review articles have been written on combustion phenomena whose understanding has been made possible through several long-term research programs including the present one. The first is on microgravity combustion (Publication No. 6) in which interpretation of the flame structure and aerodynamic response reached fruition through the present program. The second is on the role of chain mechanisms in combustion phenomena (Publication No. 6) in which chemical and aerodynamic effects on the flame structure and response are discussed from a unified viewpoint.

MAJOR PUBLICATIONS (April, 1994 – March, 1995)

1. "Response of counterflow diffusion flames to oscillating strain rates," by H. G. Im, C. K. Law, J. S. Kim and F. A. Williams, *Combustion and Flame*, Vol. 100, pp. 21-30 (1995).
2. "Counterflow diffusion flames with unsteady strain rates," by H.G. Im, J.K. Bechtold and C.K. Law, to appear in *Combustion Science and Technology*.
3. "Thermophoretic effects of seeding particles in LDV measurements of flames," by C.J. Sung, C.K. Law and R.L. Axelbaum, *Combustion Science and Technology*, Vol. 99, pp. 119-132 (1994).
4. "Further studies on effects of thermophoresis on seeding particles in measurements of strained flames," by C.J. Sung, J.S. Kistler, M. Nishioka and C.K. Law, submitted.
5. "Further considerations on the determination of laminar flame speeds with the counterflow twin flame technique," by C.M. Vagelopoulos, F.N. Egolfopoulos and C.K. Law, *Twenty-Fifth Symposium (International) on Combustion*, pp. 1341-1347 (1994).
6. "Opportunities and challenges of combustion in microgravity," by C.K. Law and G.M. Faeth, *Progress in Energy and Combustion Science*, Vol. 20, pp. 65-113 (1994).
7. "The role of chain mechanisms in some fundamental combustion phenomena," by C.K. Law, submitted.
8. "Extinction of premixed methane-air flames with volumetric heat loss," by J.K. Bechtold and C.K. Law, *Combustion Science and Technology*, Vol. 100, pp. 371-383 (1994).
9. "Effects of pressure and dilution on the extinction of counterflow nonpremixed hydrogen-air flames," by P. Papas, I. Glassman and C.K. Law, *Twenty-Fifth Symposium (International) on Combustion*, pp. 1333-1339 (1994).

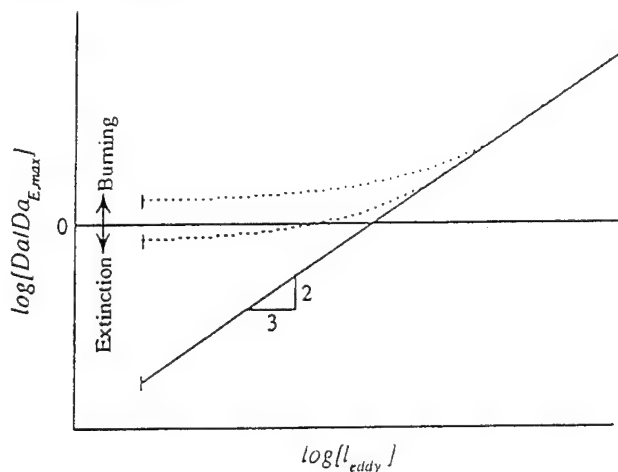


Figure 1

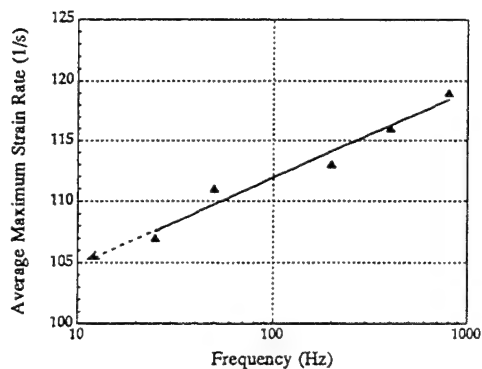


Figure 2

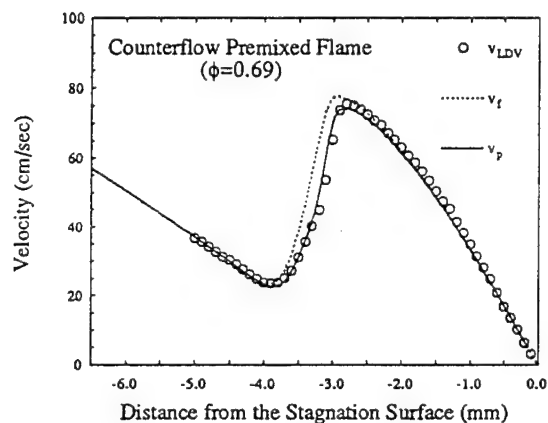


Figure 3

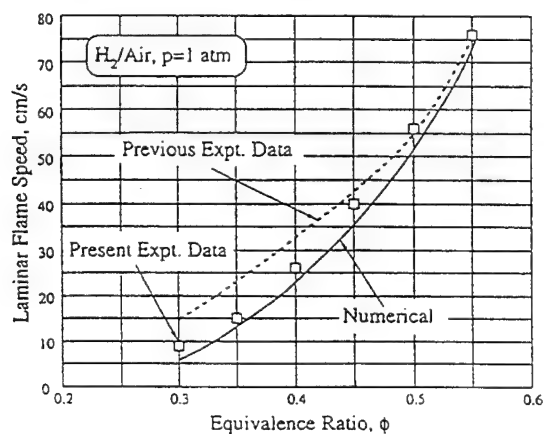


Figure 5

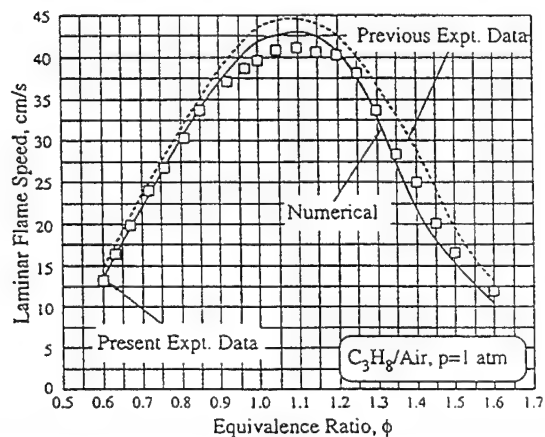


Figure 6

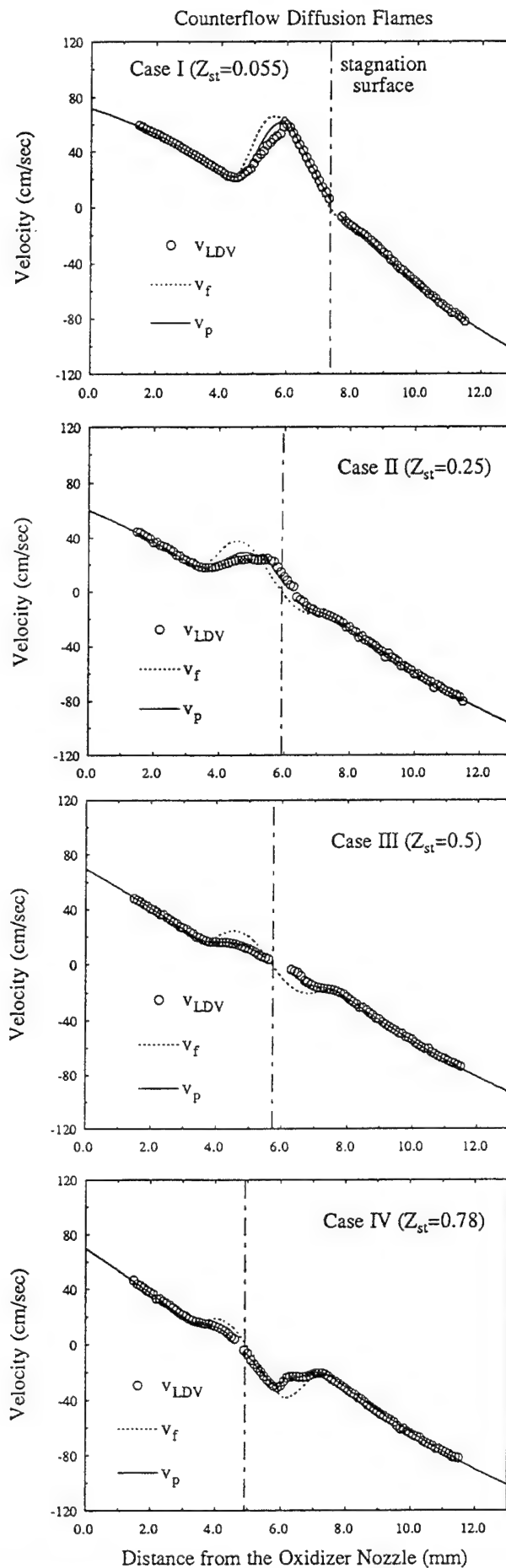


Figure 4

NUMERICAL STUDIES FOR THE RAM ACCELERATOR

(AFOSR-MIPR-95-0023)

Chiping Li, K. Kailasanath, Elaine S. Oran, and Jay P. Boris

Laboratory for Computational Physics, Code 6400
Naval Research Laboratory, Washington, DC 20375

SUMMARY/OVERVIEW

In the past year, we have focused on the projectile stability and the starting process of the thermally choked ram accelerator (Fig. 1). We used multidimensional, reactive simulations to provide the pressure information on the projectile for studying these issues. Our studies show that: (1) The pressure distribution on the front part of the projectile is controlled by a series of reflected shock and expansion waves. These reflected pressure waves are quite stable and virtually steady. A perturbation in the projectile position can result in significant changes in the strength of these shock and expansion waves, but the overall structure of these pressure waves remains the same; (2) On the rear part of projectile, there is a normal shock generated by the thermally choked combustion behind the projectile. This shock maintains the high pressure needed for the projectile acceleration. Unlike the reflected shock on the front part, this shock is transient. A perturbation in projectile position can change both the strength and location of this shock; (3) When the center of projectile mass is in the middle of the projectile, the pressure imbalance created by the perturbation in the position stabilizes the projectile if a normal shock is maintained on the rear of projectile by the thermally choked combustion. The pressure imbalance further destabilizes the projectile if the normal shock is absent. (4) The study on the starting process shows that the thermally choked combustion and the associated normal shock could be generated by either a pressure pulse, resembling that created by the obturator, or an ignition process on the rear part of projectile, resembling that generated by an on-projectile ignitor.

TECHNICAL DISCUSSION

Pressure Distribution on the Projectile

We have performed numerical simulations of the reactive flow around the projectile at different positions in the thermally choked ram accelerator filled with the $\text{H}_2:\text{O}_2:\text{N}_2/2:1:3.76$ mixture. The inlet pressure and temperature of the mixture are 25 atm and 300 K, respectively. The projectile used in this study is the same as that used in the experiments at the University of Washington and the geometric specifications of the projectile are shown Fig. 2. The projectile velocity is 1250m/s and corresponding Mach number is 3.01. The studied projectile positions are: (1) the center line is located at the axis of the ram-accelerator tube, (2) the center line is translated 1.0 mm downward from the tube axis, and (3) the center line rotated 1.5° counterclockwise around the center of mass. For each projectile position, we performed three types of simulations: (a) A nonreactive flow simulation; (b) A reactive flow simulation with a simulated starting process which initiates the thermally choked combustion: The thermally choked combustion maintains a normal shock on the rear part of the projectile. (c) A reactive flow simulation without the simulated starting process: In this case, combustion occurs in a small region behind the projectile and is too weak to change the shock structure on the projectile. Therefore, there are no normal shocks on the rear part of the projectile and the pressure distribution on the projectile is very similar to that from the nonreactive simulation. In this case, the projectile does not accelerate.

Figures. 3-5 show pressure, Mach number, temperature, and water concentration around the projectile from the type-b simulations (with the starting process). The same figures also show the pressure profile on the projectile. When the projectile is centered, the shock structures and, therefore, the pressure distributions are symmetric on the upper and lower projectile surfaces. In the translated case, the strength of the reflected shock and expansion waves are quite different on the two surfaces while the locations of these waves remain similar. However, the strength and location of the thermally choked normal shock are largely the same on the both surfaces. In the rotated case, the locations of the reflected waves still remain similar on the two surfaces while the difference in the strength is pronounced. Both the location and strength of the normal shock differ significantly on the two surfaces.

Projectile Stability

Having obtained the pressure information on the projectile, we calculated the aerodynamic torque on the projectile with different centers of mass. The following two tables show the results from the type-b and type-c simulations. The projectile with its center of mass at 7.4 cm from the tip is very similar to that used in the experiments and we will focus on this projectile. In this case, the torque on the centered projectile is quite minimal. The torque on the translated projectile is significant. Therefore, projectile translation leads to projectile rotation (canting). In the rotated case, the torque stabilizes the projectile if a normal shock is maintained on the rear part of the projectile by the thermally choked combustion. If the normal shock is absent, the torque augments the original rotation and, therefore, further destabilizes the projectile. Thus, the normal shock changes the stability characteristics of the projectile.

torque on the projectile per unit width from the type-b simulations (N-m/m) (with the normal shock generated by the thermally choked combustion)			
location of the center of mass from the projectile tip (cm)	3.4	7.4	11.4
projectile axis			
centered	-4.0 to 3.0	-6.0 to 14.0	-40.0 to 30.0
translated	$2.6 \text{ to } 5.0 \times 10^3$	$3.0 \text{ to } 5.4 \times 10^2$	$-2.3 \text{ to } -1.4 \times 10^2$
rotated	$-2.2 \text{ to } -1.5 \times 10^4$	$-9.0 \text{ to } -5.5 \times 10^3$	$2.8 \text{ to } 3.2 \times 10^3$

torque on the projectile per unit width from the type-c simulations (N-m/m) (without the normal shock generated by the thermally choked combustion)			
location of the center of mass from the projectile tip (cm)	3.4	7.4	11.4
projectile axis			
centered	-18.0 to 24.0	-2.0 to 10.0	-3.5 to 2.0
translated	$1.8 \text{ to } 2.4 \times 10^3$	$3.2 \text{ to } 4.5 \times 10^2$	$-2.8 \text{ to } -1.2 \times 10^3$
rotated	$-5.2 \text{ to } -3.5 \times 10^3$	$2.3 \text{ to } 8.5 \times 10^2$	$1.0 \text{ to } 1.6 \times 10^3$

Starting Process

The normal shock on the rear part of the projectile is not only crucial to the projectile acceleration but also important to the projectile stability. This shock is maintained by the thermally choked combustion behind the projectile. However, thermally choked combustion cannot be established without a proper starting process. In the experiments, the thermally choked combustion is initiated by a pressure pulse generated by an obturator initially located behind the projectile. Our time-accurate numerical simulation capability provides a tool to study this starting process. If a simulation is started without using any simulated starting processes, combustion is confined to a small region behind the projectile and the energy release from the combustion is far too weak to choke the flow and, therefore, to maintain a normal shock on the rear part of the projectile. The thermally choked combustion and the associated normal shock need to be generated by either a pressure pulse, resembling that created by the obturator, or an ignition process on the rear part of projectile, resembling that generated by an on-projectile ignitor. This issue requires more detailed studies.

PUBLICATIONS AND PRESENTATIONS

- Detonation Structures behind Oblique Shocks, C. Li, K. Kailasanath, and E.S. Oran, *Physics of Fluids*, 6:1600, 1994.
- Numerical Simulations of Transient Reactive Flows in Ram Accelerators, C. Li, K. Kailasanath, E.S. Oran, A.M. Landsberg, and J.P. Boris, to appear *Shock Waves*, 1995.
- Detonation Structures Generated by Multiple Shocks on Ram-Accelerator Projectile, C. Li, K. Kailasanath, and E.S. Oran, Submitted to *Combustion and Flame*, 1995
- Analysis of Pressure Distributions on Projectiles in Thermally Choked Ram Accelerators, C. Li, K. Kailasanath, and E.S. Oran, Submitted to the 2nd Int. Workshop on Ram Accelerators, 1995.

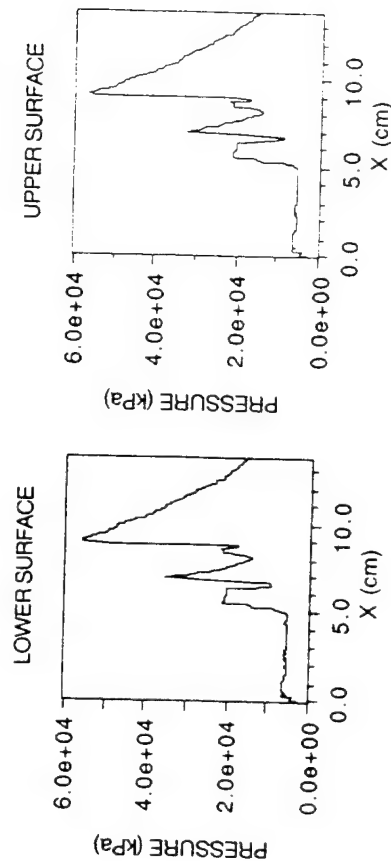
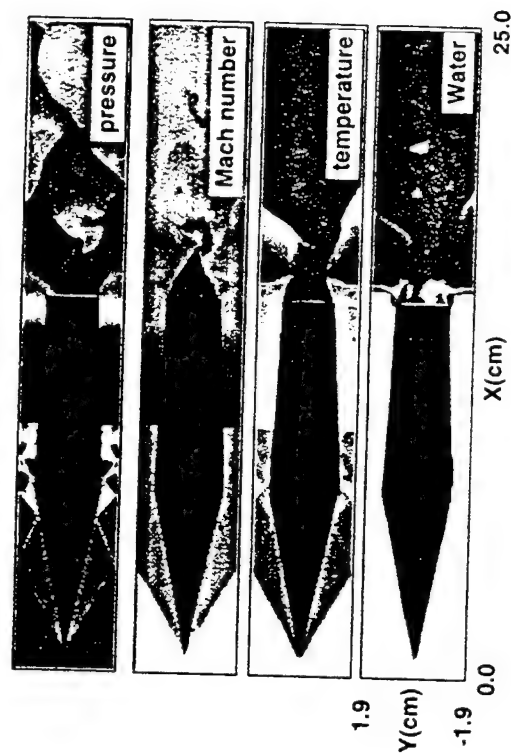


Fig. 3 Top figures: pressure, Mach number, temperature and water concentration from the simulation of the reactive flow around the projectile shown in Fig. 2 in the $H_2:O_2:N_2/2:1:3.76$ mixture. The projectile Mach number is 3.01 and, in this case, the projectile axis coincides with that of the launch tube. Bottom figures: pressure distributions on the lower and upper surfaces of the projectile from the simulation.

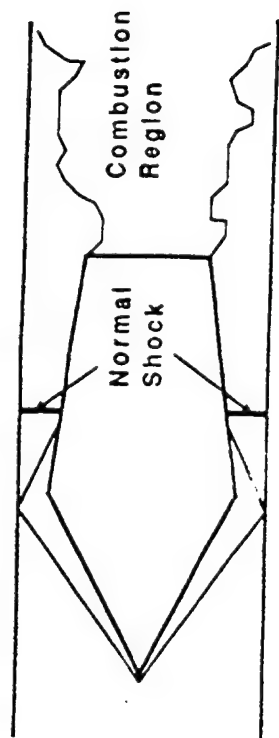


Fig. 1 Schematic of major reactive-flow features in a thermally choked ram accelerator.

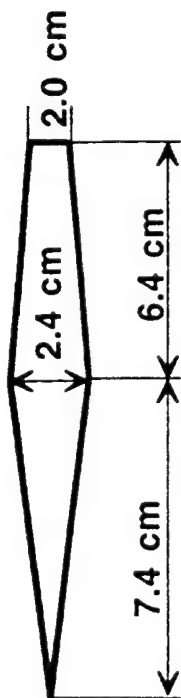


Fig. 2 Schematic of the projectile used in the simulations.

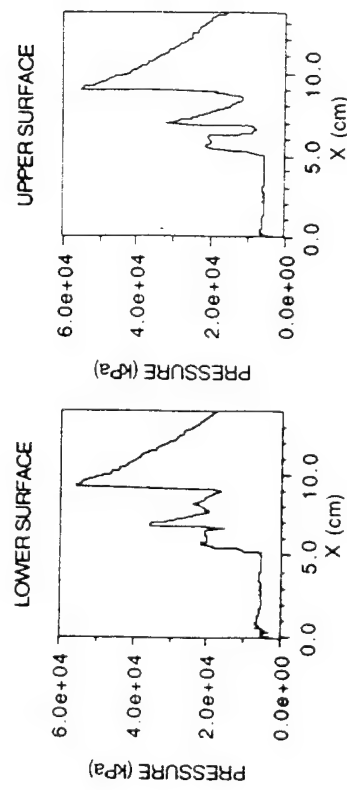
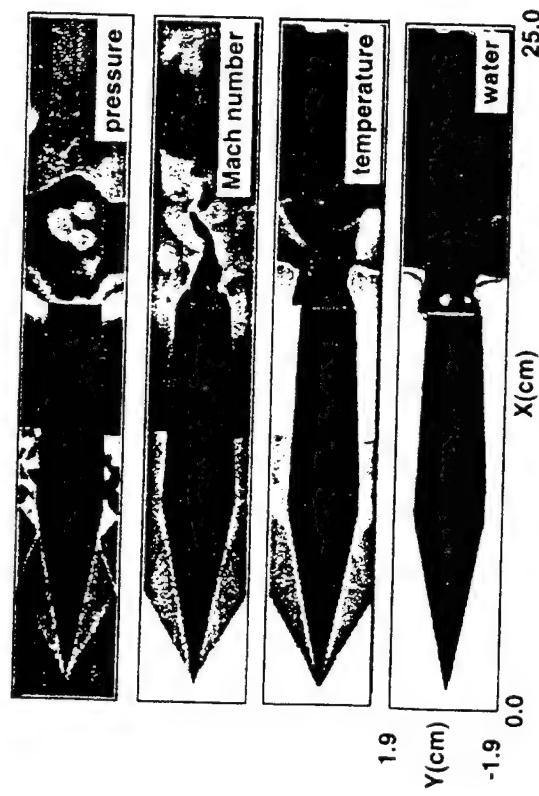
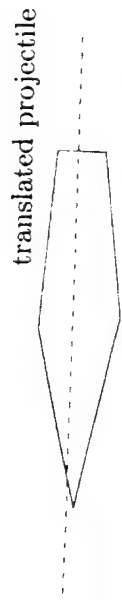


Fig. 4 Top figures: pressure, Mach number, temperature and water concentration from the simulation of the reactive flow around the projectile shown in Fig. 2 in the $\text{H}_2:\text{O}_2:\text{N}_2/2:1:3.76$ mixture. The projectile Mach number is 3.01 and, in this case, the projectile axis is translated 1.0mm downward from that of the launch tube. Bottom figures: pressure distributions on the lower and upper surfaces of the projectile from the simulation.

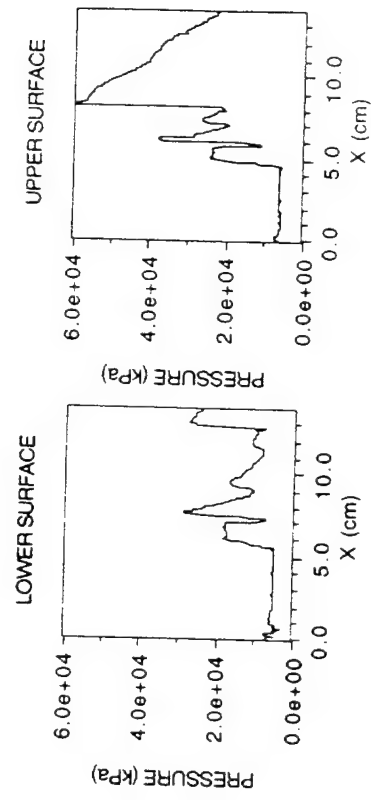
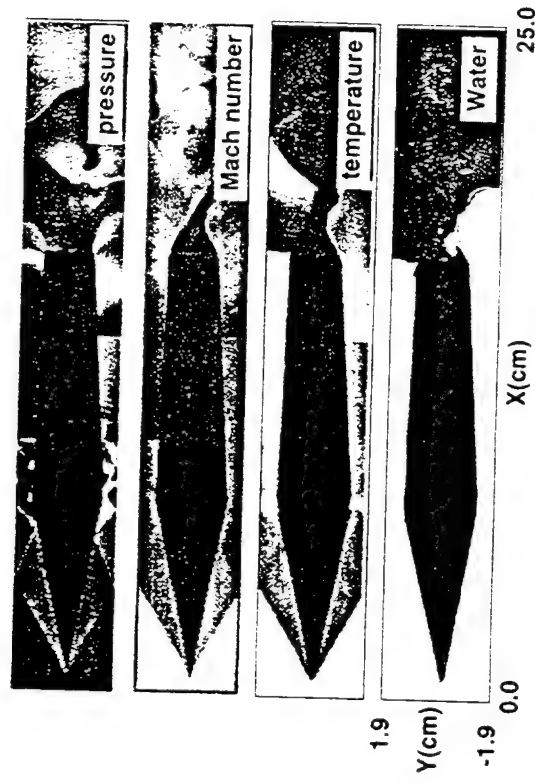


Fig. 5 Top figures: pressure, Mach number, temperature and water concentration from the simulation of the reactive flow around the projectile shown in Fig. 2 in the $\text{H}_2:\text{O}_2:\text{N}_2/2:1:3.76$ mixture. The projectile Mach number is 3.01 and, in this case, the projectile axis is rotated 1.5° counterclockwise from that of the launch tube. Bottom figures: pressure distributions on the lower and upper surfaces of the projectile from the simulation.

ABSTRACTS OF WORK UNITS NOT PRESENTED

MODELING STUDY TO EVALUATE THE IONIC MECHANISM OF SOOT FORMATION

(AFOSR Contract No. F49620-94-C-0014)

Principal Investigator: H.F. Calcote

AeroChem Research Laboratories, Inc.
P.O. Box 12, Princeton, NJ 08542

SUMMARY/OVERVIEW

This research program addresses: (1) the nucleation step in the mechanism of soot formation in flames, and (2) the mechanism of formation of the large cations observed in flames. The ionic mechanism of soot nucleation is studied by computer modeling and the results compared with experimental results. The major effort has been on development of the thermochemistry of large ions because thermochemistry dominates the process. A detailed mechanism with appropriate rate coefficients has also been developed.

At the last AFOSR meeting we reported difficulties with the mechanism when extended to ions above a mass of about 150 u. To obtain agreement between the model and experiment it was necessary to assume a flame temperature of about 1700 K, when the measured flame temperature is 2000 K. This led to rethinking several aspects of the problem. First we reconfirmed our faith in the ionic mechanism by noting that the only flame properties which change at the soot threshold are the ion concentrations and the identity of the ions. We reevaluated Steins suggestion that the ions actually observed in flame by mass spectrometry were not the ions actually present because of rapid hydrogen atom attachment in the sampling cone. This possibility was confirmed. It required development of additional thermochemical and reaction kinetic data. In reconsidering mechanism details we also examined the role of energy transfer in ion-molecule reactions.

TECHNICAL DISCUSSION

1. Why a Threshold Equivalence Ratio For Soot Formation?

Soot formation appears very abruptly as the fuel concentration is increased, at a specific C/O ratio. This usually occurs at $C/O < 1$, while it is expected from thermochemical and stoichiometry considerations that soot should appear at $C/O = 1$. Soot formation is thus generally a non-equilibrium process. It is expected that the chemistry responsible for soot formation would be evident by large changes at soot threshold in the concentration of the chemical species responsible for soot formation. The only species concentrations which changes dramatically are the ion concentrations and composition of both cations and anions. Neutral species concentrations, including large PCAH [Bockhorn et al, 1983, D'Alessio et al, 1994] and hydroxyl radicals [Inbody, 1992] do not show any such dramatic change,

2. Thermochemistry Data Base

The desire to add ionized molecules, see eg equation (1), required the addition of new ions involving partially saturated, fused ring compounds to the database. In the past we used statistical mechanics or group values of Benson and others to obtain thermochemical properties which were not available, but neither structural data nor group values were available for these new ions. For the unsaturated single ring compounds, cyclohexene and 1,3-cyclohexadiene and 1,4-hexadiene, data were available to calculate the thermochemical properties by statistical mechanics. Benson group values were also used to calculate these quantities for a straight chain hydrocarbon. The difference between the two calculated values was assumed to be the correction for a ring. When applying these ring corrections care was taken to recognize common atoms in fused rings.

3. Mass Spectrometer Sample Cone Complications

Stein [Stein, 1983] suggested that the observed ions are not the ions in the flame but ions which have been formed by ion-molecule, i.e. H atom addition reactions in the sampling cone, where the gases are cooled by expansion. This would not alter the original premise of ion growth through ion-molecule reactions, but would complicate the interpretation of mass spectral data by adding a whole new set of reactions to the mechanism, with the complication of relating the observed ion to the ion present in the flame. The proposed new ions are more stable at high temperatures. Thus, e.g., the observed $C_{14}H_{11}^+$ ion might be in equilibrium:



When this was first proposed, we examined the possibility in terms of the rate of temperature drop during the expansion process inside the sampling cone and concluded that the effect was small although possible. Because of the complications it would introduce in the model, we proceeded using only the observed ions in our model. The usual method of evaluating sampling cone effects is to evaluate the cooling effect downstream of the cone entrance. We have addressed aerodynamic cooling effects of the incoming sampled gas stream upstream of the sampling cone.

This treatment assumes a boundary layer at the cone entrance through which energy in the approaching gas stream heats the cone. We also assume choked flow in the cone entrance to calculate the rate of gas flow through the sampling cone or nozzle. The sampling is not isokinetic so that a region in front of the nozzle, in which the flow is accelerated and the gas temperature is reduced, is affected by the probe. This distance, for the specific nozzles and operating conditions of interest, extends between 0.05 and 1.0 mm upstream of the entrance orifice. This distance, corresponds to a time of between 2 and 4 X 10⁻⁵ s and a temperature drop from flame temperature, 2,000 K, to the sample cone temperature of about 1200 K.

This time is long compared with the characteristic reaction time, about 6X10⁻⁸ s (see below). Thus, there is time for the reactions to equilibrate at a new lower temperature. This is consistent with the observation that by simply lowering the assumed gas temperature [Calcote, 1994] the model can be brought into good agreement with experiment.

The above hypothesis was evaluated by assuming the sampling cone tip is located about 1.08 cm downstream of the burner and using the experimental temperature profile up to the position where the above treatment indicated the temperature should be affected by the cone. Beyond this point the temperature was assumed to be that calculate as above. This is presented in Fig. 1, in which the cone location is indicated and the distance scale, within the influence zone of the cone,

has been expanded to make the profiles clearer. The results are plotted for C₁₆H₁₀⁺ and C₁₆H₁₁⁺ as an example. The calculated ion concentrations, including the influence of the sampling cone, are now in reasonable agreement with experiment. Further, the model explains the double peaks in ion concentration profiles which have been such a mystery.

4. Energy Transfer Rates in Ion Molecule Reactions

In considering possible explanations of why reducing the measured flame temperature from 2000 K to 1700 K gave closer agreement with experiment, we investigated the possible effects of energy transfer on the ion-molecule rates and on equilibrium. The first question we asked was: how does the rate at which a flame ion, produced with excess energy in an exothermic ion-molecule reaction, lose energy compared to the rate at which it reacts in another ion-molecule reaction? The rate at which a large molecule, e.g. azulene, transfers excess vibrational energy to a variety of bath gas has been extensively studied [see e.g. Clarke et al, 1992] so these data can be used to evaluate the rate at which large ions loss energy to the bath gas.

We compared the relaxation times for the two processes. Thus $\tau_e = 1/k_e N_e$ where τ_e is the relaxation time for vibrational energy exchange with the bath gas, k_e is the rate coefficient to remove a quantum of vibrational energy $\langle E \rangle$ per collision and N_e is the concentration of the bath gas constituents removing energy. Substitution of the appropriate numbers yields $k_e = 4.6 \times 10^{-9}$ s/collision. A typical excess vibrational energy to be transferred from a product ion after an ion-molecule reaction is 400 kJ, so that about 90 collisions are involved. Thus, the total time, τ_e , to transfer all of the excess vibrational energy from a product ion is about 1.5×10^{-6} s. The relaxation time for an ion molecule reaction is $\tau_c = 1/kN$, where k is the ion-molecule reaction rate coefficient and N is the concentration of neutral reactants. Using $k = 9 \times 10^{-10}$ and N equal to the sum of C₂H₂ and C₄H₂ in the flame, we find $\tau_c = 6 \times 10^{-8}$ s.

Thus the relaxation time for excess energy loss exceeds the relaxation time for the next ion-molecule reaction to occur in the reaction series. This means that reactions are occurring with vibrationally excited ions and that some of this energy will accumulate in the growing ions. This situation is not expected to arise in neutral reactions because the energies involved are less and the reaction rates are less.

What this means for the ion-molecule mechanism of ion growth is not clear. It is not expected to increase the reaction rate coefficients when the reactions are exothermic, because reaction occurs at every collision. It would speed up endothermic reactions, but these are generally unimportant for ion-molecule reactions. It would be expected to increase the rate of dissociation of ions and recombination reactions of the type $A^+ + B \rightarrow AB^+$ would be less likely to occur. Whether dissociation back to the original reactants or to a larger ion and a smaller neutral, H or H₂ would dominate is not known. We are currently considering how to incorporate the accumulation of energy in the mechanism without overly complicating the mechanism.

ACKNOWLEDGEMENTS

The following people have participated in this program: Drs. R.J. Gill, D.G. Keil, C.H. Berman at AeroChem and Prof. F. Egolfopoulos, University of Southern California. We also acknowledge the many helpful discussions with Steve Stein and others.

REFERENCES

- Bockhorn, H., Fetting, F. and Wenz, H. W., Ber. Bunsenges, Phys. Chem. 87: 1067 (1983)
- Calcote, H. F. AFOSR Meeting, Lake Tahoe June 1994
- Clarke, D. L., Oref, I., Gilbert, R.G. and Lim, K. F., J. Chem. Phys. 96: 5983 (1992)
- D'Alessio, A., Gambi, G., Minutolo, P., and Russo, S. Twenty-Fifth Symposium on Combustion 1994, pg 645
- Inbody, M. A. 1992, PhD Thesis Purdue University, NASA Report 191099
- Stein, S. E., Comb. Flame 51: 357 (1983)

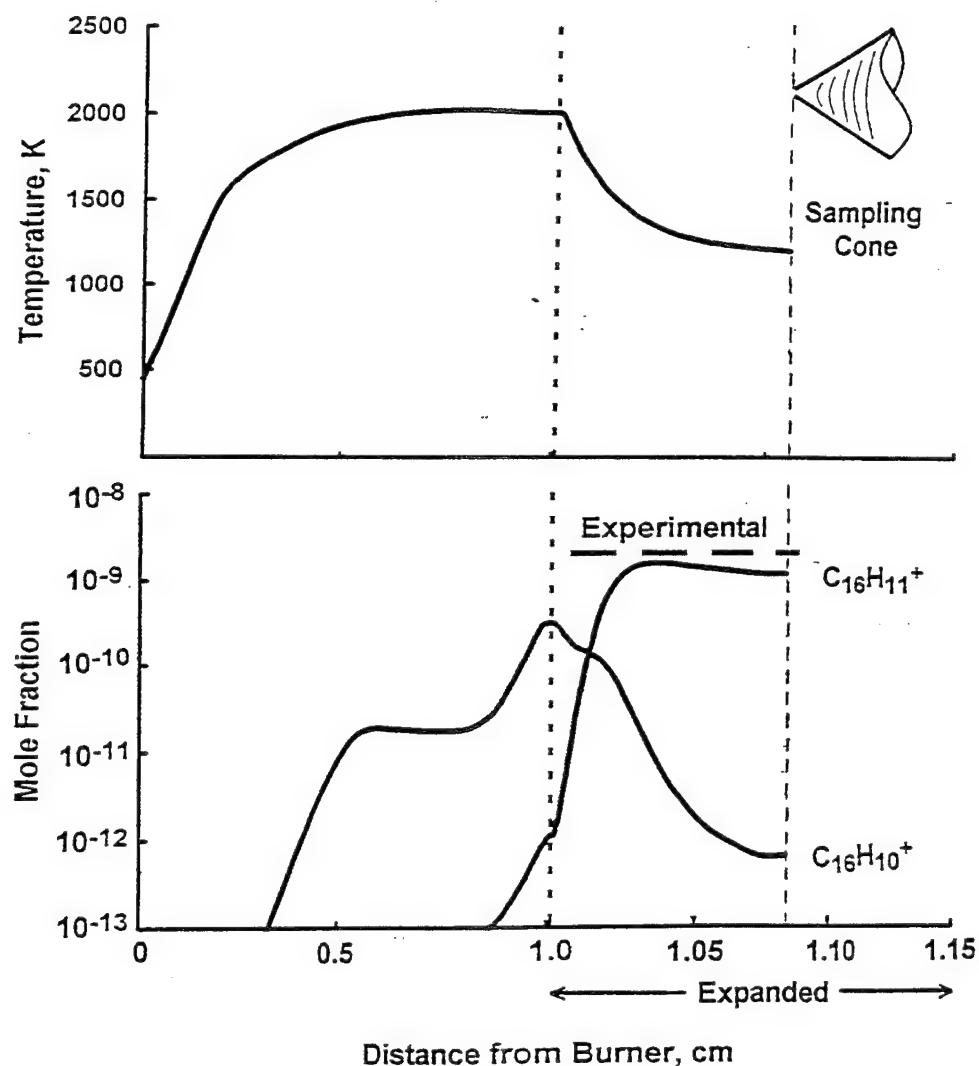


Figure 1. Effect of Mass Spectrometer Sampling Probe on Calculated Ion Profiles

STUDIES OF THE MORPHOLOGY AND DYNAMICS OF AGGLOMERATES IN CHEMICALLY REACTING FLOWS

AFOSR Grant No. F49620-92-J-0477

Principal Investigator: Tryfon T. Charalampopoulos

Combustion and Laser Diagnostics Laboratory
Mechanical Engineering Department
Louisiana State University
Baton Rouge, LA 70803

SUMMARY/OVERVIEW

Determination of the morphology of agglomerated particulates within a flame environment is useful for soot-formation studies, radiative heat transfer predictions from flames, and product quality control in material synthesis applications [1]. One of the research goals at the **Combustion and Laser Diagnostics Laboratory at Louisiana State University** is to develop, adapt, and refine laser-optics based *in situ* techniques for measuring the structural and dynamic properties of flame-generated particulates within their reacting environment. Towards this end, work is underway to adapt the technique of depolarized dynamic light scattering (DDLS) [2,3,4] to determine the dynamics of agglomerated structures within a reacting flame environment. Independent extractive sampling and subsequent transmission electron microscope (TEM) analysis of the flame-generated particulates would then provide valuable data on the relationship between the structure and non-continuum rotational dynamics of the particulates. Such information could be used to confirm any proposed theoretical models and to infer particulate structure information from experimentally determined rotational dynamics data. The dynamic light scattering studies are complemented with the development of a new in-situ approach for determining the agglomerate morphology and optical properties using the inverse scattering methodology. A summary of the exact scattering theory for agglomerates was given in last year's report and details are provided in Reference [5]. Thus the development of a robust data inversion algorithm was one of the objectives during this year's studies. A brief summary is presented in the next section.

TECHNICAL DISCUSSION

I. NON-INTRUSIVE DETERMINATION OF THE AGGLOMERATE PARAMETERS AND OPTICAL PROPERTIES OF FLAME PARTICULATES

Based on the exact theory of light scattering by agglomerated small spherical particles developed recently [5], a new computer code (AGGL) is introduced to perform light scattering computations, such as extinction, absorption, total scattering efficiency factors, and differential scattering intensities for agglomerates of arbitrary geometries. Derivatives with respect to the refractive index and size parameter are also internally generated according to the exact expressions. The program has been thoroughly tested and found to be error free. Significant efforts have resulted in more than 10 times of reduction in computational time. The accuracy, convenience, and efficiency thus warrant AGGL to be a very convenient platform for fulfilling data inversion tasks.

With AGGL available, an error response or inversion uncertainty analysis now becomes possible. Other important topics associated with data inversion, such as

pairing problem (to search for the most appropriate quantities to be measured) and sensitivity analysis (to find best detector locations), can be systematically investigated. Preliminary applications of AGGL have been made for refractive index inversion to demonstrate the new inversion methodology, characterized by the derivative formulation, pairing problem, sensitivity analysis and uncertainty evaluation. More details about the developed algorithm and its implications are presented in References [5-7].

In order to verify the developed theory for agglomerates and to assess its limitations in terms of an overall and primary particle size parameter a flame reactor system was developed that produces agglomerates of specific configurations, namely chain-like aggregates. Details about the flame reactor may be found in References [8-9]. It is to be noted that the same flame reactor is currently being used in this laboratory for studies of the rotational dynamics of agglomerated structures both in the continuum and non-continuum regimes. A brief summary of the flame reactor and of the aspect ratio distribution results are presented in the next section.

II. CONTROLLED SYNTHESIS OF AGGLOMERATED STRUCTURES

The system consists of a diffusion type carbon monoxide-air flame reactor centered around a concentric stainless steel tube. Metered carbon monoxide is supplied through the inner tube (1/4" in diameter). The iron pentacarbonyl vapor is introduced into the CO-air flame by diverting a small fraction of CO through a column of liquid $\text{Fe}(\text{CO})_5$ stored in a heated metallic stainless steel cylinder. By monitoring the temperature of the cylinder, partially saturated $\text{Fe}(\text{CO})_5$ vapor is transported by the carrier gas and injected into the inner tube of the flame. The additive-feeding system was designed in such a way that the concentration of iron pentacarbonyl vapor introduced into the flame can be controlled by adjusting either the temperature of the evaporate cylinder and/or the carrier gas flowrate. The system is calibrated so that the amount of iron pentacarbonyl vapor delivered to the fuel for different carrier flow rates is known prior to entering into the flame with an accuracy of $\pm 3.6\%$.

The particulates were extracted by a thermophoretic sampling system, which minimizes the potential for further agglomeration [10], and were deposited on a 200-mesh copper grid coated with carbon film which is stable under electron beam bombardment and can withstand relatively higher temperature.

The CO-air diffusion flame seeded with $\text{Fe}(\text{CO})_5$ vapor was tested and dominantly chain-like aggregates were produced. The size and shape of chain-like aggregates and primary particles were characterized in terms of measurable morphological parameters. The average diameter of primary particles and average aspect ratio of chain-like aggregates can be controlled by varying the concentration of iron pentacarbonyl vapor seeded into the flame. For the concentration range investigated, namely from 0.75% to 2.8% iron pentacarbonyl vapor to fuel by weight, the average diameter of primary particles and aspect ratio increased by about 30% at 25mm height above the burner surface. The average diameter of primary particles increased by 8.0% and the average aspect ratio by 28.0%, as the temperature of the heated cylinder increased from 23°C to 55°C. The total increase of average diameter was about 179% from 4 to 35 mm and the aspect ratio 62% from 15 to 35mm. Higher concentrations and residence times favor the formation of longer chain-like aggregates.

The above observations were repeated with identical results with maximum derivation of 5% from the mean values, by performing the same measurements. The data, statistically analyzed for an average of 1000 particles and 500 aggregates, are expected to provide representative picture of the particulate morphology of iron

oxide particles in this type of flame reactor. The average diameters of primary particles, average aspect ratio of chain-like aggregates, and the standard deviations were calculated for all sampling conditions. The results are summarized in Table 1. The average diameter and aspect ratio increase with height and concentration. Note that the largest increase of mean values were encountered at lower locations (short residence times) and lower concentrations. Frequency distributions for the particle diameter and aspect distributions as functions of flow rate and position in the flame are shown in Figures 1 and 2. In order to carry out the analysis of the rotational dynamics data for this type of flame system where thermophoretic velocities are also present the heterodyne correlation function which includes both velocity and Brownian diffusion coefficients as function of the scattering angle has been analyzed. Details about the results are presented in Reference [11] and a summary is presented below.

III. VELOCITIES AND BROWNIAN DIFFUSION COEFFICIENTS USING DYNAMIC LIGHT SCATTERING [11]

This part of the work may be summarized as follows:

- a) As the particle size and bulk velocity increases, the maximum acceptable scattering angle for accurate determination of the bulk velocity and Brownian diffusion coefficient increases. This occurs because increasing the size or bulk velocity increases the decay time of the correlation function with respect to its period, thus permitting more measurable oscillations of the cosine factor before the correlation function completely decays.
- b) Based on statistical considerations [11], if the uncertainty of the normalized correlation data is kept acceptably low heterodyne detection may be used to accurately infer bulk velocities greater than approximately 1 cm/s of monodisperse spherical particles with sizes larger than approximately 40 nm in the CO/air diffusion flame under consideration.
- c) Under certain special cases and limiting assumptions, these results can be extended to non-spherical particles [11]. Work is currently underway to implement this type of measurement and to determine the diffusion coefficients of the aggregates.

REFERENCES

1. Charalampopoulos, T.T. (1992) *Prog. Energy Combust. Sci.* 18:13-45.
2. Berne, B.J. and Pecora, R. (1976) *Dynamic Light Scattering*, Wiley, New York.
3. Benedek, G.B. (1969) *Polarization, Matter, and Radiation*. Presses Universitaires de France, Paris. pp. 49-84.
4. Russo, P.S., Saunders, M.J. and DeLong, M. (1986) *Analytica Chimica Acta*. 189: 69-87.
5. Lou, W. and Charalampopoulos, T.T. (1994) *J. Phys. D: Appl. Phys.* 27, 2258-2270.
6. Lou, W. and Charalampopoulos, T.T., *J. Phys. D: Appl. Phys.* Paper No. D/62946/PAP (In Review).
7. Lou and Charalampopoulos, T.T., *Proceedings of the Joint Meeting of the Combust. Institute*, San Antonio, TX, April 1995, pp. 110-115.
8. Zhang, Z. and Charalampopoulos, T.T., *Proceedings of the Joint Meeting of the Combustion Institute*, San Antonio, TX, April 1995, pp. 675-680.
9. Zhang, Z., Waguespack, G. and Charalampopoulos, T.T., "Development of a Reactor for Controlled Flame Synthesis of Materials" (Submitted for publication).
10. Dobbins, R.A. and Megaridis, C.M., *Langmuir* (1987) 3, 254-266.
11. Waguespack, G. and Charalampopoulos, T.T., "An Investigation into the Use of Dynamic Light Scattering to Infer Velocities and Brownian Diffusion Coefficients of Agglomerates in a Reacting Environment", *Proceeding of the Joint Meeting of the Combustion Institute*, San Antonio, TX, April 1995, pp 104-109.

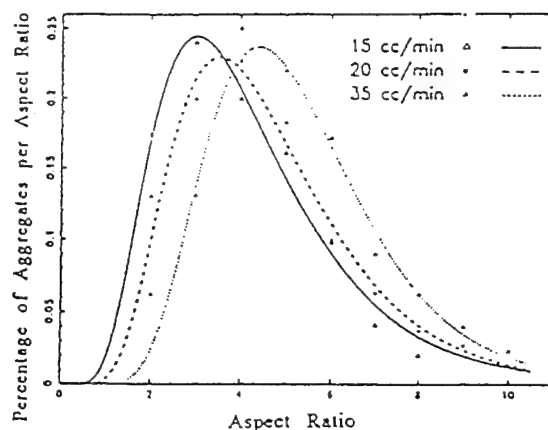
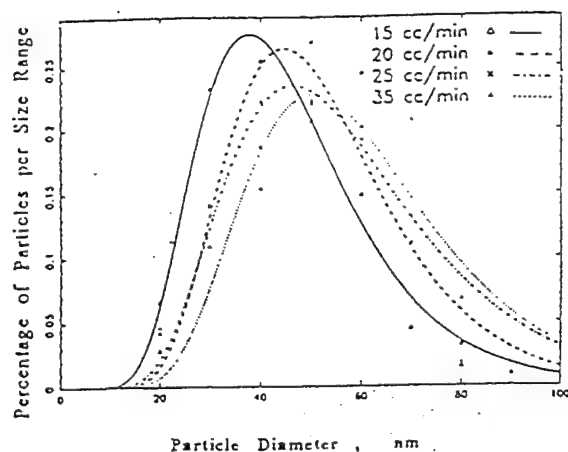


Figure 1: Frequency distributions of diameter and aspect ratio along with ZOLD fitting curves with variable carrier gas flowrate

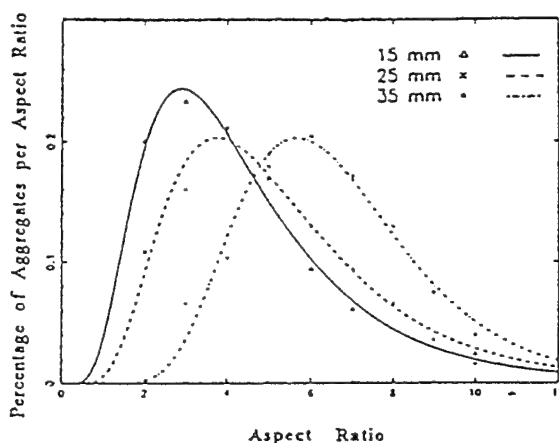
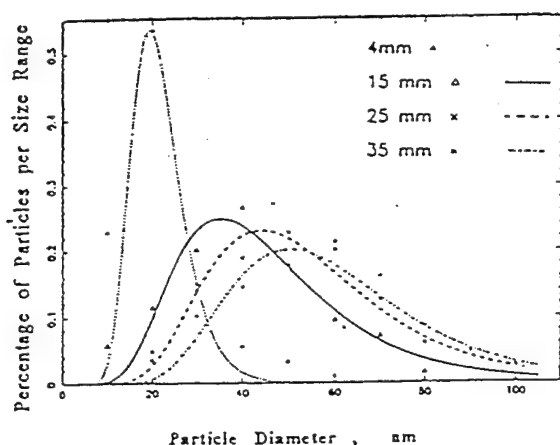


Figure 2: Frequency distributions of diameter and aspect ratio along with ZOLD fitting curves with variable height above the burner surface

Table 1: Calculated average diameter, aspect ratio, and standard deviation using ZOLD function

Variable Temperature					Variable Carrier Flowrate					Variable Height				
T (°C)	d (nm)	σ (nm)	$\overline{l/d}$	σ	Q ($\frac{cc}{min}$)	d (nm)	σ (nm)	$\overline{l/d}$	σ	H (mm)	d (nm)	σ (nm)	$\overline{l/d}$	σ
23	57.4	27.2	7.08	4.0	15	45.89	17.6	4.93	2.6	4	21.70	5.9	—	—
35	60.97	26.8	8.16	6.0	20	51.03	16.7	5.52	2.6	15	45.61	20.1	4.17	2.5
45	61.31	25.5	8.63	6.1	25	55.13	20.5	—	—	25	54.76	21.6	5.93	3.2
55	62.16	23.8	9.09	6.2	35	59.56	20.9	6.38	2.4	35	60.52	21.9	6.75	2.4

T = cylinder temperature, d = primary particle diameter, σ = standard deviation, $\overline{l/d}$ mean aspect ratio, H = Height above the burner surface, Q = carrier gas flow rate.

MECHANISMS CONTROLLING SOOT FORMATION IN DIFFUSION FLAMES

AFOSR Contract F49620-94-C-0059

Principal Investigators: Meredith B. Colket and Robert J. Hall

United Technologies Research Center
Silver Lane, E. Hartford, CT 06108

SUMMARY/OVERVIEW:

The overall objectives from this work are to (1) refine and update a pyrolytic model which describes PAH formation; (2) modify and validate an opposed jet diffusion flame code which includes soot formation and radiation and then extend model predictions over a range of flame parameters, and (3) with assistance from Prof. M. Smooke, incorporate the soot formation and radiation models into a code for a coflow laminar, diffusion flame. Experiments and modeling on alkylated aromatics will help to minimize discrepancies between known PAH formation rates and those required to explain particle inception rates in flames. Validation (and modification as necessary) of the existing opposed jet flame code with data from ethene flames will increase its reliability in predicting sooting conditions with other hydrocarbon fuels and inlet conditions. In addition, this effort should demonstrate the codes utility prior to installing soot formation and radiation routines into codes describing other flame geometries for which extensive data bases exist.

PAH Formation

Whether included in detailed chemical kinetics calculations or in a quasi-steady state expression, phenylacetylene (or styrene) is a key intermediate in many routines which attempt to model particle inception rates in flames. In addition, high temperature pyrolytic data for many hydrocarbons show phenylacetylene, in particular, and styrene, as well, to be important products. Unfortunately, there is extremely little data or established chemical kinetic models on the pyrolysis of these compounds for comparison to models used in soot formation flame codes. We have performed preliminary experiments on styrene pyrolysis and have planned experiments on the decomposition of phenylacetylene. In addition, we are reviewing literature data on the decomposition of these compounds. The new data on styrene and the recent data on phenylacetylene (Ref. 1-2) indicate similarities to the pyrolysis of toluene (Ref. 3). In particular, major products include naphthalene, biphenyl, acenaphthylene, fluorene, and phenanthrene. In the case of toluene, a host of methylated products was also observed, but for these other fuels, addition products with vinyl and ethynyl were found instead. Nevertheless, these alkylated PAHs had noticeably smaller concentrations than the PAHs. This latter result

suggests that alkylated PAHs are easily dealkylated, undergo further growth via addition processes, or rapidly isomerize to larger PAHs.

Phenylacetylene has been pyrolyzed (Ref. 1) in flow through a tube at low pressure and 1300K while radicals as well as stable products were trapped and analyzed. We have attempted to model this data starting with a mechanism modified from that presented in Ref. 3, but find that rate constants for radical initiation and addition must be much higher than accepted values. Furthermore, extremely high rates of benzene and biphenyl were observed. While the relative proportion of (PAH) products is consistent with our model, the very high concentrations of phenyl radicals, benzene, and biphenyl cannot be explained. In fact, the experimental rate of biphenyl formation is about two orders of magnitude greater than rates calculated from the known (phenyl + phenyl) and (phenyl + benzene) reactions, using the reported concentrations. This substantial uncertainty is an important issue since biphenyl can be an important intermediate leading to yet larger PAH production when burning fuels (such as practical fuels) containing substantial amounts of aromatics. Perhaps surface reactions are in part responsible for the recent experimental results, but an alternative reaction sequence, not yet identified may be partially responsible.

Opposed Jet Soot Code Comparisons

Calculations have been performed to compare predictions from our sectional soot code with the ethene-fueled, Tsuji burner measurements (Ref. 4). The calculations employed the ethene mechanism used in previous flame calculations (Ref. 5) and assumed radiative loss in the optically thin approximation (Ref. 6). These calculations are generally sensitive to the inception rate assumed, but are not sensitive to the size of the incepting species.

The fuel velocity at the burner was fixed to a value based on the fuel ejection parameter, and then the strain rate was varied until a reasonable fit to the measured temperature distributions was achieved. Examples of temperature profiles are shown in Fig. 1. A slightly higher strain rate might provide a better fit, but the boundary conditions become less certain.

Figure 2 shows the calculated soot profiles for the basic models used by Hall, Smooke, and Colket (1995;HSC), by Fairweather, Jones, and Lindstedt (1992;FJL), and by Sunderland, Koylu, and Faeth (1994;SKF). These calculations and the data are for an oxygen mole fraction of 0.22. As seen, the first two models fall short by factors of 3 to 4. While integrated soot volume fractions predicted using the SKF model are nearly comparable to those from the HSC or FJL models, the SKF model poorly predicts the general shape of the soot profile. Scaling up the surface growth in the HSC model by a factor of three (the surface growth here is Harris-Weiner with 31.6 kcal activation energy as described by HSC) results in the nice fit shown. The scaling of this magnitude is within the kind of uncertainty that presently exists. The FJL model is basically a methane model; unfortunately, the Lindstedt ethylene model is based on a functional form for the surface growth that is incompatible with sectional analysis, so a direct comparison can't be made. Radiative loss is important in these calculations, but not as important as it has

been in some of our previous results; generally speaking, it represents about a 25% effect for the Vandsburger, et al flame (Ref. 4).

Using the scaled HSC model, the agreement with the observed variation with oxygen index is amazingly good (Fig. 3). Figure 4 shows the prediction based on the Frenklach surface growth rate (as used in Ref. 5). Because our procedure does not include the 'Frenklach' inception model nor the soot oxidation model employed by Frenklach and coworkers, the direct comparison may not be fair; but it seems unlikely that his inception would be much larger than the HSC inception used here. The spatial profile of soot predicted by the Frenklach model is comparable to that from the original HSC or FJL models, but similarly an enhancement factor is needed to match the experimental profiles.

The temperature dependence of surface growth has recently been questioned; in some cases near-zero activation energies have been suggested. As is also seen in Fig. 4, satisfactory agreement can also be obtained by keeping the functional form of the Harris-Weiner surface growth rate, but decreasing the activation energy from 31.6 kcal/mole (constant A-factor). For zero activation energy, however, the agreement is not satisfactory. The failure of the SKF model must arise both from the way it treats inception and the fact that it has no temperature dependence of surface growth.

Extension of model

We are currently working on extending the arc length continuation procedure for an opposed jet flame to include the soot formation and radiation models. This version of the code will facilitate obtaining predictions of soot formation and related phenomena (e.g. sooting limits) from opposed jet flames as a function of strain rates.

References

1. K. Guthier, P. Hebgen, K.H. Homann, J. Hofmann, and G. Zimmermann, "Addition and Cyclization Reactions in the Thermal Conversion of Hydrocarbons with Ethyne Structure, II. Analysis of Radicals and Carbenes from Ethynylbenzene, in press, 1995.
2. J. Herzler and P. Frank, *Ber. Bunsenges. Phys. Chem.* Vol. 96, p. 1333 (1993).
3. M. Colket and D. Seery, Twenty-Fifth Symposium (International) on Combustion, The Combustion Institute, Pittsburgh, p. 883 (1995).
4. U. Vandsburger, I. Kennedy, and I. Glassman, *Comb. Sci. & Tech.*, Vol. 39, p. 263 (1984).
5. M. Colket and R. Hall, Proceedings of the International Workshop on Mechanisms and Models of Soot Formation (H. Bockhorn, Ed.), Springer-Verlag, Heidelberg (1994).
6. R. Hall, M. Smooke, and M. Colket, "Predictions of Soot Dynamics in Opposed Jet Diffusion Flames", *Combustion Science and Technology Book Series* (1995).
7. M. Fairweather, W. Jones, and R. Lindstedt, *Comb. & Flame*, Vol. 89, p. 45 (1992).
8. P. Sunderland, U. Koylu, and G. Faeth, *Comb. & Flame*, Vol. 100, p. 310 (1995).

Figure 1

Temperature Distribution in Counterflow Flame
Ethylene-Air; Data of Vandsburger, et. al. (1984)

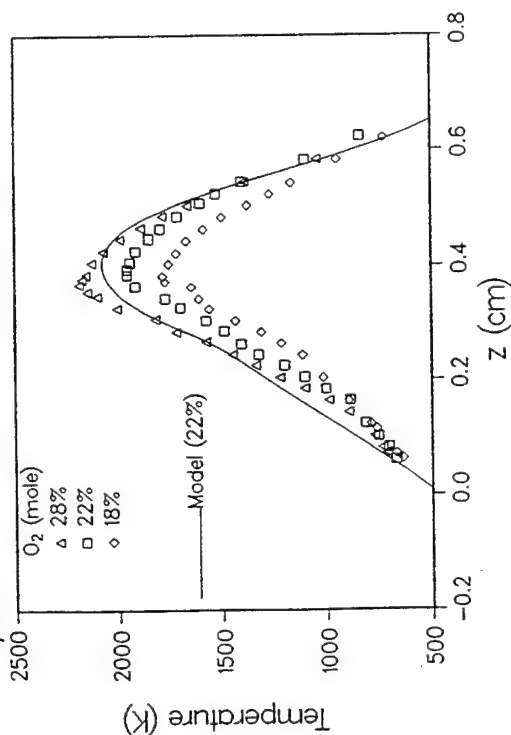


Figure 2

Soot Growth in Counterflow Flame
Ethylene-air; Data of Vandsburger, et. al. (1984)

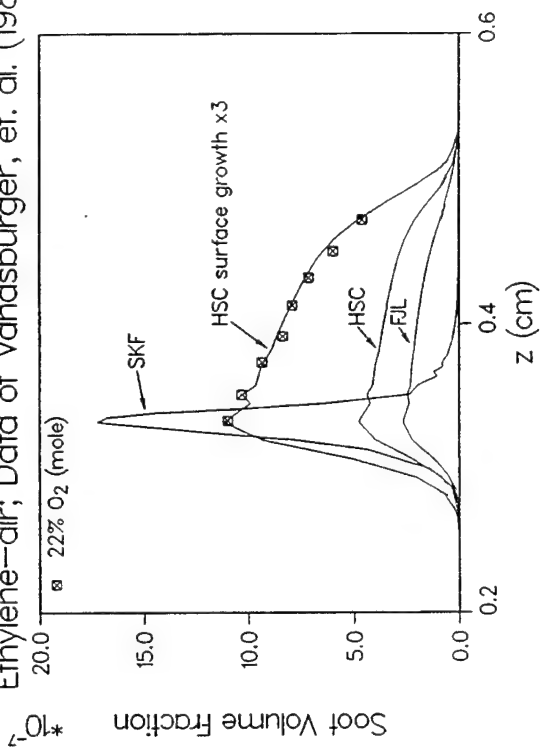


Figure 3

Soot Growth in Counterflow Flame
Ethylene-air; Data of Vandsburger, et. al. (1984)

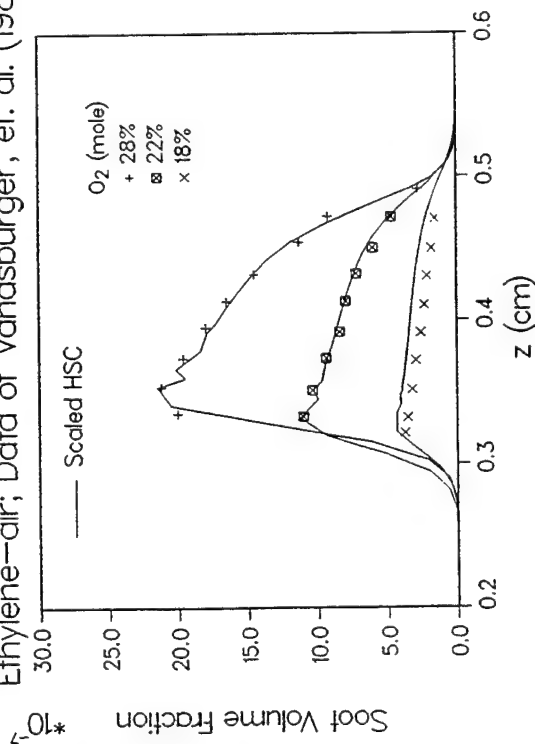
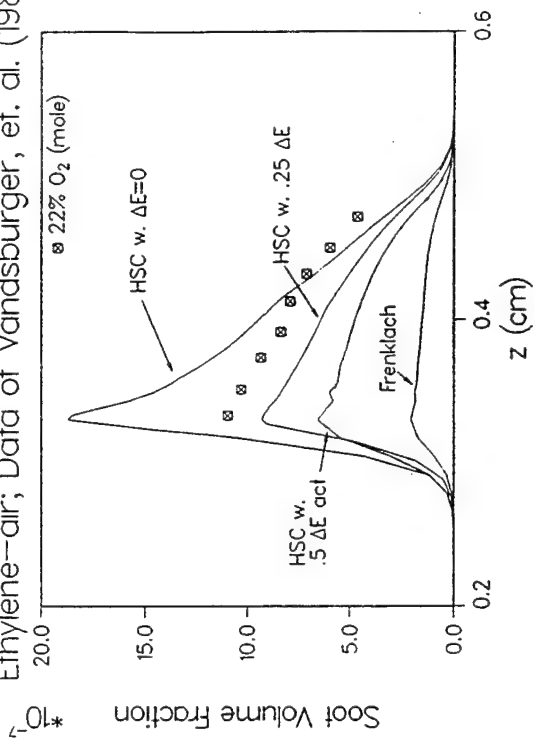


Figure 4

Soot Growth in Counterflow Flame
Ethylene-air; Data of Vandsburger, et. al. (1984)



COMPUTER SIMULATION OF MOLECULAR INTERACTIONS IN SUPERCRITICAL SOLVENTS; PARTICLE FORMATION FROM SUPERCRITICAL FLUIDS

(AFOSR Grants No. F49620-93-1-0040; AASERT F49620-93-1-0454)

Principal Investigator: Pablo G. Debenedetti

Department of Chemical Engineering
Princeton University
Princeton, NJ 08544-5263

SUMMARY/OVERVIEW

This research project consists of computational studies of solvation in supercritical fluids, and of experiments on particle formation in supercritical solvents. In the computational work we use molecular dynamics simulations to study the structure and dynamics of dilute supercritical mixtures, including the equilibrium spatial distribution of the solvent around the solute, differences between local and bulk conditions, and the rotational and translational diffusion of solute species. The goal is to understand how equilibrium and time-dependent properties depend on temperature and density in the supercritical region. In the experimental work, we form particles either by rapid expansion of a supercritical solution, or by isothermal and isobaric evaporation of a solvent into a supercritical fluid. Our goal is to understand the relationship between particle morphology and process conditions.

TECHNICAL DISCUSSION

The computational work was motivated by several reports in the literature in which appreciable differences in solvent concentration between the immediate vicinity of the solute and the bulk fluid were detected spectroscopically [1-3] or computationally [4,5]. The goal of our simulations is to investigate the mechanisms of solvation in supercritical solvents, and in particular to understand in what ways the translational and rotational motion of solutes is affected by high local solvent densities. In our most recent work [6] we have studied the system benzene (solute) - carbon dioxide (supercritical solvent). Both molecules are modelled as rigid polyatomics interacting via multi-site Lennard-Jones potentials. In addition, interactions between carbon dioxide molecules include a point quadrupole. The site parameters, as well as the technical details of the simulations are listed in Tables I and II.

Table I. Site Potential Parameters for Benzene-Carbon Dioxide Simulations^(a)

		ϵ/k (K)	σ (Å)
CO ₂	C-C	29	2.785
	O-O	83.1	3.014
Benzene	CH-CH	95.05	3.35

(a) Lorentz-Berthelot rules used for unlike pairs. CO distance = 1.16Å; CH-CH distance = 1.765 Å.

Table II. Technical Details of the Molecular Dynamics Simulations

Ensemble	Constant density and temperature
Number of molecules	256
Number of solute molecules	1
Integration time step ^(a)	0.0007
Truncation of interactions	8.355 Å
Number of steps	100,000
Equilibration steps	10,000

(a) Time is measured in units of $\sigma_{cc} (m_{CO_2}/\epsilon_{cc})^{1/2}$; one integration time step = 2.6×10^{-15} sec.

State conditions investigated so far are $T/T_c = 1.05$ and 1.1 , and $\rho/\rho_c = 0.5, 0.75, 1, 1.5, 2$ (i.e., two supercritical temperatures and a range of densities from sub-critical to liquid-like). To study the spatial distribution of carbon dioxide around benzene, we divided the space surrounding a benzene molecule into four sectors and computed center-of-mass solute-solvent distribution functions within each sector. The results, shown in **Figure 1**, indicate that benzene is preferentially solvated in the polar position, where the solvent density can be as high as seven times its bulk value. Note, however, that the difference between local and bulk conditions is more pronounced at the lowest density investigated. No unusual effects are seen at the critical density. Temperature had little effect on the microstructure of the solvent around the solute.

Figure 2 shows the translational diffusion coefficient of benzene in supercritical carbon dioxide. The diffusivity scales inversely with bulk density, and is unaffected by proximity to the solvent's critical point. We found excellent agreement between the simulated diffusivity and experimental measurements for the same system. **Figure 3** shows the in-plane and perpendicular rotational diffusion coefficient of benzene in supercritical carbon dioxide, at all the temperatures and densities investigated. Rotational motion is remarkably insensitive to bulk density. Furthermore, no anomalies are seen near the solvent's critical point. We conclude that the transport properties of solutes are unaffected by solvation effects, such as local density augmentation. In addition, the transport coefficients vary smoothly with density in the vicinity of the solvent's critical point.

Molecular dynamics allows the detailed study of solvation dynamics. Such an investigation is motivated by the knowledge that in dilute mixtures of non-volatile solutes in supercritical solvents, the density of the solvent around the solute can be substantially greater than in the bulk. Hence it is natural to inquire as to the extent of short-ranged order and temporal persistence of this denser solvation region. **Figure 4** shows the fraction of solvent molecules initially in a sphere of radius 6.7 Å centered at the center of mass of the benzene molecule which remain in the sphere after a time t . The decay can be fitted with an exponential,

$$N(t) = N(0) \exp(-t/\tau)$$

The relaxation time, τ , increases monotonically with increasing density, and decreases very slightly with increasing temperature. Typical values are 3 psec at 50% of the critical density and 7 psec at twice the critical density. We find no increase in the relaxation time at low densities (where local density augmentation is more pronounced), nor near the solvent's critical point. We conclude that increases in local density do not give rise to liquid-like short-range order.

The important conclusion from these simulations is that local density augmentation does not affect the transport properties of solutes in a supercritical solvent. The persistence time of the local

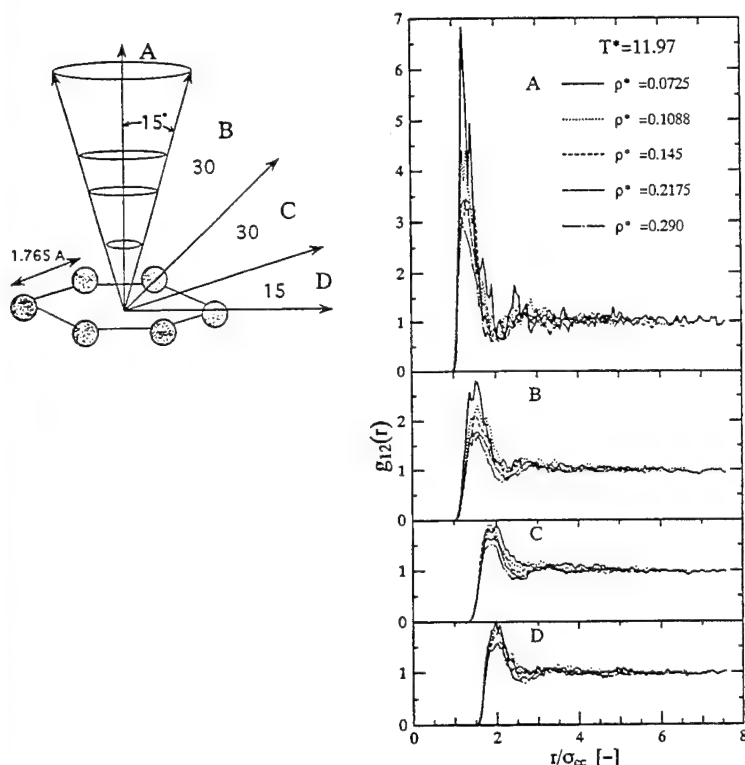


Figure 1: Sector-dependent radial distribution of supercritical carbon dioxide around benzene. g is the ratio of local to bulk density. Also shown is the geometry for the definition of sectors. $T^* = kT/\epsilon_{cc}$; $\rho^* = \rho/\sigma_{cc}^3$. $T(K) = 29 T^*$; $\rho(\text{mol/liter}) = 76.87 \rho^*$; $\sigma_{cc} = 2.785 \text{ \AA}$. For the potential parameters used in this study, $T_c = 330.6 \text{ K}$ ($T^* = 11.4$); $\rho_c = 11.15 \text{ mol/liter}$ ($\rho^* = 0.145$). Molecular dynamics simulation [6].

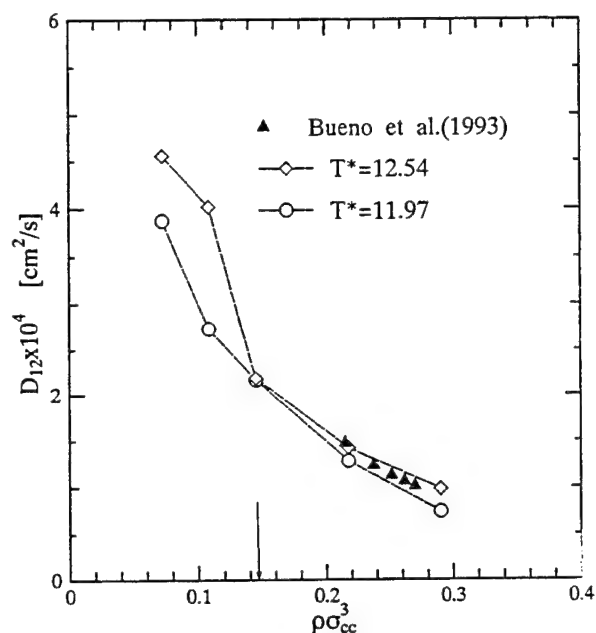


Figure 2: Translational diffusion coefficient of benzene in carbon dioxide at two supercritical temperatures. Vertical arrow indicates the solvent's critical density. Experimental data are from Bueno, Suarez, Dizy, and Molina, *J. Chem. Eng. Data*, 38, 344, 1993. $T^* = kT/\epsilon_{cc}$; $\rho^* = \rho/\sigma_{cc}^3$. $T(K) = 29 T^*$; $\rho(\text{mol/liter}) = 76.87 \rho^*$; $\sigma_{cc} = 2.785 \text{ \AA}$. For the potential parameters used in this study, $T_c = 330.6 \text{ K}$ ($T^* = 11.4$); $\rho_c = 11.15 \text{ mol/liter}$ ($\rho^* = 0.145$). Molecular dynamics simulation [6].

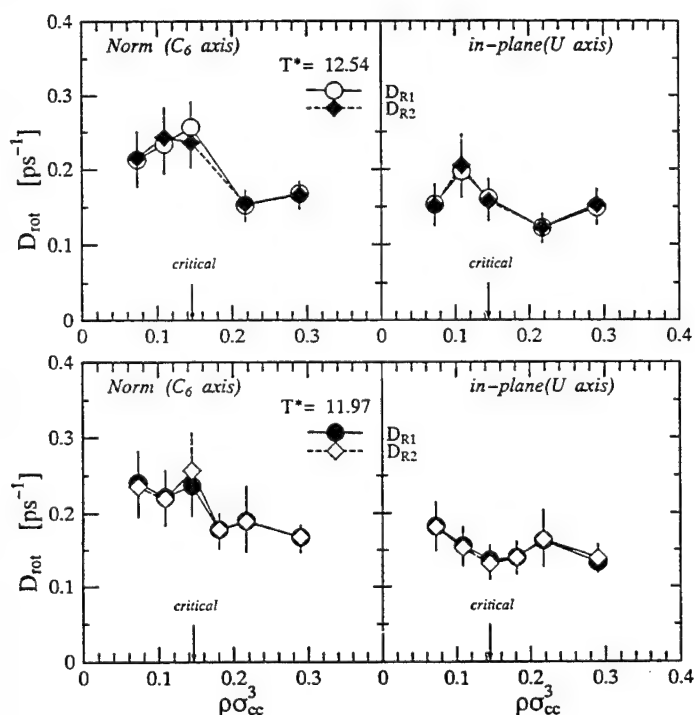


Figure 3: Rotational diffusion coefficient of benzene in carbon dioxide at two supercritical temperatures. DR_1 and DR_2 are coefficients calculated with the first two Legendre polynomials; agreement is a test of internal consistency. Both normal and in-plane rotation is shown. $T^* = kT/\epsilon_{cc}$; $\rho^* = \rho/\sigma_{cc}^3$. $T(K) = 29 T^*$; $\rho(\text{mol/liter}) = 76.87 \rho^*$; $\sigma_{cc} = 2.785 \text{ \AA}$. For the potential parameters used in this study, $T_c = 330.6 \text{ K}$ ($T^* = 11.4$); $\rho_c = 11.15 \text{ mol/liter}$ ($\rho^* = 0.145$). Molecular dynamics simulation [6].

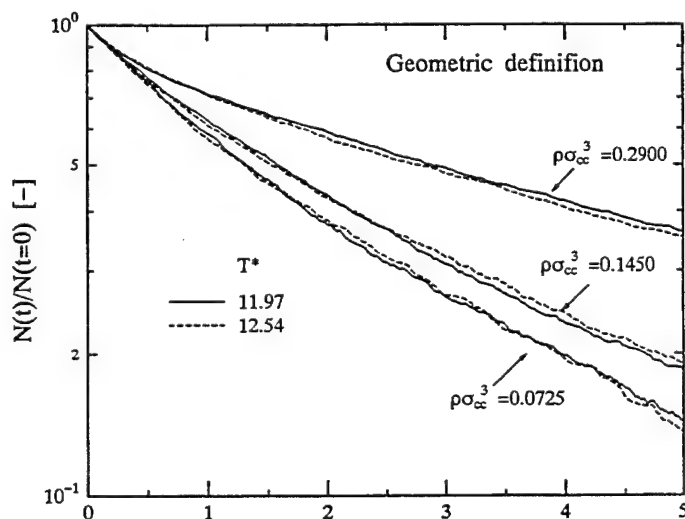


Figure 4: Decay of the fraction of tagged carbon dioxide molecules within a sphere of radius 6.7 \AA centered at benzene's center of mass that remain in the sphere at time t . $T^* = kT/\epsilon_{cc}$; $\rho^* = \rho/\sigma_{cc}^3$. $T(K) = 29 T^*$; $\rho(\text{mol/liter}) = 76.87 \rho^*$; $\sigma_{cc} = 2.785 \text{ \AA}$. For the potential parameters used in this study, $T_c = 330.6 \text{ K}$ ($T^* = 11.4$); $\rho_c = 11.15 \text{ mol/liter}$ ($\rho^* = 0.145$). Molecular dynamics simulation [6].

environment surrounding the solute is of the order of 5 psec., and suggests a highly unstructured environment in spite of the density augmentation. In addition, we see no effect of critical anomalies on the time-dependent properties of solutes dissolved in a supercritical fluid.

Particles can be formed from supercritical fluids by two routes: rapid expansion of supercritical solutions (RESS), and the supercritical anti-solvent (SAS) process. In RESS, precipitation is triggered by decompression. Because supercritical fluids are highly compressible, small changes in pressure cause large changes in density and solvent power. If a supercritical fluid contains dissolved pyrolysis or auto-oxidation products, unwanted solid formation by RESS can occur during partial expansion in a nozzle. In SAS, a solvent evaporates into a supercritical fluid, leaving behind dry powders of any previously dissolved solute.

In addition to the importance of RESS as a potential nuisance for supercritical fuels, both methods can in fact be used to make a wide variety of fine particles with interesting properties and morphologies. Recent examples in our laboratory include the formation of molecularly-oriented aromatic polyamide fibers and biologically active protein powders by SAS [7,8]. A very interesting development is the amorphization of crystalline materials by RESS [9]. Figure 5 shows x-ray diffraction patterns of caffeine obtained by RESS of carbon dioxide.

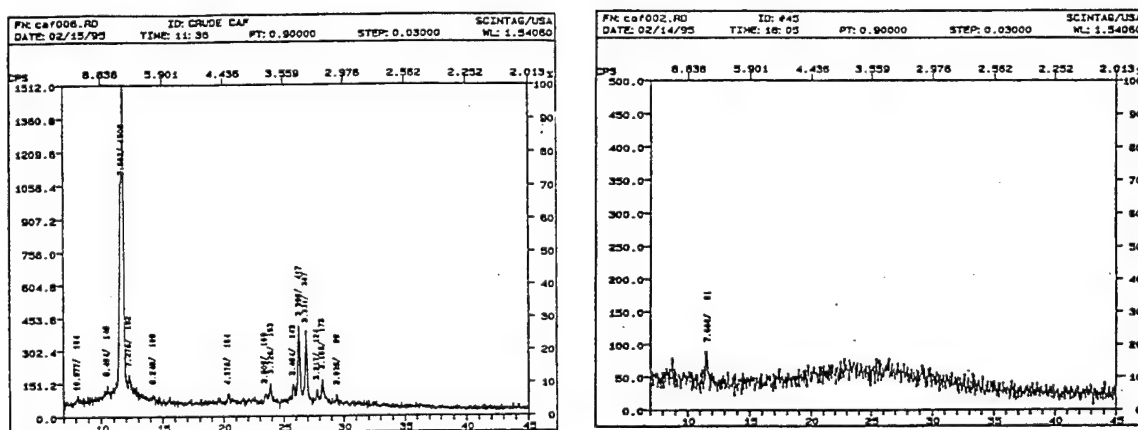


Figure 5: x-ray diffraction patterns of crystalline (left) and amorphous (right) caffeine. The amorphous material was obtained by rapid expansion in a 50 μm x 1.5 cm capillary [9].

- [1] Betts, T.A., J. Zagrobelny, and F.V. Bright. *J. Am. Chem. Soc.*, **114**, 8163, 1992.
- [2] Brennecke, J.F., D.L. Tomasko, J. Peshkin, and C.A. Eckert. *Ind. Eng. Chem. Res.*, **29**, 1682, 1990.
- [3] Carlier, C., and T.R. Randolph. *AIChEJ.*, **39**, 876, 1993.
- [4] Petsche, I.B., and P.G. Debenedetti. *J. Chem. Phys.*, **91**, 7075, 1989.
- [5] Knutson, B.L., D.L. Tomasko, C.A. Eckert, P.G. Debenedetti, and A.A. Chialvo. *ACS Symp. Ser.* **488**, Ch. 5, 1992.
- [6] Inomata, H., S. Saito, and P.G. Debenedetti. Submitted to *Fluid Phase Equilibria*, 1995.
- [7] Yeo, S.-D., P.G. Debenedetti, M. Radosz, and H.-W. Schmidt. *Macromolecules*, **26**, 6207, 1993.
- [8] Yeo, S.-D., P.G. Debenedetti, S. Patro, and T. Przybycien. *J. Pharm. Sci.*, **83**, 1651, 1994.
- [9] Subra, P., and P.G. Debenedetti, in preparation, 1995.

ADVANCED SUPERCRITICAL FUELS

AFOSR Task # 93WL002

Principal Investigators: Tim Edwards, Jim Gord, Mel Roquemore

USAF Wright Laboratory
WL/POSF Bldg 490
1790 Loop Rd N
Wright Patterson AFB, OH 45433-7103

SUMMARY/OVERVIEW:

Increases in aircraft and engine performance are increasing the heat load being transferred into an aircraft's primary coolant--the fuel. This research is aimed at understanding the limitations of operation of fuel heated to 480 °C (900 °F). Important areas are expected to be thermal stability, heat transfer/flow instabilities, and injection properties. This discussion focuses on thermal stability.

TECHNICAL DISCUSSION

"Thermal stability" refers to the ability of a fuel to absorb heat without the formation of undesirable solid deposits or other reaction products. Current jet fuels are relatively thermally stable up to temperatures of ~170 °C (325 °F). This research is aimed at determining the barriers to the use of a hydrocarbon fuel at 480 °C (900 °F). Two distinct types of fuel reactions are involved in thermal stability at these temperatures: thermal-oxidative and pyrolytic reactions. Thermal-oxidative stability has been the subject of a great deal of study for many years, but much remains to be understood about the underlying chemistry and physics of deposition [1].

New diagnostics have been developed by WL to help understand deposition mechanisms. The use of a quartz crystal microbalance (QCM) as a very sensitive, real-time, in-situ measurement of deposition in jet fuels has been pioneered by Steve Zabarnick and coworkers of the University of Dayton Research Institute at WL [2,3]. Concurrent pressure measurements allow the relationship between dissolved oxygen consumption deposition to be determined for various fuels [2]. The effects of different surface materials and fuel interactions have also been studied [3]. Static deposition tests with the QCM have shown good agreement with flowing deposition tests [21]. Several diagnostics probes have been combined in a unique flow reactor system by Viroj Vilimpoc of Systems Research Laboratories at WL [4,5,6]. Combining a flowing QCM with particle sizing by photon correlation spectroscopy (PCS) and oxygen concentration by concentration-dependent fluorescence quenching, a new level of understanding of deposition is being achieved. As shown in Figure 1, the data indicates that particle formation and deposition are intimately tied to the consumption of dissolved oxygen. Particle size, particle concentration, and surface deposition increase as dissolved oxygen is consumed. When the dissolved oxygen is (essentially) completely consumed, deposition decreases dramatically, particle concentration decreases in a similar manner as particles are transported to the wall, and

particle growth ceases. This is consistent with earlier results by Grant Jones of Systems Research Laboratories using filters to measure particulate [7]. This work, and earlier work by Terry Parker and coworkers at PSI, Inc. under WL sponsorship [8], represent the first time that oxidatively generated particles have been measured on-line in a flowing system. Significantly, the particle size is typically on the order of 100-200 nm, matching the size of the surface features seen in aircraft fuel system deposits by Schirmer [1,9], indicating that the deposits are apparently due to deposition of bulk particulate, rather than deposition of smaller precursor molecules. Further, it was found that effective deposition-suppressing additives reduce the measured particle size significantly, giving another indication of the importance of bulk particulate to surface deposition [10].

In tests of thermal-oxidative deposition, it was found that total surface deposition is independent of flow rate over a wide range of flows (and thus independent of heating rate) [11]. Interestingly, a strong effect of tube diameter (surface/volume ratio) described earlier by Jones [12] was confirmed under significantly different conditions. The decrease in deposition for larger tubes indicates that the reactive precursors (particulate/gums) are subject to other reaction pathways which compete with surface deposition. These results are being included in a CFD-based deposition model being developed by Katta and Chin of Systems Research Laboratories at WL [13-15]. The oxidation chemistry has been found to be more complex than earlier believed, with lower oxygen (reactant) concentrations leading to faster reaction [16]. This was also observed in the QCM [3]. Surface effects have also been found to be complex, with bulk fluid oxygen consumption decreasing as the surface becomes fouled with deposit [17,18]. Surfaces with vapor-deposited inert coatings have been used to examine the effect of surface activity [19,20]. It was found that the inert surface closely resembled the fouled surface in activity [19]. This supports the hypothesis that the "induction time" often seen in thermal stability tests [1] is related to the time required to cover the metal surface with a layer of deposit.

Pyrolytic deposition has also been studied in single-tube heat exchanger tests [20]. It was found that the pyrolytic deposition characteristics for various fuels in flowing tests differed substantially from the characteristics seen in earlier batch reactor tests [22]. Interestingly, multi-component jet fuels showed substantially less pyrolytic deposition than pure compounds or highly processed solvents in these tests. Apparently, some of the thousands of hydrocarbons in typical jet fuels act as hydrogen donors to minimize deposition. In contrast, the processed solvents and pure hydrocarbons produced much less thermal-oxidative deposition, as shown in Figure 2.

1. Hazlett, R. N. *Thermal Oxidation Stability of Aviation Turbine Fuels*, ASTM Monograph 1; American Society for Testing and Materials: Philadelphia, 1991.
2. Zabarnick, S., Grinstead, R. R., "Studies of Jet Fuel Additives Using the Quartz Crystal Microbalance and Pressure Monitoring at 140 C," *Industrial and Engineering Chemistry Research*, Vol. 33, 2771-2777, 1994.
3. Zabarnick, S., Zelesnik, P. M., Grinstead, R. B., "Jet Fuel Deposition and Oxidation: Dilution, Materials and Oxygen Effects," ASME-95-GT-50, to be presented at 6/95 ASME Turbo Expo, Houston, TX.
4. Vilimpoc, V., Sarka, B., "Simultaneous Application of Photon Correlation Spectroscopy and Quartz Crystal Microbalance to the Study of Thermally Stressed Jet Fuel," to be presented at 210th ACS Nat'l Meeting, 8/95, Chicago, IL. To be published in ACS Pet. Chem. Division Preprints.

5. Vilimpoc, V., Sarka, B., Weaver, W. L., Gord, J. R., "Simultaneous Measurement of Particle Size, Mass Rate of Deposition, and Oxygen Concentration in Thermally Stressed Jet Fuel," paper to be presented at ASME Forum on Measurement Techniques in Multiphase Flows, ASME Winter Annual Meeting, Nov. 12-17, 1995, San Francisco, CA.
6. Gord, J. R., Buckner, S. W., Weaver, W. L., "Dissolved O₂ Quantitation in Fuel Through Measurement of Dynamically Quenched Fluorescence Lifetimes," 16th International Congress on Instrumentation in Aerospace Simulation Facilities, WPAFB, OH, July 18-21, 1995.
7. Jones, E. G., Balster, W. J., "Phenomenological Study of the Formation of Insolubles in a Jet A Fuel," *Energy and Fuels*, Vol. 7, 968-977, 1993.
8. Parker, T. E., Blair, D., Du, H., Fraser, M. E., Rawlins, W. T., "Absorption and Scattering in Thermally Stressed Jet Fuels," AIAA Paper 94-0230, Jan. 1994.
9. Schirmer, R. M., "Morphology of Deposits in Aircraft and Engine Fuel Systems," SAE Paper 700258, April 1970.
10. Anderson, S. D., Jones, E. G., Balster, W. J., and Goss, L. P., "Effect of Additives on the Formation of Insolubles in a Jet A Fuel," paper presented at 5th International Conference on Stability and Handling of Liquid Fuels, Oct. 3-7, 1994.
11. Edwards, T. and Krieger, J., "The Thermal Stability of Fuels at 480 °C. Effect of Test Time, Flow Rate, and Additives," ASME-GT-95-68, to be presented at 6/95 ASME Turbo Expo, Houston, TX.
12. Jones, E. G., Balster, W. J., Pickard, J. M., "Surface Fouling in Aviation Fuels: An Isothermal Chemical Study," ASME-95-GT-45, to be presented at 6/95 ASME Turbo Expo, Houston, TX.
13. Chin, L. P., Katta, V. R., "Numerical Modeling of Deposition in Fuel Injection Nozzles," AIAA 95-0497, presented at 1/95 AIAA Aerospace Sciences Meeting, Reno, NV.
14. Katta, V. R., Blust, J. W., Williams, T. F., Martel, C. R., "Effects of Buoyancy on Heat Transfer and Oxygen Consumption in Fuel Thermal Stability Studies, presented at 6/94 ASME/IGTI Turbo Expo, The Hague, Netherlands, ASME-94-GT-262.
15. Heneghan, S. P., Chin, L. P., "Understanding the Oxidation of Jet Fuels Over a Range of Temperature and Flow Conditions Using Global Parameters," paper presented at 5th International Conference on Stability and Handling of Liquid Fuels, Oct. 3-7, 1994.
16. Ervin, J., Heneghan, S., Williams, T., Hanchak, M. A., "Effects of Reduced Dissolved Oxygen Concentrations on Jet Fuel Deposit Formation," to be presented at 210th ACS Nat'l Meeting, 8/95, Chicago, IL. To be published in ACS Pet. Chem. Division Preprints.
17. Jones, E. G., Balster, W. J., "Surface Fouling: Short- vs Long-Term Tests," ACS Fuel Chemistry Division Preprints, Vol. 39, No. 3, pp. 952-957, August 1994.
18. Ervin, J., Heneghan, S. P., Martel, C. R., Williams, T. W., "Surface Effects on Deposits From Jet Fuels," ASME-95-GT-103, to be presented at 6/95 ASME Turbo Expo, Houston, TX.
19. Jones, E. G., Balster, W. J., "Fouling of Stainless Steel and Silcosteel Surfaces During Aviation-Fuel Autoxidation," to be presented at 210th ACS Nat'l Meeting, 8/95, Chicago, IL. To be published in ACS Pet. Chem. Division Preprints.
20. Edwards, T. and Atria, J., "Deposition from High Temperature Jet Fuels," to be presented at 210th ACS Nat'l Meeting, 8/95, Chicago, IL. To be published in ACS Pet. Chem. Div. Preprints.
21. Heneghan, S. P., and Kauffman, R. E., "Analytic Tests and Their Relation to Jet Fuel Thermal Stability," paper presented at 5th International Conference on Stability and Handling of Liquid Fuels, Oct. 3-7, 1994.
22. Lai, W.-C., Song, C., Schobert, H., Arumugam, R., "Pyrolytic Degradation of Coal- and Petroleum-Derived Aviation Jet Fuels and Middle Distillates," ACS Fuel Chemistry Division Preprints, Vol. 37, No. 4, pp. 1671-1680, Aug. 1992.

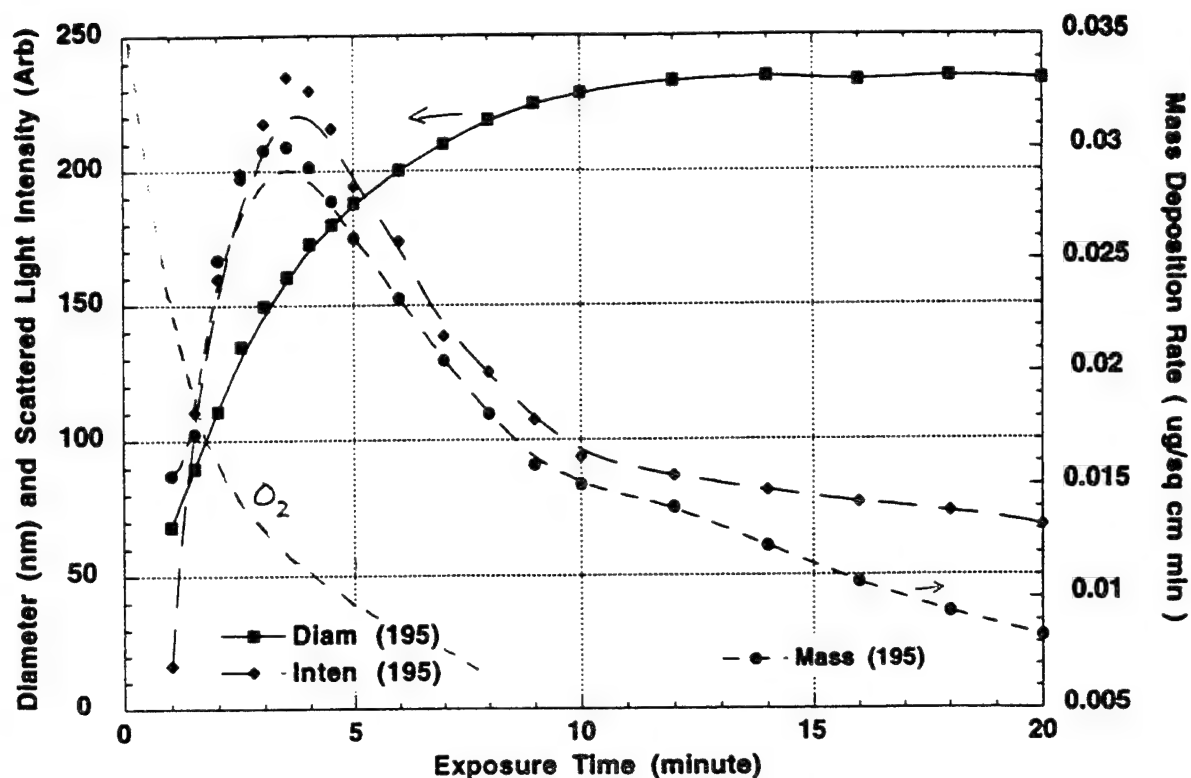


Figure 1. Particle size, scattered intensity (~particle concentration), surface deposition, and oxygen concentration from Jet A fuel at 195 °C as a function of residence time [5].

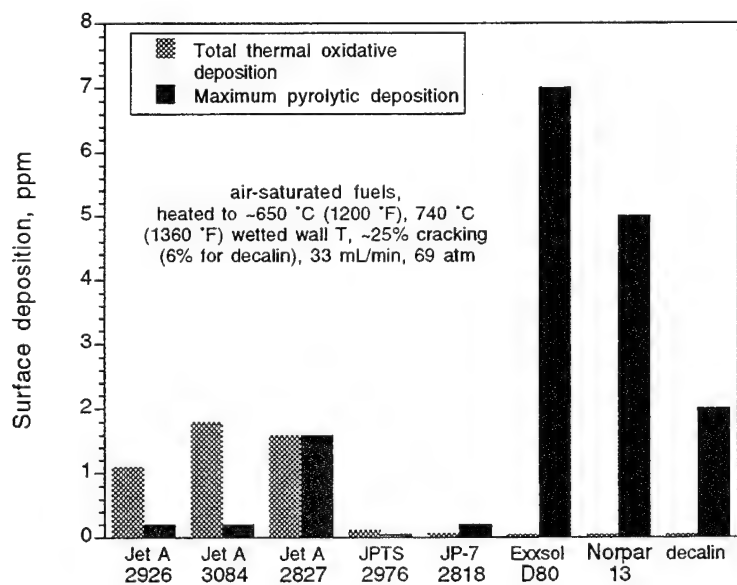


Figure 2. Relative levels of thermal oxidative and pyrolytic deposition for various fuels and processed solvents [20].

BREAKUP AND TURBULENCE GENERATION IN DENSE SPRAYS

(AFOSR Grant No. F49620-92-J-0399)

Principal Investigator: G. M. Faeth
Department of Aerospace Engineering
3000 FXB Building
The University of Michigan
Ann Arbor, Michigan 48109-2118

SUMMARY/OVERVIEW:

Secondary drop breakup and turbulence generation by drops are being studied because they are important dense spray processes. Work on secondary drop breakup has yielded information about the regimes, dynamics, and outcomes of drop deformation and breakup. Measurements are made using pulsed holography and shadowgraph photography for both shock waves and gradual disturbances. It was found that drop breakup in dense sprays must be treated as a rate process rather than by jump conditions; therefore, current work is emphasizing the evolution of drop sizes, velocities and mass as a function of time during shear breakup.

Work on turbulence generation has shown that drop-generated turbulence differs from conventional turbulence, and suggests that the flow involves a stochastic combination of randomly-arriving drop (particle) wakes. Studies of particle wakes for these conditions show that they exhibit a new laminar-like turbulent wake behavior and that stochastic synthesis of randomly-arriving wakes of this type (using Campbell's Theorem) provides a good description of turbulence generation properties. Thus, current work is emphasizing the properties of particle-generated turbulence and their synthesis to describe drop-generated turbulence.

TECHNICAL DISCUSSION

Introduction. Past work has demonstrated the importance of secondary drop breakup and turbulence generation by drops in dense sprays (Faeth, 1990; Faeth et al., 1995; Ruff et al., 1989, 1991, 1992, 1995; Tseng et al., 1992a, b, 1995; P-K. Wu and Faeth, 1993, 1995; Wu et al., 1991, 1992, 1995a,b). Thus, these processes are being studied as discussed in the following.

Secondary Drop Breakup. Studies of liquid atomization have shown that drops produced by primary breakup generally are unstable to secondary breakup (Ruff et al., 1989, 1991, 1992, 1995; P.-K. Wu and Faeth, 1993; Wu et al., 1991, 1992, 1995a,b). Thus, secondary breakup is being studied during this phase of the investigation, see Faeth et al. (1995); Hsiang and Faeth (1992, 1993, 1995) for findings thus far.

The deformation and secondary breakup of individual drops are being observed within both a shock tube and drop (liquid/gas, liquid/liquid) towers. Shadowgraph cinematography and pulsed holography are used to observe the dynamics and outcomes of breakup, while phenomenological theories are used to interpret the measurements. Various drop generating techniques are used to create drops having a wide range of properties.

Initial phases of the work showed that processes of drop breakup were retarded at the large Ohnesorge number conditions of drop breakup near the thermodynamic critical

point, rather than enhanced as thought in the past; has provided drop size and velocity distributions after secondary breakup; and has shown that secondary drop breakup occupies significant regions of space and time and must be treated as a rate process rather than by jump conditions in some instances. Thus, current work is emphasizing the rate aspects of secondary breakup.

The evolution of drop size distributions, drop velocity distributions and dispersed liquid mass, as a function of time during breakup is being studied for shear breakup and shock-wave disturbances. Some typical results are illustrated in Figs. 1 and 2, which are illustrations of the evolution of Sauter mean diameter, SMD, and dispersed drop mass as a function of time, t . Other notation on the figures are as follows: ν = kinematic viscosity of liquid, t^* = characteristic drop breakup time and We = Weber number. The measurements are in reasonably good agreement with phenomenological theories of the process which implies that viscous diffusion within the drop controls drop formation by secondary breakup even though the onset of breakup is independent of liquid viscosity at these conditions.

Current work continues to develop information about the temporal evolution of secondary breakup, with future emphasis on behavior at the large Ohnesorge number and gas/liquid density ratio conditions relevant to secondary breakup near the thermodynamic critical point.

Turbulence Generation. Turbulence generation by drops controls the turbulence properties of dense sprays (Faeth, 1990; Ruff et al., 1991, 1992). Drop-generated turbulence differs from conventional turbulence because mean velocity distributions in randomly-arriving drop wakes contribute to the turbulent velocity field; however, stochastic analysis exploiting Campbell's Theorem, accounting for the random presence of drop wakes, appears to be promising for describing the flow (Parthasarathy and Faeth, 1990; Mizukami et al., 1992). Earlier work developed information about drop wakes at intermediate Reynolds numbers in nonturbulent and turbulent environments needed by the stochastic theory (Wu and Faeth, 1993, 1994, 1995a). Current work is emphasizing evaluation of the stochastic approach (Wu and Faeth, 1995b).

Evaluation of stochastic predictions is based on earlier measurements of flow properties due to turbulence generation in water and air from Parthasarathy and Faeth (1990) and Mizukami et al. (1992). Predicted and measured streamwise and cross stream velocity fluctuations, \bar{u}' and \bar{v}' , are illustrated in Fig. 3 as a function of the rate of dissipation of the mechanical energy of the dispersed phase, ϵ . Other notation on the plot is as follows: U = relative velocity of particle, d = diameter of particle and θ = initial momentum thickness of the wake. Predictions with and without consideration of wake turbulence are shown. In the case of streamwise fluctuations, consideration of wake turbulence has a small effect because mean wake velocities dominate flow properties; therefore, both nonturbulent and turbulent predictions are reasonably good. For cross stream velocity fluctuations, however, predictions based on mean properties underestimates the measurements by a factor of 1000, and velocity fluctuations in particle wakes dominate flow properties so that only predictions allowing for wake turbulence are effective.

Measurements and stochastic predictions of cross stream spatial correlations in particle-generated turbulence are illustrated in Fig. 4. Notation on this plot includes: t = time, X, Y = streamwise and cross stream test point location; y = cross stream displacement of second test point, and L_{uy} = cross stream spatial integral scale based on

streamwise velocity. Predictions suggest relatively small effects of relative turbulence intensity on spatial correlations, which is in reasonable agreement with the measurements.

In spite of the promising agreement between measurements and predictions seen in Figs. 3 and 4, however, other properties are not predicted as well while lack of information about wake properties at low relative turbulence intensities has prevented evaluation of predictions at low-dimensionless dissipation rates (see Fig. 3). Thus, present work is focusing on measurements of both turbulence generation and particle wake flow properties at low relative turbulence intensities in order to help improve our understanding of turbulence generation in sprays.

REFERENCES

- Faeth, G.M. (1990) Twenty-Third Symposium (International) on Combustion, The Combustion Institute, Pittsburgh, 1315-1352.
- Faeth, G.M., Wu, P.-K., Ruff, G.A. and Hsiang, L.-P. (1995) Ann. Rev. Mult. Flow, invited
- Hsiang, L.-P. and Faeth, G.M. (1992) Int. J. Multiphase Flow, 18, 635-652.
- Hsiang, L.-P. and Faeth, G.M. (1993) Int. J. Multiphase Flow, 19, 721-735.
- Hsiang, L.-P. and Faeth, G.M. (1995) Int. J. Multiphase Flow, in press.
- Mizukami, M., Parthasarathy, R.N. and Faeth, G.M. (1992) Int. J. Multiphase Flow, 18, 397-412.
- Parthasarathy, R.N. and Faeth, G.M. (1990) J. Fluid Mech., 220, 485-537.
- Ruff, G.A., Sagar, A.D. and Faeth, G.M. (1989) AIAA J., 27, 901-908.
- Ruff, G.A., Bernal, L.P. and Faeth, G.M. (1991) J. Prop. Power, 7, 221-230.
- Ruff, G.A., Wu, P.-K., Bernal, L.P. and Faeth, G.M. (1992) J. Prop. Power, 8, 280-289.
- Ruff, G.A. and Faeth, G.M. (1995) Prog. Astro. Aero., in press.
- Tseng, L.-K., Ruff, G.A. and Faeth, G.M. (1992a) AIAA J., 30, 1537-1544.
- Tseng, L.-K., Wu, P.-K., and Faeth, G.M. (1992b) J. Prop. Power, 8, 1157-1166.
- Tseng, L.-K., Ruff, G.A., Wu, P.-K. and Faeth, G.M. (1995) Prog. Astro Aero, in press.
- Wu, J.-S. and Faeth, G.M. (1993) AIAA J., 31, 1448-1455.
- Wu, J.-S. and Faeth, G.M. (1994) AIAA J., 32, 535-541.
- Wu, J.-S. and Faeth, G.M. (1995a) AIAA J., 33, 171-173.
- Wu, J.-S. and Faeth, G.M. (1995b) Int. J. Multiphase Flow, in preparation.
- Wu, P.-K. and Faeth, G.M. (1993) Atom. Sprays, 3, 265-289.
- Wu, P.-K. and Faeth, G.M. (1995) Phys. Fluids A, submitted.
- Wu, P.-K., Ruff, G.A. and Faeth, G.M. (1991) Atom. Sprays, 1, 421-440.
- Wu, P.-K., Tseng, L.-K. and Faeth, G.M. (1992) Atom. Sprays, 2, 295-317.
- Wu, P.-K., Miranda, R.F. and Faeth, G.M. (1995a) Atom. Sprays, in press.
- Wu, P.-K., Hsiang, L.-P. and Faeth, G.M. (1995b) Prog. Astro. Aero., in press.

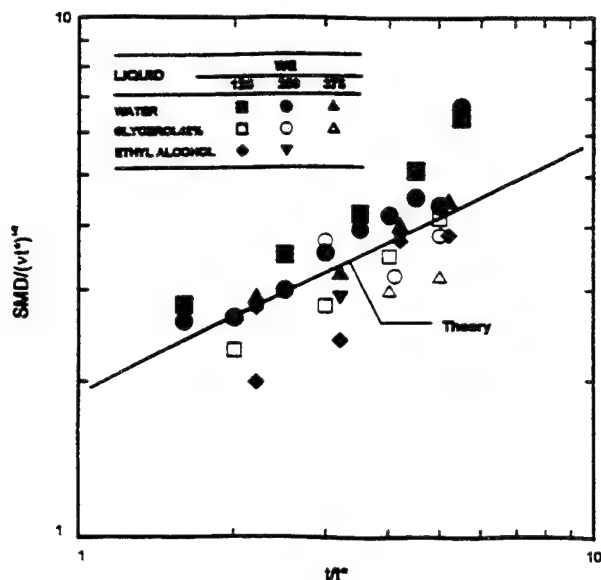


Fig. 1 Evolution of SMD as a function of time during shear breakup.

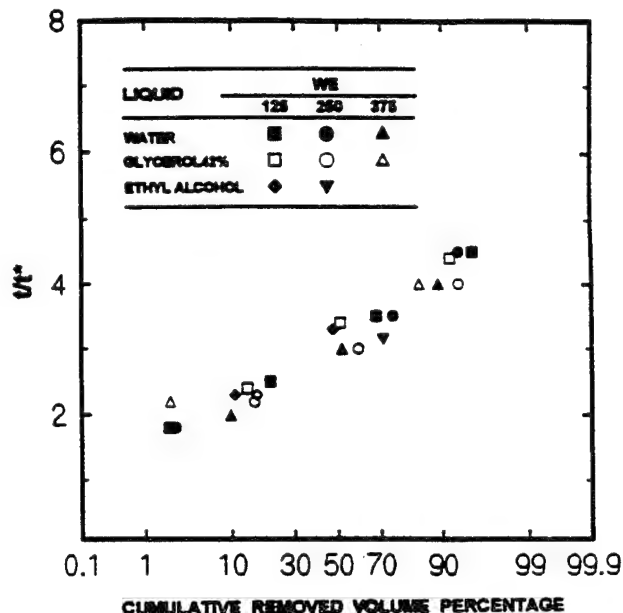


Fig. 2 Evolution of dispersed drop mass as a function of time during shear breakup.

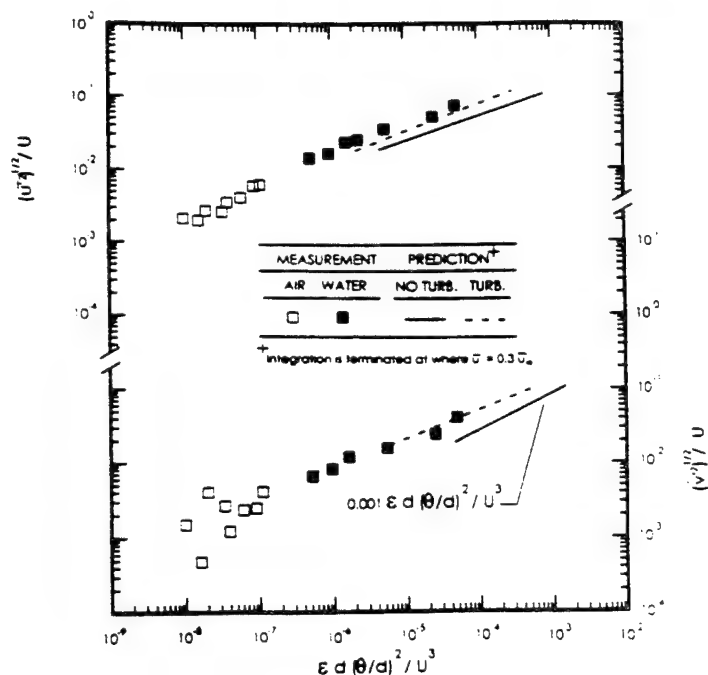


Fig. 3 Velocity fluctuations caused by turbulence generation as a function of dissipation rate.

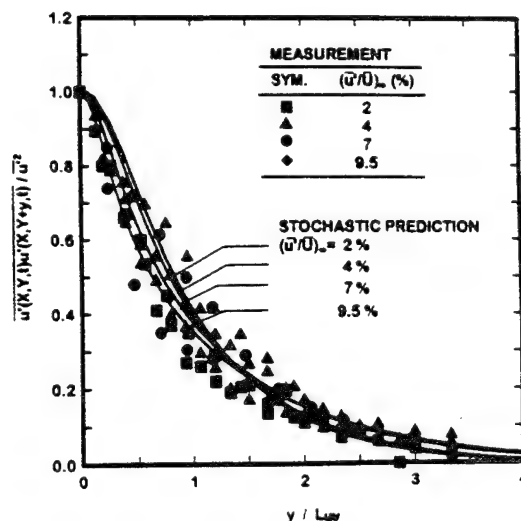


Fig. 4 Cross stream spatial correlations in turbulence caused by turbulence generation.

DEVELOPMENT OF PREDICTIVE REACTION MODELS OF SOOT FORMATION

(AFOSR Grant No. F4620-94-1-0226)

Principal Investigator: M. Frenklach

Fuel Science Program
Department of Materials Science and Engineering
The Pennsylvania State University
University Park, PA 16802-2303

SUMMARY/OVERVIEW:

The ultimate goal of this program is to develop a predictive reaction model for soot formation in hydrocarbon flames. The specific objectives of the current 3-year period are to extend modeling of soot formation to environments closer related to practical combustors, to undertake a theoretical investigation into the chemistry and physics of soot-particle surface processes and their relationship to particle dynamics, and to further refine the underlying reaction chemistry and physics of soot formation. During the past year, progress has been made in the following areas: theoretical calculations were completed of the rate coefficients for the chemically activated reactions of acetylene with vinylic and aromatic radicals, which constitute one of the principal classes of reactions controlling formation and growth of polycyclic aromatic hydrocarbons (PAH), the gaseous soot precursors; a new parametrization method for rate coefficients of unimolecular and bimolecular chemically-activated reactions was developed, which allows an accurate representation of rates of such reactions, critical to soot formation, over wide ranges of temperature and pressure; and extension of the present soot formation model beyond the free-molecular coagulation regime was examined.

TECHNICAL DISCUSSION

Calculations of Rate Coefficients for the Chemically Activated Reactions of Acetylene with Vinylic and Aromatic Radicals. Semiempirical quantum mechanical AM1 calculations were performed for the chemically activated reactions of acetylene with vinyl, 1-buten-3-yn-1-yl, 1,3-butadien-1-yl, phenyl, 1-ethynylphenyl, 2-naphthyl and 4-phenanthryl radicals. The reaction rate coefficients were then calculated on the Rice-Ramsperger-Kassel-Marcus (RRKM) level of theory, using the AM1 molecular parameters corrected to reproduce available experimental data. The results obtained support the hypothesis that reactions of multi-ring aromatic species are in principle similar to those of benzene and phenyl. The calculated rate coefficients were tabulated for the conditions of interest to combustion modeling.¹

Parametrization of Chemically-Activated Reactions Involving Isomerization. Parametrization of theoretical rate coefficients for chemically-activated reactions involving isomerization of activated complexes was examined. The theoretical rate coefficients were computed for chosen test reaction systems using the Rice-Ramsperger-Kassel-Marcus theory. The low- and high-pressure-limit rate coefficients were found to be proportional to $[M]^i$, where $[M]$ is the bath gas

density and i identifies a specific reaction channel. Several parametrization approaches to the pressure dependence of the rate coefficients were tested. The formulas based on a fall-off broadening factor and the generalized interpolation between the pressure limits produced generally large errors. Modifications were introduced that improve the accuracy of these previously suggested formulas. The most promising parametrization formula discovered in the present study contains only three temperature-dependent adjustable parameters and demonstrates a high level of accuracy, with maximum errors below 1 % for most cases tested, including both chemically-activated and unimolecular reactions.²

Extension of the soot formation model beyond the free-molecular coagulation regime. Previous results³ indicated that modeling of soot formation in high-pressure turbulent combustion requires consideration of not only the free-molecular regime of coagulation, which was sufficient to describe soot formation in subatmospheric and atmospheric laminar premixed flames, but also the transition regime.

The present model⁴ of soot formation describes the evolution of soot particle size distribution function (PSDF) using a method of moments.⁵ It was shown⁵ that both free-molecular and continuum regimes of coagulation can be treated by this method. The ways of describing coagulation in the transition regime were examined during the last year.

Equations describing PSDF moments are derived on the basis of average values of coagulation constant

$$\begin{aligned}\langle \beta_0 \rangle &= \int_0^\infty \int_0^\infty \beta(z_1, z_2) n(z_1) n(z_2) dz_1 dz_2, \quad \langle \beta_2 \rangle = 2 \int_0^\infty \int_0^\infty z_1 z_2 \beta(z_1, z_2) n(z_1) n(z_2) dz_1 dz_2, \\ \langle \beta_3 \rangle &= 3 \int_0^\infty \int_0^\infty z_1^2 z_2 \beta(z_1, z_2) n(z_1) n(z_2) dz_1 dz_2, \text{ etc.}\end{aligned}$$

The coagulation constant in the transition regime is usually expressed by a semiempirical interpolation formula suggested by Fuchs⁶

$$\beta(z_1, z_2) = \beta_{cs}(z_1, z_2) \left[\frac{z_1^{1/3} + z_2^{1/3}}{z_1^{1/3} + z_2^{1/3} + 2(g_1^2 + g_2^2)^{1/2}} + \frac{\beta_{cs}(z_1, z_2)}{\beta_f(z_1, z_2)} \right]^{-1}, \quad (1)$$

where z_1 and z_2 are dimensionless masses of colliding partners,

$$z_i = \frac{4}{3\pi\lambda^3\rho} m_i, \quad g_i = z_i^{1/3} \left[\frac{(1 + X_i)^3 - (1 + X_i^i)^{3/2}}{3X_i^2} - 1 \right], \quad X_i = \frac{\pi}{\gamma} \frac{z_i^{1/6}}{C_s(z_i)}, \quad i = 1, 2,$$

ρ is bulk density of particle material, λ is gas mean free path, m_i is the mass of particle i , and β_{cs} and β_f are coagulation constants in continuum regime with slip correction and free-molecular regime, respectively. Slip correction $C_s(z)$ is given by an empirical equation of Millikan.⁷ It follows from Eq. 1 that transition from free-molecular to continuum regime is controlled by sizes of colliding particles and by dimensionless parameter γ determined by the properties of the surrounding fluid, $\gamma = (2k_B T \rho / 27 \lambda \mu^2)^{1/2}$ where μ is the viscosity, T the temperature, and k_B the Boltzmann constant.

Unfortunately, an analytical expression for $\langle \beta_r \rangle$ feasible to be incorporated into the method of moments cannot be obtained. Pratsinis⁸ suggested to approximate $\langle \beta_r \rangle$ by the harmonic mean of the corresponding free-molecular average, $\langle \beta_{f,r} \rangle$, and continuum-with-slip-correction average, $\langle \beta_{cs,r} \rangle$,

$$\langle \beta_r \rangle \approx \frac{\langle \beta_{cs,r} \rangle \langle \beta_{f,r} \rangle}{\langle \beta_{cs,r} \rangle + \langle \beta_{f,r} \rangle} \quad (2)$$

Equation 2 reproduces the original Fuchs expression (1) within 14 % for a monodisperse PSDF. However, it has not been tested for other distribution functions and for higher moments. To check the performance of the harmonic mean approximation, we carried out numerical calculations for a series of distribution functions, those listed in Table 1. For each distribution function the value of z_0 was varied to cover a range of $\langle z \rangle$ from 10^{-5} to 10^5 .

An example of a calculated transition curve is shown in Figure 1 and the maximum relative deviations between the harmonic mean approximation calculated by Eq. 2 and the results of exact numerical integration using Fuchs expression (1) are listed in Table 1. These tabulated deviations appear to be reasonably small for all PSDF moments and functional forms tested, thus indicating that Eq. 2 provides a reasonable approximation to Eq. 1. The advantage of the mathematical form of Eq. 2 over that of Eq. 1 is the ease of implementation with the method of moments.

To complete the testing of Eq. 2 one has also to consider multimodal distribution functions. For instance, bimodal PSDFs were observed for particle dynamics with nucleation and surface growth occurring simultaneously.⁹ To perform such tests, a set of 170 randomly generated multimodal log-normal distributions was generated. The number of modes was selected from 2 to 4, the values of z_0 corresponding to mode locations were varied from 10^{-4} to 10^4 , the values of parameter σ were changed from 1.18 to 1.45 and parameter γ was randomly chosen from the range 10^{-5} – 10^2 corresponding to its physical limits. Similarly to the previous series of tests, approximation (2) demonstrated a good performance, giving the maximum relative deviation of 27 % for $\langle \beta_0 \rangle$ (see Figure 2) and 17 % for both $\langle \beta_2 \rangle$ and $\langle \beta_3 \rangle$.

The performed tests thus show that the harmonic mean formula provides a reasonable approximation to the Fuchs coagulation expression for the use with the method of moments. The maximum relative deviations caused by this approximation were below 30 % and mostly below 20 % for a wide range of PSDF functional forms and external physical conditions, such as pressure, temperature and fluid viscosity. Attempts to develop more accurate approximations were undertaken but resulted in multi-parameter formulas without a substantial gain in accuracy.

REFERENCES

1. Wang, H., and Frenklach, M., *J. Phys. Chem.* **98**, 11465 (1994).
2. Kazakov, A., Wang, H., and Frenklach, M., *J. Phys. Chem.* **98**, 10598 (1994).
3. Y. Yoshihara, A. Kazakov, H. Wang and M. Frenklach, *Twenty-Fifth Symposium (International) on Combustion*, The Combustion Institute, in press.
4. M. Frenklach and H. Wang, in *Soot Formation in Combustion. Mechanisms and Models*, H. Bockhorn, Ed., Springer-Verlag, Heidelberg, 1994, p. 165.
5. M. Frenklach and S. J. Harris, *J. Colloid Interface Sci.*, **118**, 252 (1987).
6. N. A. Fuchs, *The Mechanics of Aerosols*, Pergamon, New York, 1964.
7. R. A. Millikan, *Phys. Rev.*, **22**, 1 (1923).
8. S. E. Pratsinis, *J. Colloid Interface Sci.*, **124**, 416 (1988).
9. C. M. Megaridis and R. A. Dobbins, *Aerosol Sci. Technol.*, **12**, 240 (1990).

Table 1. Particle size distribution functions used in testing of Equation 2.

Distribution function		Parameters	Maximum relative error (%)		
			$\langle\beta_0\rangle$	$\langle\beta_2\rangle$	$\langle\beta_3\rangle$
monodisperse	1 for $z = z_0$ and 0 otherwise		14	14	14
uniform	$1/z_0$ for $z < z_0$ and 0 otherwise		18	18	18
exponential	$z_0^{-1} \exp(-z / z_0)$		18	18	18
log-normal	$\frac{1}{3\sqrt{2\pi z \ln \sigma}} \exp\left(-\frac{\ln^2(z/z_0)}{18 \ln \sigma}\right)$	$\sigma = 1.26 - 2.28$	18	18	25
gamma	$\frac{1}{z_0 \Gamma(p)} \left(\frac{z}{z_0}\right)^{p-1} \exp\left(-\frac{z}{z_0}\right)$	$p = 2, 3$	17	17	17
Weibull	$\frac{1}{z_0 p} \left(\frac{z}{z_0}\right)^{p-1} \exp\left[-\left(\frac{z}{z_0}\right)^p\right]$	$p = 1.5, 2$	18	18	18

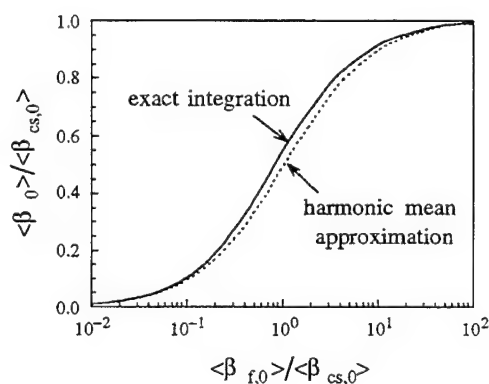


Figure 1. Normalized average coagulation constant calculated for an exponential distribution function with $\langle z \rangle = 1$.

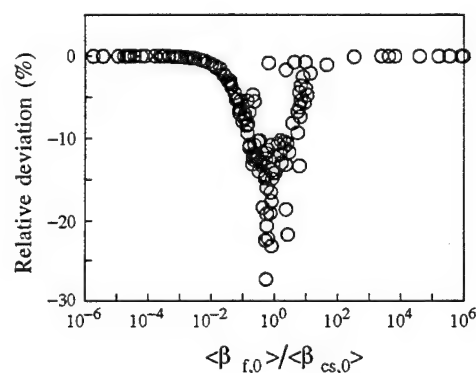


Figure 2. Relative deviations between normalized coagulation constant $\langle\beta_0\rangle/\langle\beta_{cs,0}\rangle$ and the harmonic mean approximation calculated for 170 randomly generated multimodal distribution functions.

FUELS COMBUSTION RESEARCH

(AFOSR GRANT F49620-95-1-0016)

Principal Investigators: I. Glassman and K. Brezinsky

Department of Mechanical and Aerospace Engineering
Princeton University
Princeton, NJ 08544

SUMMARY

Continued progress has been achieved in our integrated research program which focuses on: 1) the thermal degradation of jet fuel components under sub- and super-critical conditions; 2) the pyrolysis and oxidation of prototypical endothermic fuels; 3) the oxidation kinetics of aromatic fuels, including the polynuclear aromatics, and aromatic-aliphatic fuel blends; and 4) soot formation and destruction processes.

TECHNICAL DISCUSSION

1) Sub- and Super-Critical Fuel Degradation Study

During the last year, three major accomplishments have been made in the examination of methyl cyclohexane chemistry at super critical conditions.

First, the pressure control in the reactor was changed to allow for increased residence time. This involved replacing the manually-controlled needle-valve assembly with a dome-type automatic pressure regulator. With the new regulator, pressure can now be controlled to within a steady ± 3 psi. Better pressure regulation permits slower flows and therefore allows almost an order of magnitude increase in reactor residence time (for example, 1 minute to 8 minutes for a fixed coil length). In order that no chemical changes due to the back-pressure regulator would be observed, the point of sample collection was moved from downstream of the back-pressure-regulator to upstream of it.

Second, the previously obtained experimental results with a silica-lined stainless steel tube were verified using the same dimension and length of unlined stainless steel. Excellent agreement between the results from the two surfaces were obtained up to 798 K (the lowest temperature verified was 671 K). Slight changes were noticed above 798 K probably due to a small degree of uncertainty in the experimental temperature control coupled with the exponential growth of the reaction rate with temperature. In each case, significant cracking of the fuel molecule occurs around 810 K - about 10% of the fuel has decomposed around this temperature at a 1 minute residence time reaction. The agreement in results from two different reactor materials suggests that homogenous chemistry free of wall catalysis can now be observed.

Thirdly, a study of the rate of the production of possible fuel-line-fouling precursors was begun. At temperatures above 800 K, the formation of significant (fractions of a percent for a 1 minute reaction) amounts of aromatic species can be observed. Larger aromatic species appear to be forming from the smaller ones, agglomerating, and fouling the line. The ability of these aromatic species to foul a fuel line was demonstrated by the blocking of the silica-lined reactor coil at a temperature of 800 K with an 8 minute residence time in the 6.4 meter coil (total experiment time was 50 minutes). The rate of production of

these precursor species increases significantly (probably exponentially) with increasing temperature; the highest experimental temperature used has been 831 K. Continued examination is planned of the rate of production of the precursors at constant temperatures but varying pressures. Special emphasis will be given to pressures near the critical point.

2) Pyrolysis and Oxidation of Endothermic Fuels and Fuel Blends

Examination of pure MCH during pyrolysis and oxidation revealed that ethane, butadiene, methane and propene were the major stable intermediates. Since the pyrolysis and oxidation characteristics of these intermediates had already been studied in the program, the overall mechanistic character of these processes now appear to be understood.

The oxidation experiments of MCH/toluene blends have led to three significant findings relevant to component selection in multi-component JP fuels. They are:

1) Toluene, commonly thought to be a reaction inhibitor, has little effect on the rate of oxidation of MCH.

2) Early in the oxidation process MCH produces an extensive radical pool which is not only sufficient to insure MCH's rapid oxidation, but also to serve to accelerate the oxidative pyrolysis of toluene.

3) When oxidized as a blend, MCH/toluene, despite sharing a radical pool, each appear to follow their own oxidation mechanism as pure species.

These results have been submitted for publication to Combustion and Flame.

3) The Oxidation and Pyrolysis of Hydrocarbons

During the past year a study that complements the study of methyl cyclohexane/toluene blends was continued. This examination of the interactive chemistry of blends of C₄ aliphatics and monocyclic aromatics has both experimental and modeling aspects, and is being conducted to better understand in a fundamental way the effects of fuel blending on combustion chemistry.

Several pure fuel and binary blend fuel oxidation experiments have been conducted using toluene, an alkylated aromatic, n-butane, a straight chain alkane and two olefins - isobutene and butadiene. These experiments were performed to establish good control of experimental initial conditions, to improve carbon atom accountability, to improve species identification, and to establish repeatability of results. Thus far, blend oxidation data show the formation of no new intermediate species other than those already expected from each pure fuel component. Additionally, experiments and tests were conducted to discount any catalytic effects in the flow reactor which might have affected the results.

Modeling work has also begun over the past year. Model predictions and experimental results for toluene oxidation are in accord. For the oxidation of C₄ species several models exist and n-butane experimental results are currently being compared against these. Once the C₄ model is identified that best predicts flow reactor profiles, it will be merged with one for toluene for comparison with flow reactor blend results.

4) Soot Formation and Destruction Processes

Even though the efforts on soot formation and destruction continue to diminish, the extensive experience gained still permits analysis of soot problems which arise. Last period it was reported that in flames a critical temperature for soot nucleation appears to exist and that temperature is of the order of 1650 K. In co-annular diffusion flames, then, the critical temperature isotherm, say 1650 K, is the point at which soot particles nucleate. In co-annular flame height tests, then, the soot volume fraction grows by mass addition to the particles until the particles enter the higher temperature flame front. As the volumetric flow rate of the flow is increased, the separation distance of the flame and critical temperature isotherms remains essentially the same, but the amount of particles nucleated increase the soot volume fraction so that the particles penetrate the flame front and a smoke height is reached. Different fuels will form a different number of nucleated particles at the 1650 K isotherm, so different smoke heights are obtained for different fuels. When the fuel is diluted with an inert gas, the flame temperature drops and the 1650 K isotherm moves closer to the flame temperature isotherm. Thus the growth period of the nucleated particles decreases and the soot volume fraction entering the flame is less. To create a smoke point for this diluted condition, the volumetric flow rate of the fuel-inert mixture must be increased so that more particles will form. This description was in the report of last year. Subsequently it has been proven that this insight of the smoke height can explain the diversity of results that various investigators have obtained when dilution is used to analyze the sooting tendency of various fuels. This insight reveals that when dilution is used, it is not only necessary to control the flame temperature, but also the temperature profile from the nucleation point (1650 K) to the flame. For example, in a co-annular flame in which a small amount of oxygen is added to the fuel and the temperature of the inlet mixture reduced from ambient to give the same flame temperature, it will produce a smaller soot volume fraction than pure fuel. Considering the case where the oxygen does not affect the soot pyrolysis, the temperature profile does indeed change as a quasi-steady moving boundary heat transfer analysis shows. The importance of this concept with respect to soot processes is significant enough that soot experimentation will be re-implemented.

PARTICLE DISPERSION IN A TURBULENT SHEAR FLOW

AFOSR Grant F49620-92-J-0418

Principal Investigators: Ian Kennedy and Wolfgang Kollmann

Department of Mechanical and Aeronautical Engineering,
University of California,
Davis CA 95616.

SUMMARY

The project consists of an experimental and a numerical component. The experimental research is concerned with obtaining reliable, Lagrangian measurements of particle dispersion and vaporization in turbulent jets and sprays. The goal is to eventually obtain data on the transport and the mass transfer in liquid fuel droplets in an unsteady two phase flow such as a spray flame. Data have been obtained in turbulent jets over a range of time scales for droplets and flow fields that show that droplet dispersion at long times is approximately linear with time with a diffusivity that is almost independent of droplet response time. Savings in computational time for sprays may be achieved by making use of these results. Initial results have been obtained in a spray with a fluorescent droplet that show the impact of the spray on the development of the turbulent jet. An imaging spectrograph is being installed to measure droplet lasing from the fluorescent dye with a view to measuring droplet diameters and vaporization rates. The numerical component of the project continued the development of the solution procedure for the Navier-Stokes and the particle equations. Large Eddy Simulations of dilute sprays using the Smagorinsky model for the sub-grid-scale motion of the fluid phase and a particle-source-in-cell method for the effect of the particle phase on the fluid phase were completed. The dispersion of tagged droplets was measured and simulated and the influence of the spray on the flow structures in the near field was determined numerically. The solution method was improved by developing more accurate time integration methods based on Runge-Kutta type single step schemes.

TECHNICAL DISCUSSION

Experimental

Particle dispersion and particle velocities were measured with laser sheets and a position sensitive photo multiplier tube to track particles¹. Monodisperse hexadecane droplets were injected onto the centerline of a turbulent air jet in which their radial dispersion, axial velocities, and times of flight were measured as a function of axial position. Because the liquid was hexadecane and the droplets were only in the measurement field for a short time ($\ll 1$ s), the particles were considered to be non vaporizing. Droplet diameters were determined from the terminal velocities of the droplets. A large number of samples were collected in order to give statistically meaningful results. No particle interaction was present since particles were injected more than 1000 diameters apart.

The time and length scales of the jet were varied through the control of the jet exit velocity and nozzle diameter. Nozzle diameters of 7 mm and 12.6 mm were used. Reynolds numbers were in the range of 10,000 - 32,400. Two different droplet diameters were used viz., 60 μ m and 90 μ m. Variations in the droplet response time, the velocity of the jet and the nozzle diameter produced a range of values for the Kolmogorov, turbulent, and acceleration Stokes numbers. The times-of-flight data were used to analyze the dispersion measurements in terms of true Lagrangian statistics. It was found that the use of a mean time of flight to present the data incurred quite small errors relative to the exact Lagrangian statistics.

Particle dispersion (σ_p^2) was found to be linear with time for sufficiently long times. It has been shown that particles over a wide range of nozzle Stokes numbers ($\tau_p U/D$) satisfy conditions in the far field of a round jet for dispersion to follow the theory that was developed by Batchelor ² and Monin and Yaglom ³ for fluid particles viz., that a particle's mean downstream location scales with time of flight as $\bar{X}(t) \sim t^{1/2}$. This leads to the observation that the time scale (τ_f) of the fluid motion to which the droplet is exposed is itself simply proportional to time of flight i.e., $\tau_f \sim t$. Linear behavior with time was found to arise when the turbulent Stokes number (based on the droplet response time and local eddy lifetime, τ_e) was less than one. Dispersion data at long times of flight (when dispersion was linear with time) were analyzed over the entire range of nozzle diameters, particle diameters and exit velocities to obtain the Lagrangian particle

diffusivity that is defined as $\frac{1}{2} \frac{d\sigma_{p,x_2}^2}{dt}$. Close analysis of the results showed that the particle Peclet number was almost independent of droplet diameter once $\tau_p/\tau_e \leq 1$. It reached a value that was almost twice the Eulerian fluid diffusivity. The results suggest that it may not be necessary to extend computations with, for example, a stochastic simulation in a self preserving flow once the turbulent Stokes number is less than one. A considerable saving in computational effort may be realized.

The experiment has been modified to accommodate the inclusion of a spray. Droplets tagged with fluorescent dye were injected into a round turbulent jet into which a dispersed, liquid spray had been added. The location of the tagged particle was followed through the jet with an optical detection system that was a modification of an earlier technique ^{1,4}. This experimental approach provides a simple two phase flow with well defined boundary conditions without the significant complications that are introduced by spray atomization.

An ultrasonic atomizer is used produce a fine spray of water with a SMD of around 50 μm . The size distribution of the spray that the ultrasonic atomizer produced was measured by using a slide impaction technique. A MgO coated slide was exposed to the spray and the resulting craters were imaged. The digitized images were corrected for the calibration factor and the statistics of droplet size were collected with software. The size distribution is shown in Fig. 1. The spray is introduced tangentially to the flow of air through a chamber. The chamber is designed to have a small flow of air through the walls and through the central tube to prevent the spray hitting the walls and creating drips. Single droplets of water that are seeded with fluorescein dye are formed at the top of the chamber with a piezoelectric droplet generator. The fluorescent droplets pass through the chamber along with the spray to leave the nozzle on the centerline. As the fluorescent droplet passes through an Argon ion laser sheet, it emits fluorescence at a longer wavelength. The fluorescence is detected by a position sensing photomultiplier tube to yield a measure of the location and velocity of the particle. The dispersion of water droplets with a diameter of 60 μm have been studied in the near field of a round jet with $Re = 10,000$. The nozzle diameter is 14 mm.

Sprays with mass loadings from 0 up to 7% have been added to the jet. The signal to noise ratio under these conditions is about 110. The mean square displacement of the fluorescent droplet was measured at varying x/D from the exit of the nozzle. The dispersion is shown in Fig. 2 for a pure air jet and for a spray with varying mass loadings. It is apparent that the spray contributes to the breakdown of the jet with larger spray loadings resulting in greater dispersion of the tagged fluorescent droplets that were added to the flow. Another interesting feature of the results is the decrease in the dispersion at around $x/D \approx 8 - 10$.

The experiment is currently being developed so that measurements of droplet diameter can be obtained. An imaging spectrograph will be used to analyze the lasing emission from the tagged, dye containing droplet. The morphology dependent resonances are very size dependent. Accurate, direct measurements of droplet vaporization rates within a turbulent spray will be feasible with this approach.

Theory and Computation

The dispersion of the tagged particle has been measured for comparison with the results of a Large Eddy Simulation of the particle laden jet. The dispersion of tagged droplets was measured and computed with the LES model and the influence of the spray on the flow structures in the near field of the jet was determined numerically. The turbulent jet used in the experiment for the study of droplet dispersion has a sufficiently low Mach number such that the flow of an incompressible fluid containing particles can be considered for the numerical simulations. The Navier-Stokes equations for the incompressible fluid phase are set up for the conditions of a flow laden with fine particles. The case of dilute sprays of small particles was considered, where the particle size is much smaller than the smallest length scale of the flow and the volume of the particles can be neglected. Hence, the displacement effect of the particles is neglected but not the forces exerted by the particles on the fluid. The Navier-Stokes equations emerge then in the usual form ^{5,6} with the momentum balance

$$\frac{\partial v_\alpha}{\partial t} + v_\beta \frac{\partial v_\alpha}{\partial x_\beta} = -\frac{1}{\rho_g} \frac{\partial p}{\partial x_\alpha} + \frac{\partial}{\partial x_\beta} \left(v_\beta \frac{\partial v_\alpha}{\partial x_\beta} \right) + g_\alpha + M_\alpha$$

containing the effect M_α of the particles on the fluid phase. This effect is evaluated by integration over a small subdomain \mathcal{D} (grid cell) and the force exerted by the particles on the fluid phase is then given by (subscript f indicates fluid phase)

$$M_\alpha = -\frac{\rho_p}{\rho_f} \sum_{i=1}^{N_c} \frac{V_i}{V} F_\alpha^i$$

where the F^i are the forces on the N_c individual particles (with volumes V_i) in the grid cell \mathcal{D} with volume V_c . This force is then distributed among the grid points of the cell using Crowe's ⁷ Particle-Source-In-Cell method. The LES simulations provided the details on the flow structure to understand the plateau in the particle dispersion observed in the experiment (Fig. 2). The numerical simulations could not reach the mass loading of the experimental spray, but they show distinctly the same phenomenon (Fig. 3). At the location of the dispersion plateau seen in Fig. 3 in the range $10 \leq x/D \leq 13$ a significant thinning of the particle distribution off the axis is observed. This indicates that behind the first interaction region of the ring vortices (about $6 \leq x/D \leq 11$), which are generated by the Kelvin-Helmholtz instability of the cylindrical shear layer, a region exists where the particles suffer acceleration in axial direction with significant lateral transport towards the jet axis.

A significant part of the project work during the past year was spent on the improvement of the numerical solution method for the Navier-Stokes equations. The Adams-Bashforth time integration scheme used so far is only second order accurate and it is known to be unstable for the inviscid case. Hence, more accurate and conditionally stable explicit time integration schemes were developed. They are based on the classical Runge-Kutta schemes for ordinary differential equations of third and fourth order accuracy. The major modification required for their application to the Navier-Stokes equations is the treatment of mass balance. This was done first for the two-dimensional Navier-Stokes equations to save CPU time during the development phase. The results for the fourth order scheme were very promising as the Fig. 3 shows, where a plane jet was simulated at the Reynolds number $Re=5000$. Similar results were obtained for the third order scheme and the latter is currently being implemented into the three-dimensional jet code.

References

1. Call, C. J., and Kennedy, I. M. 1992: Measurements and simulations of particle dispersion in a turbulent flow. *Int. J. Multiphase Flow* **18**, 891-903.
2. Batchelor, G. K. 1957: Diffusion in free turbulent shear flows. *J. Fluid Mech.* **3**, 67-80.
3. Monin, A. S. and Yaglom, A. M. 1979: *Statistical Fluid Mechanics Vol. 1*, MIT Press, Cambridge MA.
4. Call, C. and Kennedy, I. M. 1994: Measurements of Droplet Dispersion in Heated and Unheated Turbulent Jets, *A.I.A.A. J.* **32**, No. 4, 874 - 875.
5. Eaton, J.K., 1994: Experiments and simulations on turbulence modification by dispersed particles, *Appl. Mech. Review*, **47**, S44-S48.
6. Elghobashi, S.E. and Truesdell, G.C., 1991: On the Interaction between Solid Particles and Decaying Turbulence, Eighth Symp. Turbulent Shear Flows, Munich, Germany, 731-736.
7. Crowe, C.T., 1982: Review - Numerical methods for dilute gas-particle flows, *J. Fluids Engrg.* **104**, 297-303.

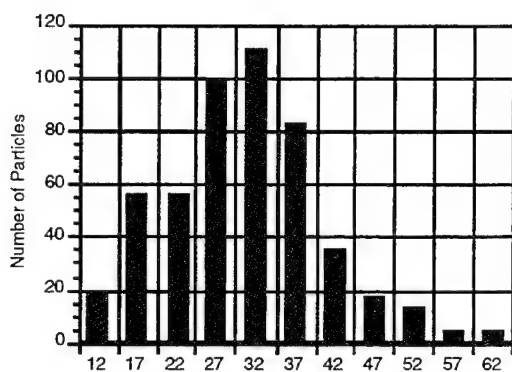


Fig. 1 Spray size distribution

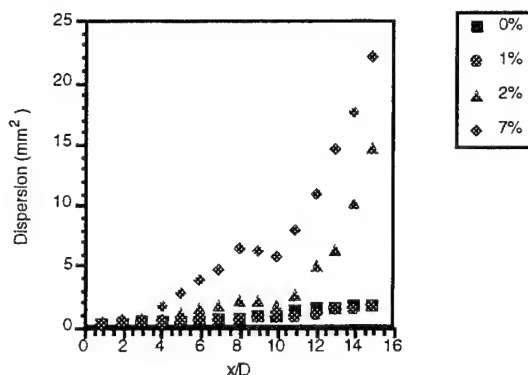


Fig. 2 Dispersion of a 60 μm water droplet in sprays with varying mass loadings

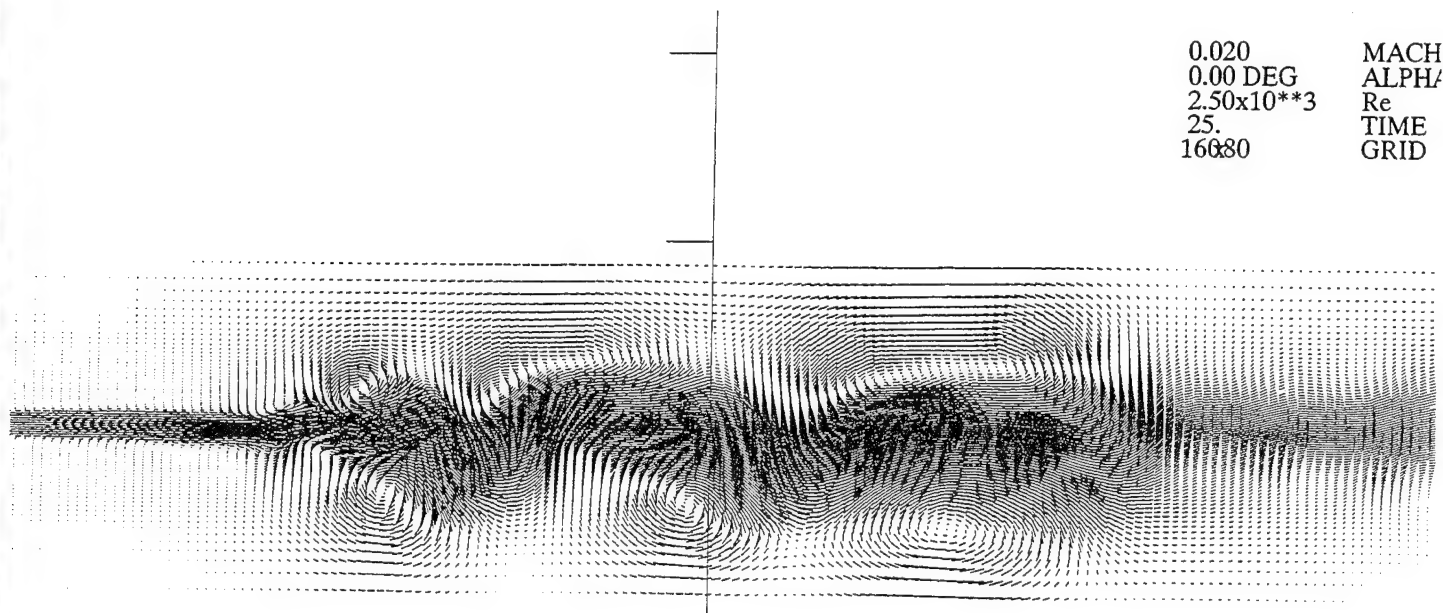


Fig. 3 LES simulation of a turbulent plane jet

FLUORESCENT DIAGNOSTICS AND FUNDAMENTAL DROPLET PROCESSES

ARO Grant DAAH04-94-G-0020

Principal Investigator: Lynn A. Melton
Co-Principal Investigator: Michael Winter*

Department of Chemistry
University of Texas at Dallas
Richardson, TX 75083-0688

SUMMARY/OVERVIEW:

In this presentation, the extension of Droplet Slicing Imaging (DSI) techniques to the imaging of droplets as they pass through the flame front of a diffusion flame will be discussed. This experimental environment, in which droplets are ejected from an aerodynamic droplet generator along the core of the diffusion flame, provides changing shear velocities and a high temperature zone, in which droplet evaporation will be significant. These experiments appear to be more feasible at pressures above one atmosphere. The DSI studies of flow patterns within the droplets will provide significant information about heat and mass transfer processes for droplets in combustion environments.

TECHNICAL DISCUSSION:

During the previous year, investigations at the University of Texas at Dallas (UTD) have focused on (1) the development of experimental methods for the measurement of the transient temperature field in a cold hydrocarbon droplet which is injected into a hot ambient gas and (2) the development of fluorescence-based thermometry systems which are resistant to perturbation by oxygen. In the latter task, strongly fluorescent liquid phase systems have been identified for which the total fluorescence is virtually independent of oxygen concentration and temperature and the change in the band shape with temperature can be used to measure the liquid phase temperature. These systems will be described in further reports.

The material presented in the remainder of this abstract arises from work carried out at United Technologies Research Center (UTRC).

*United Technologies Research Center, East Hartford, CT 06108

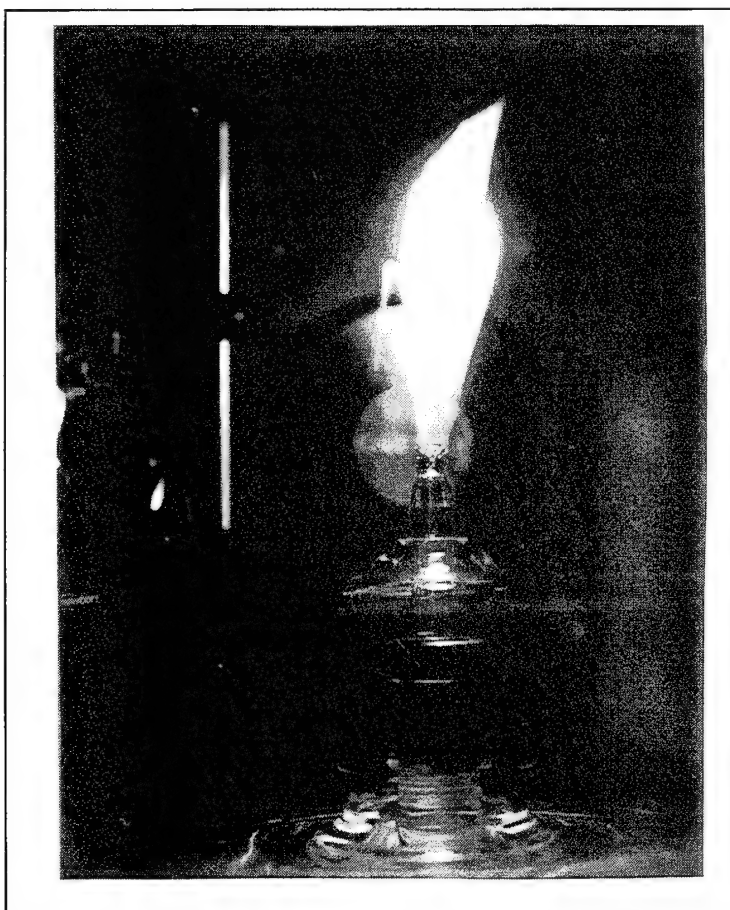
Program Objectives

The purpose of the droplet slicing experiments is to investigate the shear-induced, internal motion of single fuel droplets and characterize the mass and thermal transport effects. The program utilizes 2-D images of laser-induced fluorescence from equatorial planes in the droplets to measure flow and temperature patterns. The slicing experiments have been performed in cold-flow, inert conditions and will be extended to a combustion environment with the further extension to a high pressure regime. Differences in the data from the various regimes will be evaluated and compared to model predictions.

Droplet Slicing Experiments

Experiments were performed with the aerodynamic droplet generator configured to produce decane droplets with acetone condensed on their surface. The drops were allowed to fall into an ambient atmosphere. Laser excitation at 266 nm induces fluorescence from the acetone while the decane is not excited. Internal circulation was observed as the acetone was convected inwards from the surface. Because the acetone fluorescence is not sensitive to oxygen quenching, special requirements, e.g. dry nitrogen background (as for exciplex fluorescence), were not needed and the ambient gas was normal room air. The bi-component droplet experiments enable the next phase of the program; experiments of droplet flow patterns and heat transfer effects as the drops are subjected to sudden temperature changes.

Droplets are injected into the fuel flow of a methane/air diffusion flame and travel through the flame core where they experience a rapid temperature rise in their environment. The nozzle is positioned to eject the droplets upward because the flame behavior is optimized in that configuration. Figure 1 is a picture of the flame/injector apparatus and shows a single (burning) droplet exiting from the post flame gases after being injected through the fuel flow nozzle. Droplet slicing measurements are usually made in the inside of the non-premixed flame. Current experiments are characterizing the gaseous flows in an attempt to match the aerodynamic variables (such as Reynolds and Weber number) between the cold flow and combustion regimes.



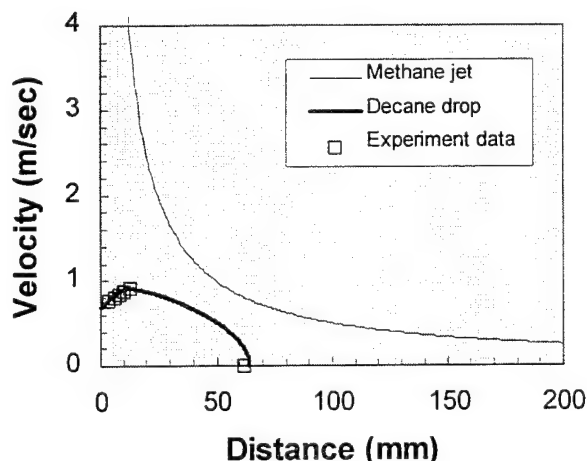
An analytical model of the aerodynamic droplet generator is being developed to help design an unambiguous experiment to

elucidate shear-induced internal circulation by providing flow conditions that result in shear reversal during the droplet trajectory. Shear reversal was observed in the fluorescent images from the cold flow experiments and its effect on the internal motion of the droplet was studied. This behavior may only result if the droplet velocity which is initially less than the gas velocity, exceeds the gas velocity to allow reversal of flow patterns. Comparison with data from a high temperature environment is desired as well as data from the high pressure regime to more closely simulate conditions within a gas turbine combustor.

The droplet trajectory is calculated from the balance of forces on the drop. The droplet is accelerated by the drag force from the jet flow while gravity acts to decelerate the drop in this configuration. The flow from an axisymmetric jet is composed of a potential core which has a constant velocity that persists for approximately 5-10 orifice diameters downstream. This core region is followed by the axisymmetric decay region where the velocity decays as $(y/a)^{-1}$, 'a' being the orifice diameter.

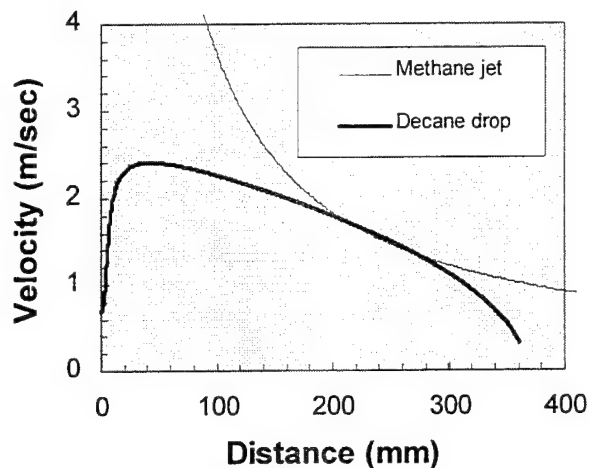
$$\frac{d}{dt} \left(\frac{dy}{dt} \right) = \frac{A_{\text{drop}} \cdot C_D}{m_{\text{drop}}} \cdot \frac{\rho_M}{2} \cdot \left[u(y) - \frac{dy}{dt} \right]^2 - \frac{\rho_d \cdot g \cdot V_d}{m_{\text{drop}}}$$

C_D is the drag coefficient, a function of Reynolds number and A_{drop} and m_{drop} are the area and mass of the decane droplet. V_d is the volume of the drop, ρ_d and ρ_M are the densities of decane and methane and, g is the acceleration of gravity. The jet flow velocity is a function of distance from the orifice and is modeled by the function $u(y)$. The nozzle orifice is 1 mm for the UTRC droplet generator. The differential equation is solved for the position and velocity of the drop as a function of height above the nozzle orifice. Results are shown in the following figure for isothermal conditions with a 600 micron diameter decane droplet in a 293 cm³/min methane flow.



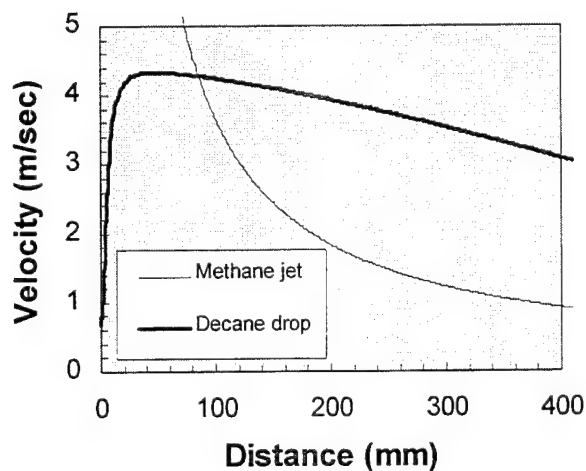
The box symbols are experimental measurements from our apparatus and the thin curve is the methane jet velocity. The calculation predicts the droplet trajectory very well.

Combustion heat release will cause a perturbation of the methane velocity due to the temperature field. The adiabatic flame temperature for methane/air is 2210 K and the flame height is proportional to methane flow rate. Including buoyancy in the calculation produces the following result.



The droplet and methane jet velocities are increased due to the flame heating and their relative velocities are near zero over the region from 20 to 30 cm above the nozzle.

Increasing the pressure has a beneficial effect on the shear velocity; the relative velocities of the drop and methane flow are predicted to reverse 10 cm above the nozzle as shown in the following calculation for 5 atm.



As seen in the figure, this analysis provides the design of an unambiguous experiment to elucidate shear-induced internal circulation by providing flow conditions that result in shear reversal during the droplet trajectory.

APPLICATION OF PARALLEL PROCESSING TO THE INVESTIGATION
OF SUPERCRITICAL DROPLET EVAPORATION AND COMBUSTION USING
MOLECULAR DYNAMICS

AFOSR Grant No. F49620-94-1-0133

M. M. Micci and L. N. Long

Dept. of Aerospace Engineering
The Pennsylvania State University
University Park, PA 16802

SUMMARY/OVERVIEW:

The evaporation and combustion of LOX droplets in the combustion chambers of current liquid propellant rocket motors occurs under supercritical pressures and temperatures, however little is known about droplet phenomena above the critical point. The complete evaporation of a three-dimensional submicron droplet under subcritical conditions has been modelled using molecular dynamics. The two-phase system consisted of 2048 argon atoms modeled using a Lennard-Jones 12-6 potential distributed between a single droplet and its surrounding vapor. The computed evaporation rate obtained by observing the droplet regression agrees with that predicted by Knudsen aerosol theory. The collision of two droplets in a vacuum was also modelled.

TECHNICAL DISCUSSION:

The complete evaporation of a three-dimensional submicron droplet under subcritical conditions has been modelled using molecular dynamics. The two-phase system consisted of 2048 argon atoms modeled using a Lennard-Jones 12-6 potential distributed between a single droplet and its surrounding vapor. The algorithm used was a time-stepping, second-order accurate leap-frog MD algorithm (Verlet). The time step is chosen to be very small to avoid errors and for stability and is roughly 10 femtoseconds for argon.

If a known configuration at a given state is available it can be read in as the initial conditions. When there is no pre-existing configuration, molecules are arranged as a solid-like face-centered-cubic (f.c.c.) lattice (or with a dense lattice embedded in a gas lattice). The velocities of the molecules in the lattice are assigned according to a Maxwellian distribution. It is then run for an equilibration period.

The simulated molecules are placed in a unit box with periodic boundary conditions. For non-heated, non-evaporating droplet simulations, simple periodic boundary conditions are used. For evaporation simulations, the temperature of the boundary cells is modified. The velocities of the atoms in these cells are adjusted to a prescribed temperature at specified intervals. This is accomplished by first computing the temperature in the boundary cells and then scaling the velocities of all the molecules such that the new temperature would be the desired temperature. Heat flux could also be specified if so desired (instead of a constant temperature condition). There are only three translational degrees of freedom in monatomic molecules. Therefore the kinetic energy of the system is purely translational and temperature is directly proportional to kinetic energy. Figure 1 compares the droplet radius versus time for our simulated droplet with the formula for a Knudsen aerosol which follows a diameter versus time evaporation rate.¹ The agreement between theory and simulation is quite good. This is, as far as we know, the first ever molecular dynamics simulation of a completely evaporating droplet.

Figures 2 and 3 show simulations of two colliding droplets. The relative velocity in these two cases are 159 and 474 meters/second, respectively. There are 446 argon atoms in each drop, and the drops are identical. The domain size is 40σ , with periodic boundary conditions. The drop temperature is 80K. Figure 2 shows that at low speeds the two droplets simply coalesce into one larger droplet. Figure 3 shows that at a higher speed the two droplets completely disintegrate into individual atoms (a gas).

The first non-spherically symmetric molecule being modelled in this program is the oxygen, O_2 , molecule in both the gaseous and liquid (LOX) states. Oxygen has been modelled previously using molecular dynamics^{2,4} but its evaporation using MD has never been examined. Molecules can be modelled by one of two means: treating each atom in the molecule as a separate Lennard-Jones site (site-site); or by defining a central site with corrections for angular dependency. Luo and Hoheisel⁵ modelled N_2 using both methods and found that they both gave the same results, however site-site seems to be the method of choice for diatomic molecules.

The equations of motion, which now contain angular dependencies, are solved by one of two methods. The first method starts with the Newton-Euler equations of motion. Because singularities appear when written in terms of the Euler angles, the equations of motion are written in terms of quaternions which are then solved in matrix form⁶. The other method consists of solving the equations of motion for each atomic site subject to a constraint with is the fixed bond length. This is referred to as constraint dynamics. The constraint results in a force which is added to the potential force. Constraint dynamics is computationally simpler for small molecules and was chosen for implementation in this study and the modelling of O_2 has been initiated. Future work will include vibrational energy storage, which is not considered significant at temperatures representative of oxygen in its liquid or just evaporated states.

The coding work to date has concentrated on the IBM SP2. The SP2 has a significant level of memory on each processor. Typical nodes located at Penn State and NASA Ames have 256 MB. Some of the nodes have as much as a gigabyte. This abundance of storage on each node allows a new approach to partitioning a molecular dynamic model in a parallel code. The approach consists of assigning the responsibility for computing displacements of a fixed number of molecules to each node. There are immediate benefits and costs associated with this concept.

Domain decomposition, the term used to describe the geometric partitioning of molecular dynamics problems, is very unbalanced when applied to non-uniform systems. The workload is heavily dependant on the force computations, therefore a balanced workload requires a balanced density for domain decomposition approaches. Due to the two-phase nature of our studies, partitioning independent from physical domains was investigated. The non-physical partitioning consists of assigning fixed responsibilities for atomic displacements at the onset of the simulation run. To achieve load balancing, the assigned atoms on each node will be found uniformly throughout the entire physical domain. This ensures a balanced average density regardless of the irregularities found in the system. An equal number of atoms will be assigned to each node, and given a statistically large enough system, the random, and therefore balanced, densities should be maintained throughout the simulation. Nearly perfect molecular dynamics load balancing is achieved independent of system irregularities (such as a round drop in a cube).

To allow the uniformly diverse atom assignment on each node, the nodes must be aware of all atomic positions at all times. The memory capability of the SP2 allows this large, global array to exist on all processors simultaneously, but how is such an array updated? If the nodes require significant communications, the balancing will be meaningless. The code will simply be slowed too far by parallel operation losses (i.e., communications). To accomplish efficient communications, an SP2 Message Passing Library (MPL) tool, MP-CONCAT⁷, was used. With each node working an evenly partitioned set of position coordinates, this command generates the required global position array in just three applications (one for each x, y, and z coordinate). Before generating the complete code, a test program was written to quantify the performance of the concatenation command. The evaluation was performed on the Penn State SP2, and a set of four nodes were set aside for dedicated use. Initial runs led to the development of a performance estimation equation based on latency (communications initialization period) and completely parallel communications of the multi-broadcasted information. The equation is

$$t_{comm}(n) = C \left(\frac{n-1}{n} \right) N + t_{comm}(1) \quad (1)$$

where t_{comm} is the communication time, n is the number of nodes, N is the size of the resultant global array, and C is a constant. After a series of runs on the 4 node array, the value of C was found to remain constant to within one percent. This repeated consistency was later verified on the NASA Ames SP2 for well over 60 nodes. For double precision communications, C has the value 0.29×10^{-6} sec.

Equation 1 reveals a significant performance characteristic of the concatenation command. The time required to broadcast a given size global array over three processors is 33 percent greater than over two processors. The time to broadcast over 50 processors is only 2 percent greater than over 25 processors. In other words, for

a given problem size, the concatenation communications approach a constant value. As a fixed problem size is partitioned across additional processors, the relative cost of the communications will increase compared to the shared computation load. The predicted performance of the proposed code was formulated using Equation 1 and the results were promising. A computation of a block of liquid was performed and the radial distribution function computed. Comparisons to plots in both Allen and Tildesley⁶ and Haile⁸ proved the accuracy of the code. Complete load balancing and relatively small communications requirements were evidenced.

REFERENCES

1. Davis, E. and Ray, A.K., "Submicron Droplet Evaporation in the Continuum and Non-Continuum Regimes," *J. Aerosol Sci.*, 1978, pp. 411-422.
2. Frenkel, D. and MacTague, J.P.; "Molecular Dynamics Studies of Orientational and Collision-Induced Light Scattering in Molecular Fluids," *J. Chem. Phys.*, Feb. 15, 1980.
3. Ladanyi, B. M., "Higher-Order Interaction-Induced Effects on Depolarized Light Scattering from Fluids of Optically Anisotropic Molecules," *Chem. Phys. Lett.*, Vol. 121, No. 4, Nov., 1985.
4. Chahid, A., Bermejo, F.J., Martinez, J.L., M. Garcia-Hernandez, E. Enciso, and F.J. Mompean; "Magnetic Dynamics in Liquid Oxygen," *Europhys. Lett.*, Vol. 20, No. 1, Sept., 1992.
5. Luo, H. and Hoheisel, C.; "Collective Transport in a Molecular liquid with Quadrupole Interaction," *Phys. Rev. A*, Vol. 43, No. 4, 1991.
6. Allen, M. P. and Tildesley, D. J., *Computer Simulation of Liquids*, Clarendon Press, Oxford, 1987.
7. IBM AIX *Parallel Environment Programming Primer*, Release 2.0, IBM Corp., 1993.
8. Haile, J. M., *Molecular Dynamics Simulation: Elementary Methods*, John Wiley and Sons, New York, 1992.

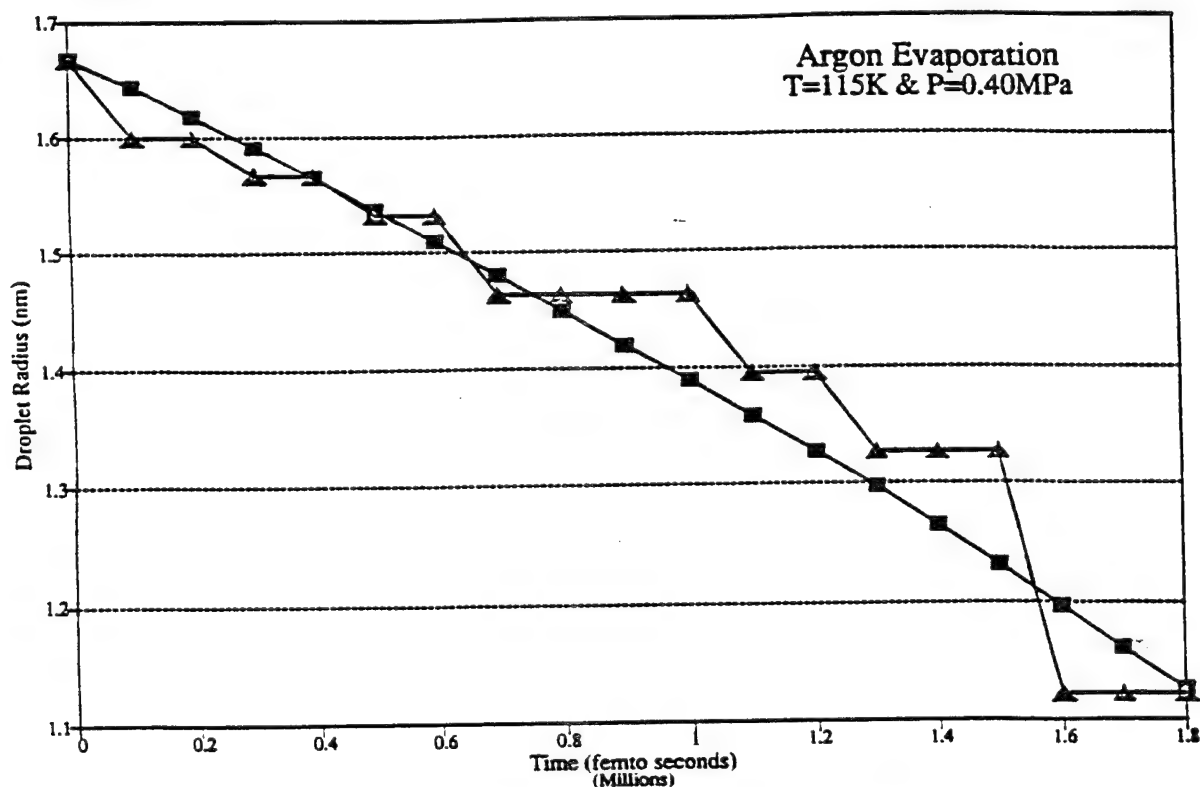


Figure 1. Evaporation rate for argon droplet into argon gas compared to theoretical rate.

(Theory = ■ and MD Simulation = ▲)

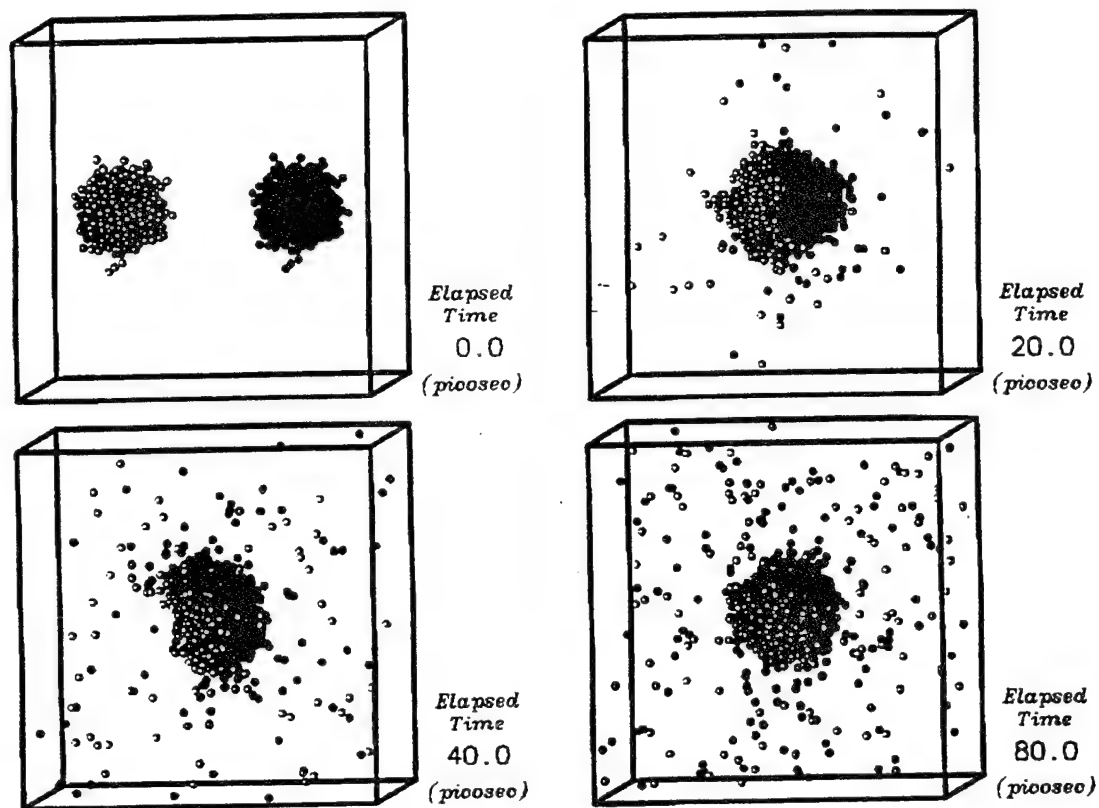


Figure 2. MD simulation of two colliding droplets with relative speed of 159 m/s.

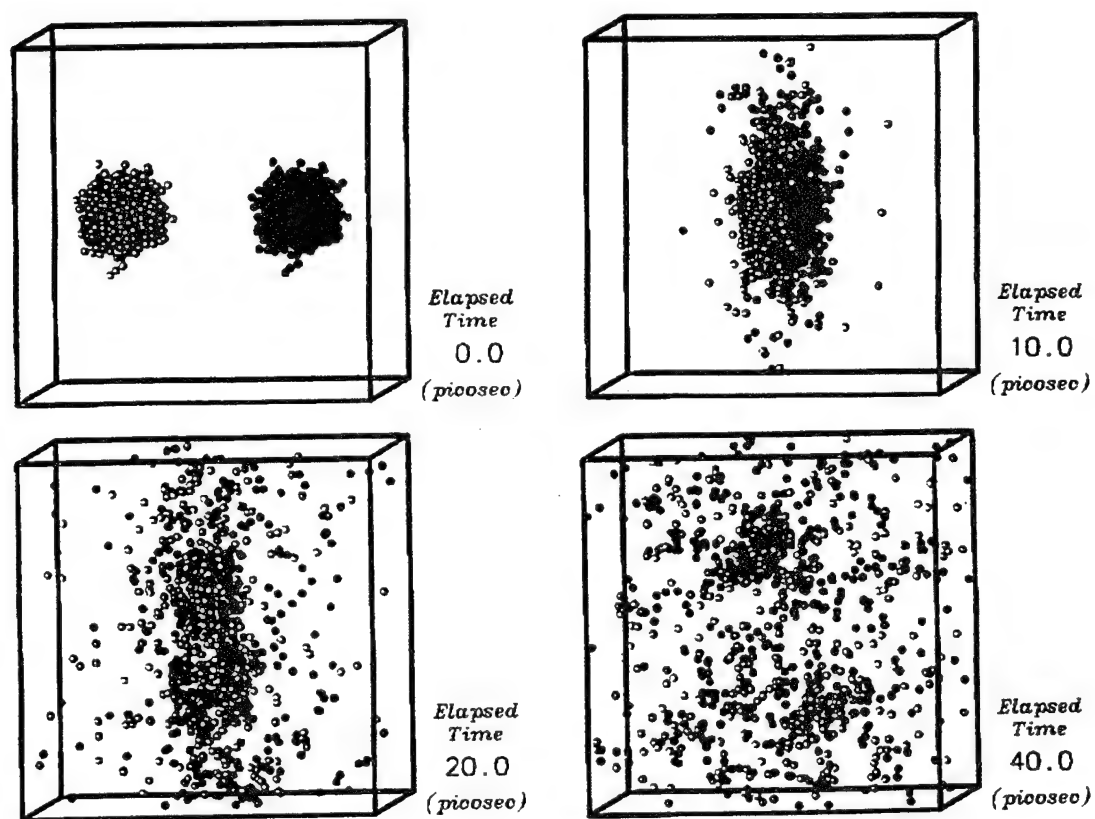


Figure 3. MD simulation of two colliding droplets with relative speed of 474 m/s.

TRANSPORT PHENOMENA AND INTERFACIAL KINETICS IN MULTIPHASE COMBUSTION SYSTEMS[†]

AFOSR Grant No. 94-1-0143



Principal Investigator: Daniel E. Rosner[‡]
High Temperature Chemical Reaction Engineering Laboratory
Department of Chemical Engineering, Yale University
New Haven, CT 06520-8286, USA

SUMMARY / OVERVIEW

The performance of ramjets burning slurry fuels (leading to oxide aerosols and deposits), and gas turbine engines in dusty atmospheres depends upon the formation and transport of small particles, often in non-isothermal combustion gas boundary layers (BLs). Even airbreathing engines burning "clean" hydrocarbon fuels can experience soot formation/deposition problems (e.g., combustor liner burnout, turbine blade erosion,...). Moreover, particle formation and transport are important in chemical reactors used to synthesize or process aerospace materials (turbine coatings, optical waveguides, ceramic precursor powders,...). Accordingly, our research is directed toward providing chemical propulsion system and aerospace materials engineers with new techniques and quantitative information on important particle- and vapor-mass transport mechanisms and rates. An interactive experimental/theoretical approach is being used to gain an understanding of performance-limiting chemical-, and mass/energy transfer-phenomena at or near interfaces. This includes the development and exploitation of seeded laboratory burners (Fig. 1a), flow-reactors (Fig. 7), and new diagnostic/characterization techniques (Figs. 1b,3,4). Resulting experimental data (Figs. 2,3,8), together with the predictions of asymptotic theories (Fig.8), are then used to propose and verify simple viewpoints and rational engineering correlations for future design/optimization.

TECHNICAL DISCUSSION / RECENT RESEARCH PROGRESS

Most of our results obtained under Grant AFOSR 94-0143 during 6/94-6/95[†] can be divided into the subsections below:

2.1. SEEDED LAMINAR COUNTERFLOW DIFFUSION FLAME EXPERIMENTS: FORMATION, COAGULATION, TRANSPORT AND STABILITY OF COMBUSTION-GENERATED PARTICLES

Based on our recent measurements of the *thermophoretic diffusivity* of flame-generated submicron "soot" particles using a $\text{TiCl}_4(\text{g})$ -seeded low strain-rate counterflow laminar diffusion flame (CDF-) technique (Gomez and Rosner, 1993) we showed that a knowledge of the relative positions of the gas and particle phase stagnation planes and the associated local chemical environments, can be used to control the composition and morphology of flame-synthesized particles. These factors will also influence particle production and *radiation* from *turbulent* non-premixed "sooting" flames.

To obtain fundamental information on the nucleation, coagulation, growth and restructuring kinetics of flame-generated aggregates, during this past year we have exploited an improved "slot-type" burner (Fig.1a) seeded with the $\text{Al}_2\text{O}_3(\text{s})$ vapor precursor trimethyl aluminum (TMA) to carry out *in situ* measurements of primary particle nucleation, aggregate formation/dynamics and morphology evolution. For the latter we use the morphology-insensitive *thermophoretic sampling* technique (Rosner, Mackowski and Garcia-Ybarra, 1991) with carbon film-coated copper grids to extract aggregates from various positions in the seeded-CDF for analysis using transmission electron microscope (TEM-)images (Figs. 1b,4). Computer analysis of projected images of aggregates yields nanometer range primary particle diameters, number (N) of primary particles in aggregates, and aggregate geometric and fractal dimension (D_f). Laser light scattering measurements are also being carried out (Fig. 3) to obtain the CDF local number density of condensed alumina based on the Rayleigh-Debye-Gans approximation for fractal aggregates. Corresponding local gas temperatures (Fig.2) are measured using a thermocouple in CDFs with flame temperatures (*ca.* 2000K) high enough to cause the sintering of $\text{Al}_2\text{O}_3(\text{s})$

[†] AFOSR Contractors' Mtg : Airbreathing Combustion/Propulsion-Diagnostics, June 13,14, 1995, Ann Arbor MI

[‡] For research collaborators consult REFERENCES

aggregates formed further upstream from the flame (Fig.1b). The associated changes in projected areas of aggregates as a function of position within the CDF are shown in Fig. 4. Our immediate goal is to understand, and ultimately be able to predict reliably (see Section 2.2), how changes in seed level, flame stoichiometry and strain rate influence the nature of the particles formed in this class of well-defined *laminar* mixing/reaction zones, and to assess the relevance of this information to particle-producing *turbulent* non-premixed reactors.

2.2 THEORY OF TRANSPORT AND RESTRUCTURING PROPERTIES OF FLAME-GENERATED AGGREGATES

The ability to reliably predict the transport properties and morphological stability of *aggregated* flame-generated *particles* (carbonaceous soot, Al_2O_3 , SiO_2 ,...) is important to many technologies, including chemical propulsion and refractory materials fabrication. Needed are methods to anticipate coagulation and ultimate deposition rates of suspended populations of such particles in combustion systems. Toward this end we are developing efficient methods for predicting the transport properties of large 'fractal' aggregates *via* a spatially variable, effective porosity pseudo-continuum model (see, *eg.*, Rosner and Tandon, 1994, and Tandon and Rosner, 1995). Since "young" small aggregates are frequently "stringy" (fractal dimensions much less than 2) we are also introducing an aggregate statistical characterization based on the *pdf* of angles between triplets of primary particles, and developing methods to predict the evolution of such *pdfs* due to the *restructuring* mechanisms of Brownian motion, surface energy driven viscous flow (Tandon and Rosner, 1995), and/or capillary-condensation (Cohen and Rosner, 1993, 1994). Indeed, these factors determine the observed size of the apparent "primary" particles comprising soot particles, the "collapse" of surface area observed in some high temperature systems (*eg.*, see Fig.1b), and the associated evolution of particle transport properties (see, *eg.*, Tandon and Rosner, 1995).

These new methods/results, together with our recent estimates of the *spread* of aggregate sizes in *coagulating* populations, are now being used to predict particle *capture rates* on solid surfaces by the mechanisms of convective-diffusion, turbulent eddy-impaction, and thermophoresis (Rosner, Tassopoulos and Tandon, 1993, 1994). Also under development are methods to predict interactions between aggregates and their surrounding *vapor* environment---interactions which can lead to primary particle growth, or (for carbonaceous soot in the presence of oxidizing species) burn-out. Toward this end, we have also developed new and efficient methods to predict the "accessible surface area" of populations of aggregates (Rosner and Tandon, 1994), including its dependence on mean aggregate size (\bar{N}), probing molecule reaction probability α , and pressure level for aggregates of a prescribed structure (D_f). We have also developed convenient pseudo-continuum methods to predict the *total sintering time* for large fractal aggregates (Fig. 5, after Tandon and Rosner, 1995), as well as *transport property evolution* during restructuring by sintering.

We are now carrying out theoretical studies on the structure of thin reaction-nucleation-coagulation 'sublayers' within laminar mixing- and boundary- layers, including stagnation flows similar to those achieved in our counterflow burner (Fig. 1a) and CVD-impingement flow reactor (Fig. 7). An account of our recent studies of the *unusual population dynamics* of coagulating absorbing-emitting particles in strong *radiation fields* will be found in *Aerosol Sci. Tech.* (Mackowski *et.al.*, 1994). For an earlier overview of our work on these effects (energy transfer on particle dynamics), see our *IEC-Research* paper: Rosner, *et. al.*, 1992.

2.3 EROSION BEHAVIOR OF CERAMIC OR METAL TARGETS IN HIGH-SPEED ABRASIVE STREAMS

By capturing with simple formulae the essential features of available *erosion yield* experiments (carried out using planar targets with suspended particles of a single size), we have developed an efficient method to predict local and total surface *erosion rates* for metal or ceramic targets of simple geometry exposed to a 'polydispersed' population of abrasive particles suspended in a high-speed mainstream (Rosner, Tandon and Labowsky, 1995, Kho, Rosner and Tandon, 1995, Khalil and Rosner, 1995). For a circular cylinder target over the entire Stokes number range 'universal' graphs have been provided covering the anticipated dimensionless parameter ranges of greatest interest. An example is provided in Fig. 6, which is a polar plot of

the *dimensionless local erosion rate* of a *metal* target over a range of values of the number-mean particle size (volume) to the 'critical' size required to impact under the prevailing conditions. Based on our summary of available experimental data, we also provide representative sets of numerical values of the key phenomenological erosion yield parameters that emerge from our formulation, albeit at $T_w \approx 300\text{K}$. To deal with more general, or 'singular' cases of particular interest to the reader, the required correlation formulae and associated quadrature expressions have been provided (Rosner, Tandon and Labowsky, 1995, Kho, Rosner and Tandon, 1995, Khalil and Rosner, 1995).

Among other things, the present model and our results make it clear that erosion rates will be directly proportional to the abrasive particle mass loading in the mainstream, and quite sensitive to mainstream velocity; viz.: even more sensitive than U^{n+1} (where, for metals, often, $n \approx 2.5$) at intermediate Stokes numbers. Our present results also explain why initially 'blunt'-nosed *metal* objects tend to become 'wedge-shaped' (sharpened) as a result of erosion (*cf.* Fig 6 in the vicinity of the forward stagnation line; Rosner, Tandon and Labowsky, 1995), whereas blunt *ceramic* objects tend to become still blunter (Khalil and Rosner, 1995).

2.4 FORMATION KINETICS AND MORPHOLOGY OF CVD-MATERIALS: THEORY OF MULTI-PHASE BOUNDARY LAYERS WITH NUCLEATION, GROWTH AND THERMOPHORESIS

A small impinging jet (stagnation flow) reactor (Fig. 7) has been developed at Yale and used to study the chemical vapor deposition (CVD-) rates of refractory layers on inductively (over-)heated substrates in the presence of complicating homogeneous reactions of the vapor precursor (Collins, 1994). These measurements are being used to understand deposition rates and associated deposit microstructures observed in highly non-isothermal, often particle-containing local CVD environments. Figure 8 shows (logarithmic ordinate) our apparent deposition probability, ϵ , vs. reciprocal surface temperature for $\text{TiO}_2(\text{s})$ films obtained from $\text{TTIP}(\text{g})$ over the broad surface temperature range: 600-1600K. An asymptotic mathematical model incorporating finite-rate reagent depletion near the hot surface (Castillo and Rosner, 1995) captures the experimentally observed deposition rate trends (Fig. 8; curve marked $\text{Dam}_{\text{hom}} = A_{\text{hom}} \delta^2/D = 2.0 \times 10^{14}$). A more detailed mathematical/numerical model (Tandon, 1995) tracks the size distributions of nucleated particles within such BLs, including the particle+vapor "co-deposition" rate at the surface $y=0$, and the associated *surface roughness*.

Missing from previous predictions of film deposition rates has been essential information about *deposit microstructure* and ancillary thermophysical properties. Toward this end we have developed a rational correlation of vapor *deposit grain densities* based on the notion that close-packed dense deposits should be possible only when the characteristic time for adatom(molecule) *surface diffusion* is short compared to the time for *surface reaction* and "burial". Our preliminary results are encouraging (Kho, Collins and Rosner, 1995) and the addition of further relevant characteristic times to this scheme may open the door to the correlation/'anticipation' of other important deposit characteristics.

CONCLUSIONS, FUTURE RESEARCH

In our 1994-1995 AFOSR-sponsored Yale HTCRL Lab research (briefly described above, and in greater detail in the archival references cited and updated below) we have shown that new methods for rapidly measuring vapor- and particle-mass transfer rates, combined with advances in multiphase transport theory, provide useful means to identify and incorporate important, often previously neglected, transport phenomena in propulsion/materials engineering design/ optimization calculations. As indicated in Section 2, we are now extending our work on transport effects involving *aggregated particles* to include their stability (with respect to high temperature *restructuring* (Fig. 1b) leading to a loss of surface area and increase in mobility). For this purpose an improved CDF burner has been employed (Fig. 1a), along with supplementary optical (Fig. 3) and thermophoretic sampling/TEM diagnostics (Figs. 1b,4). These techniques, together with closely coupled theoretical calculations of particle birth/dynamics in mixing/boundary layers, are leading to a valuable understanding of combustion-generated ultra-fine particles and films (including their deposition or *erosion* characteristics (Rosner and Tandon, 1994, Kho, Rosner and Tandon, 1994), Khalil and Rosner (1995)).

REFERENCES

- Albagli, D., Xing, Y. and Rosner, D.E., "Experimental Studies of the Morphology of Combustion-Generated Ultrafine Particles", (in preparation, 1995).
- Castillo, J.L., and Rosner, D.E., Role of High Activation Energy Homogeneous Chemical Reactions in Affecting CVD-Rates and Deposit Quality for Heated Surfaces", *Chemical Engineering Science* (in press, 1995)
- Cohen, R.D., and Rosner, D.E., "Kinetics of Restructuring of Large Multi-Particle Aggregates", in prep., 1995.
- Collins, J., **Effects of Homogeneous Reaction on the Chemical Vapor Deposition of Titanium Dioxide**, Yale University Graduate School, PhD Dissertation, May, 1994
- Collins, J. and Rosner, D.E., "Deposition Rates and Deposit Quality for Heated Surface CVD in the Presence of Simultaneous Homogeneous Reaction: Deposition of TiO_2 Films from TTIP", in prep. for *J. Electrochem. Soc.* (1995)
- Gomez, A., and Rosner, D.E., "Thermophoretic Effects on Particles in Counterflow Laminar Diffusion Flames", *Combust. Sci. and Tech.* **89**, 335-362 (1993).
- Khalil, Y.F., and Rosner, D.E., "Erosion Rate Prediction Technique for Ceramic Surfaces Exposed to High Speed Flows of Abrasive Suspensions", *J. Amer. Ceramic Soc.*, submitted March 1995)
- Kho, T., Collins, J. and Rosner, D.E., "Development, Preliminary Testing and Future Applications of a Rational Correlation for the Grain Densities of Vapor-Deposited Materials", *J. Materials Science*, in press, 1995
- Kho, T., Rosner, D.E. and Tandon, P., "Simplified Erosion Rate Prediction Technique for Cylindrical Targets in the Crossflow of Abrasive 'Polydispersed' Suspensions", *ASME-J. Propulsion Power* (submitted, 1994)
- Konstandopoulos, A.G. and Rosner, D.E., "Inertial Effects on Thermophoretic Transport of Small Particles to Walls With Streamwise Curvature---I. Experiment, II. Theory", *Int. J. Heat Mass Transfer* (in press 1995).
- Koylu, U., Tandon, P. Xing, Y., and Rosner, D.E., Experimental and Theoretical Studies of the Structure of Inorganic Particle-Producing Seeded Laminar Counterflow Diffusion Flames", *AIChE 1995 Mtg.*, Miami Beach FL, November 1995
- Mackowski, D.W., Tassopoulos, M. and Rosner, D.E., "Effect of Radiative Heat Transfer on the Coagulation Dynamics of Combustion-Generated Particles", *Aerosol Sci. Technol (AAAR)* **20**, 83-99 (1994).
- Rosner, D.E., **Transport Processes in Chemically Reacting Flow Systems**, Butterworth-Heinemann (Stoneham MA), 3d Printing (1990) sold out; for 4th printing contact author directly.
- Rosner, D.E., Cohen, R.D. and Tandon, P., "Development of Pseudo-Continuum Theories of the Restructuring Kinetics of Large (Multi-Particle) Aggregates in Combustion Systems", presented at **AAAR 1993 Annual Mtg.**, Oak Brook, IL (Oct. 11-15, 1993).
- Rosner, D.E., Collins, J. and Castillo, J.L., "Onset Conditions for Gas Phase Reactions and Particle Nucleation/Growth in CVD Boundary Layers", *Proc. 12th International Conference on CVD*, Electrochem. Soc., Proc. Vol. **93-2**, 1993, pp. 41-47
- Rosner, D.E., Konstandopoulos, A.G., Tassopoulos, M., and Mackowski, D.W., "Deposition Dynamics of Combustion-Generated Particles: Summary of Recent Studies of Particle Transport Mechanisms, Capture Rates, and Resulting Deposit Microstructure/Properties", *Proc. Engineering Foundation/ASME Conference: Inorganic Transformations and Ash Deposition During Combustion*, ASME/Engineering Fdn. pp585-606 (1992).
- Rosner, D.E., Mackowski, D.W. and Garcia-Ybarra, P., "Size and Structure-Insensitivity of the Thermophoretic Transport of Aggregated 'Soot' Particles in Gases", *Comb. Sci & Technology* **80** (1-3), 87-101 (1991).
- Rosner, D.E., Mackowski, D.W., Tassopoulos, M., Castillo, J.L., and Garcia-Ybarra, P., "Effects of Heat Transfer on the Dynamics and Transport of Small Particles in Gases", *I&EC-Research (ACS)* **31** (3), 760-769 (1992).
- Rosner, D.E. and Tandon, P., "Prediction and Correlation of Accessible Area of Large Multi-Particle Aggregates", *AIChE J.* **40** (7) 1167-1182 (1994)
- Rosner, D.E., Tandon, P. and Labowsky, M.J., "Rapid Estimation of (Metal-)Cylinder Erosion Rates in Abrasive Dust-Laden Streams", *AIChE J.* **41** (5) (in press) (1995)
- Rosner, D.E. and Tassopoulos, M., "Deposition Rates from 'Polydispersed' Particle Populations of Arbitrary Spread", *AIChE J.* **35** (9) 1497-1508 (1989)
- Rosner, D.E., Tassopoulos, M. and Tandon, P., "Prediction/Correlation of Particle Deposition Rates From Dilute Polydispersed Flowing Suspensions, and the Nature/Properties of Resulting Deposits", **Proc. 1st Intl. Particle Technology Forum (AIChE)**, Vol.2, pp. 374-381 (1994).
- Tandon, P., and Rosner, D.E., "Translational Brownian Diffusion Coefficient of Large (Multi-particle) Suspended Aggregates", *Industrial & Engineering Chemistry* (Amer. Chem Soc.) Invited Paper to Celebrate 35th Anniv. of **Transport Phenomena** (Bird, Stewart and Lightfoot) : Submitted September 1994.
- Tandon, P., and Rosner, D.E., "Sintering Kinetics and Transport Property Evolution of Large Multi-Particle Aggregates", *Chem. Eng. Communic.* (S.K. Friedlander issue), (submitted March 1995)
- Tandon, P., **Transport Theory for Particles Generated in Combustion Environments**, PhD Dissertation, Yale U. Grad School, May 1995
- Xing, Y., Koylu, U.O., and Rosner, D.E., "Formation and Restructuring of Al_2O_3 Particles in Laminar Counterflow diffusion Flames", To be Presented at *14th AAAR Meeting*, Pittsburgh PA, Oct. 13, 1995

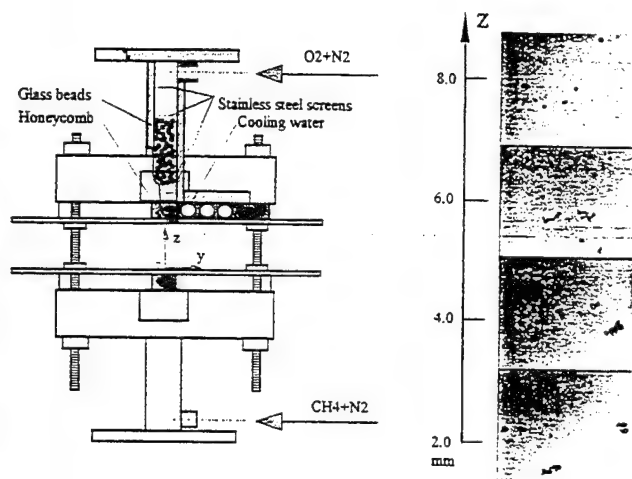


Fig. 1a "Slot"-type, water-cooled counterflow diffusion flame (CDF-) burner for *in situ* and extractive experimental studies of the nucleation, coagulation, growth, transport and restructuring of aggregates in flames (after Albagli, Xing, Koylu, and Rosner, 1995; see, also, Gomez and Rosner, 1993); 1b: TEM images of Al_2O_3 aggregates thermophoretically extracted from the CDF (at the indicated positions along the axis); after Xing, Köylü, and Rosner, 1995. (Note morphological evidence of sintering.)

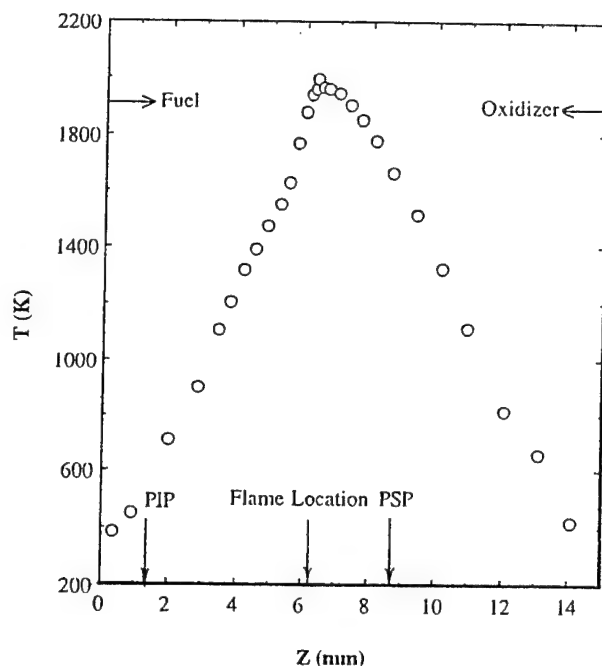


Fig. 2 Radiation-corrected thermocouple-derived axial temperature profile in laminar $\text{CH}_4/\text{O}_2/\text{N}_2$ CDF at nominal strain rate: 13 s^{-1} . Shown are locations of particle inception, peak temperature (flame), and particle stagnation plane (PSP); after Xing, Koylu, and Rosner, 1995.

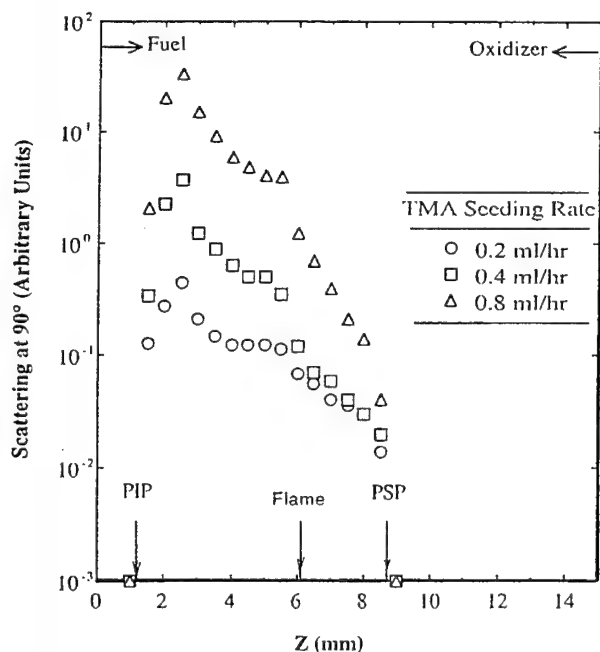


Fig. 3. Laser light scattering profiles (90°) for the TMA-seeded CDF conditions shown in Fig. 2. Data shown for 3 indicated TMA seed levels; after Xing, Köylü, and Rosner, 1995.

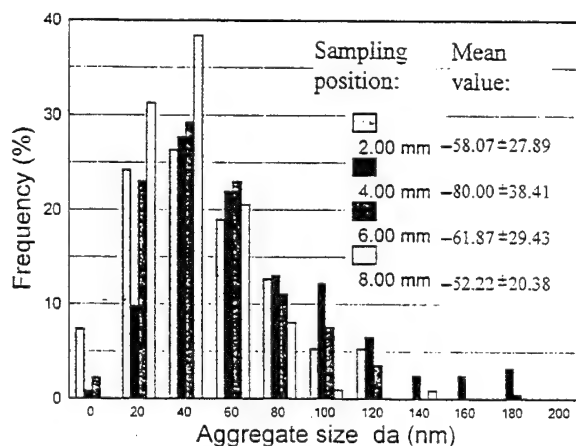


Fig. 4 Thermophoretic sampler/TEM-derived Al_2O_3 aggregate size distribution data at several positions within the $\text{CH}_4/\text{O}_2/\text{N}_2$ CDF for the flame conditions of Figs. 2,3; after Xing, Koylu, and Rosner, 1995. Indicated size is (projected) area-equivalent sphere diameter (nm).

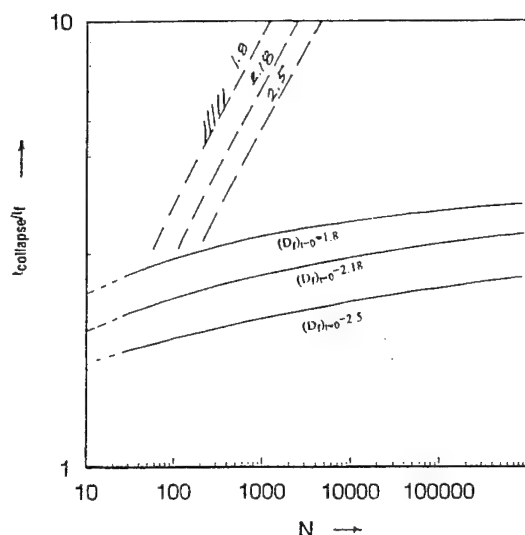


Fig. 5. Predicted total required coalescence time (in multiples of the characteristic sintering time: $\mu \cdot (R_1)_{t=0} / \sigma$) as a function of initial aggregate size, N , for three particular (initial) fractal dimensions; after Tandon and Rosner, 1995; Dashed behavior is that expected based on model of restructuring at constant fractal dimension.

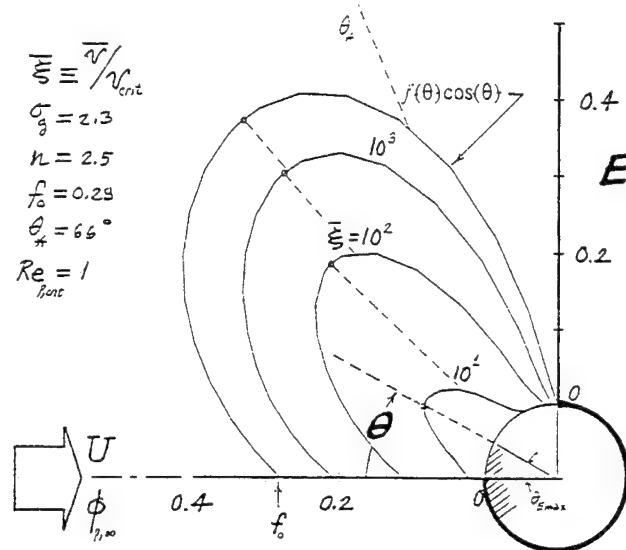


Fig. 6. Predicted angular dependence of nondimensional erosion rate on an initially circular metal cylinder in high Reynolds number crossflow (after Rosner, Tandon, and Labowsky 1994). Here $\theta^* = 66^\circ$ (incidence angle of maximum erosion yield), $f_0 = 0.28$ (ratio of erosion yield at normal incidence to that at angle θ^* , velocity exponent $n = 2.5$, and log-normal population spread, σ_g , is 2.3)

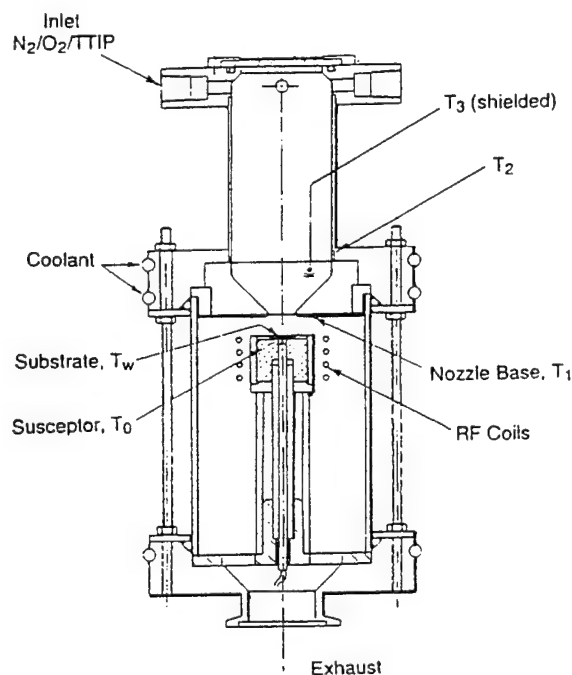


Fig. 7. Axisymmetric impinging jet CVD-flow reactor with inductively heated "pedestal" for well-defined laboratory studies of vapor + particle co-deposition across laminar BLs (after Rosner, Collins and Castillo, 1993; Collins, 1994)

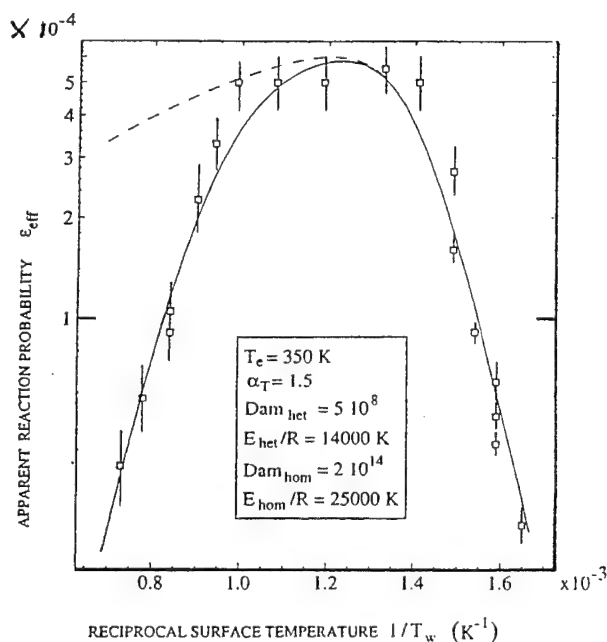


Fig. 8. $\text{TiO}_2(\text{s})$ deposition rate data (Collins, 1994) reported as apparent heterogeneous reaction probability ϵ from $\text{TTIP}/\text{O}_2/\text{N}_2$ mainstream showing calculated deposition rate behavior in presence of homogeneous reactions to form non-depositing species (solid curve: asymptotic BL theory of Castillo and Rosner, 1995)

DROPLET-TURBULENCE INTERACTIONS OVER A WIDE SPECTRAL RANGE

AFOSR Grant/Contract No. F49620-93-1-0028

PRINCIPAL INVESTIGATOR:

W.A. Sirignano

Department of Mechanical and Aerospace Engineering
University of California
Irvine, CA 92717

SUMMARY/OVERVIEW:

The research program concerns the detailed three-dimensional interactions of vortical structures with individual droplets. Initially cylindrical vortices advect past a sphere. Navier-Stokes equations describe the unsteady flow field. Finite-difference computations yield flow properties plus temporal behavior of lift, drag, and moment coefficients and Nusselt numbers. The effects of one pair of like rotating vortices are considered and correlations are obtained for the coefficients. An infinite array of vortices is also considered and droplet or particle deflections are predicted. Also the case of very large vortex-to-droplet diameter ratio is examined.

AUTHORS

W.A. Sirignano S.E. Elghobashi I. Kim M. Masoudi

TECHNICAL DISCUSSION

I. Droplet – Turbulent Interaction Over a Wide Spectral Range

A theoretical/computational analysis of the interactions of droplets with vortical structures is being conducted. Both the high-frequency domain where length scales of the vortices are comparable to droplet size and the low-frequency domain where length scales are much larger than droplet size have been analyzed. This study is leading to fundamental insights about droplet-turbulent interactions. To simulate the three-dimensional, unsteady interactions, a Navier-Stokes solver was developed. The alternating-direction-predictor-corrector scheme and a pressure correction equation are employed.

In our earlier study (JFM 1995), we examined the unsteady, three-dimensional interactions between an advected cylindrical vortex tube and a fixed spherical particle whose diameter is of the same order of magnitude as the initial diameter of the vortex. The particle Reynolds number based on the freestream velocity and the particle diameter was in the range $20 \leq Re \leq 100$. The initial size of the cylindrical vortex tube was in the range $0.25 \leq \sigma \leq 4$, where σ is the radius of the vortex tube normalized by the particle radius. We found that the maximum positive lift coefficient and the rms lift coefficient of the sphere are linearly proportional to the circulation of the vortex tube at small values of σ . However, at large values of σ , they are linearly proportional to the maximum fluctuation velocity induced by the vortex tube but independent of σ .

The above work was extended to study the interactions between a pair of advected vortex tubes and a stationary spherical particle. A counter-clockwise rotating pair of cylindrical vortex tubes were initially located ten radii upstream from the center of the sphere. The lift and moment coefficients of the sphere interacting with a pair of vortex tubes as a function of time are nearly identical, respectively, to those of the sphere interacting with a single vortex tube if the separation distance between the tube centers is less than $2\sqrt{\sigma}$ vortex tube diameter for the lift coefficient and less than $\sqrt{\sigma}$ vortex tube diameter for the moment coefficient, and the total maximum fluctuation velocity due to the vortex tubes is used in the case of a pair of vortex tubes.

Our results from a spherical particle interacting with a single vortex and with a pair of vortices can be used to estimate the trajectory of a moving spherical particle interacting with an array of vortex tubes. This extension provides a better simulation of a droplet in a turbulent flow. A spherical particle is injected into an array with an infinite number of counter-clockwise rotating vortices which are located on the negative X-axis and are separated from one another by the nondimensional distance 24. The particle trajectory as a function of time is computed by solving a system of two ordinary differential equations that are the nondimensional form of the Newton's equation of motion in the X and Y directions. The gravity force is neglected in this formulation.

Figure 1 shows the trajectories of the sphere during the dimensionless time period between 0 and 24 for initial particle Reynolds numbers 100 and 50 with particle-to-fluid density ratio 200. The initial vortex size is three times larger than that of the sphere, and the initial offset distance of the sphere is zero. The initial maximum fluctuation velocity of the vortex is 0.4 normalized by the initial sphere velocity. The sphere initially moves upward due to the upwash of the vortex and then moves downward due to the downwash. The maximum positive deflection for the case of $Re_o = 50$ is higher than that of $Re_o = 100$.

Figure 2 shows two trajectories of the sphere which are traced from the initial injection until particle Reynolds number reaches one for initial particle Reynolds numbers 100 and 50 with the same initial parameters as in Figure 1. A counter-clockwise rotating vortex tube produces not only upwash downstream of itself and downwash upstream of itself but it also causes a shear flow across the sphere when it passes the sphere. The combined effect of the downwash and the shear flow causes the magnitude of the maximum negative lift to be greater than the magnitude of the maximum positive lift. Therefore, the average lift coefficient averaged over the time span 24 (the interaction time with the vortex) is small but negative due to the shear flow effect. This small negative value of the average lift coefficient becomes important when the sphere interacts with an array of many vortices. Thus, the sphere travels upward only for the short initial time period and then moves downward for the most of the time until it stops. The final deflection ratios defined by $|Y_f/X_f|$ are 1/27 for the case of $Re_o = 100$ and 1/23 for the case of $Re_o = 50$. However, the final deflection for the case of $Re_o = 100$ is higher than that of $Re_o = 50$, because the sphere for the case of $Re_o = 100$ possesses higher initial momentum and it travels farther than the sphere with $Re_o = 50$.

So far, we examined the trajectory of a spherical particle interacting with an array of vortices whose sizes are in the Kolmogorov length scale range and are comparable to the sphere size. In order to understand completely a particle (or droplet) motion in a turbulent field, we must investigate the motion of a particle interacting with a vortex with large (integral) length scale which is in the opposite end of the spectrum to the previous case. In the following paragraphs, we discuss the motion of a spherical particle interacting with a large vortex.

Initially, a spherical particle is injected into a counter-clockwise rotating large vortex which is

located at the origin of the coordinates. The upstream flow boundary conditions relative to the sphere are obtained by superimposing the sphere velocity and the induced velocity due to the vortex tube at the location of the sphere, and the pressure field due to the vortex tube at the location of the sphere is imposed as the pressure boundary condition at the computational outer boundary relative to the sphere.

Figure 3 shows two trajectories of the sphere traced from the initial location $X = 300$ to $X = -300$ for initial Reynolds numbers 100 and 50 with density ratio 200. The half circle in Figure 4 represents the large vortex tube. The initial vortex size is 200 times that of the sphere, and the initial offset distance of the sphere is zero. The initial maximum fluctuation velocity of the vortex is 0.4 normalized by the initial sphere velocity. The sphere initially moves upward due to the upwash of the vortex and then moves downward due to the downwash of the vortex. The maximum deflection for the case of $Re_o = 50$ is higher than that of $Re_o = 100$. The maximum deflection rates are $1/6$ for the case of $Re_o = 100$ and $1/3.4$ for the case of $Re_o = 50$. These deflection rates are much larger than those from the case of an array of small vortices for the same maximum fluctuation velocity. Furthermore, we know that a vortex with the integral scale size produces higher fluctuation velocity than does a small vortex.

As expected, it is found that the large vortex causes larger deflection of the particle than does an array of small vortices. Also, the preliminary run for the large vortex showed that our formulation and computer code produce reasonable and believable solutions. We are now in the production stage and will investigate the particle deflection as a function of initial Reynolds number, vortex size, density ratio, and maximum fluctuation velocity.

II. The Temperature Field and Vaporization

There is an ongoing parallel study focusing on enhancement of heat transfer and vaporization of the liquid droplet due to small-scale turbulence. To gain confidence in the code employed, we calculated droplet Nusselt number for an axisymmetric flow and thus successfully benchmarked our code against published literature.

Following that, we have since then included the advecting cylindrical vortex tube in the simulation and, analogous to our parallel fluid dynamics study, traced the changes in the temperature field due to four parameters: the vortex upstream offset distance (d_{off}), flow field maximum velocity fluctuations represented by the vortex initial maximum radial velocity (v_{max}), vortex initial radius (σ), and the flow field Reynolds number (Re).

Variations in the droplet Nusselt number due to the first three parameters have been determined. The influence of flow field Reynolds number on vortex interaction with the droplet heat transfer is currently under study. Next, we will attempt to find correlations between the observed changes and the four parameters involved. It has been observed that the droplet temperature field could be appreciably affected due to its collision with the vortex tube. Preliminary calculations have shown that under 'favorable' initial conditions of the vortex, the droplet Nusselt number can change, e.g. due to the parameter (d_{off}), by up to 9% through its interaction with the vortex. This is shown in Figure 4. A compound effect of parameters is yet to be studied. Also, we anticipate that, when subsequently we model the domain using an initially stratified temperature field (as opposed to a currently initially uniform temperature field), more profound variations in the droplet Nusselt number will be observed due to the advecting vortex.

Our investigation has also revealed that these increased values of Nusselt number are a consequence of the modification of the near field flow configuration; the advecting vortex induces a

secondary vortical perturbation in the sphere wake which changes orientation depending on the location of the parent vortex. Future calculations will include a stratified gas; in such a case, larger fluctuations in Nusselt number should occur. Vaporizing droplets will also be considered.

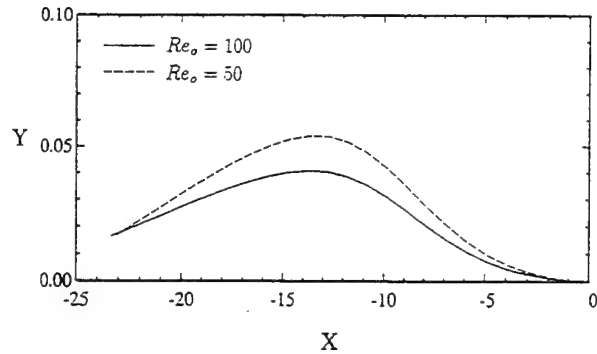


Fig. 1. Two trajectories of the sphere during the time period between 0 and 24 for initial particle Reynolds numbers 100 and 50.

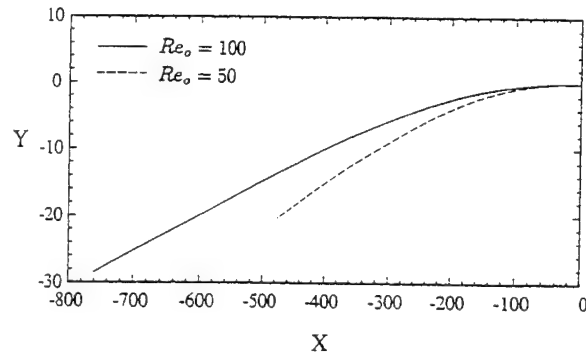


Fig. 2. Two trajectories of the sphere traced from the initial injection until particle Reynold number reaches one for initial particle Reynolds numbers 100 and 50.

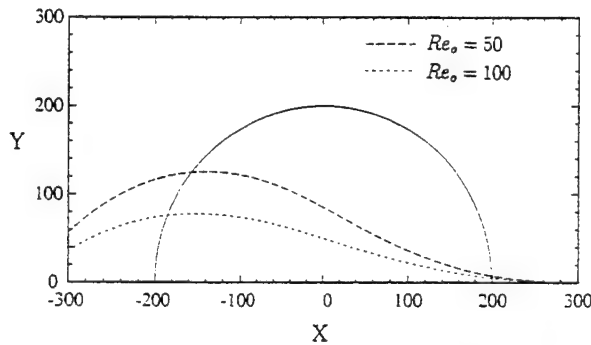


Fig. 3. Two trajectories of the sphere traced from the initial location to $X = -300$ for initial particle Reynolds numbers 50 and 100.

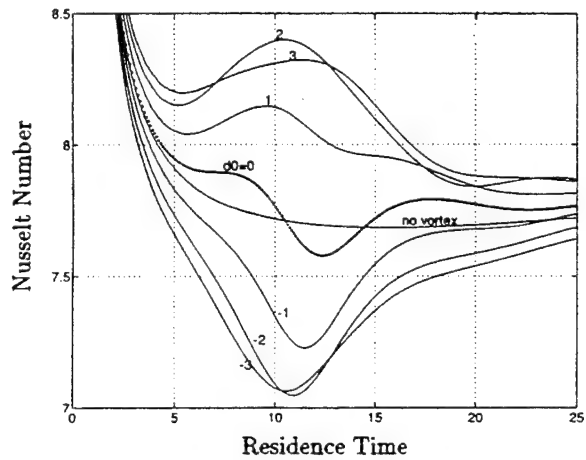


Fig. 4. Variation of the droplet Nusselt number versus the vortex initial offset distance. (This result is for $v_{max} = 0.4$, $Re = 100$, and $\sigma = 1$.)

AFOSR SPONSORED RESEARCH IN AIRBREATHING COMBUSTION

PROGRAM MANAGER: JULIAN M. TISHKOFF

AFOSR/NA

**110 Duncan Avenue, Suite B115
BOLLING AFB DC 20332-0001**

SUMMARY/OVERVIEW: The Air Force Office of Scientific Research (AFOSR) program in airbreathing combustion currently is focused on six areas of study: supersonic combustion, turbulent combustion, soot, sprays, kinetics, and supercritical fuel behavior. An assessment of major research needs in each of these areas is presented.

TECHNICAL DISCUSSION

AFOSR is the single manager for Air Force basic research, including efforts based on external proposals and in-house work at Air Force laboratories. Airbreathing combustion is assigned to the AFOSR Directorate of Aerospace and Materials Sciences along with programs in rocket and space propulsion, propulsion diagnostics, fluid and solid mechanics, and structural materials.

Interests of the AFOSR airbreathing combustion subarea are given in the SUMMARY section above. Many achievements can be cited for these interests, yet imposing fundamental research challenges remain. The objective of the program is publications in the refereed scientific literature describing significant new understanding of multiphase turbulent reacting flow. Incremental improvements to existing scientific approaches, hardware development, and computer codes fall outside the scope of this objective.

Decisions on support for research proposals are based on scientific opportunities and technology needs. In recent years two major emphases have defined the main thrusts of this research activity: issues affecting the future utilization of hydrocarbon fuels and supersonic combustion to support hypersonic airbreathing propulsion technology.

Future airbreathing propulsion systems will require fuels to absorb substantial thermal energy, raising fuel temperatures to supercritical thermodynamic conditions. Understanding and controlling fuel properties at these conditions will be crucial for avoiding thermal degradation and for optimizing subsequent processes within the combustor. Environmental concerns and the availability of petroleum supplies also will contribute to future propulsion system design and operational needs. Novel gas turbine design methodology affecting both high performance and reduced harmful emissions was chosen to be the Air Force representative subject area in a new Department of Defense

program, the Focused Research Initiative, that couples university, industry, and Government laboratory research beginning in 1995.

Designing propulsion systems that will offer reliability, maintainability and long service life represents a new motivation for propulsion research. Future budgets likely will dictate the acquisition of reduced quantities of new operational aerospace vehicles, with a corresponding increase in requirements for durability. Research topics such as soot and supercritical fuel behavior will be relevant to these new service constraints.

Beginning in fiscal year 1996 AFOSR will fund an initiative addressing integrated scramjet combustor design for hypersonic propulsion. A specific research objective related to combustion will explore the sensitivity and stability of supersonic combustion to transient behavior. Transients can be viewed in two evolutionary stages: initial random transients, for example as a consequence of a random atmospheric disturbance or a flight vehicle maneuver; and follow-on transients introduced to restore nominal combustion performance. This initiative, if successful, should provide the physicochemical basis for subsequent research to formulate dynamic scramjet combustor control methodology.

A new concept under consideration by AFOSR is the establishment of multi-investigator university research centers with links to industry and the Air Force laboratories. These centers also are intended to enhance the university-industry-Government research infrastructure.

The purpose of this abstract has been to communicate AFOSR perceptions of research trends to the university and industrial research communities. However, communication from those communities back to AFOSR also is desirable and essential for creating new research opportunities. Therefore, all proposals and inquiries for fundamental research are encouraged even if the content does not fall within the areas of emphasis described herein. Comments and criticisms of current AFOSR programs also are welcome.

NONLINEAR SPECTROSCOPY OF MULTICOMPONENT DROPLETS

(AFOSR Grant No. 94-1-0135)

Co-Principal Investigator: Richard K. Chang

Yale University
Department of Applied Physics and Center for Laser Diagnostics
New Haven, Connecticut 06520-8284

SUMMARY/OVERVIEW

In the past, we have demonstrated that nonintrusive in-situ optical diagnostics techniques have the potential to determine the chemical species and physical properties of multicomponent liquid droplets in a spray combustion. During the past year, we have been developing a technique which might be used to deduce the droplet temperature, which is an important parameter in combustion modeling. Our research is directed toward the understanding of nonlinear optical interactions occurring within individual droplets which decrease in size because of the evaporative process, which deformed in shape because of inertial effects, and which cools or heats depending on the surrounding gas temperature. One of the key objectives of the research is to extract from the nonlinear optical spectra, information pertaining to the evaporation rate of closely spaced flowing droplets, to droplet shape deformations, and, more recently, to droplet temperature. The two main research results during the past year are: (1) the observation of temperature-dependent wavelength shifts of the dye lasing spectra with a thermochromic additive;¹ (2) the demonstration that efficient pumping of the stimulated Raman scattering (SRS) of minority species can be achieved by the SRS of the majority species in a microdroplet of a binary mixture.²

TECHNICAL DISCUSSION

The spherical liquid-air interface of a droplet, with radius a much larger than the wavelength, acts as an optical cavity. The normal modes of a dielectric sphere are referred to as morphology-dependent resonances (MDRs), which occur at discrete size parameters $x_{n,\ell} = 2\pi a/\lambda_{n,\ell}$, where $(\lambda_{n,\ell})$'s are discrete wavelengths, which depends on the droplet radius a , index of refraction of the liquid, and on the droplet shape. The index n designates the MDR mode number, which is equal to 1/2 of the number of intensity maxima around the equatorial plane. The index ℓ designates the MDR radial mode order, which is the number of angle-averaged intensity maxima along the radial direction. For a perfect sphere, a MDR at $x_{n,\ell}$ is $(2n + 1)$ degenerate, i.e., the frequency of this MDR is independent of the azimuthal mode number m , which can assume values $\pm n, \pm(n - 1), \dots, 0$.

To achieve lasing, the round-trip gain must overcome the total round-trip loss. The condition for lasing at any wavelength, λ , can be written as:

$$n_1 \sigma_e(\lambda) \geq \alpha_{\text{leakage}}(\lambda) + \alpha_{\text{abs}}(\lambda, T) + n_0 \sigma_a(\lambda), \quad (1)$$

where $\sigma_e(\lambda)$ and $\sigma_a(\lambda)$ are the stimulated emission and absorption cross-section (cm^2) of the fluorescent dye. The total number of fluorescent dye molecules per unit volume is $n_T = n_0 + n_1$, where n_1 is the number density of molecules in the first excited electronic single state and n_0 is the number density of molecules in the ground electronic single state. The radiation leakage loss out of the droplet cavity is $\alpha_{\text{leakage}}(\lambda)$ and the absorption loss of a temperature-dependent absorber, a

thermochromic absorber, is $\alpha_{\text{abs}}(\lambda, T)$. If the fluorescent wavelength λ is not at a MDR wavelength, $\alpha_{\text{leakage}}(\lambda)$ is large and then lasing condition is not satisfied.

Figure 1(a) shows the absorption spectra [$\alpha_{\text{abs}}(\lambda, T)$] of the thermochromic absorber, $\text{CoCl}_2 \cdot 6\text{H}_2\text{O}$ in 85% iso-propanol and 15% water at several liquid temperatures. The CoCl_2 is the thermochromic absorber. Figure 1(b) shows the usual $\sigma_e(\lambda)$ and $\sigma_a(\lambda)$ of Rhodamine B in ethanol. The Rhodamine B is the lasing dye known to have a large wavelength separation between the $\sigma_e(\lambda)$ peak and the $\sigma_a(\lambda)$ peak, commonly referred to as having a large Franck-Condon shift. Both the thermochromic absorber and the lasing dye are placed in the liquid droplet, consisting mainly of 85% iso-propanol and 15% water.

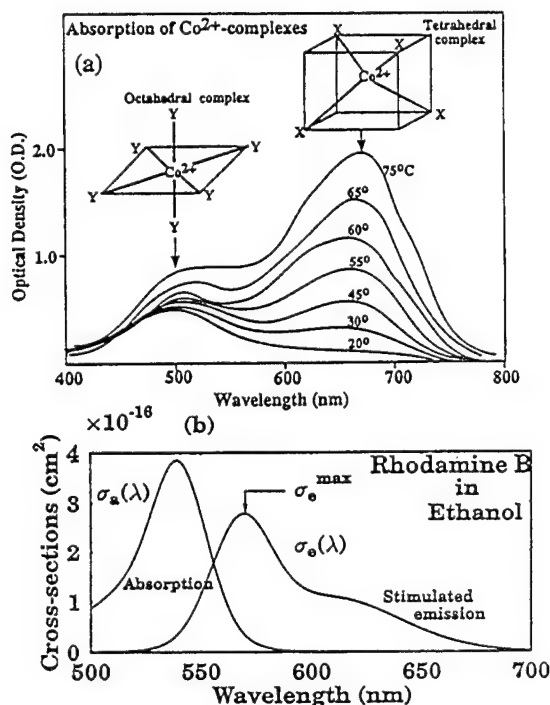


Figure 1

(a) The schematic of the thermochromic absorption spectra of $\text{CoCl}_2 \cdot 6\text{H}_2\text{O}$ in a solution of 85% iso-propanol and 15% water. The inset shows the octahedral and tetrahedral configurations which are responsible for the absorption bands of the Co^{2+} complexes. (b) The absorption $\sigma_a(\lambda)$ and the stimulated emission spectrum $\sigma_e(\lambda)$ of Rhodamine B in ethanol.

The mechanism responsible for the temperature-dependent absorption change in $\text{CoCl}_2 \cdot 6\text{H}_2\text{O}$ is known to be related to the temperature-dependent configuration change in the Co^{2+} complexes in the presence of Cl^- ions and H_2O molecules. In an octahedral configuration of six identical ligands, the electronic transition of Co^{2+} is parity forbidden, because of inversion symmetry associated with the octahedral configuration. In the $\text{CoCl}_2 \cdot 6\text{H}_2\text{O}$ solution, the absorption around 500 nm is not completely forbidden, because strict octahedral symmetry is not maintained as the six ligands are not all identical at all times. In a tetrahedral configuration of four identical ligands, the electronic transitions of Co^{2+} is electric dipole allowed. The tetrahedral complex can be mono-, di-, or tri-chloro complexes.

The temperature-dependent configurational change in the complexes can be described by the following type of reactions:



In the $\text{CoCl}_2 \cdot 6\text{H}_2\text{O}$ solution, the absorption around 650 nm increases with temperature because there are more tetrahedral configurations formed as the temperature is raised. The addition of heat decreases the octahedral symmetry by increasing the vibration of the ligand molecules and by replacing a few H_2O molecules by iso-propanol. Thereby, the dipole transition and the absorption at 500 nm is more allowed even though there are fewer octahedral sites at increasingly higher temperatures.

Figure 2 shows the lasing and fluorescence spectra of a single droplet as the vibrating orifice temperature (T_{orifice}) is changed from 21 °C to 92 °C. The series of peaks in the spectra correspond to the cavity resonances of the droplet. Note that as the T_{orifice} increases, the lasing band shift to the blue. The dye lasing wavelength shifts to the blue because of the increased absorption around 650 nm associated with the thermochromic absorber as the T_{orifice} is raised. Similar blue shift in the lasing spectra of Rhodamine B dye has been observed when we increased concentration and, thereby the absorption of a temperature-independent absorber, nigrosin.³

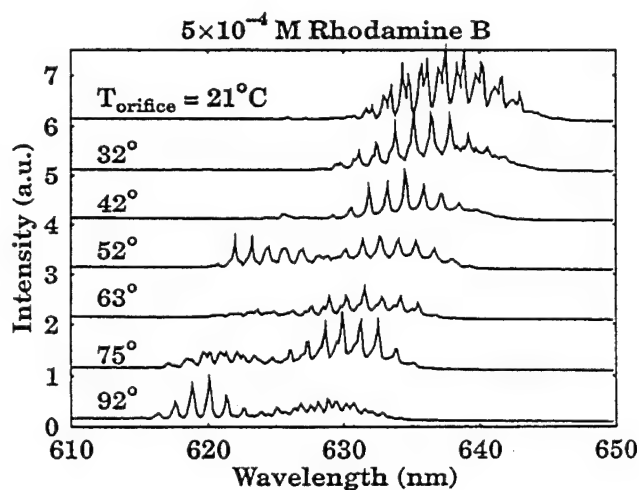


Figure 2

Lasing spectra from microdroplets (with radius $\sim 35 \mu\text{m}$) with 5×10^{-9} M Rhodamine B in 0.1 M $\text{CoCl}_2 \cdot 6\text{H}_2\text{O}$ solution of 85% iso-propanol and 15% water at $T_{\text{orifice}} = 21, 32, 42, 52, 63, 75$ and 95 °C, respectively. The pump laser power is fixed at $\sim 10 \text{ MW/cm}^2$.

Figure 3 shows the red-end portion of the lasing spectra shown in Fig. 2. The wavelength λ_{trans} marks the intensity transition of lasing (as indicated by a sharp rise) from fluorescence (as shown with a gradual decrease with wavelength). Attempts are being made to deduce the droplet temperature from the temperature dependence of λ_{trans} .

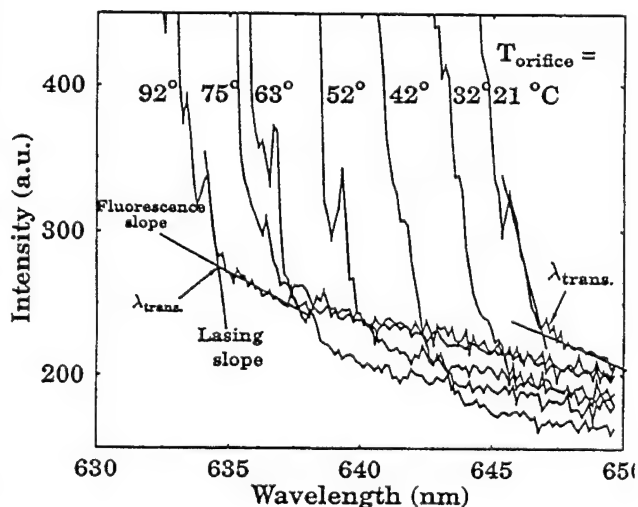


Figure 3

The long wavelength portion of each measured lasing spectrum in Fig. 2 is expanded in order to determine the transition wavelength λ_{trans} between lasing and fluorescence in the microdroplets.

We continued our research efforts in the area of stimulated Raman scattering (SRS) of minority species in the multicomponent fuel droplet, in an attempt to use the SRS as a means of identifying the minority species as well as their concentration. We have observed that in a binary mixture droplet, the SRS from the highest-gain mode of the majority species pumps the SRS from the minority species more efficiently than does the input laser.² The spatial overlap between the pumping field and the SRS field is an important factor in determining the pumping efficiency. We have numerically studied the effect of the spatial overlap on SRS pumping.

REFERENCES

1. Md. Mohiuddin Mazumder, Gang Chen, Peter J. Kindlmann, R. K. Chang, and James B. Gillespie, "Temperature-dependent Wavelength Shifts of Dye Lasing in Microdroplets with a Thermochromic Additive," (Submitted to Optics Letters).
2. Md. Mohiuddin Mazumder, Karl Schaschek, Richard K. Chang, and James B. Gillespie, "Efficient Pumping of Minority Species Stimulated Raman Scattering (SRS) by Majority Species SRS in a Microdroplet of a Binary Mixture," Chemical Physics Letters, (To be published).
3. Md. Mohiuddin Mazumder, Gang Chen, Richard K. Chang, James B. Gillespie, "Wavelength Shifts of Dye Lasing in Microdroplets: Effect of Absorption Change", Opt. Lett. 20, 287 (1995).

ADVANCED DIAGNOSTICS FOR REACTING FLOWS

AFOSR 95-1-0041

Principal Investigator: Ronald K. Hanson

High Temperature Gasdynamics Laboratory
Mechanical Engineering Department
Stanford University, Stanford, CA

SUMMARY/OVERVIEW:

This research is aimed at establishing advanced laser-based techniques for nonintrusive measurements in reacting gases and plasmas, with emphasis on high speed, high temperature, and high pressure propulsion flowfields. The primary flowfield quantities of interest are species concentrations, temperature, pressure, mass and electron densities, velocity, and quantities derivable from these primary parameters. Principal techniques studied in the past year include laser absorption, planar laser-induced fluorescence (PLIF) and degenerate four-wave mixing.

TECHNICAL DISCUSSION

In the following paragraphs we highlight primary activities of the past year. A list of related publications/presentations is given at the end of this abstract.

Diode Laser Absorption Diagnostic for High-Enthalpy Air

Gases at high temperatures can have significant populations in excited electronic states, thereby suggesting the use of either laser absorption or laser-induced fluorescence to monitor gaseous properties through detection of the strong and optically accessible electronic transitions which occur between these states. During the past year we extended our effort to detect atomic oxygen and nitrogen at temperatures in the range 6000K to 13,000K. Experiments were conducted behind reflected shock waves using fixed-wavelength and scanned-wavelength strategies with diode laser sources operating at 772 nm (for O) and 822 (for N). The scanned-wavelength measurements enable rapid determination of kinetic temperature and, in some instances, electron density and static pressure. The fixed-wavelength measurements provide data on the continuous time-history of excited-state densities as the shock-heated gas undergoes dissociation, electronic excitation and ionization; such data will facilitate development of kinetic models for the nonequilibrium behavior of air in hypersonic flows.

Plasma Diagnostics

We are continuing work on the development of diagnostic techniques for xenon plasmas using cw semiconductor diode lasers (AlGaAs). The techniques are based on a thorough understanding of the dependence of spectrally resolved absorption lineshapes on plasma parameters. As a rare gas with low ionization potential and high molecular weight, xenon is the logical propellant in ion thrusters. Non-intrusive measurements of parameters in the exhausts of these satellite electric propulsion devices are needed to further the understanding of their operation.

Single-point laser-induced fluorescence is used to obtain the lineshapes as it offers the high spatial resolution required to probe nonuniform plasma environments. The high temperatures involved allow the more accessible excited electronic quantum states to be probed. Measurements of two lines have been made in a low pressure dc discharge. The 6s-6p transition at 823 nm has been used to measure kinetic **temperature** as its lineshape is predominantly broadened by the

Doppler effect. A sample trace is shown in Fig. 1. The spectra obtained are complicated by xenon's hyperfine splitting. Xenon has nine stable isotopes (3 with abundances greater than 20%) and two of these isotopes are further split by nuclear spin effects. The resulting 21 individual spectral features that convolve to form the measured 823 nm lineshape are included in the figure. This structure must be taken into account to model the fluorescence lineshape. A second 6s-6p transition at 828 nm, composed of 12 individual features, has also been probed by LIF. The width of its lineshape is largely affected by resonance broadening, which is a specific type of collisional effect that is dependent on the **pressure** of the probed environment. Resonance broadening is important for transitions involving metastable states and is of fundamental interest for xenon as it has not yet been studied in the heavy inert gases. The diode laser's narrow linewidth enables measurement of these hyperfine-split lineshapes with sufficient resolution to determine plasma temperature from the 823 nm transition and pressure from the 828 nm transition.

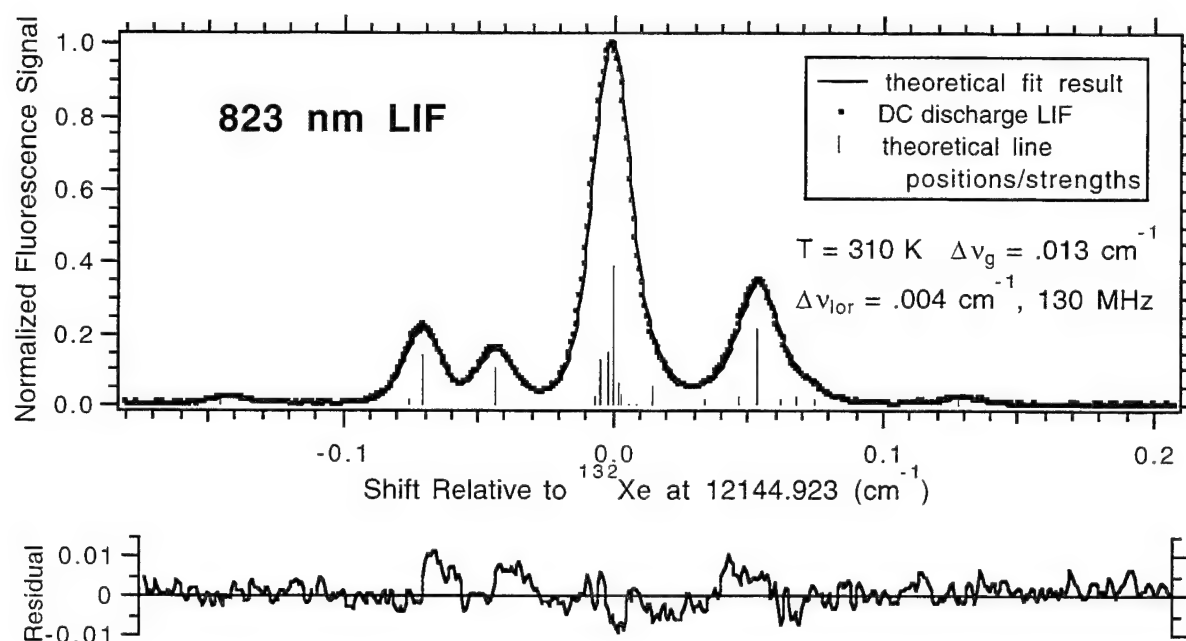


Figure 1. Comparison of measured xenon LIF $6s[3/2]O_2-6p[3/2]_2$ spectrum to calculated fit result.

Multiplexed Diode Laser Absorption

We have made significant progress in the development of multiplexed diode-laser sensors for measurement of multiple gasdynamic parameters along a common path. A multiplexed sensor system, composed of multiple diode lasers and fiber-optic splitters and couplers, is capable of monitoring several wavelength regions simultaneously using both scanned- and fixed-wavelength laser-absorption spectroscopy techniques. The sensors have been used to sensitively measure temperature, H_2O and O_2 in high-speed flows, flames, arcjets, and static cells. We are currently characterizing diode lasers to probe absorption transitions in the spectral regions near 1650 nm, 670 nm and 430 nm associated with vibrational and electronic transitions of hydrocarbon and NO_x species.

Figure 2 (left side) schematically illustrates the setup used to record multiple gasdynamic parameters along a single path. In the scanned-wavelength method, two InGaAsP lasers were current tuned at a 2-kHz rate across H_2O vibrational transitions near 1343 nm and 1392 nm. Gas temperature was determined from the ratio of single-sweep integrated line intensities. Species mole

fraction was calculated from the measured line intensity. In the fixed-wavelength method, the wavelength of each laser was fixed near the peak of an absorption feature. Gas temperatures were inferred at a 1-MHz rate from the ratio of measured peak line intensities. The right side of Figure 2 compares temperature measurements recorded in the post-flame gases of a premixed $\text{H}_2\text{-O}_2$ flame and a heated cell. The excellent agreement between the laser-based measurements obtained using scanned- and fixed-wavelength methods with those recorded with thermocouples demonstrates the effectiveness of the multiplexed diode-laser sensor system and the potential for rapid, continuous measurements of gasdynamic parameters in flows with difficult optical access.

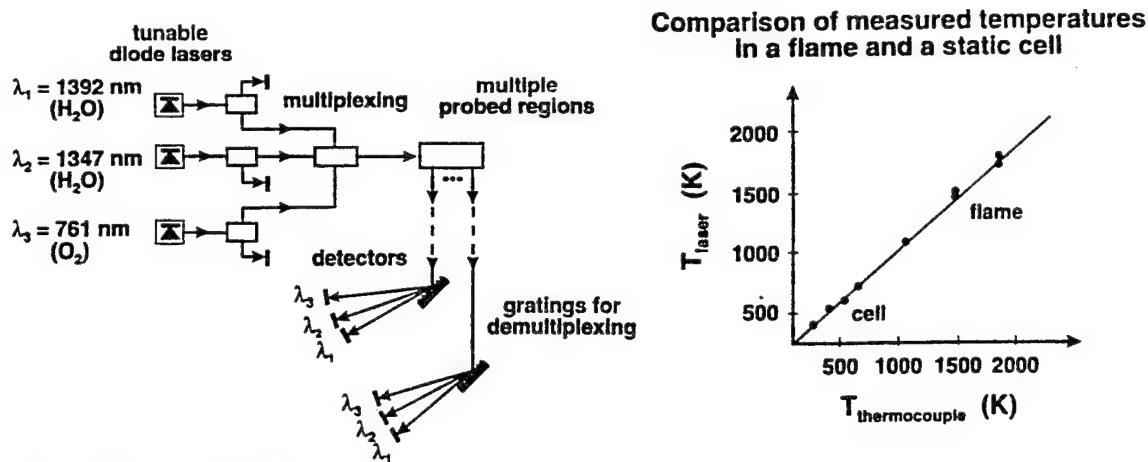


Fig. 2. Multiplexed diode-laser absorption diagnostic for simultaneous measurements of temperature, H_2O and O_2 .

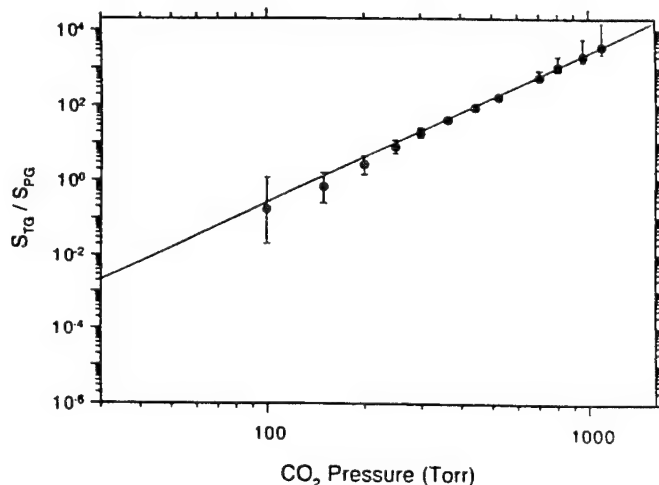


Fig. 3. Ratio of thermal and population grating signals of NO dilute in CO_2 at room temperature; theory (solid line) and data are shown.

Degenerate Four-Wave Mixing

We have continued development of a degenerate four-wave mixing (DFWM) diagnostic. DFWM is a nonlinear spectroscopic technique that shows potential for quantitative measurements of temperature and concentration. Specifically, it can be used to probe dark (non-fluorescing) molecules, it results in a collimated signal beam that is useful in luminous environments, and it shows potential as a temperature diagnostic at high pressures. In collaboration with researchers at Sandia National Laboratories, in Livermore, CA (supported by DOE, BES) we have recently experimentally observed contributions from two different DFWM mechanisms: the population-grating (PG) and thermal-grating (TG) mechanisms. These two

mechanisms are fundamentally different, the first attributed to perturbations in level populations and the second attributed to index perturbations in the bulk gas caused by collisional relaxation of absorbed energy. We developed a model for the ratio, S_{TG}/S_{PG} , of the signal intensities (S) of these two mechanisms which scales as $P^4T^{-4.4}$. By developing techniques to distinguish the two mechanisms, we measured the ratio over a wide range of experimental conditions. Figure 3 shows the agreement of experimental results with this model based on experiments in NO/CO₂ mixtures with pulsed, narrow-linewidth excitation of NO near 226 nm. We also verified the temperature dependence of the model by performing measurements in an atmospheric-pressure flame.

Other Diagnostics Efforts

During the past year we initiated an effort to enhance the use of acetone as a flowfield tracer for PLIF diagnostics. We are investigating the temperature and pressure dependence of acetone fluorescence, as a function of excitation wavelength, in order to optimize a new two-wavelength diagnostic for simultaneous imaging of temperature and acetone concentration. We also made good progress in extending laser absorption and fluorescence diagnostics to high pressures. A new high-pressure shock tube is being utilized to study absorption spectra at pressures up to a few hundred atm, and in a second study, we have made detailed measurements of the combined NO/O₂ fluorescence which occurs under the high-pressure, lean combustion conditions relevant to future gas turbine combustion systems. These spectra suggest that new strategies will be needed for imaging of low levels of NO in such environments.

PUBLICATIONS/PRESENTATIONS

1. R. J. Cedolin, R. K. Hanson, and M. A. Cappelli, "LIF Lineshape Analysis of the Xenon $6s[3/2]_2^0$ - $6p[3/2]_2$ and $6s[3/2]_1^0$ - $6p[1/2]_0$ Transitions in a Glow Discharge," AIAA 95-1969, 26th Plasmadynamics and Lasers Conference (June 1995).
2. M. P. Arroyo, T. P. Birbeck, D. S. Baer and R. K. Hanson, "Dual Diode-Laser Fiber-Optic Diagnostic for Water Vapor Measurements," Optics Letters **19**, 1091-1093 (1994).
3. S. Langlois, T. P. Birbeck and R. K. Hanson, "Temperature-Dependent Collision-Broadening Parameters of H₂O Lines in the 1.4 μ m Region using Diode Laser Absorption Spectroscopy, J. Mol. Spec. **167**, 272-281 (1994).
4. S. Langlois, T. B. Birbeck and R. K. Hanson, "Diode Laser Measurements of H₂O Line Intensities and Self-Broadening Coefficients in the 1.4 μ m Region," J. Molec. Spectroscopy **163**, 27-42 (1994).
5. B. Yip, A. Lozano and R. K. Hanson, "Sensitized Phosphorescence: A Gas-Phase Molecular Mixing Diagnostic," Experiments in Fluids **17**, 16-23 (1994).
6. M. P. Arroyo, S. Langlois, and R. K. Hanson, "Diode Laser Absorption Technique for Simultaneous Measurements of Multiple Gasdynamic Parameters in High-Speed Flows Containing Water Vapor," Applied Optics **33**, 3296-3307 (1994).
7. B. K. McMillin, J. M. Seitzman and R. K. Hanson, "Comparison of NO and OH PLIF Temperature Measurements in a Scramjet Model Flowfield," AIAA J. **32**, 1945-1952 (1994).
8. D. S. Baer, V. Nagali, E. R. Furlong, R. K. Hanson and M. E. Newfield, "Scanned- and Fixed-Wavelength Absorption Diagnostics for Combustion Measurements using Multiplexed Diode-Laser Sensor System," AIAA-95-0426 at 33rd AIAA Aerospace Sciences Meeting, Reno, NV, Jan. 9-12, 1995.
9. D. S. Baer, R. K. Hanson, M. E. Newfield and N. K. J. M. Gopaul, "Multi-Species Diode-Laser Sensor System for H₂O and O₂ Measurements," paper AIAA-94-2643 at AIAA 18th Ground Test Conference, Colorado Springs, CO, June 20-23, 1994.
10. D. S. Baer, V. Nagali, T. Furlong and R. K. Hanson, "Wavelength-Multiplexed Diode-Laser Sensor System for Multi-Species and Multi-Parameter Measurements in Combustion Flowfields," 31st AIAA Joint Propulsion Conference, San Diego, July 10-12, 1995.

NONLINEAR DIAGNOSTICS FOR COMBUSTION AND PLASMA PROCESSES

(AFOSR Contract F49620-94-C-0027)

Principal Investigators: David L. Huestis, Gregory W. Faris, and Jay B. Jeffries

SRI International
Molecular Physics Laboratory
Menlo Park, California 94025

SUMMARY/OVERVIEW

Task 1: UV and VUV Generation and Detection Techniques

We are developing techniques to extend laser-based diagnostics into the vacuum ultraviolet (vuv) region for the detection of atomic ions, planar imaging of light atoms, and other applications. We have previously developed a high power vuv source and applied this source to two-photon-excited fluorescence (TPEF) in atomic neon at 133 nm. To extend the TPEF technique to atomic ions, we need to improve the vuv power. We are using a windowless cell to evaluate approaches for minimizing vuv generation inefficiencies due to optics and dispersion of the mixing gas.

Task 2: Laser-Excited Amplified Spontaneous Emission (ASE)

Two-photon-excited ASE of atomic hydrogen and oxygen has been explored in a variety of low-pressure flames as a method to determine atom concentration. Previously we discovered ASE is more sensitive to the collisional environment than LIF, which makes quantitative interpretation of the ASE signal quite difficult. We demonstrated direct gain measurements of a probe laser to provide atom concentration measurements. We have developed a model of the ASE signal and have tested this model in the low-pressure flame environment. We find excellent agreement for the relative variation of ASE signals for flames with different atom concentrations and we find the prediction of the absolute ASE signal to agree within a factor of four with the measurement.

TECHNICAL DISCUSSION

Task 1: UV and VUV Generation and Detection Techniques (G. W. Faris)

We are investigating approaches to two interesting problems in laser-based diagnostics; the detection of atomic ions and the single-photon detection of a light ions. Both of these detection problems require high power vacuum ultraviolet radiation.

The quantitative detection of atomic ions is important for studying plasma propulsion, highly-ionized flows, plasma etch lithography, magnetically-confined fusion, astronomy, and astrophysics. Detection of light atomic ions is difficult because the single-photon transitions from the ground state lie in the extreme ultraviolet (xuv) and no window materials are available in this region. Our approach is to use two-photon-excited fluorescence in the vuv, allowing the use of windows of materials such as MgF_2 and LiF .

An existing technique for the detection of light atoms is through two-photon excitation in the near ultraviolet region. An alternative technique to two-photon detection is single-photon detection using vuv. While more complicated than the two-photon approaches, single-photon

vuv detection of light atoms allows more sensitive detection, can avoid photo-induced changes due to high optical intensities, and provides the possibility for planar imaging. Areas where single-photon detection techniques may prove useful include arc jets and hot rarified flows. Other applications of vuv diagnostics include single- or multiple-photon ionization for very high sensitivity detection techniques and single-photon calibration of multiple-photon diagnostic techniques.

To produce high-power widely-tunable, vuv radiation, we have developed a source based on two-photon-resonant difference-frequency generation.¹ In this approach the output of a tunable ArF excimer laser at frequency ν_{ArF} is mixed with the fundamental or frequency-doubled output from a Nd:YAG-pumped dye laser at frequency ν_{dye} to produce radiation at frequency $\nu_{\text{vuv}} = 2 \times \nu_{\text{ArF}} - \nu_{\text{dye}}$. Enhanced efficiency is provided by tuning the ArF laser onto resonance with two-photon transitions in the mixing gas (krypton or hydrogen). By tuning the dye laser frequency, the vuv wavelength can be varied from 110 to 180 nm. To date, we have obtained over 65 μJ at a wavelength of 133 nm using this technique. Larger powers can be obtained over a limited tuning range by directly Raman-shifting the ArF laser output.²

We have demonstrated the feasibility of performing two-photon-excited fluorescence in the vuv through TPEF in neon using 133 nm light.³ In this manner we have performed detection through a state over $150,000 \text{ cm}^{-1}$ above the ground state. Although this excitation energy is high enough for detection of atomic ions, the vuv power is too low. The neon measurements were performed at a pressure of about 100 torr, which corresponds to a higher density than desirable for atomic ion detection.

We are now working on approaches to improve the vuv power. Two primary limitations are related to materials problems in the vuv. First, the vuv power is short lived due to what seems to be color center formation in the optics.³ Second, the vuv generation efficiency is limited by the dispersion of the mixing gas. To better examine these problems, we are now performing the mixing in a windowless cell. Without windows on the cell, we are not limited to short experimental runs by the optics, and we can insert and withdraw optics in the beam to study decay in the transmission through the optics.

We have tried three different windowless cells to date. The first consisted of a pulsed valve filling a 10 cm long glass tube within a vacuum cell. We found that 10 cm was too short a gain region for production of vuv through ASE in hydrogen,⁴ a technique we find valuable for vuv studies using only the excimer laser. The second attempt used a differentially pumped cell with a 300 μm hole. This cell was found to be too difficult to align through the spectrometer used to separate the generated vuv from the input laser. The current cell uses a pulsed valve filling a longer cell, one end of which is coupled into vacuum. This cell has been performing satisfactorily.

We have used ASE vuv to irradiate MgF_2 optics for degradation studies. Surprisingly, we found no degradation from the ASE alone. We are now preparing to perform two-photon-resonant mixing to generate light near 127 nm for continuing study of optics degradation as well as phasematching approaches to improve the vuv generation efficiency.

Task 2: Laser-Excited Amplified Spontaneous Emission (ASE) (Jay Jeffries)

Hydrogen atoms have been observed in low-pressure, laminar, one-dimensional flames using two-photon laser-induced fluorescence (LIF) and amplified spontaneous emission (ASE). Measurements were made in 7 Torr H_2/O_2 and 30 Torr CH_4/Air flames. ASE and LIF signals are simultaneously collected as a function of reaction time (height above the burner). The gas temperature variation with reaction time is determined by LIF measurements of OH rotational distributions, and used to constrain a model of the flame chemistry. The ASE signal is predicted by a coupled rate model including the hydrogen atom concentration, the collisional quenching rate, the laser power density, and the gas temperature. The predicted absolute ASE signal, the

predicted variation in signal between rich and lean H_2/O_2 flames and the signal variation versus height above the burner all agree well with the measured values.

Two-photon excitation of the 3S and 3D states of atomic hydrogen followed by the detection of the red $n=3 \rightarrow n=2$ Balmer α radiation avoids absorption of the vuv excitation and signal light from the flame gases. Sequential application of two, single photon, selection rules allows only excitation to the 3S or 3D states which do not have an allowed single photon transition back to the ground state; instead these states radiate Balmer α to the 2P state. If the pumping rate is fast enough, the laser excitation produces a population inversion on the Balmer α transition, and spontaneously emitted photons can experience gain forward and backward along the optical axis of the excitation laser. The ASE literature for optically pumped lasers is quite rich. Especially relevant for diagnostics measurements are the theoretical papers by Allen and Peters,⁵⁻⁷ and the experimental diagnostics work on CO.⁸

We report measurements of H atoms observed with two-photon LIF and simultaneously acquired ASE from Balmer α in a 7.2 Torr H_2/O_2 flame and a 30 Torr CH_4/Air flame. Measurements are made in fuel rich, stoichiometric, and lean hydrogen/oxygen flames. A model of the flame chemistry provides concentrations of the major species as a function of reaction time (height above the burner), using the Sandia 1-D flame code⁹ constrained by LIF temperature measurements and a first order correction for radial diffusion.¹⁰ LIF measurements are corrected for collisional quenching using the model results and agree quite well with the model predictions for the atomic hydrogen concentration versus reaction time and as a function of fuel/oxidizer stoichiometry. The ASE measurements in the three hydrogen/oxygen flames are compared with the predictions of a coupled rate model. The absolute ASE signal intensity and the variation with stoichiometry are in remarkable agreement with the prediction; however, the variation with reaction time has less than adequate agreement with the coupled rate model of the ASE signal.

The dynamics of the atomic population and coupled ASE photon field are described by a mirrorless cavity for ASE signal gain in the confocal volume of the incident pump beam. By adapting coupled rate equations,^{11,12} we describe the density of the atoms in the cavity for each of the three atomic levels, the density of the ions generated via a 2+1 REMPI process, the density of the ASE photons, and the density of the photons which leave the cavity and are detected. These coupled rate equations are suitable for modeling physical situations in which the atomic gain is modest. For high gain situations the spatial dependence of the gain must be included.¹³

The ASE coupled rate model is solved using a fourth-order Runge-Kutta scheme using commercial MathCad software. Figure 1 shows the time evolution of the hydrogen atom state densities predicted by the model for the conditions of the 7.2 torr H_2/O_2 flame at 2.0 cm above the burner surface. Time zero on the x-axis denotes the arrival of the leading edge of the pump pulse. Due to the

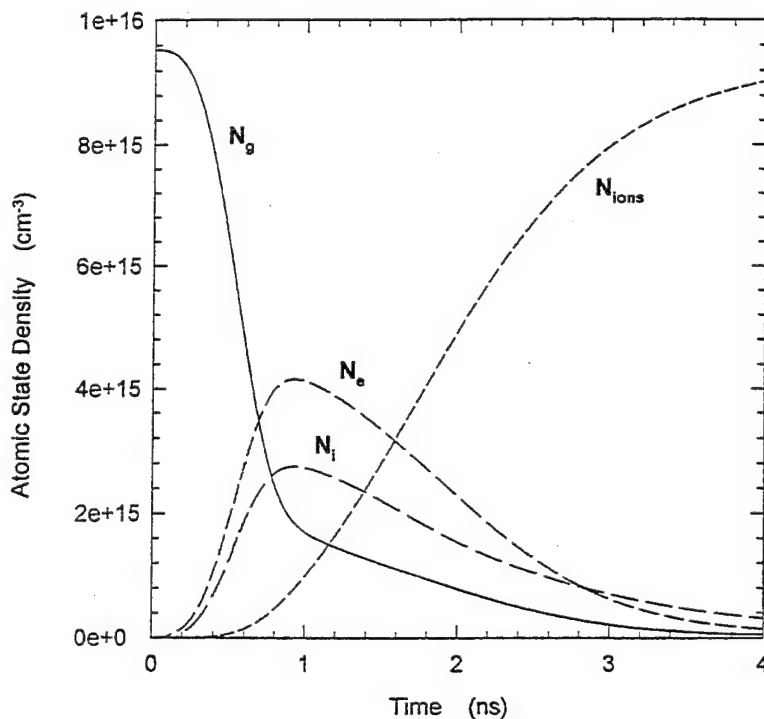


Fig. 1. The time evolution of the atomic state densities for the conditions stated in the text.

high pumping rate of a focused 200 μJ the majority of the ground state atoms eventually become ionized through a 2+1 REMPI process.

Figure 2 compares the measured and predicted ASE signals in the lean and rich H_2/O_2 flames. The open symbols are the ASE measurements and the closed symbols the model predictions. The ASE measurements are normalized to the absolute value of the model predictions in the burnt gases of the rich flame. The variation between the rich and lean flame for the measured peak ASE agrees well with the prediction. However, observed ASE rises much faster than predicted in the rich flame and falls much faster than predicted in the lean flame. This deviation is consistent with lower gain in the experiment than in the model. The absolute ASE signal observed is approximately four times smaller than the ASE signal predicted.

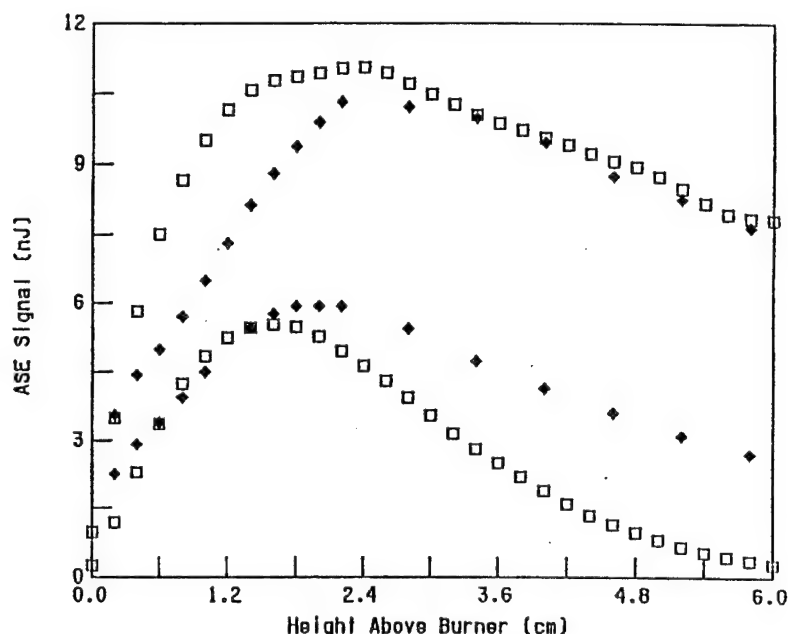


Fig. 2. Measured ASE (open symbols) and predicted ASE (closed) for 7.2 Torr rich and lean H_2/O_2 flame.

REFERENCES

1. G. W. Faris and M. J. Dyer, in *Short Wavelength Coherent Radiation: Generation and Applications*, Philip H. Bucksbaum and Natale M. Ceglio, Eds. (Optical Society of America, Washington, DC, 1991).
2. G. W. Faris and M. J. Dyer, *J. Opt. Soc. Am. B*, **10**, 2273 (1993).
3. G. W. Faris and M. J. Dyer, *Opt. Lett.* **18**, 382 (1993).
4. H. Pummer, H. Egger, T. S. Luk, T. Srinivasan, and C. K. Rhodes, *Phys. Rev. A* **28**, 795 (1983).
5. G. I. Peters and L. Allen, *J. Phys. B* **4**, 238 (1971).
6. L. Allen and G. I. Peters, *J. Phys. B* **4**, 377 (1971).
7. L. Allen and G. I. Peters, *J. Phys. B* **4**, 564 (1971).
8. U. Westblom, S. Agrup, M. Alden, H. M. Hertz, and J.E.M. Goldsmith, *Appl. Phys. B* **50**, 463 (1990).
9. R. J. Kee, F. M. Rupley, and J. A. Miller, Sandia Laboratory Report, SAND87-8215, 1987.
10. J. B. Jeffries, G. P. Smith, D. E. Heard, and D. R. Crosley, *Ber. Bunsenges. Phys. Chem.* **96**, 1410 (1992).
11. M. S. Brown and J. B. Jeffries, *Appl. Opt.* **33**, 8744 (1994).
12. Y. L. Huang and R. J. Gordon, *J. Chem. Phys.* **97**, 6363 (1992).
13. L. W. Casperon, *J. Appl. Phys.* **48**, 256 (1977).

RAPID CONCENTRATION MEASUREMENTS BY PICOSECOND TIME-RESOLVED LASER-INDUCED FLUORESCENCE

AFOSR Grant No. AFOSR-91-0365

Principal Investigators: Galen B. King and Normand M. Laurendeau

Flame Diagnostics Laboratory
School of Mechanical Engineering
Purdue University
West Lafayette, IN 47907

SUMMARY/OVERVIEW

This research is concerned with the development of a laser-based diagnostic technique for the measurement of minor species concentrations in turbulent flames called picosecond time-resolved laser-induced fluorescence (PITLIF). Current diagnostic techniques have the capability to measure probability distribution functions (PDFs), but in many cases they lack the temporal resolution needed to measure power spectral densities (PSDs). The PITLIF instrument employs a high repetition rate mode-locked laser which gives it the temporal resolution and power necessary to rapidly obtain PSDs in addition to PDFs. The specific objective of this project is to develop the PITLIF instrument and to demonstrate its viability for obtaining PDFs and PSDs of radical concentrations in turbulent flames.

TECHNICAL DISCUSSION

Turbulent flames are characterized by random fluctuations in flow variables such as velocity or concentration. These fluctuations must be described statistically using PDFs and PSDs. Laser-induced fluorescence (LIF) is commonly employed for the measurement of minor species concentrations.¹ Typically, CW or Q-switched laser systems are employed for LIF measurements of PDFs, but these systems lack the power and temporal resolution necessary to measure PSDs of concentration in turbulent flames. We report here on current investigations with picosecond time-resolved laser-induced fluorescence (PITLIF), a new diagnostic technique which has the potential to rapidly and simultaneously measure both PDFs and PSDs of concentration in a turbulent flame.

A block diagram of the PITLIF instrument is shown in Figure 1. The laser system consists of a broadband dye laser synchronously pumped by a mode-locked frequency-doubled Nd:YAG laser. The laser system delivers a series of mode-locked laser pulses with a width of ~20 ps and a repetition rate of 4 MHz. The laser system irradiates a region of the flame, and through interaction with atoms or molecules in the flame, light is absorbed and spontaneously emitted. The detector, a photomultiplier tube, measures some of this emitted

¹M. C. Drake and R. W. Pitz. Comparison of turbulent diffusion flame measurements of OH by planar fluorescence and saturated fluorescence. *Experiments in Fluids* 3, 283 (1985).

light. The output of the detector is fed into two parallel data acquisition channels. The low-bandwidth acquisition system uses a low-pass filter to filter out individual laser pulses and records the integrated fluorescence signal which provides a measure of the low frequency (<10 kHz) fluctuations in the LIF signal. The high-bandwidth acquisition system (0-2 GHz) has the temporal resolution necessary to record each laser pulse, and thus can be used to measure the lifetime of the decay for the excited state. Thus, when the high-bandwidth system is used in conjunction with the low-bandwidth system, the PITLIF instrument can be used to measure concentration fluctuations in systems where collisional quenching varies.

Previously, we have applied the PITLIF instrument to measure number densities and lifetimes of sodium doped into a laminar $\text{H}_2/\text{O}_2/\text{Ar}$ flame². More recently, we have measured the hydroxyl (OH) fluorescence signal in two laminar flat-flame burners by modifying the laser and detection systems to allow us to excite and monitor OH. Fluorescence emission was collected perpendicular to the beam axis and focused onto the entrance slit of a 0.25-m monochromator which was centered at 309 nm. The spectral width of the detection system was 26 nm (assuming a negligible entrance slit width). The excitation line was the $Q_1(7)$ transition of the $\text{A}^2\Sigma^+ - \text{X}^2\Pi$ ($v'=0, v''=0$) system ($\lambda = 308.9734$ nm).

Hydroxyl lifetimes were measured in flames produced by two different burner systems. The first system utilized a nonpremixed square 25mm x 25mm Hencken burner; it is composed of a bundle of stainless steel tubing, each tube for the fuel flow being surrounded by six tubes for the flow of an oxidant/diluent mixture. The other burner utilized was a premixed water-cooled, sintered-bronze, 6-cm diameter McKenna burner. Both burners used a similar mixture of $\text{CH}_4\text{-O}_2\text{-N}_2$ with a diluent/oxidizer ratio of 3.76.

The Hencken burner was operated at equivalence ratios (ϕ) in the range 1.0 - 1.5. A typical fluorescence decay obtained via equivalent-time sampling 5 mm above the Hencken burner at $\phi = 1.0$ is displayed in Fig. 2(a), along with the excitation pulse collected from laser scattering and the fit determined with a convolute-and-compare algorithm. The resulting lifetimes obtained 5 mm above the center of the Hencken burner are displayed in Fig. 3(a) for different equivalence ratios. Each point displayed on the figure represents the average of six trials, with the error bars representing the 95% confidence interval of the mean.

The McKenna burner was operated at equivalence ratios in the range $\phi = 0.8 - 1.4$. As in our study of the Hencken burner, Fig. 3(b) displays fluorescence lifetimes obtained via equivalent-time sampling versus equivalence ratio for the premixed McKenna burner. Similar to the data obtained with the Hencken burner, there is a noticeable decrease in lifetime with increasing equivalence ratio.

Figure 3(b) includes the fluorescence lifetime obtained from real-time measurements at stoichiometric conditions. The point at $\phi = 1.0$ represents the average of 20 lifetimes obtained in the real-time mode for the McKenna burner, with the error bars representing the 95% confidence interval of the mean. The stoichiometric flame was chosen for this investigation due to its relatively high SNR (~4). We have already demonstrated the viability of real-time fluorescence measurements for atomic sodium; thus, only one equivalence ratio was investigated for the case of OH.

Figure 2(b) shows a typical waveform obtained using real-time acquisition at $\phi = 1.0$, including the excitation pulse and the fit determined through convolution. Seventeen files were acquired and combined to obtain a single lifetime, resulting in a total sampling time of

²Klassen, M. S., Thompson, B. D., Reichardt, T. A., King, G. B. and Laurendeau, N. M. (1994). Flame Concentration Measurements using Picosecond Time-Resolved Laser-Induced Fluorescence. *Combust. Sci. and Tech.* **97**, 391.

348 μ s. While the real-time fluorescence lifetimes exhibit more statistical scatter than the equivalent-time data (as evidenced by the acquisition of 20 lifetimes to obtain a reliable average), the average value agrees favorably with that obtained using equivalent-time sampling, as shown in Fig. 3(b).

At atmospheric pressure, the fluorescence lifetime τ (s) is equivalent to the inverse of the quenching rate coefficient Q_{21} (s^{-1}). The collisional cross-sections for all molecules considered in the lifetime calculations of OH were taken from tabulated coefficients given by Paul³ and Garland and Crosley⁴. For the Hencken burner, the number densities required for the prediction were obtained by assuming chemical equilibrium. However, to account for radiative and conductive heat losses, the predicted lifetimes shown in Fig. 3(a) were obtained by assuming temperatures both 100 K and 200 K less than the adiabatic flame temperature.

Similarly, predicted fluorescence lifetimes for the McKenna burner are shown in Fig. 3(b). In this case, the species number densities for the fluorescence lifetime calculations were obtained from the Sandia steady, laminar, 1-D, premixed flame code⁵, while the temperatures for these calculations were obtained from radiation-corrected thermocouple measurements.

Figure 3 demonstrates the favorable agreement between the measurements and predictions of the fluorescence lifetime. The quenching rate models for both burners show that the fluorescence lifetime decreases with increasing equivalence ratio, a trend which we also observed for the experimental results. In addition, the Hencken burner flames modeled at 200 K less than the adiabatic flame temperature exhibit excellent quantitative agreement with the measured fluorescence lifetimes. Figure 3 represents the first extensive comparisons between fluorescence lifetimes obtained experimentally in atmospheric flames and those obtained from computer modeling.

Low-bandwidth data were also obtained using the McKenna burner to demonstrate the ability of the PITLIF system to determine OH number densities. The low-bandwidth fluorescence signal was corrected for both laser power fluctuations (by monitoring the laser power with a radiometer) and background emission (via synchronous detection). The flames probed with the low-bandwidth system were also investigated through computer modeling. We measured the low-bandwidth fluorescence signal as a function of height above the burner for $\phi = 1.0$. The results are displayed in Fig. 4. Because our lifetime measurements showed that the quenching environment is relatively constant with height above the burner for this flame, we did not correct the number densities for collisional quenching. The results of the kinetic modeling are also displayed in Fig. 4. While good agreement exists between the predicted and experimental results up to a height of 5 mm above the burner, the model predicts consistently higher number densities than were experimentally measured at greater heights. This deviation is likely due to the inability of the computer code to account for radiative heat losses. Such losses will decrease the temperature of the post-flame gases and thus decrease the relative OH concentration.

³Paul, P. H. (1994). A model for temperature-dependent collisional quenching of OH A²⁺. *J. Quant. Spectrosc. Radiat. Transfer* **51**, 511.

⁴Garland, N. L. and Crosley, D. R. (1986). On the collisional quenching of electronically excited OH, NH and CH in flames. *Twenty-first Symposium (International) on Combustion*, The Combustion Institute, Pittsburgh, PA, 1693.

⁵Kee, R. J., Grcar, J. F., Smooke, M. D., and Miller, J. A. (1985). A Fortran program for modeling steady laminar one-dimensional premixed flames. Sandia Report SAND85-8240.

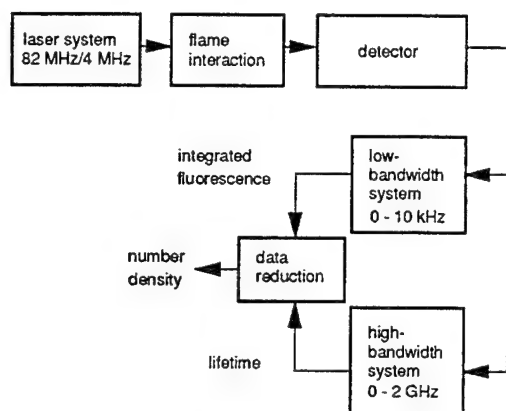


Figure 1. Block diagram of the PITLIF instrument.

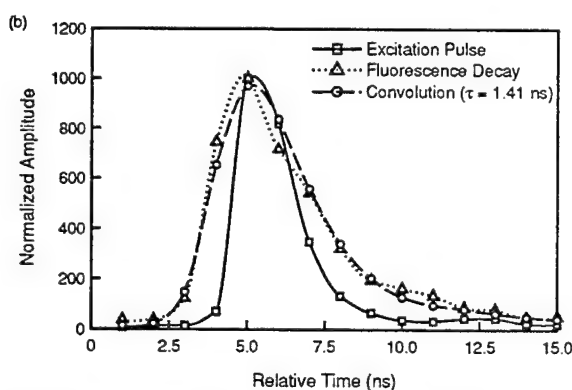
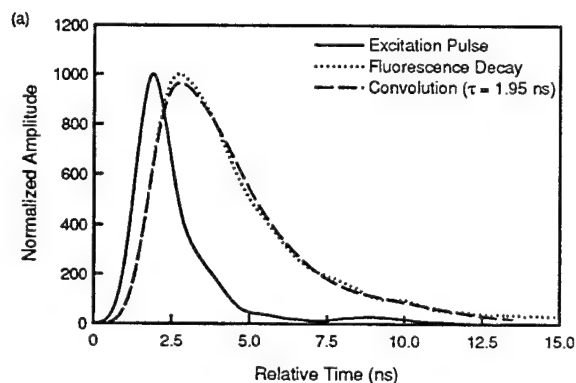


Figure 2. (a) Normalized equivalent-time excitation pulse and OH fluorescence decay with fit found in the Hencken burner. (b) Normalized real-time excitation pulse and OH fluorescence decay with fit found in McKenna burner.

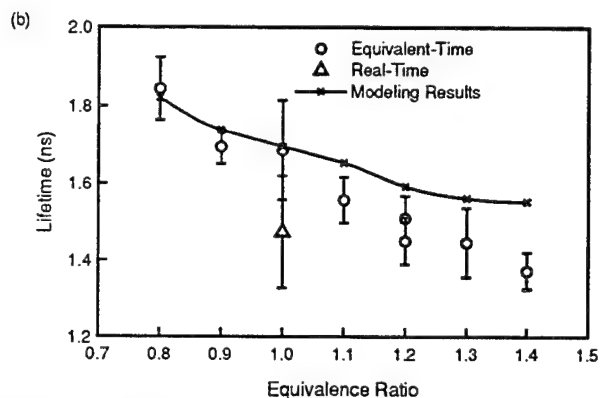
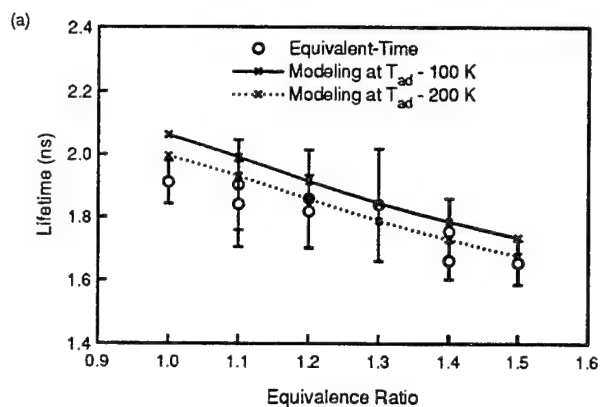


Figure 3. Fluorescence lifetimes over (a) the Hencken burner and (b) the McKenna burner. All measurements were made 5 mm above the burner.

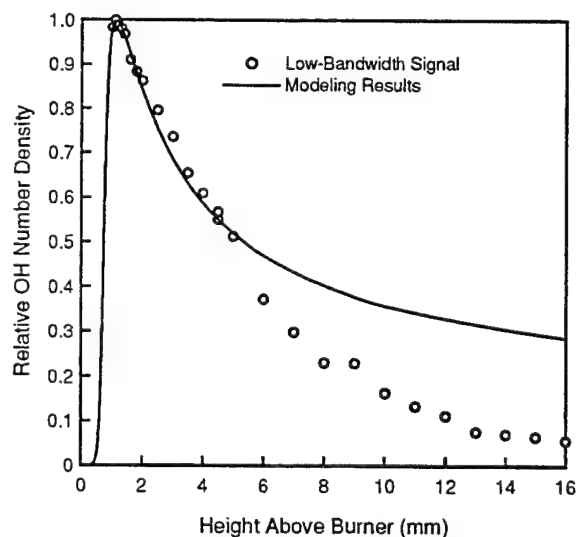


Figure 4. Axial profile of the LIF signal found as a function of height above the McKenna burner. The results from kinetic modeling are also displayed.

AFOSR SPONSORED RESEARCH IN PROPULSION DIAGNOSTICS

PROGRAM MANAGER: JULIAN M. TISHKOFF

AFOSR/NA

110 Duncan Avenue, Suite B115

BOLLING AFB DC 20332-0001

SUMMARY/OVERVIEW: The Air Force Office of Scientific Research (AFOSR) program in propulsion diagnostics currently is focused on three areas of study: gas-phase measurements, plasmas, and particle/droplet measurements. An assessment of major research needs in each of these areas is presented.

TECHNICAL DISCUSSION

AFOSR is the single manager for Air Force basic research, including efforts based on external proposals and in-house work at Air Force laboratories. Airbreathing combustion is assigned to the AFOSR Directorate of Aerospace and Materials Sciences along with programs in rocket and space propulsion, airbreathing combustion, fluid and solid mechanics, and structural materials.

Interests of the AFOSR propulsion diagnostics subarea are given in the SUMMARY section above. This program, now in its thirteenth year, has produced many "first-ever" laser-based measurements. The instrumentation with which these measurements were made is becoming commonly available for laboratory and bench test utilization. Measurements range from microscopic to macroscopic scales with relevance to: plasma acceleration; combustion aerothermochemistry; the behavior and synthesis of advanced energetic materials; characterization of exhaust plume formation and radiation; and dynamic control of propulsion, weapon and power generation systems.

Decisions on support for research proposals are based on scientific opportunities and technology needs. Research areas with the greatest growth potential are: spectroscopy at high pressures, $>10\text{MPa}$; plasma diagnostics; micro measurement capability for propulsion control; and measurements in supercritical fluids.

In the rapidly changing international environment we also are examining how we conduct our research activities in relation to both Air Force and civilian needs. We now recognize a new set of research objectives, including achieving rapid technology transitioning and dual military and civilian technological use for Air Force basic research. We welcome your ideas on fostering better working relationships among universities, industry, and Government scientists and technologists.

The purpose of this abstract has been to communicate AFOSR perceptions of research trends to the university and industrial research communities. However, communication from those communities back to AFOSR also is desirable and essential for creating new research opportunities. Therefore, all proposals and inquiries for fundamental research are encouraged even if the content does not fall within the areas of emphasis described herein. Comments and criticisms of current AFOSR programs also are welcome.

AIRBREATHING COMBUSTION

Invitees

Dr. M. S. Anand
Allison Engine Company
P.O. Box 420
Speed Code T-14
Indianapolis IN 46206-0420
(317)230-2828
FAX:230-3691
iems@agt.gmeds.com

Dr Griffin Anderson
NASA Langley Research Center
M/S 168
Hampton VA 23665
(804)864-3772

Dr Scott Anderson
Department of Chemistry
State University of New York
Stony Brook NY 11794-3400
(516)632-7915

Dr K Annamalai
Mechanical Engineering Dept
Texas A&M University
College Station TX 77843-3123

Dr Kurt Annen
Aerodyne Research, Inc.
45 Manning Road
Manning Park Research Center
Billerica MA 01821-3976
(508)663-9500
FAX:663-4918
kannen@aerodyne.com

Dr Simon Bauer
Department of Chemistry
Cornell University
Ithaca NY 14853-1301

Dr S L Baughcum
Boeing Company
P O Box 3999, MS 87-08
Seattle WA 98124
(206)965-0426
FAX:234-4543

Dr Howard Baum
National Institute of
Standards and Technology
Center for Fire Research
Gaithersburg MD 20899
(301)975-6668

Dr John Bdzil
Los Alamos National Laboratory
Los Alamos NM 87545

Dr H L Beach
NASA Langley Research Center
MS 168
Hampton VA 23665-5225
(804)864-3772
(804)864-2658

Dr. Bruce Beaver
Department of Chemistry
Duquesne University
Mellon Hall
Pittsburgh PA 15282-1503
(412)434-6340
FAX:434-5683

Dr Josette Bellan
Applied Technologies Section
Jet Propulsion Laboratory
4800 Oak Grove Drive
Pasadena CA 91109
(818)354-6959

Dr Michael Berman
AFOSR/NC
110 Duncan Avenue, Suite B115
Bolling AFB DC 20332-0001
(202)767-4963
DSN 297-4963

Dr Mitat Birkan
AFOSR/NA
110 Duncan Avenue, Suite B115
Bolling AFB DC 20332-0001
(202)767-4938
DSN 297-4938
FAX:767-4988
birkan@afosr.af.mil

Dr Paul Bonczyk
United Technologies Research
Center
Silver Lane
East Hartford CT 06108
(203)727-7162

Dr Kevin Bowcutt
Rockwell International
Mail Code NA40
12214 Lakewood Boulevard
Downey CA 90241
(213)420-0317

Dr C T Bowman
Department of Mechanical
Engineering
Stanford University
Stanford CA 94305-3032
(415)723-1745
FAX:723-1748
bowman@navier.stanford.edu

Dr K N C Bray
University of Cambridge
Department of Engineering
Trumpington Street
Cambridge CB2 1PZ, England UK
0223 332744
0223 337733
FAX0223 332662

Dr Robert Breidenthal
Department of Aeronautics and
Astronautics
University of Washington, FS10
Seattle WA 98195
(206)685-1098

Dr Kenneth Brezinsky
Department of Mechanical and
Aerospace Engineering
Princeton University
Princeton NJ 08544-5263
(609)258-5225
FAX:258-5963
kenb@cougarxp.princeton.edu

Dr Garry Brown
Department of Mechanical and
Aerospace Engineering
Princeton University
Princeton NJ 08544-5263
(609)258-6083

Dr R C Brown
Aerodyne Research, Inc.
45 Manning Road
Manning Park Research Center
Billerica MA 01821-3976
(508)663-9500
FAX:663-4918

Dr John D Buckmaster
Department of Aerospace
Engineering
University of Illinois
Urbana IL 61801

Dr Dennis Bushnell
NASA Langley Research Center
Mail Stop 168
Hampton VA 23665
(804)864-4546

Dr Ron Butler
WL/POSF
Building 490
1790 Loop Road, N
Wright-Patterson AFB OH 45433-7103

Dr T D Butler
Group T-3
Los Alamos National Laboratory
Los Alamos NM 87545
(505)667-4156

Dr H F Calcote
AeroChem Research Laboratories
Inc.
P. O. Box 12
Princeton NJ 08542
(609)921-7070
FAX:329-8292
cb@acm.princeton.edu

Mr. Donald Campbell
NASA Lewis Research Center
21000 Brookpark Road
Mail Stop 3-2
Cleveland OH 44135
(216)433-2929
(216)433-5266

Dr Graham V Candler
Department of Aerospace
Engineering & Mechanics
University of Minnesota
Minneapolis MN 55455

Dr Brian Cantwell
Department of
Mechanical Engineering
Stanford University
Stanford CA 94305-3032
(415)723-4825

Dr Leonard Caveny
BMDO/TRI
The Pentagon
Washington DC 20301-7100
(703)412-3439
FAX:412-4857

Dr Chine I Chang
AFOSR/NA
110 Duncan Avenue, Suite B115
Bolling AFB DC 20332-0001
(202)767-4987
DSN 297-4987
FAX:767-4988
chang@afosr.af.mil

Dr Tryfon Charalampopoulos
Mechanical Engineering Dept.
Louisiana State University
Baton Rouge LA 70803
(504)388-5792
(504)388-5799
FAX:388-5894

Dr Lea D Chen
Mechanical Engineering Dept
University of Iowa
Iowa City IA 52242
(319)335-5674
FAX:335-5669
ldchen@icaen.uiowa.edu

Dr Norman Chigier
Department of Mechanical
Engineering
Carnegie-Mellon University
Pittsburgh PA 15213-3890
(412)578-2498

Dr Robert Childs
Nielsen Engineering and
Research, Inc.
510 Clyde Avenue
Mountain View CA 94043-2287
(415)968-9457

Dr S Y Cho
Department of Mechanical and
Aerospace Engineering
Princeton University
Princeton NJ 08544-5263

Dr M-S Chou
Building R1, Room 1044
TRW Space and Technology Group
One Space Park
Redondo Beach CA 90278
(310)812-0469
FAX:812-7589

Mr R.W. Claus
NASA Lewis Research Center
21000 Brookpark Road
Cleveland OH 44135-3127
(216)433-5869

Capt Keith Clutter
WL/MNAA
Eglin AFB FL 32542-6810
(904)882-0207
DSN 872-0207
FAX: 872-0341
clutter@eglin.af.mil

Dr M B Colket
United Technologies Research
Center
Silver Lane
East Hartford CT 06108
(203)727-7481
(203)658-9502
FAX:727-2151
colket%vfs2@utrcgw.utc.com

Dr S M Correa
GE Research Center
K1-ES210
P. O. Box 8
Schenectady NY 12301
(518)387-5853
FAX:387-7258
correa@crd.ge.com

Dr E T Curran
WL/PO
Building 18
1921 Sixth Street, Suite 5
Wright-Patterson AFB OH 45433-7650
(513)255-2520
DSN 785-2520
FAX:476-4657

Dr Werner Dahm
Department of Aerospace
Engineering
The University of Michigan
Ann Arbor MI 48109-2118
(313)764-4318
(313)761-2026
FAX:763-0578
wdahm@engin.umich.edu

Dr Sanford M Dash
Science Applications
International Corporation
501 Office Ctr Dr, Suite 420
Fort Washington PA 19034-3211
(215)542-1200
FAX:542-8567

Mr Stephen Corda
Applied Physics Laboratory
Johns Hopkins University
Johns Hopkins Road
Laurel MD 20707-6099
(301)953-5000
Ext 4654

Dr Clayton Crowe
Department of Mechanical
Engineering
Washington State University
Pullman WA 99164-2920
(509)335-3214

Dr Eli Dabora
Mechanical Engineering Dept
University of Connecticut
Box U-139 ME
Storrs CT 06268
(203)486-2415
(203)486-2189

Dr John Daily
Center for Combustion Research
Mechanical Engineering Dept
University of Colorado
Boulder CO 80309
(303)492-7151

Dr Ron Davis
Chemical Science and Techn Lab
Building 221, Room B312
National Inst of Stds & Tech
Gaithersburg MD 20899

Dr Pablo G Debenedetti
Department of Chemical
Engineering
Princeton University
Princeton NJ 08544-5263
(609)258-5480
PDEBENE@pucc.princeton.edu

Dr George Deiwert
NASA Ames Research Center
MS 230-2
Moffett Field CA 94035
(415)604-6198

Dr R W Dibble
Department of Mechanical Eng
6159 Etcheverry Hall
University of California
Berkeley CA 94720
(415)642-4901
FAX:642-6163

Dr Paul Dimotakis
California Institute of Tech
1201 East California Blvd.
MC 301-46
Pasadena CA 91125
(818)395-4456
(818)395-4447
pavlos@caltech.edu

Mr Lee Dodge
Southwest Research Institute
P O Drawer 28510
San Antonio TX 78284
(512)684-5111
Ext 3251

Dr David Dolling
Department of Aerospace Engrg
and Engineering Mechanics
University of Texas at Austin
Austin TX 78712
(512)471-4470
(512)471-7593

Dr Michael Drake
Physical Chemistry Department
General Motors Research Labs
Twelve Mile and Mound Roads
Warren MI 48090-9055

Dr. James F. Driscoll
Department of Aerospace Engrg
3004 FXB Building
University of Michigan
Ann Arbor MI 49109-2118
(313)939-0101
james_driscoll@um.cc.umich.edu

Dr Frederick Dryer
Department of Mechanical and
Aerospace Engineering
Princeton University
Princeton NJ 08544-5263
(609)258-5206

Dr C Dutton
Department of Mechanical and
Industrial Engineering
University of Illinois
Urbana IL 61801

Dr Harry Dwyer
Department of Mechanical
Engineering
University of California
Davis CA 95616

Dr. Charles A. Eckert
Department of Chemical Engrg
Georgia Institute of
Technology
Atlanta GA 30332-0100
(404)853-9344
FAX:894-6956

Dr Raymond Edelman
WC 70
Rocketdyne
6633 Canoga Avenue
Canoga Park CA 91304
(805)371-7196

Dr J T Edwards
WL/POSF
Building 490
1790 Loop Road, N
Wright-Patterson AFB OH 45433-7103
(513)255-1945
DSN 785-1945
FAX:255-1125

Ms Charlotte Eigel
WL/POSF
Building 490
1790 Loop Road, N
Wright-Patterson AFB OH 45433-7103
(513)255-5106
DSN 785-5106

Dr Said Elghobashi
Department of Mechanical
Engineering
University of California
Irvine CA 92717
(714)856-6002

Dr Phillip Emmerman
Harry Diamond Laboratories
Attn. SLCHD-ST-RD
2800 Powder Mill Road
Adelphi MD 20783-1197
(301)394-3000

Dr K C Ernst
Pratt and Whitney Aircraft
Group
Government Products Division
West Palm Beach FL 33402

Mr John Facey
Code RP
NASA
400 Maryland Avenue, SW
Washington DC 20546
(202)453-2854

Dr G M Faeth
Department of Aerospace
Engineering
University of Michigan
Ann Arbor MI 48109-2118
(313)764-7202
FAX:763-0578
gmfaeth@um.cc.umich.edu

Dr. Daniel Fant
South Carolina Energy Research
and Development Center
386-2 College Avenue
Clemson SC 29634-5180
(803)656-2267

Dr Francis Fendell
TRW Space and Technology Group
Building R1, Room 1022
One Space Park
Redondo Beach CA 90278
(213)812-0327

Dr Michael Frenklach
202 Academic Projects Building
The Pennsylvania State
University
University Park PA 16802
(814)865-4392
(814)238-4308
FAX:865-3075
mfrenklach@psu.edu

Mr Jack Fultz
WL/POPR
Wright-Patterson AFB OH 45433-6563
(513)255-2175
DSN 785-2175

Dr David Fyfe
Laboratory for Computational
Physics & Fluid Dynamics
Naval Research Laboratory
Washington DC 20375-5344
(202)767-6583
DSN 297-6583

Dr Alon Gany
Department of Aeronautical Eng
Technion-Israel Institute of
Technology
32000 Haifa, ISRAEL
04-292308

Dr Alan Garscadden
WL/CA-P
Building 18
1921 Sixth Street, Suite 5
Wright-Patterson AFB OH 45433-7650
(513)255-22246
DSN 785-2246
FAX:476-4657

Dr Ahmed Ghoniem
Department of Mechanical
Engineering
MIT
Cambridge MA 02139
(617)253-2295
FAX:253-5981
ghoniem@mit.edu

Mr R Giffen
General Electric Company
Aircraft Engine Group
Neumann Way
Cincinnati OH 45215

Dr P Givi
Department of Mechanical and
Aerospace Engineering
State University of New York
Buffalo NY 14260

Dr Irvin Glassman
Department of Mechanical and
Aerospace Engineering
Princeton University
Princeton NJ 08544-5263
(609)258-5199
(813)442-1118
FAX:258-5963
glassman@pucc.edu

Dr Frederick Gouldin
Department of Mechanical and
Aerospace Engineering
Cornell University
Ithaca NY 14853-1301
(607)255-5280

Dr Ephraim Gutmark
Research Department
Code 3892
Naval Air Warfare Center
China Lake CA 93555-6001
(619)939-3745
DSN 437-3745

Dr Howard Hanley
Chem & Sci Tech Lab
National Inst of Stds & Tech
325 Broadway
Boulder CO 80303-3328
(303)497-3320

Dr Helmut Hellwig
AFOSR/CC
110 Duncan Avenue, Suite B115
Bolling AFB DC 20332-0001
(202)767-5017
DSN 297-5017
FAX:767-6213
hellwig@afosr.af.mil

Dr A D Gosman
Department of Mechanical Engrg
Imperial College of Science
and Technology
London W7 2BX UK

Dr F Grinstein
Laboratory for Computational
Physics & Fluid Dynamics
Naval Research Laboratory
Washington DC 20375-5344

Dr. Robert B. Hall
SAF/AQT
1919 South Eads Street
Suite 100
Arlington VA 22202-3053
(703)746-8914
DSN 286-8914
(703)746-8918
hall@aqpo.hq.af.mil

Dr Stephen Harris
Physical Chemistry Department
General Motors Research Labs
30500 Mound Road
Warren MI 48090-9055
(313)986-1305

Dr S Henbest
Aeronautical Research Labs
506 Lorimer St, Fishermen's Bn
Box 4331, P O
Melbourne, Victoria AUSTRALIA 3207
(03)647 7585
FAX:646 6771
henbests@aedmel.arl.dsto.gov.au

Dr James Hermanson
Propulsion Technology
United Technologies Research
Center
East Hartford CT 06108

Mr Norman Hirsch
WL/POPR
Wright-Patterson AFB OH 45433-6563
(513)255-2175
DSN 785-2175

Dr David Hofeldt
125 Mechanical Engineering
111 Church Street, S E
University of Minnesota
Minneapolis MN 55455
(612)625-2045

Mr Robert Holland
United Technologies Chemical
Systems Division
P O Box 49028
San Jose CA 95161-9028
(408)224-7656

Dr Hans G Hornung
Graduate Aeronautical Labs
California Institute of
Technology
Pasadena CA 91125
(818)395-4551

Dr Lawrence Hunter
Applied Physics Laboratory
Johns Hopkins University
Johns Hopkins Road
Laurel MD 20707-6099
(301)953-5000
Ext. 7406

Dr M Y Hussain
ICASE, Mail Stop 132C
NASA Langley Research Center
Hampton VA 23665
(804)864-2175

Dr A K M F Hussain
Mechanical Engineering Dept
4800 Calhoun Road
University of Houston
Houston TX 77204-4792
(713)743-4545
FAX:743-4503
mece1w@jetson.uh.edu

Dr Essam A Ibrahim
Department of Mechanical
Engineering
Tuskegee University
Tuskegee AL 36088
(205)727-8974
FAX:727-8090
emeei@acd.tusk.edu

Dr T A Jackson
WL/POSF
Building 490
1790 Loop Road, N
Wright-Patterson AFB OH 45433-7103
(513)255-6462
DSN 785-6462
FAX:255-1125

Mr Gordon Jensen
United Technologies Chemical
Systems Division
P O Box 49028
San Jose CA 95161-9028
(408)365-5552

Dr Sheridan Johnston
Combustion Sciences
Sandia National Laboratories
Livermore CA 94551-0969
(510)294-2138

Dr K Kailasanath
Code 6410, LCP&FD
US Naval Research Laboratory
4555 Overlook Avenue, SW
Washington DC 20375-5344
(202)767-2402
FAX:767-4798
KAILASANATH@lcp.nrl.navy.mil

Dr Ann Karagozian
Mechanical, Aerospace and
Nuclear Engineering Department
University of California, LA
Los Angeles CA 90024
(213)825-5653

Dr Laurence R Keefe
Nielsen Engineering and
Research, Inc.
510 Clyde Avenue
Mountain View CA 94043-2287
(415)968-9457
FAX:968-1410

Dr Arnold Kelly
Department of Mechanical and
Aerospace Engineering
Princeton University
Princeton NJ 08544-5263
(609)258-5221

Dr John Kelly
Altex Technologies Corporation
650 Nuttman Road
Suite 114
Santa Clara CA 95054
(408)980-8610

Dr Lawrence A Kennedy
Department of Mechanical
Engineering
The Ohio State University
Columbus OH 43210-1107
(614)292-5782

Dr Ian Kennedy
Mechanical & Aero Engrg
University of California,
Davis
Davis CA 95616-5294
(916)752-2796
FAX:752-4158
IMKENNEDY@ucdavis.edu

Dr James Kezerle
Gas Research Institute
8600 West Bryn Mawr Avenue
Chicago IL 60631
(312)399-8331

Dr Merrill K King
NASA Headquarters
Code SNB
300 E Street, SW
Washington DC 20546
(202)358-0818

Dr William H Kirchhoff
Division of Chemical Sciences
Office of Basic Energy Science
Department of Energy
Washington DC 20585
(301)903-5820
william.kirchhoff%er@mailgw.er.doe.gov

Dr Charles Kolb
Aerodyne Research, Inc.
45 Manning Road
Manning Park Research Center
Billerica MA 01821-3976
(508)663-9500
FAX:663-4918

Dr Wolfgang Kollmann
Mechanical & Aerospace Engrg
University of California,
Davis
Davis CA 95616-5295
(916)752-4152
FAX:752-4158
wkollmann@ucdavis.edu

Dr George Kosaly
Mechanical Engineering Dept
University of Washington
Box 352600
Seattle WA 98195-2600
(206)543-6933
FAX:685-8047
kosaly@u.washington.edu

Mr David Kruczynski
Attn SLCBR-IBA
Interior Ballistics Division
Army Research Laboratory
Aberdeen Proving Gnd MD 21005-5066
(410)278-6202
DSN 298-6202

Dr Kenneth Kuo
Department of Mechanical
Engineering
Pennsylvania State University
University Park PA 16802
(814)865-6741
FAX:863-3203

Dr Samuel C Lambert
WL/CA-M
101 West Eglin Boulevard
Suite 101
Eglin AFB FL 32542-6810
(904)882-3002
DSN 872-3002
FAX:882-8689

Dr Marshall Lapp
High Temperature Interfaces
Division
Sandia National Laboratories
Livermore CA 94551-0969
(510)294-2435

Dr John Larue
Department of Mechanical
Engineering
University of California
Irvine CA 92717

Dr A Laufer
Office of Energy Research
U. S. Department of Energy
1000 Independence Avenue, N.W.
Washington DC 20585
(202)903-5820
allan.laufer%er@mailgw.er.doe.gov

Dr Moshe Lavid
ML Energia, Inc.
P. O. Box 1468
Princeton NJ 08540
(609)799-7970

Dr C K Law
Department of Mechanical and
Aerospace Engineering
Princeton University
Princeton NJ 08544-5263
(609)258-5271
FAX:258-6233
cklaw@pucc.princeton.edu

Dr C C Lee
Environmental Protection
Agency
Cincinnati OH 45268
(513)569-7520

Dr Spiro Lekoudis
Office of Naval Research
Mechanics Division, Code 432
800 North Quincy Street
Arlington VA 22217-5000
(703)696-4406

Dr Anthony Leonard
Graduate Aeronautical Labs
California Institute of
Technology
Pasadena CA 91125
(818)395-4465

Dr Jay Levine
OLAC PL/RKFA
10 East Saturn Boulevard
Edwards AFB CA 93524-7600
(805)275-6179
DSN 525-5454
FAX:275-6233
levine@plablink.ple.af.mil

Dr Chiping Li
Naval Research Laboratory
Code 6910, CCP&FD
Washington DC 20375-5344
(202)767-3254
FAX:767-4078
Li@lcp.nrl.navy.mil

Dr Paul Libby
Department of AMES 0310
9500 Gilman Drive
University of California
La Jolla CA 92093-0310
(619)534-3168
FAX:534-4543
libby@ames.ucsd.edu

Dr Wilbert Lick
Department of Mechanical and
Environmental Engineering
University of California
Santa Barbara CA 93106

Dr Hans Liepmann
Graduate Aeronautical Labs
California Institute of
Technology
Pasadena CA 91125
(818)395-4535

Dr. Milt Linevsky
National Science Foundation
4201 Wilson Boulevard
Arlington VA 22230
(703)306-1371
FAX:306-0319
mlinevsk@nsf.gov

Dr. Charles L. Liotta
Department of Chemical Engrg
Georgia Institute of
Technology
Atlanta GA 30332-0100
(404)853-9344
FAX:894-6956

Dr. Don Littrell
WL/MNAA
101 West Eglin Boulevard
Suite 346A
Eglin AFB FL 32542-6810
DSN 872-0395
(904)882-0395
FAX: 872-0341

Dr Lyle N Long
Department of Aerospace Engrg
233 Hammond Building
Pennsylvania State University
University Park PA 16802
(814)865-1172
lnl@psu.edu

Dr Marshall Long
Department of Mechanical
Engineering
Yale University
New Haven CT 06520
(203)432-4229

Dr F E Lytle
Department of Chemistry
Purdue University
West Lafayette IN 47907
(317)494-5261

Dr Andrej Macek
National Institute of
Standards and Technology
Physics Building, B-312
Gaithersburg MD 20899
(301)975-2610

Dr Edward Mahefkey
WL/POOC-5
Wright-Patterson AFB OH 45433-6563
(513)255-6241
DSN 785-6241

Mr Nick Makris
SA-ALC/SFT
Kelly AFB TX 78241-5000
AV945-8212
FAX:945-9964

Dr Oscar Manley
US Department of Energy
Office of Energy Research
1000 Independence Avenue, SW
Washington DC 20585
(202)353-5822

Dr Nagi Mansour
Computational Fluid Mechanics
Branch, RFT 202A-1
NASA Ames Research Center
Moffett Field CA 94035
(415)604-6420

Dr John Marek
NASA Lewis Research Center
21000 Brookpark Road
Cleveland OH 44135-3127

Dr James McDonald
Code 6110
Naval Research Laboratory
Chemistry Division
Washington DC 20375-5342
(202)767-3340
DSN 297-3340

Dr James McMichael
AFOSR/NA
110 Duncan Avenue, Suite B115
Bolling AFB DC 20332-0001
(202)767-4936
DSN 297-4936
FAX: 767-4988
mcmichael@afosr.af.mil

Dr David Mann
U. S. Army Research Office
Engineering Sciences Division
P. O. Box 12211
Research Triangle Pk NC 27709-2211
(919)549-4249
DSN 832-4249
FAX: 549-4310
david@aro-emh1.army.mil

Dr Frank Marble
Engrg. and Appl. Sci. Dept.
California Institute of
Technology
Pasadena CA 91125
(818)395-4784

Dr Bruce Masson
PL/LIDD
3550 Aberdeen Avenue, SE
Building 401
Kirtland AFB NM 87117-5776
(505)844-0208
DSN 244-0208

Dr D K McLaughlin
233 Hammond Building
Pennsylvania State University
University Park PA 16802
(814)865-2569

Dr Constantine M Megaridis
University of Illinois-Chicago
Mechanical Engineering Dept
842 West Taylor Street
Chicago IL 60607-7022
(312)996-3436
(312)996-5317
FAX: 413-0447
cmm@dino.me.uic.edu

Dr A M Mellor
Mech & Mats Eng Department
Station B, Box 6019
Vanderbilt University
Nashville TN 37235
(615)343-6214

Dr R Metcalfe
Department of Mechanical
Engineering
University of Houston
Houston TX 77004
(713)749-2439

Dr Michael M Micci
Department of Aerospace Engrg
233 Hammond Building
Pennsylvania State University
University Park PA 16802
(814)863-0043
(814)692-8751
FAX:865-7092
mmm@ec1.psu.edu

Dr D L Mingori
Mechanical, Aerospace and
Nuclear Engineering Dept
University of California
Los Angeles CA 90024
(213)825-1265

Dr Parviz Moin
Center for Turbulence Research
Stanford University
Stanford CA 94305-3032
(415)725-2081

Dr Lynn Melton
Programs in Chemistry
University of Texas, Dallas
P. O. Box 830688
Richardson TX 75083-0688
(214)883-2913
(214)680-2163
FAX:883-2925
melton@utdallas.edu

Maj Howard Meyer
AL/EQC
139 Barnes Drive
Suite 2
Tyndall AFB FL 32403-5319
(904)283-6038
DSN 523-6038
FAX:283-6090
MeyerH@AFCEA1.AF.MIL

Dr Richard Miller
Office of Naval Research
Mechanics Division, Code 432
800 North Quincy Street
Arlington VA 22217-5000
(202)696-4406
FAX:696-0934
miller@ocnr-hq.navy.mil

Dr Andrzej Miziolek
Ignition and Combustion Branch
Interior Ballistics Division
Army Research Laboratory
Aberdeen Proving Gnd MD 21005-5066
(410)278-6157
FAX:278-6094

Dr Peter Monkewitz
Mechanical, Aerospace and
Nuclear Engineering Dept
University of California
Los Angeles CA 90024
(213)825-5217

Dr P J Morris
233-L Hammond Building
Pennsylvania State University
University Park PA 16802
(814)863-0157

Dr Edward Mularz
Attn: AMSRL-VP-C
NASA Lewis Res. Ctr., MS 5-11
21000 Brookpark Road
Cleveland OH 44135-3191
(216)433-5850
FAX:433-5802
Edward.Mularz@lims.lerc.nasa.gov

Dr M G Mungal
Department of Mechanical
Engineering
Stanford University
Stanford CA 94305-3032
(415)725-2019
(408)257-6702
FAX:723-1748
guff@navier.stanford.edu

Dr Phillip E Muntz
Department of Aerospace Engrg
Univ of Southern California
854 West 36th Place, RRB 101
Los Angeles CA 90089-1191
(213)740-5366

Dr Arje Nachman
AFOSR/NM
110 Duncan Avenue, Suite B115
Bolling AFB DC 20332-0001
(202)767-5028
DSN 297-5028
nachman@afosr.af.mil

Dr. Hassan M Nagib
Department of Mechanical and
Aerospace Engineering
Illinois Institute of Tech
Chicago IL 60616

Dr Abdollah Nejad
WL/POPT
Building 18
1921 Sixth Street, Suite 10
Wright-Patterson AFB OH 45433-7655
(513)255-9991
DSN 785-9991
FAX:255-1759
nejadas@possum.appl.af.mil

Dr Herbert Nelson
Code 6110, Chemistry Division
Naval Research Laboratory
4555 Overlook Avenue, SW
Washington DC 20375-5342
(202)767-3686

Dr David Nixon
NWING, Inc.
883 North Shoreline Boulevard
Suite B200
Mountain View CA 94043
(415)254-0202
FAX961-9286

Dr G B Northam
NASA Langley Research Center
MS 168
Hampton VA 23665-5225
(804)864-6248

Dr A K Oppenheim
Department of Mechanical
Engineering
University of California
Berkeley CA 94720
(415)642-0211

Dr Elaine Oran
LCP&FD, Code 6404
US Naval Research Laboratory
4555 Overlook Avenue, SW
Washington DC 20375-5344
(202)767-2960
FAX:767-4798
ORAN@lcp.nrl.navy.mil

Dr Simon Ostrach
Case Western Reserve Univ
Department of Mechanical and
Aerospace Engineering
Cleveland OH 44106

Dr Richard Peterson
Department of Mechanical
Engineering
Oregon State University
Corvallis OR 97331-6001
(503)754-2567

Dr Lisa Pfefferle
Department of Chemical
Engineering
Yale University
New Haven CT 06520-8286
(203)432-2222
FAX:432-7232
pfefferle@htcre.eng.yale.edu

Dr W M Pitts
National Institute of
Standards and Technology
Center for Fire Research
Gaithersburg MD 20899
(301)975-6486

Dr Robert Pitz
Department of Mechanical and
Materials Engineering
Vanderbilt University
Nashville TN 37235
(615)322-0209
FAX:343-8730
pitzrw@ctrvan.vanderbilt.edu

Dr S B Pope
Department of Mechanical and
Aerospace Engineering
Cornell University
Ithaca NY 14853-1301
(607)255-4314
FAX:255-1222
pope@pdf.tn.cornell.edu

Dr C L Proctor II
Department of Mechanical
Engineering
University of Florida
Gainesville FL 32611
(904)392-7555

Dr Herschel Rabitz
Department of Chemistry
Princeton University
Princeton NJ 08544-1009
(609)258-3917
FAX:258-6746

Dr Saad Ragab
Engrg Sci & Mechanics Dept
Virginia Polytechnic Institute
and State University
Blacksburg VA 24061
(703)231-5950

Dr S R Ray
National Institute of
Standards and Technology
Center for Chemical Engrg
Gaithersburg MD 20899

Dr. Mohan K. Razdan
Allison Engine Company
P.O. Box 420
Speed Code T-14
Indianapolis IN 46206-0420
(317)230-6404
FAX:230-3691
iemkr@agt.gmeds.com

Mr. Robert Reed
Sverdrup Technology, Inc.
AEDC
1099 Avenue C
Arnold AFB TN 37389-9013
(615)454-4648
DSN 340-4648
(615)454-6317

Dr R G Rehm
National Institute of
Standards and Technology
Center for Fire Research
Gaithersburg MD 20899
(301)975-2704

Dr Rolf D Reitz
Mechanical Engineering Dept
University of Wisconsin
1500 Johnson Drive
Madison WI 53706
(608)262-0145
FAX:262-6717

Dr M Renksizbulut
Department of Mechanical
Engineering
University of Waterloo
Waterloo, Ontario CN N2L 3G1
(519)885-1211
Ext 3977

Dr Eli Reshotko
Case Western Reserve Univ
Department of Mechanical and
Aerospace Engineering
Cleveland OH 44106
(216)368-6447
FAX:368-6445
exr3@po.cwru.edu

Dr David Reuss
Fluid Mechanics Department
General Motors Research Labs
30500 Mound Road
Warren MI 48090-9055
(313)986-0029

Dr William Reynolds
Department of Mechanical
Engineering
Stanford University
Stanford CA 94305-3032
(415)723-3840

Dr James Riley
Mechanical Engineering Dept
University of Washington
Seattle WA 98195
(206)543-5347

Dr Michael Roco
National Science Foundation
Chemical and Thermal Syst Div
4201 Wilson Boulevard
Arlington VA 22230
mroco@nsf.gov

Mr Wayne Roe
OLAC PL/XXR
5 Pollux Drive
Edwards AFB CA 93523-5000
(805)275-5206
DSN 525-5206
FAX:275-5852

Dr U S Rohatgi
Department of Nuclear Energy
Brookhaven National Laboratory
Upton NY 11973
(516)282-2475

Dr Glenn Rolader
Science Applications
International Corporation
1247-B N Eglin Parkway
Shalimar FL 32579
DSN 872-0391
(904)882-0391

Dr W M Roquemore
WL/POSC
Building 490
1790 Loop Road, N
Wright-Patterson AFB OH 45433-7103
(513)255-6813
DSN 785-6813
FAX:255-1125
Roquemwm@wl.wpafb.af.mil

Dr Anatol Roshko
Graduate Aeronautical Labs
California Institute of
Technology
Pasadena CA 91125
(818)395-4484

Dr Daniel Rosner
Department of Chemical
Engineering
Yale University
New Haven CT 06520-8286
(203)432-4391
FAX:432-7232
rosner@htcre.eng.yale.edu

Dr John Ross
Department of Chemistry
Stanford University
Stanford CA 94305-3032
(415)723-9203

Dr Gabriel Roy
Office of Naval Research
Mechanics Division, Code 1132
800 North Quincy Street
Arlington VA 22217-5000
(703)696-4405
FAX:696-0934
roy@ocnr-hq.navy.mil

Mr Kurt Sacksteder
NASA Lewis Research Center
MS 500-217
21000 Brookpark Road
Cleveland OH 44135
(216)433-2857

Dr Leonidas Sakell
AFOSR/NA
110 Duncan Avenue, Suite B115
Bolling AFB DC 20332-0001
(202)767-4935
DSN 297-4935
FAX:767-4988
sakell@afosr.af.mil

Dr Michael Salkind
President
Ohio Aerospace Institute
2001 Aerospace Parkway
Brookpark OH 44142
(216)891-2100

Dr Mohammad Samimy
Ohio State University
Mechanical Engineering Dept
206 West 18th Street
Columbus OH 43210-1107
(614)422-6988
(614)848-9439
FAX:292-3163
msamimy@magnus.acs.ohio-state.edu

Dr G S Samuelsen
Department of Mechanical
Engineering
University of California
Irvine CA 92717
(714)856-5468

Dr Billy Sanders
University of California
Davis CA 95616

Dr Joseph Sangiovanni
United Technologies Research
Center
Silver Lane
East Hartford CT 06108
(203)727-7328

Dr Lakshmi Sankar
School of Aerospace Engrg
Georgia Institute of
Technology
Atlanta GA 30332
(404)894-3014

Dr Domenic Santavicca
Department of Mechanical
Engineering
Pennsylvania State University
University Park PA 16802
(814)863-1863

Dr R J Santoro
Department of Mechanical
Engineering
Pennsylvania State University
University Park PA 16802-2320
(814)863-1285
FAX:865-3389
rjs@ec1.psu.edu

Dr Satanu Sarkar
Department of Applied Mech
and Engr Science, MC 0411
University of California
La Jolla CA 92093-0411
(619)534-8243
FAX: 534-7078
sarkar@ames.ucsd.edu

Mr William Scallion
NASA Langley Research Center
Mail Stop 408
Hampton VA 23665
(804)864-5235

Dr Klaus Schadow
Naval Air Warfare Center
Code 3892
China Lake CA 93555-6001
(619)939-6532
DSN 437-6532
FAX:939-6569

Dr John Schaefer
Energy and Environmental Div.
Acurex Corporation
555 Clyde Ave., P. O. Box 7555
Mountain View CA 94039

Dr W H Schofield
Aeronautical Research Labs
506 Lorimer St, Fishermen's Bn
Box 4331, P O
Melbourne, Victoria AUSTRALIA 3001

Maj Scott Schreck
AFOSR/NM
110 Duncan Avenue, Suite B115
Bolling AFB DC 20332-0001
(202)767-5028
DSN 297-5028
schreck@afosr.af.mil

Dr D J Seery
United Technologies Research
Center
Silver Lane
East Hartford CT 06108

Dr Hratch Semerjian
National Institute of
Standards and Technology
Chem Sci & Tech Laboratory
Gaithersburg MD 20899
(301)975-3145
FAX:975-3845
HRATCH@micf.nist.gov

Dr K Seshadri
Center for Energy and
Combustion Research, 0411
University of California
La Jolla CA 92093-0411
(619)534-4876

Dr G S Settles
309 Mechanical Engrg Building
Pennsylvania State University
University Park PA 16802
(814)863-1504

Dr Robert Shaw
Division of Chemical and
Biological Sciences
U S Army Research Office
Research Triangle Park NC 27709-2211
(919)549-0641

Mr David Siegel
Chief of Naval Research,
804 BCT1
800 North Quincy Street
Arlington VA 22217-5660
(703)696-4771
FAX:696-4274

Dr Neeraj Sinha
Science Applications
International Corporation
501 Office Ctr Dr, Suite 420
Fort Washington PA 19034-3211
(215)542-1200
FAX:542-8567

Dr William Sirignano
Department of Mechanical and
Aerospace Engineering
University of California
Irvine CA 92717-3975
(714)824-3700
FAX:824-3773
sirignan@uci.edu

Dr F Dee Stevenson
Office of Basic Energy Science
U. S. Department of Energy
1000 Independence Avenue, N W
Washington DC 20585

Dr David Stewart
Department of Theoretical and
Applied Mechanics
University of Illinois
Urbana IL 61801

Dr Anthony Strawa
NASA Ames Research Center
MS 230-2
Moffett Field CA 94035
(415)604-3437

Dr F D Stull
WL/POPS
Wright-Patterson AFB OH 45433-6563
(513)255-5210
DSN 785-5210

Dr Geoffrey J Sturgess
Pratt & Whitney Aircraft Group
United Technologies Corp
400 Main Street M/S 163-16
East Hartford CT 06108
(203)565-5437
(203)557-0687

Dr B Sturtevant
Engrg and Appl Sci Dept
California Institute of
Technology
Pasadena CA 91125

Dr G Sullins
Applied Physics Laboratory
Johns Hopkins University
Johns Hopkins Road
Laurel MD 20707-6099
(301)953-5000

Dr Larry Talbot
Department of Mechanical
Engineering
University of California
Berkeley CA 94720
(415)642-6780

Dr. Douglas Talley
OLAC PL/RKFA
9 Antares Road
Edwards AFB CA 93524-7660
(805)275-6174
DSN 525-6174

Dr Richard Tam
Department of Mathematics
Indiana University-Purdue
University
Indianapolis IN 46205

Dr Christopher Tam
Department of Mathematics
Florida State University
Tallahassee FL 32306-3027
(904)644-2455

Dr. Richard Tankin
Mechanical Engineering Dept
Northwestern University
Evanston IL 60208-3111
(708)491-3532
FAX:491-3915

Dr Julian Tishkoff
AFOSR/NA
110 Duncan Avenue, Suite B115
Bolling AFB DC 20332-0001
(202)767-0465
DSN 297-0465
FAX:767-4988
tishkoff@afosr.af.mil

Dr T Y Toong
Department of Mechanical
Engineering
MIT
Cambridge MA 02139
(617)253-3358

Dr Michael Trenary
Department of Chemistry
The University of Illinois
Chicago IL 60680

Dr Timothy Troutt
Department of Mechanical
Engineering
Washington State University
Pullman WA 99164-2920

Dr Allen Twarowski
Rockwell International Sci Ctr
1049 Camino dos Rios
P O Box 1085
Thousand Oaks CA 91360
(805)373-4576
FAX:373-4775
ajtwarow@scimail.remnet.rockwell.com

Dr A D Vakili
University of Tennessee
Space Institute
Tullahoma TN 37388

Dr Earl VanLandingham
National Aeronautics & Space
Administration, Code RB
400 Maryland Avenue, SW
Washington DC 20546
(202)453-2847

Dr P J Waltrup
Applied Physics Laboratory
Johns Hopkins University
Johns Hopkins Road
Laurel MD 20707-6099
(301)953-5000
Ext. 5626

Dr David Weaver
OLAC PL/RKFA
10 East Saturn Boulevard
Edwards AFB CA 93524-7660
(805)275-6177
DSN 525-6177
FAX:275-5471
weaver@scihpl.ple.af.mil

Dr C J Ultee
United Technologies Research
Center
Silver Lane
East Hartford CT 06108

Dr S P Vanka
Department of Mechanical
and Industrial Engrg
University of Illinois
Urbana IL 61801

Dr Juan A. Vitali
WL/FIVCO (Stop 37)
139 Barnes Drive, Suite 2
Tyndall AFB FL 32403-5323
(904)283-9708
DSN 523-9708
FAX:283-9707
75023.56@compuserve.com

Dr Joe Wanders
AL/EQS
139 Barnes Drive
Tyndall AFB FL 32403-5319
(904)283-6026
DSN 523-6026

Dr Charles Westbrook
Lawrence Livermore National
Laboratories
P. O. Box 808
Livermore CA 94550

Dr. Phillip R. Westmoreland
Department of Chemical
Engineering
University of Massachusetts
Amherst MA 01003
(413)545-1750
(413)545-2507
(413)545-1647
westm@ecs.umass.edu

Dr Forman Williams
Center for Energy and
Combustion Research, 0310
University of California
La Jolla CA 92093-0310
(619)534-5492
(619)534-4285
FAX: 534-5354
faw@ames.ucsd.edu

Mr Steve Wirick
WL/AAWW-3
Wright-Patterson AFB OH 45433-6543
(513)255-4174
DSN 785-4174
FAX:476-4642

Dr J M Wu
University of Tennessee
Space Institute
Tullahoma TN 37388

Dr Pui-kuen Yeung
School of Aerospace Engrg
Georgia Institute of
Technology
Atlanta GA 30332-0150
(404)894-9341
FAX:894-2760
yeung@peach.gatech.edu

Dr James Whitelaw
Department of Mechanical Engrg
Imperial College of Science
and Technology
London SW7 2BX UK

Dr Michael Winter
United Technologies Research
Center
411 Silver Lane, MS/90
East Hartford CT 06108
(203)727-7805
(203)397-1420
FAX:727-7911
mw@utrc.utc.com

Dr Bernard T Wolfson
Wolfson Associates
International
4797 Lake Valencia Blvd West
Palm Harbor FL 33563
(813)786-3007

Dr Richard Yetter
Department of Mechanical and
Aerospace Engineering
Princeton University
Princeton NJ 08544-5263

Dr Shaye Yungster
Institute for Computational
Mechanics in Propulsion
NASA Lewis Research Ctr
Cleveland OH 44135
(216)433-6680

Dr Michael Zachariah
National Institute of
Standards and Technology
Center for Chemical Engrg
Gaithersburg MD 20899
(301)975-2063

Mr Fred Zarlingo
Code 3246
Naval Air Warfare Center
China Lake CA 93555-6001
(619)939-7395
DSN 437-7395

Dr E E Zukoski
Engrg. and Appl. Sci. Dept.
California Institute of
Technology
Pasadena CA 91125
(818)395-4785

PROPULSION DIAGNOSTICS

Invitees

Dr William Bachalo
Aerometrics, Inc.
550 Del Rey Avenue
Unit A
Sunnyvale CA 94086
(408)738-6688

Dr Edward Beiting
Aerophysics Lab, Prop & Env Sc
The Aerospace Corporation
P O Box 92957, M5/754
Los Angeles CA 90009-2957
(310)336-7035

Dr Richard Chang
Applied Physics Department
P. O. Box 208284
Yale University
New Haven CT 06520-8284
(203)432-4272
FAX: 432-4274
RK_CHANG@RAMAN.ENG.YALE.EDU

Dr Wai K Cheng
Department of Mechanical
Engineering
MIT
Cambridge MA 02139
(617)253-4531

Dr David Crosley
Molecular Physics Department
SRI International
333 Ravenswood Avenue
Menlo Park CA 94025-3696
(415)326-6200

Dr Robert Dibble
Department of Mechanical Eng
6159 Etcheverry Hall
University of California
Berkeley CA 94720
(415)294-2825

Dr Gregory Dobbs
United Technologies Research
Center - Mail Stop 90
Silver Lane
East Hartford CT 06108
(203)727-7145

Dr A C Eckbreth
United Technologies Research
Center
Silver Lane
East Hartford CT 06108
(203)727-7269

Dr Thomas Ehlert
Department of Chemistry
Marquette University
Milwaukee WI 53233
(414)288-7066

Dr Gregory Faris
SRI International
333 Ravenswood Avenue
Menlo Park CA 94025-3493
(415)859-4131
FAX: 859-6196
faris@mplvax.sri.com

Dr Richard Field
U. S. Army Armament R&D Center
DRSMC-LCA-G(D)
Building 382-S
Dover NJ 07801
(201)724-5844
(201)724-5682

Dr Bish Ganguly
WL/POOC-3
Wright-Patterson AFB OH 45433-6563
(513)255-2923
DSN 785-2923
FAX:476-4095

Dr Alan Garscadden
WL/CA-P
Building 18
1921 Sixth Street, Suite 5
Wright-Patterson AFB OH 45433-7650
(513)255-2246
DSN 785-2246
FAX:476-4657

Dr Larry Goss
Research Applications Division
Systems Research Labs, Inc.
2800 Indian Ripple Road
Dayton OH 45440-3696
(513)252-2706

Dr Ronald Hanson
Department of Mechanical
Engineering
Stanford University
Stanford CA 94305-3032
(415)723-1745
FAX:723-1748
hanson@navier.stanford.edu

Dr D L Hartley
Sandia National Laboratories
MS0735
Albuquerque NM 87185-5800

Dr Cecil F. Hess
MetroLaser
18006 Skypark Circle
Suite 108
Irvine CA 92714-6428
(714)553-0688
FAX:553-0495

Dr L Hesselink
Department of Aeronautics and
Astronautics
Stanford University
Stanford CA 94305-3032
(415)723-3466

Dr E D Hirleman
Department of Mechanical and
Aerospace Engineering
Arizona State University
Tempe AZ 85287
(602)965-3895
FAX:965-1384

Dr David Huestis
SRI International
333 Ravenswood Avenue
Menlo Park CA 94025-3493
(415)859-3464
(415)325-4568
FAX:859-6196
huestis@mplvax.sri.com

Dr Thomas Ishii
Department of Electrical
Engineering
Marquette University
Milwaukee WI 53233
(414)288-6998
FAX:288-7082

Dr Jay Jeffries
SRI International
333 Ravenswood Avenue
Menlo Park CA 94025-3493
(415)859-6341
(415)473-1553
FAX:473-6196
jeffries@mplvax.sri.com

Dr Sheridan Johnston
Combustion Sciences
Sandia National Laboratories
Livermore CA 94551-0969
(510)294-2138

Dr G B King
Department of Mechanical
Engineering
Purdue University
West Lafayette IN 47907
(317)494-6518
kinggb@mn.purdue.edu

Dr Roman Kuc
Department of Electrical
Engineering
Yale University
New Haven CT 06520
(203)432-4891

Dr Normand Laurendeau
Department of Mechanical
Engineering
Purdue University
West Lafayette IN 47907
(317)494-2713

Dr Marshall Long
Department of Mechanical
Engineering
Yale University
New Haven CT 06520
(203)432-4229

Dr Bruce MacDonald
Research Applications Division
Systems Research Labs, Inc.
2800 Indian Ripple Road
Dayton OH 45440-3696
(513)252-2706

Dr T E Parker
Engineering Division
Colorado School of Mines
Golden CO 80401-1887
(303)273-3657
FAX:273-3602
tparker@mines.colorado.edu

Dr Timothy Parr
Naval Air Warfare Center
Weapons Division
C02392
China Lake CA 93555-6001
(619)939-3367
FAX:939-6569
t.parr@genie.geis.com

Dr S S Penner
Center for Energy and
Combustion Research, 0411
University of California
La Jolla CA 92093-0411
(619)534-4284

Dr Emil Pfender
Department of Mechanical Engrg
125 Mechanical Engineering
The University of Minnesota
Minneapolis MN 55455

Dr Won B Roh
Department of Engrg Physics
Air Force Institute of
Technology
Wright-Patterson AFB OH 45433-6583

Dr Gregory Smith
Department of Chem Kinetics
SRI International
333 Ravenswood Avenue
Menlo Park CA 94025-3493
(415)859-3496

Dr Alan Stanton
Southwest Sciences, Inc.
1570 Pacheco Street
Suite E-11
Santa Fe NM 87501
(505)984-1322

Dr James Trolinger
MetroLaser
18006 Skypark Circle
Suite 108
Irvine CA 92714-6428
(714)553-0688
FAX:553-0495
jtrolinger@vmsa.oac.uci.edu

Dr John Vanderhoff
Ballistic Research Laboratory
DRSMC-BLI(A)
Aberdeen Proving Ground MD 21005
(410)278-6642

Dr James Verdieck
Rockwell International
Rocketdyne Div, M/S FA26
6633 Canoga Avenue
Canoga Park CA 91303
(818)700-4709

Dr Joda Wormhoudt
Aerodyne Research, Inc.
45 Manning Road
Manning Park Research Center
Billerica MA 01821-3976
(508)663-9500
FAX:663-4918